Methodologische studie van de waterstofdiffusie in staal
met behulp van elektrochemische permeatie

Methodological Study of the Hydrogen Diffusion in Steel
by Means of Electrochemical Permeation

Emilie Van den Eeckhout

Promotoren: prof. dr. ir. K. Verbeken, prof. dr. ir. Y. Van Ingelgem
Proefschrift ingediend tot het behalen van de graad van
Doctor in de ingenieurswetenschappen: materiaalkunde

UNIVERSITEIT
GENT

Vakgroep Materialen, Textiel en Chemische Proceskunde
Voorzitter: prof. dr. P. Kiekens
Faculteit Ingenieurswetenschappen en Architectuur
Academiejaar 2018 - 2019

ISBN 978-94-6355-205-9
NUR 971
Wettelijk depot: D/2019/10.500/13

Members of the examination board

em. prof. dr. ir. Daniël De Zutter
Voorzitter, Universiteit Gent

prof. dr. Abdelali Oudriss
Université de La Rochelle

prof. dr. ir. Iris De Graeve
Vrije Universiteit Brussel

dr. Antonin Prévoteau
Universiteit Gent

dr. ir. Tom Depover
Universiteit Gent

dr. ir. Cédric Georges
Centre de Recherches Métallurgiques
Liège

Dankwoord

Mijn woord van dank, veruit de meest bekeken, al dan niet gelezen, pagina van dit werk. Zoals je wel weet, heb ik dit doctoraat niet in mijn eentje tot een goed einde gebracht. Eerst en vooral was er geld nodig. Enerzijds om mijn rekening aan te dikken, anderzijds om de nodige apparatuur, vereist voor dit doctoraat, te kunnen aankopen. Dit geld was te danken aan het MaDuRos (SIM) programma wat deel uitmaakte van het DeMoPreCI-MDT project. Ten tweede moest er iemand bereid zijn dat geld aan mij te spenderen, iemand die in mij geloofde.

Mijn eerste werk- of schooldag, aan jou de keuze, startte op 1 september 2014. Dat had ik vooral te danken aan mijn promotor Kim Verbeken. Maar ook mijn ouders en grote broer hebben daar een deel van uitgemaakt. Zonder hen zou ik niet de persoon zijn wie ik nu ben en dus ook zeker niet wie Kim wou aannemen een viertal jaar geleden. Zij hebben me gesteund in alle keuzes, groot of klein, die ik heb moeten maken. En enkel zij weten hoe goed ik daar in ben… Bij deze, mama, papa, broer, een oprechte merci omdat jullie er altijd voor me zijn.

Kim, ook jij hebt me steeds gesteund in de keuzes die ik heb moeten maken tijdens dit doctoraat. Door me mijn eigen weg te laten gaan, en in mij te geloven, heb ik veel bijgeleerd waar ik je echt dankbaar voor ben.

Concluderend, zonder Kim en mijn familie zou ik nu hier niet zitten schrijven dat mijn voorbije vierenhalf jaar echt boeiend, leerrijk en leuk was. Het leuke gedeelte heb ik mede te danken aan mijn collega's. Het is inderdaad een cliché om de collega's te bedanken, maar hier en nu, meen ik het ook echt. We hebben gelachen, gegeten, gediscussieerd, soms geweend, gedronken, gedanst, en veel gepraat. Vooral veel gepraat ja. Eerlijk gezegd, ik heb nu al wat schrik dat het niet beter zal worden dan dit.

Naast de collega's zijn er ook vrienden die ik graag wil bedanken voor de vele leuke momenten in de afgelopen jaren. Zij zorgden en zorgen er nog steeds voor dat ik niet elke dag thuis in de zetel moet zitten. Behalve op zondag dan. Maar met wat geluk kan ik dan terugvallen op Mathieu, mijn lief, want die zit daar op zondag meestal ook. Bij deze wil ik hem ook in het bijzonder eens bedanken, gewoon, om er te zijn.

Familie, collega's en vrienden. Schone verdeling. Maar dan heb ik ook nog **Aurélie**, iemand die voor mij behoort tot de drie zojuist genoemde categorieën. *(Ja Aurélie, je staat in mijn dankwoord, en speciaal in het vet zodat je niet lang hoefde te zoeken naar jouw naam.)* Tijdens de afgelopen vier jaar was jij er altijd. Antwoorden op bijna al mijn vragen, een al dan niet wetenschappelijke discussie, een knuffel, een reisje, een geheim briefje, motivatie, hulp in het labo, het verbeteren van mijn tekst, een vieruurtje,… Voor dit alles, en waarschijnlijk nog veel meer, kon, en kan, ik bij jou terecht. Ook al vind ik dat woorden hier tekortkomen, wil ik je toch echt graag bedanken voor je steun. Nu jij hier bij Kim blijft, wat trouwens niet

de afspraak was, wordt het nu wel eens tijd dat je je gsm begint bij te houden voor als ik je nog eens nodig zou hebben.

Michel. Ik mag van geluk spreken dat Michel af en toe eens op bezoek kwam met de vraag: “Oe ist maske?”. Toegevoegde waarde, dat heb ik aan hem te danken. Zijn kennis en passie voor onderzoek, daar sta ik van versteld. “Merci Michel, en veel plezier op den tennis!”

Niet te vergeten, ook een dikke merci aan de mannen van de Sterre die geholpen hebben met het bouwen van de nieuwe opstelling. Voor het uitvoeren van testen wil ik oprecht bedanken: Ives De Baere, Kim De Weerdt, Kitty Baert, Kannaki Pondicherry, en Joachim Neri. Yves Van Ingelgem, bedankt voor de antwoorden op mijn elektrochemische twijfels. Onze techniekers, Marnix, Alex, Pascal en Luc, merci om te luisteren en mij te helpen waar nodig. Ook zonder jullie was het niet gelukt.

Summary

Nowadays, hydrogen is known as a clean and environmentally friendly alternative for the finite fossil fuels. As no CO_2 emissions are provoked by its combustion, a hydrogen economy would be one solution to the problem of climate change. Decarbonizing of the gas grid by replacement of the domestic supply with hydrogen and using hydrogen as a fuel in the automotive industry are two examples to illustrate the potential beneficial impact on the climate change the world is currently facing. Alternatively, lowering the fuel consumption is also a very relevant approach to make transportation more ecological and to meet the targets on CO_2 emission. Steels with an increased strength level are therefore necessary to create safe and lower weight structures, resulting in a decrease of the fuel consumption. Material scientists have developed such materials to satisfy the high structural and cost-efficient requirements from industry. However, there is the possibility for these materials to come into contact with a hydrogen containing environment. As such, to guarantee safety issues, these materials cannot be used when the hydrogen induced degradation problem is not fully understood or solved as these advanced high strength steels are reported to be prone to hydrogen embrittlement.

Also in the offshore industry the hydrogen embrittlement phenomenon cannot be ignored. The high strength steels used for offshore applications may be protected against corrosion by the use of an imposed current. The electric current ensures that the steel acts as a cathode and thus protects the constructions against anodic dissolution. However, at (too) high currents, the reduction of water becomes prominent and hydrogen is formed which can be absorbed in the material. Therefore, in order to preclude unforeseen failure of the construction, it is necessary to understand the effect of hydrogen on the used high strength steel.

The detrimental effect of hydrogen on steel is that it reduces the mechanical performance. As such, there is an increased tendency for crack formation leading to a potentially unpredictable failure. Nonetheless, a certain hydrogen concentration is required to initiate and propagate a crack in the microstructure. The susceptibility of the material to hydrogen induced damage depends thus on the amount of hydrogen able to diffuse to critical, for example highly stressed, regions in the microstructure. Since hydrogen is attracted to these regions, the required concentration for crack propagation can be reached more easily. However, next to the hydrogen concentration, the ability to reach the critical stress zones is a very important parameter which cannot be ignored. This ability factor can be associated with the hydrogen diffusion coefficient of the material which can be obtained via the electrochemical hydrogen permeation technique.

In this work, first the basic concepts of the hydrogen/material interaction and hydrogen diffusion are elaborated in a literature study. In the following experimental chapter, two standard permeation test methods are described which are used during this research. Moreover, the way the diffusion coefficient was calculated is described.

In chapter III, several experimental parameters of the permeation experiment were evaluated in detail in order to obtain a better control and understanding concerning the electrochemical hydrogen permeation technique. For this study, pure Armco iron and dual phase steel were investigated. It was found that the surface roughness and the purity of the electrolyte are of significant importance for realizing a stable entrance surface state, i.e. hydrogen entry flux. Due to the specific texture of the surface, the hydrogen gas bubble formation was modified and iron oxidation was hindered, leading to a more consistent hydrogen uptake. An even more stable entrance potential, i.e. surface state, was obtained by using ultrapure Milli Q water instead of demi water for making the electrolyte. It was observed that cations, present in the demi water, were deposited at the cathodic surface causing an increase in the hydrogen uptake during the experiment. This resulted in a relevant deflection of the experimental transient from the theoretical one based on Fick's law. The high resistivity of the Milli Q water mainly excluded this undesired effect and as such, almost a perfect fit was obtained.

The effect of cold deformation and subsequent annealing on hydrogen diffusion and blister formation of pure Armco iron was investigated in Chapter IV. Cold deformation and a recovery heat treatment were applied to vary the dislocation density and modify grain boundary characteristics. With this study, a deeper insight was obtained concerning the influence of dislocations and grain boundaries on the hydrogen diffusivity in pure Armco iron. The diffusivity results were correlated with the accompanying microstructural changes of the material. A higher degree of deformation reduced the hydrogen diffusivity and resulted in a more heavily blistered sample surface. Due to the cold deformation process, additional barriers for hydrogen diffusion and suitable nucleation places for blisters were created.

The recovery heat treatment of the deformed material resulted in the annihilation of vacancies, vacancy clusters, and in rearrangements of the dislocation configurations as EBSD measurements did not reveal a decrease of the geometrically necessary dislocation density. The statistically stored dislocation density was also considered to be constant as the hardness drop, due to the heat treatment, was minimal. Furthermore, the heat treatment caused an increased hydrogen diffusion coefficient and a decreased number of potential blister nucleation sites. Therefore, it was argued that the hydrogen diffusivity cannot be directly correlated with the dislocation density, but rather with dislocation configurations and internal stresses of the material's microstructure.

Chapter V discusses the influence of W_2C, $Cr_{23}C_6$, TiC and V_4C_3, together with other potential trapping sites in the microstructure, on the shape of the permeation transient and hydrogen diffusivity. The materials were four carbide containing quenched and tempered Fe-C-X alloys, with X = W, Cr, Ti or V. The delay of the permeation transient, i.e. hydrogen breakthrough time, was associated with the overall trap density while the slope of the transient was related to the amount of reversible trapping sites. The highest trapping ability was observed for the V-based alloy followed in decreasing order by the Fe-C-Ti, Fe-C-Cr and the Fe-C-W material. All carbides, except for the W-based ones, had the ability to lower the hydrogen diffusion in the material and thus, to trap hydrogen. Next to the carbide amount and size, the martensitic matrix

characteristics and hydrogen desorption activation energy of the trapping sites played a crucial role in the hydrogen diffusivity of the material.

When steel is used in structural applications, it will experience different levels of stress during its lifespan. Plastic deformations may be at hand during production, whereas elastic stresses are ubiquitous in most structural applications. If the hydrogen diffusivity increases with these stresses, critical concentrations necessary for hydrogen induced damage will be reached more easily. Therefore, the influence of a constant load on the hydrogen diffusion was studied in Chapter VI.

Results showed that elastic tensile stresses increased the hydrogen diffusion coefficient of DP steel and Armco iron. Due to the elastic stress, the lattice expanded which was beneficial for the hydrogen diffusivity. This statement was verified by studying the concentration dependence of the diffusion coefficient as a higher hydrogen uptake in the subsurface of the specimen with increasing strain could also be responsible for the increased diffusion rate. From a constant load of 100% of the YS and higher, the diffusivity again decreased which was associated to the formation of lattice defects such as vacancies, vacancy clusters and dislocations.

Samenvatting

Waterstof als energiedrager staat bekend als een milieuvriendelijk alternatief voor de eindige voorraad aan fossiele brandstoffen. Aangezien er geen CO_2 gegenereerd wordt bij de verbranding ervan, zou een economie gebaseerd op waterstof één van de oplossingen zijn om de klimaatopwarming tegen te gaan. Het decarboniseren van het gasnet door aardgas te vervangen met waterstof en ook het gebruik van waterstof in de automobielindustrie, zijn twee voorbeelden die een voordelige impact zouden hebben op de klimaatverandering. Een alternatief om het brandstofverbruik in de automobielindustrie te verminderen en dus de eisen omtrent CO_2-reductie tegemoet te komen, kan ook mede gerealiseerd worden door het maken van lichtere wagens. Om dit te verwezenlijken moet staal ontwikkeld worden met een verhoogde sterkte. Op die manier wordt de sterkte van de structuur behouden wanneer een kleiner volume aan materiaal wordt gebruikt. Wetenschappers hebben reeds materialen ontwikkeld die voldoen aan die hoge structurele en economische eisen van de industrie. Desalniettemin zijn er talloze mogelijkheden voor deze materialen om in contact te komen met waterstof en jammer genoeg zijn deze hoogsterktestalen extra gevoelig aan waterstofverbrossing. Om veiligheidsredenen, kunnen deze materialen dus niet gebruikt worden tot wanneer het schadelijk effect veroorzaakt door waterstof, volledig begrepen is.

Ook in de offshore industrie kan het schadelijke effect van waterstof op staal niet genegeerd worden. De hoogsterkte-staalsoorten die worden gebruikt voor offshore toepassingen kunnen worden beschermd tegen corrosie door het opleggen van een elektrische stroom. Deze stroom zorgt ervoor dat het staaloppervlak als kathode fungeert en weerhoudt dus op die manier het anodisch oplossen van de constructie. Bij (te) hoge stromen zal echter ook de reductiereactie van water prominent optreden en wordt er waterstof gevormd dat kan geabsorbeerd worden in het materiaal. Om dus het onverwachte falen van de constructie uit te sluiten is het noodzakelijk om het effect van waterstof op het gebruikte hoogsterktestaal te begrijpen.

De aanwezigheid van waterstof in staal kan een verzwakking van de mechanische eigenschappen veroorzaken. Op die manier is er een verhoogde kans op scheurinitiatie en propagatie, wat de kans verhoogt op een mogelijks onverwacht falen van de structuur. Dergelijk onvoorspelbare scheurvorming is natuurlijk problematisch. Er is echter een bepaalde waterstofconcentratie vereist om een scheur in de microstructuur te initiëren en te laten propageren. De weerstand van het materiaal tegen waterstof-geïnduceerde schade hangt dus af van de hoeveelheid waterstof die kan diffunderen naar kritische plaatsen in de microstructuur. Een mogelijk kritische plaats is bijvoorbeeld een regio met een verhoogde spanningstoestand, bijvoorbeeld een scheurtip. Aangezien waterstof wordt aangetrokken tot deze plaatsen, kan de vereiste concentratie voor scheurinitiatie en -propagatie sneller worden bereikt. Naast de waterstofconcentratie is ook de snelheid

waarmee waterstof deze verhoogde spanningszones kan bereiken een uitermate belangrijke factor die niet kan worden genegeerd. De snelheid waarmee waterstof doorheen het rooster diffundeert, is gelinkt met de waterstofdiffusiecoëfficiënt welke kan worden bepaald met behulp van de elektrochemische permeatietechniek.

In dit onderzoek worden eerst de basisconcepten omtrent de interactie tussen waterstof en staal toegelicht. Het daaropvolgende experimentele hoofdstuk beschrijft twee standaard testmethodes voor permeatie die tijdens dit onderzoek werden toegepast. Bovendien wordt ook toegelicht op welke manier de diffusiecoëfficiënten werden berekend.

In hoofdstuk III worden verschillende experimentele parameters van de permeatietechniek geëvalueerd. Door het wijzigen van deze parameters en de resultaten te verwerken, werd een groter begrip en controle verkregen omtrent deze meettechniek. Voor deze studie werd gebruik gemaakt van zuiver Armco ijzer en 'dual phase' staal. Om de stabiliteit van de oppervlaktetoestand van het materiaal te garanderen is een bepaalde oppervlakteruwheid en zuiverheid van de elektrolyt van groot belang. Vanwege de specifieke textuur van het oppervlak werd de H_2 vorming zodanig gewijzigd dat de oxidatie van het staal geminimaliseerd werd. Dit leidde tot een meer stabiele potentiaal aan de ingang, welke gelinkt is met de oppervlaktetoestand van het monster. Op die manier werd dus een constante flux van waterstofopname bekomen. Een nog meer standvastige ingangspotentiaal werd verkregen door het gebruik van ultra zuiver Milli Q water, in plaats van demi water, voor het maken van de elektrolyt. De kationen, aanwezig in het demi water, werden tijdens de permeatietest gereduceerd op het kathodisch oppervlak. Dit veroorzaakte een toename in de waterstofopname tijdens het experiment, wat op zijn beurt resulteerde in een afwijking van de experimentele permeatiecurve ten opzichte van de theoretische transiënt gebaseerd op de diffusiewet van Fick. Door het gebruik van het Milli Q water, met een zeer lage concentratie kationen en dus een hoge soortelijke weerstand, werd dit ongewenst effect geminimaliseerd en werd een bijna perfecte fit verkregen.

Het effect van koudvervorming en een daarna uitgevoerde gloeibehandeling op de waterstofdiffusie en op de vorming van waterstofblisters op het oppervlak van zuiver Armco ijzer wordt besproken in hoofdstuk IV. De vervorming en gloeibehandeling werden toegepast om op die manier de dislocatiedichtheid en korrelgrenskarakteristieken te wijzigen. Met deze studie werd dan ook meer inzicht verkregen over de invloed van dislocaties en korrelgrenzen op de diffusie van waterstof door het zuiver Armco ijzer. De permeatieresultaten werden gelinkt met de microstructurele veranderingen van het materiaal. Een hogere hoeveelheid koudvervorming leidde tot een vertraagde diffusiesnelheid en een grotere hoeveelheid blisters

op het oppervlak. Dit was te wijten aan de extra barrières voor waterstofdiffusie en geschikte blister nucleatieplaatsen, gecreëerd door het koudvervormingsproces.

De gloeibehandeling van het vervormde materiaal resulteerde in de annihilatie van vacatures, vacature clusters en in een herschikking van de dislocatie configuraties. Deze laatste vaststelling was gebaseerd op EBSD metingen die geen afname van de geometrisch noodzakelijke dislocatiedichtheid vertoonde. De statistisch opgeslagen dislocatiedichtheid werd ook als constant beschouwd aangezien de verlaagde hardheid van het monster, als gevolg van de warmtebehandeling, minimaal was. Verder veroorzaakte de warmtebehandeling een verhoogde diffusiecoëfficiënt en een verminderd aantal potentiële blisternucleatieplaatsen. De conclusie kon getrokken worden dat de diffusie van waterstof niet direct gecorreleerd kan worden met de dislocatiedichtheid, maar eerder met de dislocatieconfiguraties en interne spanningen van de microstructuur van het materiaal.

In hoofdstuk V wordt de invloed van W_2C, $Cr_{23}C_6$, TiC and V_4C_3, en andere microstructurele elementen, op de vorm van de permeatiecurve en waterstofdiffusie besproken. De materialen waren vier Fe-C-X generische legeringen met X zijnde elk hun carbidevormend element, namelijk W, Cr, Ti en V. De microstructuur was afgeschrikt en ontlaten. De laterale verschuiving van de permeatiecurve, gelinkt met de waterstof doorbraaktijd, kon worden geassocieerd met alle waterstoftraps aanwezig in de microstructuur. De helling van de curve daarentegen, was gerelateerd aan de reversibele trap hoeveelheid. De legering met V vertoonde de hoogste capaciteit om waterstof te vangen, gevolgd in afnemende volgorde door het Fe-C-Ti, Fe-C-Cr en het Fe-C-W-materiaal. Alle carbides, behalve de W-carbides, vertraagden de waterstofdiffusie in het materiaal door het waterstof te vangen. Naast de carbidehoeveelheid en grootte, speelden de kenmerken van de martensitische matrix en de desorptie activeringsenergie van de traps een cruciale rol in de waterstofdiffusie van het materiaal.

Wanneer staal wordt gebruikt in structurele toepassingen zal het gedurende zijn levenscyclus verschillende niveaus van stress ervaren. Tijdens de productie zijn plastische vervormingen mogelijk, terwijl elastische spanningen alomtegenwoordig zijn in de meeste structurele toepassingen. Als de diffusie van waterstof toeneemt met de opgelegde spanningstoestand, zal de kritische concentratie, nodig voor het ontstaan van waterstofschade, sneller worden bereikt. Daarom werd de invloed van een constante belasting op de waterstofdiffusie bestudeerd. De resultaten worden besproken in Hoofdstuk VI.

Wanneer een constante elastische trekspanning op het staal werd aangelegd gedurende het permeatie experiment, werd een verhoogde waterstofdiffusiecoëfficiënt van het ‘dual phase’ staal en Armco ijzer

waargenomen. Vanwege de elastische spanning vergrootte de eenheidscel van het kristalrooster, hetgeen gunstig was voor de diffusie van waterstof doorheen het materiaal. Deze vaststelling werd geverifieerd door de concentratieafhankelijkheid van de diffusiecoëfficiënt te bestuderen. Wanneer een spanning wordt aangebracht op een materiaal, is een verhoogde waterstofopname mogelijk. Deze verhoogde concentratie zou dan op zijn beurt ook verantwoordelijk kunnen zijn voor een verhoogde diffusiesnelheid. De verhoogde diffusiecoëfficiënt werd in dit geval gecorreleerd aan de uiteenzetting van het kristalrooster. Vanaf een constante belasting van 100% van de vloeigrens werd opnieuw een vertraging in de diffusiesnelheid waargenomen, als gevolg van de vorming van roosterdefecten zoals vacatures, vacature-clusters en dislocaties die geïnitieerd werden door de plastische vervorming.

List of publications

Journals

1. E. Van den Eeckhout, A. Laureys, Y. Van Ingelgem, and K. Verbeken, Hydrogen permeation through deformed and heat-treated Armco iron, *Materials Science and Technology,* vol. 33, pp. 1515-1523, 2017.
2. E. Van den Eeckhout, T. Depover, and K. Verbeken, The effect of microstructural characteristics on the hydrogen permeation transient in quenched and tempered martensitic alloys, *Metals*, vol. 8, 779, 2018.
3. T. Depover, E. Van den Eeckhout, and K. Verbeken, The impact of hydrogen on the ductility loss of bainitic Fe–C alloys, *Materials Science and Technology*, vol. 32, pp. 1625-1631, 2016.
4. T. Depover, E. Van den Eeckhout, and K. Verbeken, Hydrogen induced mechanical degradation in tungsten alloyed steels, *Materials Characterization*, vol. 136, pp. 84-93, 2018.
5. T. Depover, A. Laureys, D. P. Escobar, E. Van den Eeckhout, E. Wallaert, and K. Verbeken, Understanding the Interaction between a Steel Microstructure and Hydrogen, *Materials*, vol. 11, 2018.
6. A. Laureys, E. Van den Eeckhout, R. Petrov, and K. Verbeken, Effect of deformation and charging conditions on crack and blister formation during electrochemical hydrogen charging, *Acta Materialia*, vol. 127, pp. 192-202, 2017.
7. A. Laureys, L. Claeys, T. De Seranno, T. Depover, E. Van den Eeckhout, R. Petrov, K. Verbeken, The role of titanium and vanadium based precipitates on hydrogen induced degradation of ferritic materials, *Materials Characterization*, vol. 144, pp. 22-34, 2018.
8. L. Vecchi, H. Simillion, R. Montoya, D. Van Laethem, E. Van den Eeckhout, K. Verbeken, et al., Modelling of hydrogen permeation experiments in iron alloys: Characterization of the accessible parameters–Part I–The entry side, *Electrochimica Acta*, vol. 262, pp. 57-65, 2018.
9. L. Vecchi, H. Simillion, R. Montoya, D. Van Laethem, E. Van den Eeckhout, K. Verbeken, et al., Modelling of hydrogen permeation experiments in iron alloys: Characterization of the accessible parameters–Part II–The exit side, *Electrochimica Acta*, vol. 262, pp. 153-161, 2018.

Conference contributions

1. T. Depover, E. Van den Eeckhout, E. Wallaert, Z. Zermout, and K. Verbeken, Evaluation of the effect of TiC precipitates on the hydrogen trapping capacity of Fe-C-Ti alloys, *Advanced Materials Research*, vol. 922, 2014.
2. E. Van den Eeckhout, A. Laureys, and K. Verbeken, Experimental Study on Hydrogen Induced Cracking in Deformed and Heat Treated Armco Pure Iron, *International Hydrogen Conference*, Wyoming (USA), 2016.
3. T. Depover , E. Van den Eeckhout, K. Verbeken, Comparison of the role of four different carbides in the hydrogen induced mechanical degradation of lab cast Fe-C-X alloys, *International Hydrogen Conference*, Wyoming (USA), 2016.

Oral presentations

1. E. Van den Eeckhout, T. Depover, K. Verbeken, The impact of the carbon content on hydrogen diffusion and its influence on hydrogen embrittlement for lab-cast bainitic Fe-C steels, *DPG Spring Meeting*, Berlin (Germany), 2015.
2. E. Van den Eeckhout, K. Verbeken, The role of microstructural defects on hydrogen diffusion in Armco iron, *SNEAC workshop*, Trondheim (Norway), 2016.
3. E. Van den Eeckhout, T. Depover, K. Verbeken, The hydrogen trapping effect of carbides on hydrogen permeation in Fe-C-X alloys, *Hydrogen symposium*, Ghent (Belgium), 2018.

Poster presentations

1. E. Van den Eeckhout, T. Depover, K. Verbeken, The impact of the hydrogen diffusivity on the mechanical performance of lab-cast Fe-C steel, *DPG Spring Meeting*, Berlin (Germany), 2015.
2. E. Van den Eeckhout, A. Laureys, K. Verbeken, Hydrogen diffusion through deformed and heat treated Armco iron, *International Hydrogen Conference*, Wyoming (USA), 2016.
3. E. Van den Eeckhout, Hydrogen diffusion through deformed and heat treated Armco iron, *The challenges of hydrogen and metals*, London (England), 2017.
4. E. Van den Eeckhout, T. Depover, K. Verbeken, The hydrogen trapping effect of carbides on hydrogen permeation in Fe-C-X alloys, *Steely Hydrogen*, Ghent (Belgium), 2018.

Table of contents

List of symbols

C	Carbon
C	Concentration
C_0	Sub-surface hydrogen concentration
CO_2	Carbon dioxide
Cr	Chromium
D	Diffusion coefficient
D_{app}	Apparent diffusion coefficient
E	Voltage
E_a	Activation energy for detrapping
E_B	Binding energy of a trap
E_D	Diffusional energy
E_S	Activation energy for trapping
F	Faraday constant
Fe	Iron
H	Hydrogen
H_{abs}	Absorbed hydrogen
H_{ads}	Adsorbed hydrogen
I	Current (density)
i_0	Exchange current density
I_{back}	Background current density
I_{norm}	Normalized current density
J	Flux
J_∞	Steady state flux
K_w	Water ionization constant
L	Material thickness
M	Molar concentration
n	Number electrons
Pd	Palladium
Pt	Platinum
r	Distance between atoms
R	Ohmic resistance
R	Molar gas constant
S_{dr}	Interfacial area ratio
T	Temperature
t	Time
Ti	Titanium

U	Cohesive energy
V	Vanadium
W	Tungsten
x	Diffusion distance
α	Charge transfer coefficient
ε	Strain
η	Overpotential
ν	Poisson’s ratio
σ	Cohesive stress
Φ	Hydrogen flux
τ	Dimensionless time

List of abbreviations

AIDE	Adsorption-induced dislocation emission
BCC	Body centred cubic
BCT	Body centred tetragonal
CC	Constant concentration
CE	Counter electrode
CF	Constant flux
DIC	Digital image correlation
DP	Dual phase
EDX	Energy dispersive X-ray
FCC	Face centred cubic
FEM	Finite element method
HAC	Hydrogen assisted cracking
HCP	Hexagonal close packed
HE	Hydrogen embrittlement
HEDE	Hydrogen enhanced decohesion
HELP	Hydrogen enhanced localized plasticity
HER	Hydrogen evolution reactions
HIC	Hydrogen induced cracking
HID	Hydrogen induced degradation
HV	Vickers hardness
ICCP	Impressed current cathodic protection
OM	Optical microscopy
OPU	Colloidal silica suspension
RE	Reference electrode
rpm	Rotations per minute
SEM	Scanning electron microscopy
SHE	Standard hydrogen electrode
TD plane	Transverse direction plane
TDS	Thermal desorption spectroscopy
TEM	Transmission electron microscopy
TRIP	Transformation induced plasticity
WE	Working electrode
wppm	Weight parts per million
wt %	Weight percent
XPS	X-ray photoelectron spectroscopy
YS	Yield stress

CHAPTER I

Literature study

I.1 Hydrogen and metals

Hydrogen has a negative public reputation due to catastrophic incidents in the past, for instance the crash of the airship "Hindenberg" at Lakefield, New Jersey on the 6th of May 1937. In this case, the hydrogen was ignited whereupon the zeppelin exploded. Besides the high flammability of hydrogen gas, the interaction between elementary hydrogen and metals is an issue which attained increased attention from both academic and industrial point of view over the past decade. The particular detrimental effect of hydrogen on the material's integrity is known as the hydrogen embrittlement (HE) phenomenon or hydrogen assisted cracking (HAC). This phenomenon was already reported for the first time in 1875 by W.H. Johnson [1] when he described: "*This change is at once made evident to any one by the extraordinary decrease in toughness and breaking strain of the iron so treated, and is all the more remarkable as it is not permanent, but only temporary in character, for with lapse of time the metal slowly regains its original toughness and strength*". This harmful effect of hydrogen became of interest to metallurgists, chemists and physicists in the decades following the 1920s with an important revival recently. So far, much research has been performed and several mechanisms to explain HE have been proposed, but still no consensus among the scientists has been obtained. A broader term which comprises all hydrogen damaging related issues like HE and hydrogen induced cracking (HIC), is called hydrogen induced degradation (HID).

Material scientists have developed materials, like high strength steels, to satisfy the high structural and economic requirements from industry. For example, steels with an increased strength level are necessary to meet the targets on CO_2 emission through vehicle weight reduction. These are currently to some extent available for the automotive sector. However, to avoid safety issues, these materials cannot be used when the hydrogen induced degradation problem is not fully understood or solved [2]. Additionally, these advanced high strength steels, which are thus excellent candidates to fulfil the abovementioned requirement, are reported to be prone the HE [3, 4]. The hydrogen might originate from the production process, product assembling, and finishing, or from service environment exposure. For example, electrodeposition processes could be accompanied by hydrogen production [5]. Also the offshore industry encounters difficulties coming along with hydrogen. When cathodic protection is applied to control the corrosion processes of the steel, hydrogen is produced and can be absorbed by the material [6]. Besides, in wind turbines, the rolling contact fatigue life of bearing steels is severely limited due to hydrogen. Repair of these contacts is extremely expensive and difficult due to the location of the construction. The presence of hydrogen at these locations may originate from to the use of long-life lubricants which contain certain additives to extend the

turbine maintenance intervals. However, these additives contribute to the lubricant decomposition and hydrogen generation [7].

Understanding the fundamentals of HID is necessary for numerous upcoming material developments, which will aid at establishing a possible hydrogen based economy in the future. This hydrogen economy would be one solution to the problem of climate change which is a consequence of the CO_2 emissions. Decarbonizing of the gas grid by replacement of the domestic supply with hydrogen and using hydrogen as a fuel in the automotive industry are two examples to illustrate the potential beneficial impact on the climate change the world is currently facing [2].

In this chapter, general aspects of the hydrogen/steel interaction will be introduced in order to elucidate the hydrogen embrittlement phenomenon. Further, a literature overview is included about the hydrogen permeation technique and the diffusion laws of Fick. Also, a brief summary is given concerning the research of Lorenzo Vecchi, a PhD-student with whom I collaborated in the frame of the SIM-Maduros program, considering the modelling part of a permeation experiment. Finally, the scope designates the significance of this work.

I.2 Hydrogen metal interaction

In general, the HID phenomenon is controlled by three main factors. First, there is the amount of atomic hydrogen present in the microstructure. To enter the material, the hydrogen is first adsorbed at the metal surface and then absorbed in the material, a process which will be explained further. A second factor is the microstructure of the metal playing a decisive role on the hydrogen transport through the lattice. Grain boundaries, dislocations, second phase particles and other lattice imperfections, all affect both the hydrogen diffusion and trapping behaviour and thus the degree of the HID. Finally, there is the driving force for diffusion which can be a result of an external applied load. For example, stresses introduced in the microstructure will affect the diffusion of hydrogen through the lattice.

I.2.1. Hydrogen Entry

The mechanical properties of metals or alloys are, amongst others, affected by the diffusion of elementary hydrogen through the material. The importance of the hydrogen diffusivity is nicely demonstrated in the work of Depover *et al.* [8]. They observed a higher degree of embrittlement although a lower amount of hydrogen was present with increasing hydrogen diffusion coefficient. This lower amount of hydrogen was obtained by decreasing the material's carbon amount, i.e. hydrogen trapping sites. As such, hydrogen was able to diffuse faster to critical regions and damage was induced more rapidly. Nevertheless, before hydrogen diffusion and damage can take place, it needs to enter the microstructural matrix. The first step of the entry mechanism is the adsorption of hydrogen at the metal surface. There are two possible adsorption mechanisms: at first chemisorption, which is adsorption from the gas phase, and, secondly, electrochemical

adsorption, being adsorption through electrolysis. In a gaseous phase, hydrogen is present as molecular hydrogen (H_2) which is too large to enter the metal via the surface [9]. In that case, the hydrogen molecule needs to dissociate. Gaseous charging depends on the pressure, temperature, time, and gas concentration. The main benefit is that, by the use of thermodynamic laws such as Sievert's law, the hydrogen content and distribution can be determined.

The second method is charging via electrochemical adsorption. Hydrogen protons (acid media) or water molecules (alkaline media) present in the electrolyte are converted at the cathodic surface to atomic hydrogen. By imposing an appropriate current or potential, following reduction reactions are initiated (Volmer reaction):

$$H^+ + e^- \rightarrow H_{ads} \quad \text{(I-1)}$$

$$H_2O + e^- \rightarrow H_{ads} + OH^- \quad \text{(I-2)}$$

Once hydrogen is adsorbed, the atom may be transferred across the metal surface into the absorbed state in the subsurface layer (Equation I-3). However, hydrogen entering the metal passes through the same adsorbed state on the metal surface that leads to hydrogen evolution. So parallel to H absorption, two different hydrogen recombination reactions can take place. The detachment of adsorbed hydrogen atoms from the metal surface can occur by either chemical desorption (Equation I-4, Tafel reaction) or electrochemical desorption (Heyrovski reaction). The electrochemical desorption reaction differs from acid and alkaline medium, presented in Equation I-5 and Equation I-6, respectively. Generally, both recombination reactions occur simultaneously, often, one of them predominating. The reactions at the metal-solution interface in aqueous solution are illustrated schematically in Figure I-1. The recombination reaction which is favoured depends on the composition of the charging solution, the metal surface condition and the surface hydrogen coverage which is related to the applied current or potential. It was suggested by several authors [10-12] that the hydrogen evolution reaction is followed by predominantly chemical desorption at low overpotentials and by mainly electrochemical desorption at high overpotentials. A more detailed description of these processes is beyond the scope of this work. More information concerning the kinetics can be found in specialized literature [13-15].

$$MH_{ads} \rightarrow MH_{abs} \quad \text{(I-3)}$$

$$MH_{ads} + MH_{ads} \rightarrow H_2 + M \quad \text{(I-4)}$$

$$MH_{ads} + H^+ + e^- \rightarrow H_2 + M \quad \text{(acid media)} \quad \text{(I-5)}$$

$$MH_{ads} + H_2O + e^- \rightarrow H_2 + OH^- + M \quad \text{(alkaline media)} \quad \text{(I-6)}$$

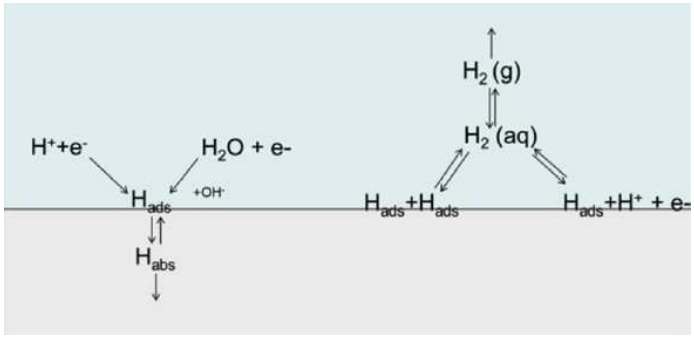

Figure I-1 Reaction processes occurring at the metal charging surface [16].

An important hydrogen source in offshore industry is originating from the applied impressed current cathodic protection (ICCP) system. Cathodic protection is used to withhold constructions from corrosion. The structure, which requires protection, is forced to act as a cathode. In this way, the steel is prevented from oxidation and mainly reduction reactions occur at the metal surface, while oxidation reactions take place at the anode. The highly conductive anodes, required for an ICCP system, usually have a more positive potential than the protected structure. Moreover, they must have a low solubility and a high resistance against impact, abrasion or vibrations. The anodes are thus anodically stable noble metals, or materials which form a conducting stable oxide film on their surface [17]. Figure I-2 shows schematically how the potential of iron is pushed down from the corrosion potential E_{corr} to E' by imposing a current equal to ($|I'_c|$-I'_a). At E_{corr}, the anodic reaction rate of the metal will be higher than the rate I'_a at a potential equal to E'. In other words, corroding processes at the metal are minimized. However, at E', the external applied current must be sufficient to sustain the total cathodic reaction, and thus both oxygen reduction and hydrogen evolution reaction [18]. Normally the oxygen reduction reaction is the dominant one in aqueous environments, but at large negative potentials, water reduction becomes more relevant. Parts of the construction which are subjected to these large negative potentials are thus overprotected and originate from the heterogeneous current distribution of the ICCP system.

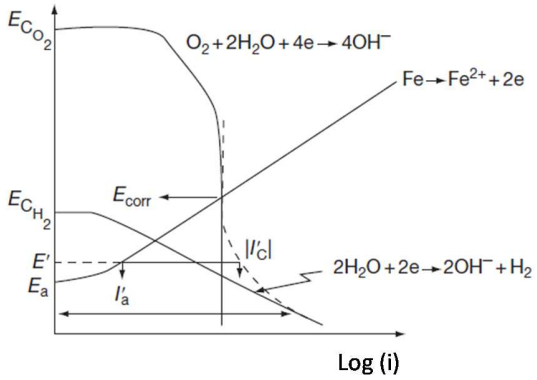

Figure I-2 Polarization diagram showing corrosion, cathodic protection and the role hydrogen evolution plays. The dotted line represents the total cathodic current due to hydrogen evolution and oxygen reduction [18].

I.2.2. Hydrogen transport

Hydrogen is able to diffuse through the microstructure when absorbed in the material. The two main diffusion models that dominate are substitutional and interstitial diffusion. For substitutional diffusion vacancies are needed in the metal lattice and atoms basically switch positions with the vacancy. In the case of interstitial diffusion, the dissolved atom diffuses more rapidly as it is not hold by the lattice. This is the main mechanism when hydrogen diffuses through the metal [19]. The hydrogen atom is sufficiently small and is therefore able to make interstitial jumps. Even at room temperature, hydrogen can diffuse through the metal lattice. Temperature, chemical composition and crystal structure are three important parameters which can alter the diffusivity and solubility [20]. The diffusion coefficient D (m^2/s) expresses the diffusivity in a material and can be calculated for hydrogen by performing hydrogen permeation experiments. The permeation technique, and the corresponding theory where it relies on, is elucidated in section I.3.

As hydrogen transport happens via the interstitial sites of the lattice, diffusion rate and solubility will depend on the metallic structure. In Figure I-3, tetrahedral and octahedral interstitial sites for a face centred cubic (fcc), hexagonal close packed (hcp) and body centred cubic (bcc) crystal are illustrated. The most common structure for steel at room temperature is bcc, the ferritic structure. It has an open lattice configuration and shows a high diffusion rate and low solubility. Some specific steels like TRIP steel contain an fcc austenitic phase at room temperature. This structure is a closer packed lattice structure compared to bcc and can be compared with a reservoir for hydrogen as the H diffusivity is very low while the solubility is high. Hydrogen prefers the tetrahedral sites for bcc and the octahedral sites for fcc lattices [21]. The martensitic structure is mostly body centred tetragonal (bct), however, Olden et al. [22] mentioned a rising tendency of hexagonal martensite formation with increasing carbon content. Both structures are closer packed than bcc leading to a diffusion rate in between ferrite and austenite. Just like in fcc lattices, hydrogen prefers the octahedral sites [23].

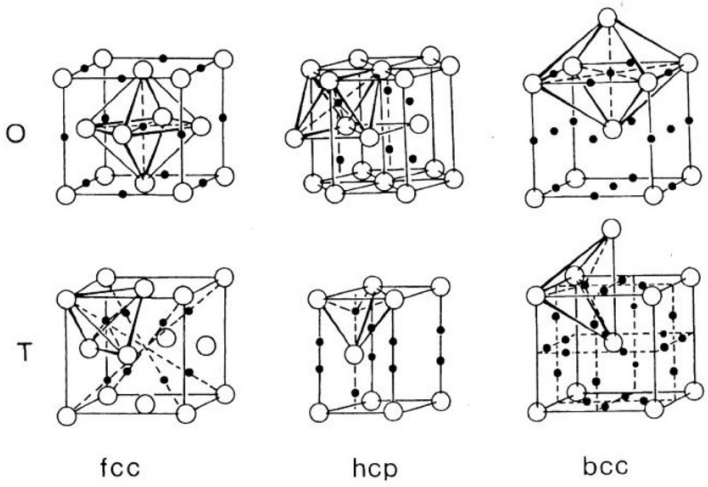

Figure I-3 Interstitial sites (octahedral - O and tetrahedral – T) in fcc, hcp and bcc lattices [24].

Another way for hydrogen to move through the lattice is via dislocation displacements [25]. In this way, hydrogen is able to move faster and much more hydrogen atoms can be transported in one moment. The binding energy between the atom and the dislocation is higher compared to a normal lattice location. So when dislocations are moving in the matrix, the hydrogen can be dragged along, resulting in a much faster diffusion through the lattice. Although the binding energy between a hydrogen atom and dislocation is stronger compared to a normal lattice site, it is still weakly trapped and therefore detrimental for the mechanical properties of the metal [26]. A more detailed explanation concerning hydrogen trapping sites is given in next section.

I.2.3. Hydrogen trapping

Besides interstitial lattice sites, there are other locations in the microstructure where hydrogen can be present. These other sites are lattice imperfections such as dislocations, grain boundaries, second phase particles, vacancies, voids etc. At these localized regions, hydrogen has a residence time which is considerably longer compared to a normal interstitial site. Consequently, lattice imperfections will delay hydrogen diffusion through the material. In the extreme case, some heterogeneities can act as a sink and can retain hydrogen even during a thermo-mechanical loading. Generally, lattice imperfections that slow down hydrogen movement are called hydrogen trapping sites [27, 28]. Possible hydrogen trapping sites present in a steel matrix are illustrated in Figure I-4.

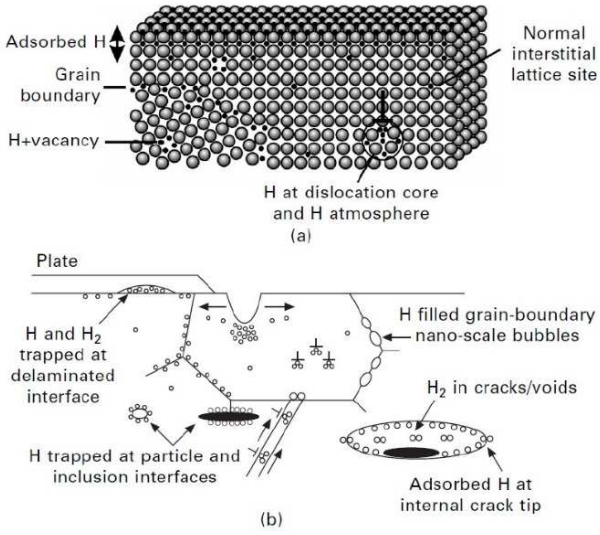

Figure I-4 Possible hydrogen trapping sites in a material on the (a) atomic scale and (b) microscopic scale [28].

When hydrogen is found in these lattice imperfections or traps, it is in a lower energy state compared to its normal interstitial position. This is due to the deepening of the associated potential well (Figure I-5). The activation energy E_A is the energy needed for a hydrogen atom to escape from the trap. A higher temperature or an applied stress can provide the required energy. Based on E_A, trapping sites are generally divided in reversible and irreversible traps. E_D is the activation energy that is needed for hydrogen diffusion through a

perfect lattice. If the hydrogen atom is found in an interstitial place next to a trap, a saddle point, it will preferentially diffuse to the trap as this corresponds with a lower amount of energy ($E_S < E_D$). Finally, the trap binding energy E_B depends on the trap characteristics.

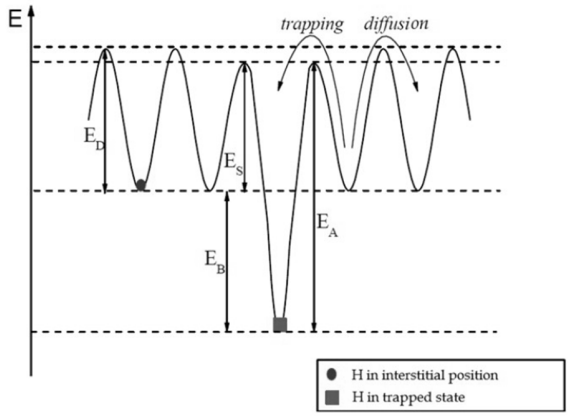

Figure I-5 Potential energy of hydrogen in interstitial and trapped position [29].

Hydrogen in reversible traps is in equilibrium with the hydrogen in the lattice. These traps have rather low activation energies and thus it is easy for hydrogen to leave the trapping site and to diffuse further through the metal lattice. When hydrogen is trapped irreversibly, the probability to escape is very low. The desorption activation energy barrier between reversible and irreversible traps is rather arbitrary assumed to be 60 kJ/mol [30-32]. Nevertheless, the reversible behaviour of a trap depends strongly on the temperature, the trap occupancy and the interaction time [32]. Dislocations [32, 33] and grain boundaries [34] are considered to be reversible traps although different activation energies are reported in literature (Table I-1). Hydrogen is trapped and released in a relatively short time frame, even at room temperature. Therefore, reversible traps play an important role in the HID phenomenon as they serve as a storage for diffusible hydrogen and provide hydrogen to fracture initiation sites [35]. Irreversible traps, on the other hand, hold hydrogen for a much longer time and hence they might decrease the materials' susceptibility to HID [28, 36]. Examples are retained austenite [37] and carbides [38]. Beeler and Johnson [39] performed some theoretical analysis and found that the binding energy for a hydrogen-vacancy complex increased with the cluster size. However, an upper limit of 77.2 kJ/mol exists for clusters of more than six vacancies. More information concerning trapping sites, i.e. trapping activation energies, can be obtained by performing thermal desorption spectroscopy (TDS) analysis. Although the analysis procedure to obtain the corresponding activation energies linked to the deconvoluted peaks in the TDS spectrum is not straightforward, TDS results provide valuable information concerning the trapping behaviour of the material. Beside TDS, also the permeation technique can be used [40]. In this work, permeation tests are performed to determine the corresponding diffusion coefficients and to gain deeper insight in the experimental technique itself, which is further elaborated in detail in Chapter II and III. Some literature data on activation energies are given in Table I-1.

Table I-1 Activation and binding energies for different trapping sites.

Trapping site	Activation energy (kJ/mol)	Reference
Retained austenite	55	[41]
Retained austenite	90	[37]
Lath martensite	27	[34]
Microvoids	27.6 - 35.15	[33]
Dislocations	19.2	[33]
Dislocations	24.1 – 29.9	[32]
Grain boundary	29 – 58	[34]
TiC	86.9	[38]
Trapping site	**Binding energy (kJ/mol)**	**Reference**
Vacancy	57	[42]
Vacancy	60	[43]
Vacancy	44	[44]

I.2.4. Hydrogen embrittlement

Hydrogen embrittlement or hydrogen assisted cracking is the phenomenon leading to unpredictable failure of the material. In this case, the ductility loss of the material is caused by hydrogen diffusion through the microstructure. The first observations of the HE effect were made at the end of the 19th century. Since then, researchers are aiming to clarify the mechanism responsible for the detected decrease in mechanical performance. Although a lot of knowledge has been gained, still no consensus has been obtained about the exact mechanism behind this phenomenon. In this section, the three main different models, which have been developed to describe the HAC phenomenon, are explained. The permeation technique and theory, used for studying hydrogen diffusion, are described in section I.3.

The first proposed mechanism was the hydrogen enhanced decohesion (HEDE) model. This model was introduced by Zapffe *et al.* [45] and was improved by Troiano *et al.* [46] and Oriani [47]. It is based on the increased hydrogen solubility in a tensile strain field, e.g. tri-axial stress zones at crack tips or tension fields of dislocations. The presence of these stress regions causes the chemical potential of hydrogen to be sufficiently low which can result into a higher hydrogen concentration compared to neighbouring zones with higher chemical potential [48]. The hydrogen then decreases the cohesive forces enabling crack propagation. This model predicts that the fracture should be cleavage-like and is supported by the fact that HE can take place in the absence of an external applied deformation. Figure I-6 illustrates the mechanism of the HEDE model. U represents the cohesive energy required to separate two half solids along the cleavage plane to a separation larger than a critical distance (r). $U^0_{cohesion}$ and $U^H_{cohesion}$ are the cohesive energies in

the absence or presence of hydrogen, respectively. It is clear that $U^{H}_{cohesion}$ is smaller than $U^{0}_{cohesion}$ indicating that hydrogen atoms are able to decrease the cohesive energy. Also the effect on the cohesive stress $\sigma_{cohesion}$, the stress needed to disrupt the atomic bonds, is shown [49].

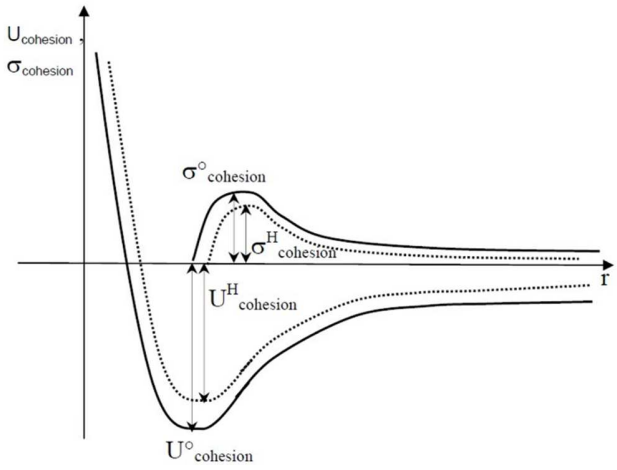

Figure I-6 Effect of hydrogen on the cohesive energy (U) and on the cohesive stress (σ) of a material [49].

Instead of considering the cohesive force between atoms in the HEDE model, the hydrogen enhanced localized plasticity (HELP) mechanism, developed by Beachem *et al.* [50], is based on an increased dislocation mobility. The model, elaborated in more detail by Birnbaum *et al.* [51], states that hydrogen reduces the repulsive elastic interactions between dislocations and other microstructural obstacles such as carbon atoms and grain boundaries. As such, the dislocation interaction energy is lowered, promoting their planar gliding [52]. This was verified by in-situ Transmission Electron Microscopy (TEM) experiments performed by Ferreira *et al.* [53]. This mechanism results in two different kinds of regions existing in the matrix. On the one hand, there are ductile regions, due to the shielding effect of hydrogen, and, on the other hand, less ductile regions where dislocations are stuck in a pile-up [54]. At the macroscopic scale, a hydrogen fracture is a brittle fracture due to the macroscopic ductility loss. However, fractographic studies show that HE can be related with locally enhanced plasticity at the crack tip, supporting the HELP mechanism. This localized plasticity is a local softening which leads to a fracture with limited ductility on the macroscopic scale [55].

A third model to describe the HE phenomenon was proposed by Lynch [56] and is called the Adsorption-Induced Dislocation Emission (AIDE) mechanism. It arises from the combination of the previous discussed HEDE and HELP mechanism. The interatomic iron-iron bonds are weakened, similar to the HEDE model, and dislocation nucleation and movement are facilitated, like in the HELP model. It was stated that these processes only occur in the first few atomic layers of the material, for example at a crack tip. Dislocations, which move away from the crack tip, facilitate the crack propagation process giving rise to a macroscopic ductility drop of the material. In 2009, Moro *et al.* [57] compared crack propagation in the

presence and absence of hydrogen. Decohesion of the metal atoms was favoured and dislocation emission at the crack tip increased in the presence of hydrogen. These findings are consistent with the proposed AIDE model.

I.2.5. Hydrogen induced cracking

When hydrogen is responsible for the initiation of the crack, a phenomenon called hydrogen induced cracking (HIC) is taking place. The microstructural heterogeneities are, next to impeding hydrogen diffusion, ideal nucleation sites for hydrogen induced cracks. Such cracks develop when the material is excessively charged with hydrogen. At these heterogeneities, hydrogen can recombine, resulting in the formation of high pressure hydrogen gas bubbles [58, 59]. This phenomenon was clarified by the internal pressure theory by Zapffe and Sims [45] and Tetelman and Robertson [60]. When the internal hydrogen gas pressure reaches a certain threshold, plastic deformation takes place. Consequently, crack initiation and propagation can occur, even without an externally applied stress. When this phenomenon takes place just below the sample surface, the metal top layer is lifted up by the gas pressure and a blister is formed [61]. Laureys *et al.* [62] demonstrated that the presence of deformation induced defects, such as dislocations and microvoids, promote blister formation. At first, defects hinder hydrogen diffusion through the lattice and secondly, more stresses are present around a lattice defect compared to the normal lattice. Hence, it is easier for a crack to initiate at these locations.

I.3 The electrochemical permeation technique

It is of significant importance to study hydrogen transport in metals as diffusible hydrogen is one of the main factors responsible for unpredictable failure of the material. The diffusion of hydrogen depends mainly on temperature and microstructure and is closely related to the magnitude of the hydrogen damage. This was proven by Depover *et al.* [63], who observed an increased HE effect when lowering the carbon content, and thus the hydrogen content, in a bainitic Fe-C alloy. Although a lower amount of diffusible hydrogen was present, an additional ductility loss was observed. This remarkable result was attributed to the faster hydrogen transport through the microstructure having the lowest carbon amount. This research demonstrated clearly that, next to the amount of diffusible hydrogen, the hydrogen diffusion coefficient of the investigated microstructure needs to be incorporated when considering the hydrogen/material interaction.

Considering the HIC phenomenon, Laureys *et al.* [64] showed that deformation induced defects strongly promoted blister formation. The present defects hindered hydrogen diffusion, favoured hydrogen accumulation and facilitated crack initiation. Hence, the susceptibility to hydrogen damage was not only linked to the diffusivity and the trapping of hydrogen, but also whether cracks were easy to initiate or not.

The hydrogen diffusivity in metals can be determined by permeation methods. All the permeation techniques involve the measurement of time needed for hydrogen to enter, to migrate through the thickness of the specimen and to be detected at the exit side. In 1962, pioneers Devanathan and Stachurski [65] created a permeation technique where a thin metal membrane was placed between two independent electrochemical cells. Hydrogen was introduced into the metal from an aqueous solution by either, galvanostatic or potentiostatic electrochemical charging. Nowadays, most permeation techniques are based on their set-up, which is schematically depicted in Figure I-7. A possible reaction route is presented in Figure I-8. In order to calculate the corresponding diffusion coefficient of hydrogen through the metal, the results must be correlated to a diffusion theory. Most researchers use the ideal diffusion theory based on Fick's laws, as these are the most straightforward. Other models, developed by McNabb and Foster [66], Oriani *et al.* [67] and Leblond and Dubois [68, 69], take into account trapping phenomena. Due to the lack of knowledge of parameters used in aforementioned models, in this work, permeation analysis was limited to the ideal diffusion described by Fick's laws.

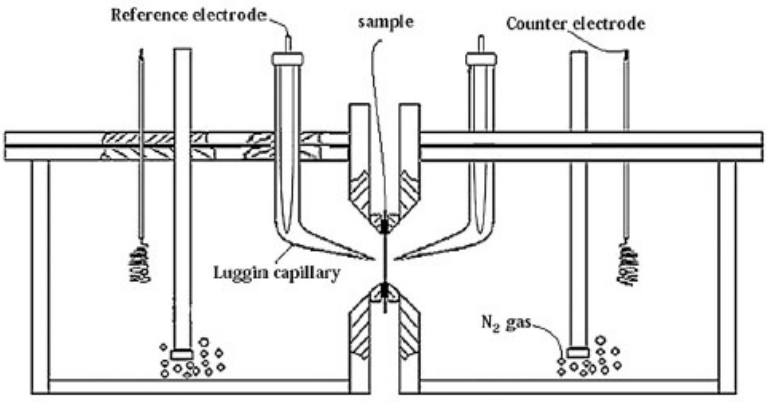

Figure I-7 Sketch of the electrochemical permeation method [70].

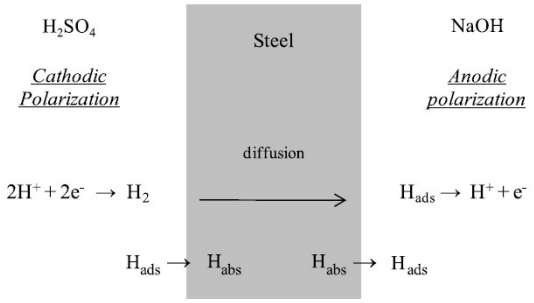

Figure I-8 Reactions occurring in the electrochemical permeation technique [71].

I.3.1. Fick's diffusion laws

Without any trapping or barrier effect at the entry and exit side, the hydrogen permeation flux can be described by Fick's first and second law, given in Equation I-7 and I-8, respectively. D represents the diffusion coefficient in m²/s, C the hydrogen concentration in mol/m³, x the distance in m, t the hydrogen charging time in s and J the diffusion flux in mol/(m²·s).

$$J(x) = -D\frac{\partial C(x)}{\partial x} \tag{I-7}$$

$$\frac{\partial C(x,t)}{\partial t} = D\frac{\partial^2 C(x,t)}{\partial x^2} \tag{I-8}$$

Taking into account suitable boundary conditions, these equations can be solved. A first assumption is that the residual hydrogen in the bulk of the material does not influences the diffusion and trapping and thus for $t = 0, C(x,0) = 0$. Secondly, the hydrogen concentration at the exit side is assumed to be zero as hydrogen oxidizes immediately when it reaches the surface. Therefore, $C(L,t) = 0$, with L the sample thickness. At the entry side two different models can be defined, the constant concentration (CC) and the constant flux (CF) model. For the CC case, the concentration C_0 at the entrance face is assumed to be constant, whereas in the CF case the incoming hydrogen flux J_0 is constant. The boundary conditions for the CC and CF model in a metallic membrane is schematically shown in Figure I-9 (a) and (b), respectively. During the charging transient, the profiles evolve differentially (curve I), but at steady state (curve II), both hydrogen concentration profiles are equal. The model here represents the ideal system without hydrogen barrier effects. In practice, it is assumed that the CC boundary conditions are achieved by applying a constant potential at the entrance side, while the CF conditions are accomplished by a constant cathodic current.

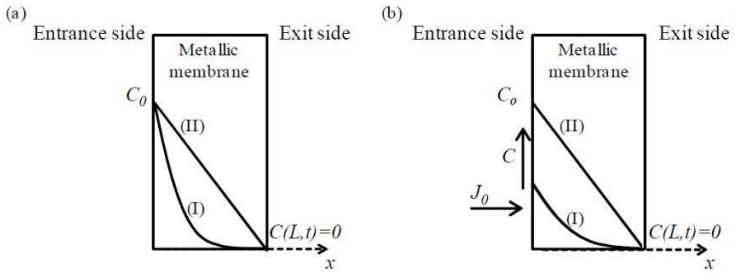

Figure I-9 Boundary conditions of the CC (a) and CF (b) model. (I) hydrogen concentration during the charging transient, (II) hydrogen concentration profile at steady state [72].

The solution of Fick's equations can be obtained for each model by a Fourier transformation, given in Equation I-9 for the CC model and Equation I-10 for the CF model [71, 73, 74]. Equivalent results were obtained by Laplace transformation published by McBreen *et al.* [75] and Fallahmohammadi *et al.* [76]. For each condition, two analytical solutions exist to model the diffusion phenomenon. Both solutions, together with the boundary conditions for each model, are given and illustrated in Table I-2. It is clear that the

boundary conditions strongly influence the permeation transient as it takes longer time to reach the steady state flux in case of the CF model compared to the CC model.

CC model
$$\frac{J}{J_\infty} = 1 + 2\sum_{n=1}^{\infty}(-1)^n \exp(-n^2\pi^2\tau) \quad \text{(I-9)}$$

CF model
$$\frac{J}{J_\infty} = 1 - \frac{4}{\pi}\sum_{n=0}^{\infty}\frac{(-1)^n}{2n+1}\exp[-\frac{1}{4}(2n+1)^2\pi^2\tau] \quad \text{(I-10)}$$

In the next section, different methods to calculate the diffusion coefficient, based on Fick's diffusion laws, are elaborated.

Table I-2 Boundary conditions and Fick's analytical solutions to model the diffusion phenomenon with constant concentration and constant flux at the entrance surface. C, hydrogen concentration, dimensionless time τ = (Dt)/L²; t, time; L, sample thickness; D, diffusion coefficient; J, the measured permeation flux and J_∞, the steady state permeation flux.

Constant Concentration	**Constant Flux**
$C(x,0) = 0$ (I-11) $C(L,t) = 0$ $C(0,t) = C_0$	$C(x,0) = 0$ (I-12) $C(L,t) = 0$ $J(0,t) = constant$ $J_\infty = D\frac{C(0,\infty)}{L} = constant$
$\frac{J}{J_\infty} = \frac{2}{\sqrt{\pi\tau}}\exp\left(\frac{-1}{4\tau}\right)$ $for\ \tau < 0.3$ (I-13)	$\frac{J}{J_\infty} = 2erfc\left(\frac{1}{2\sqrt{\tau}}\right)$ $for\ \tau < 0.3$ (I-14)
$\frac{J}{J_\infty} = 1 - 2\exp(-\pi^2\tau)$ (I-15) $for\ \tau > 0.2$	$\frac{J}{J_\infty} = 1 - \frac{4}{\pi}exp\left(-\frac{\pi^2\tau}{4}\right)$ (I-16) $for\ \tau > 0.2$
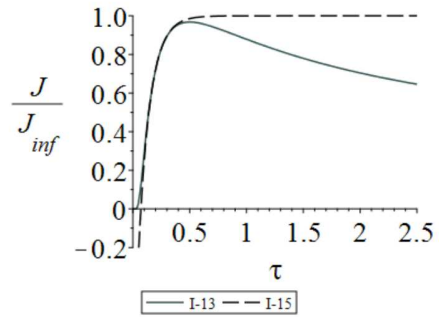	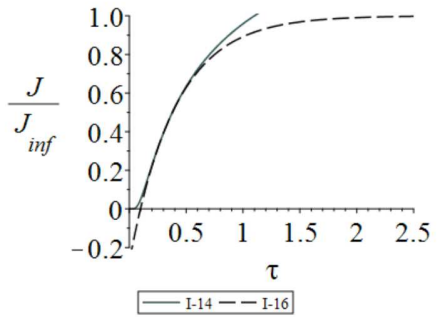

I.3.2. Diffusion coefficients

Nowadays, numerous ways to calculate the hydrogen diffusion coefficient are available of which some are explained in this section. Important to note is that diffusion coefficients, experimentally defined from Fick's solution, will be labelled as apparent diffusion coefficients (D_{app}) as the data processing does not consider phenomena such as surface effects and trapping mechanisms. When performing electrochemical permeation tests, the diffusion coefficient could be determined by using the steady state current density (I_{ss}) measured at the exit surface of the specimen. Figure I-10 shows a schematic representation of a permeation transient where the steady state current density is indicated. Since the permeation current is associated with the oxidation of hydrogen atoms and

$$I = F * J \tag{I-17}$$

where F is Faraday's constant ($s \cdot A \cdot mol^{-1}$), the hydrogen permeation flux J ($mol \cdot m^{-2} \cdot s^{-1}$) can be replaced by the recorded permeation current density I ($A \cdot m^{-2}$).

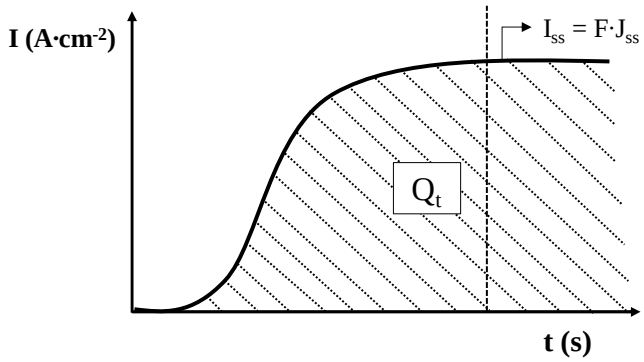

Figure I-10 A schematic representation of the experimentally recorded permeation transient. The steady state current density (I_{ss}) and the amount of diffused hydrogen (Q_t) are indicated.

One way to determine the value of D is by fitting the normalized experimental transient curve with Equation I-9 or Equation I-10. Another method, called the 'time-lag' method, is probably the most well-known. This method involves the integration of the permeation curve with respect to time in order to obtain the amount of hydrogen which diffused through the sample in a certain time period (Q_t), with Q_t indicated in Figure I-10. In the case of potentiostatic conditions at the entry side and for $t >> L^2/(6 \cdot D_{app})$, the following expression is obtained [77]:

$$Q_t = \frac{D_{app} C_0}{L} \left(t - \frac{L^2}{6 D_{app}}\right) \tag{I-18}$$

For t >> $L^2/(6 \cdot D_{app})$, the extrapolation of the linear part of the curve of Q_t(t) intercepts the x-axis at the time-lag [72]:

$$t_{lag} = \frac{L^2}{6D_{app}} \tag{I-19}$$

where t_{lag} is called the 'time-lag' (s), L is the sample thickness (m) and D_{app} the apparent diffusion coefficient (m^2/s). It corresponds to the time needed for the hydrogen flux to reach 62.9% of its steady-state value. The time-lag offers, in good approximation, an expression to calculate D_{app}. If the same procedure is followed in case of galvanostatic boundary conditions, t_l corresponds to the time necessary to reach 61.7% of the steady-state value and is given by [72]:

$$t_{lag} = \frac{L^2}{2D_{app}} \tag{I-20}$$

Next to the 'time-lag', also other points of the permeation transient may be used to determine D_{app}. This can be done by the following mathematical relation derived from Fick's solutions (Table I-2):

$$D_{app} = \frac{L^2}{Mt_x} \tag{I-21}$$

L is the specimen thickness (m), t_x the time (s) where the normalized flux (J_{t_x}/J_∞) equals x and M an adimensional constant which depends on the charging method and the chosen time value t_x. M is determined by using $\tau = (Dt)/L^2$ and $D = L^2/(Mt)$ in Fick's solutions (Table I-2) and by plotting the normalized flux with respect to the M value. As such, M is known for every value of the normalized hydrogen flux. Calculated values for M at different points of the normalised charging transient for the CC and CF condition are given in Table I-3. Until now, no work has been published which demonstrates which kind of polarization method is the most convenient to provide reproducible permeation experiments. In this work, a constant cathodic current will be applied as then the hydrogen coverage, which is linked with the hydrogen evolution and absorption mechanisms, should be controlled [78].

Table I-3 M-values at different moments of the normalized permeation flux (J/J_∞).

M / J/J_∞	Potentiostatic	Galvanostatic
0.01	25.3	15.7
0.1	15.1	7.7
0.3	9.9	4.1
0.5	7.2	2.6
0.9	3.3	0.97

Another method to determine the apparent diffusion coefficient was developed by Frappart *et al.* [71]. This technique, called the "Regime 1 technique", left out the steady state permeation current since this value could be affected by surface evolution or trapping processes during the first permeation transient. The method allowed to verify that D_{app} was coherent with the apparent diffusion coefficient calculated with other methods. It was based on the beginning of the transient where D_{app} was determined by fitting the experimental results to a simple mathematical Equation I-18, which was related to Equation I-13.

$$\frac{\partial \ln(j)}{\partial t} = -\frac{1}{2t} + \frac{L^2}{4D_{app}t^2} \tag{I-22}$$

D_{app} could depend on the evolution of the surface state and on trapping processes. In the research of Frappart *et al.* [71], the diffusion coefficients for a permeation experiment were calculated by both the method at 10% of the steady state current and the "Regime 1" method. Regardless the technique, the value of D_{app} was similar which indicated that the influence on the steady state value by trapping phenomena and surface changes could be neglected for determining D_{app}.

I.3.3. Diffusion through a multilayer system

In the previous section, no trapping or barrier effects were considered. In practice, hydrogen must diffuse through a multilayer system consisting of layers with different hydrogen diffusion coefficients and solubilities. Metal coatings, for example, can be used as barriers as they strongly reduce the hydrogen permeability. These coatings reduce the hydrogen embrittlement susceptibility and most common ones are made of cadmium, platinum, nickel and copper [79]. On the other hand, metal coatings can also be used to favour hydrogen absorption in steels by increasing the hydrogen activity. For this purpose, palladium (Pd) is the most common element used in the electrochemical permeation technique. Besides enhancing hydrogen absorption, it also impedes the oxidation of the metal surface. Many researchers plate a Pd-layer at the entrance and/or exit side of a permeation membrane to avoid surface phenomena associated with the presence of oxide layers. Zakroczymski *et al.* [80] investigated the Pd-layer at the entrance side and concluded that palladium impedes the hydrogen entry when compared to an uncoated iron membrane. The influence of the Pd-layer on the hydrogen diffusion at the exit surface was considered by Manolatos *et al.*

[81, 82]. They stated that a Pd-layer was required at the detection side to ensure the reliability of a permeation experiment. Although it is well known that palladiums avoids corrosion of the steel and enhances the hydrogen oxidation at the exit side, defects and/or oxides at the metal/Pd interface are easily introduced during the plating process. These heterogeneities will affect the hydrogen diffusion in an uncontrolled manner, which is not desirable. Several authors [71, 83, 84] carried out permeation experiments without a Pd-layer and concluded that palladium deposition was not necessary. The major risk of its absence is the uncomplete oxidation of hydrogen, but at low fluxes and in bcc steels this should not be a problem [85]. This was also proven by Frappart *et al.* [78] who obtained comparable diffusion coefficients with and without a Pd-layer, confirming hydrogen diffusion is controlled by the bulk material in this case.

Passive films and natural air grown oxides are shown to be barriers for hydrogen permeation [86, 87]. The diffusion of hydrogen through the layer is determined by the nature of the oxide. In a permeation experiment, air-formed oxides are present at the entrance side, while a passive layer is formed at the exit surface. During the permeation experiment the natural film on the cathodic surface is reduced. In alkaline solutions, the reduction occurs partially, while in acid media the film reduction is fast [80, 88]. Distortions in the recorded permeation current can sometimes be associated to the evolution of the hydrogen concentration with time at the entrance surface [89].

In the absence of a Pd-layer, a stable passive layer must be created at the exit surface to prevent the surface from corroding. Although researchers agree on the barrier effect of the passive layer, no agreement has yet been obtained on the stability during permeation. Casanova *et al.* [84] stated that the passive layer formed in a de-aerated NaOH solution was perfectly stable. This implied that the hydrogen charge transfer took place at the iron-oxide interface and that hydrogen migrated through the film as a proton [90]. Other authors claimed that the diffusion of hydrogen atoms reduced the film, and lowered its thickness and oxygen content [91].

Generally, the entrance and exit surface state of the metal membrane is a very important factor to take into account when interpreting the obtained permeation data. Comparing results based on permeation experiments of different authors is therefore very complex when the experimental procedure differs. Vecchi *et al.* [92, 93] pointed out the complexity of modelling a permeation experiment and highlighted the importance of the entry and exit surface states. This should, according to their work, be incorporated when modelling the overall hydrogen transport through a metal membrane. A small summary of this work is given in setion I.5, however, first, in the next section, the influence of stresses on the hydrogen diffusivity is considered.

I.4 The influence of stresses on the hydrogen diffusivity

When steel is used in structural applications, it will experience different levels of stress during its lifespan. Plastic deformations typically occur during production, whereas elastic stresses are ubiquitous in most mechanical applications. If the hydrogen diffusivity increases with these stresses, the critical concentrations necessary for hydrogen induced damage will be reached sooner. Moreover, when a crack is already present in the microstructure, during crack propagation, the crack tip could be under plastic straining while the regions away from the crack tip could be subjected to elastic stresses. Therefore, it is important to study the influence of both elastic and plastic stresses on the hydrogen transport through the material. This can be performed by permeation experiments combined with a tensile loading device.

Zhao *et al.* [94] performed hydrogen permeation tests combined with a slow-strain-rate tensile test in which stress was applied to obtain a constant strain rate. Figure I-11 shows the stress as well as the permeation current density measured at the exit side of the sample. In the first part of the curve (a-b), an increased elastic tensile stress resulted in a higher permeation current density. On the one hand, this could be correlated with a higher diffusion coefficient. On the other hand, applied stresses could increase the hydrogen evolution reaction rate, leading to a higher hydrogen uptake [95]. However, this increasing current density does not extend for the entire elastic range. At point b in Figure I-11, the permeation current density started to decrease. The authors claimed that a phenomenon called micro-plasticity caused a transition from a pure elastic deformation state to an elastic-plastic coexisting state. As such, lattice defects were created before reaching the yield stress. The increasing permeation current density at stresses higher than the yield stress (c-d), could be attributed to the enhanced hydrogen transport by dislocation movement.

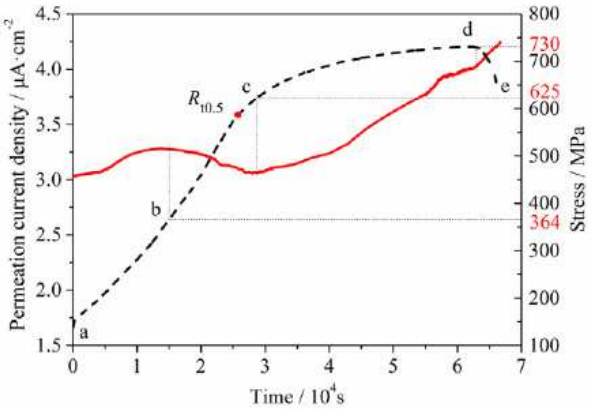

Figure I-11 Stress (dotted line) and hydrogen permeation current density (solid line) vs time [94].

It is generally known that plastic deformation increases the amount of lattice defects, i.e. hydrogen trapping sites, in the material. As such, the hydrogen diffusivity decreases, while the solubility of the material

increases [96-98]. Elastic stresses also cause an increased hydrogen uptake, however, no consensus in literature has been found concerning the effect on the hydrogen diffusion coefficient.

I.5 Modelling the permeation experiment [92, 93]

Preceding sections indicated that still no agreement has been reached among researchers on the most appropriate procedure to perform a permeation test. Therefore, it is necessary to get more insights on the electrochemical reactions occurring at the entry and exit side of the metal membrane during a hydrogen permeation test. Moreover, on the trapping and detrapping processes which are taking place in the bulk of the material. Lorenzo Vecchi, researcher of the SURF group at the VUB, investigated the hydrogen adsorption, absorption, trapping and desorption through the development of a numerically based model representing the experimental permeation technique based on the Devanathan and Stachurski method. He verified how to evaluate the input parameters of the model and reported their impact on the results. All steps taking place in the hydrogen transport process, i.e. adsorption, absorption, diffusion, trapping, detrapping and desorption, are described by a numerical time-dependent model based on the finite element method (FEM). For this purpose, experimental data from permeation tests performed at Ghent University were used. Appropriate input parameters were taken from literature and used to validate the robustness of the model. When a good fitting of the model with trapping parameters was achieved, the impact of the hydrogen adsorption-absorption process on the resulting hydrogen flux was investigated (section I.5.1). The complexity of the surface state at the exit side is then further discussed in section I.5.2.

I.5.1. The entry side

Once hydrogen is in the adsorbed state, three parallel phenomena will occur: hydrogen absorption, chemical hydrogen recombination (Tafel) and electrochemical recombination (Heyrovski). The absorption reaction is the least favourable and the competition among the aforementioned processes depends on the pH of the electrolyte, the applied overpotential or current, and on the surface state which affects the process' kinetics. In Figure I-12, the effect of the electrochemical recombination constant K on the hydrogen oxidation current is shown. The experimental result, illustrated in the graph, was obtained by testing deformed Armco iron by permeation test method 1 (cf. section II.1). It is clear that an increase in K, used in the model, produces a big variation on the resulting hydrogen oxidation curve. By increasing this constant, less hydrogen is provided to the subsurface and the time for reaching the steady state current is delayed. As such, Vecchi *et al.* [92] stated that when a misinterpretation of the surface-subsurface equilibrium occurs, the modelled permeation curve, and thus the obtained diffusion coefficient, is not reliable.

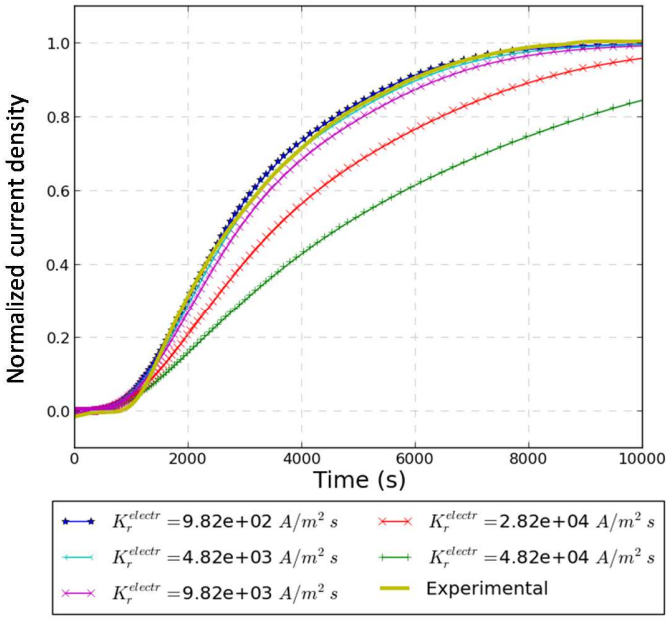

Figure I-12 Effect of the electrochemical recombination constant K on the resulting hydrogen oxidation current. The experimental permeation curve was performed on 50% deformed Armco iron [92].

Next to the electrochemical recombination constant, also the applied cathodic current and absorption/desorption ratio was modified in order to investigate the influence on the hydrogen transport through a metal membrane. Finally, it was demonstrated that the hydrogen adsorption-absorption step had a severe influence on the modelled permeation transient. Both the applied cathodic current and adsorption-absorption equilibrium were incorporated in the authors newly proposed equation.

I.5.2. The exit side

Before charging the hydrogen in the metal membrane, a passive layer is stimulated to grow at the exit side. In this way, corrosion processes are avoided and only the hydrogen oxidation current can be recorded. In general, a zero hydrogen concentration at the exit side is assumed, but this does not always reflect reality. Therefore, a subsurface-surface equilibrium is added to the model by which the hydrogen oxidation reaction (inversed Volmer) as well as the chemical recombination reaction (Tafel) is included. The complexity of the desorption-oxidation process is of high degree, most certainly when there is no Pd-coating present. Besides, the presence of the oxide layer is not included due to the lack of consistent literature.

Based on the model results, there is a clear indication that the exit surface of the metal membrane must be included in the simulations to obtain a correct reproduction of the experimental results. Due to the presence of a subsurface-surface equilibrium, a non-zero hydrogen concentration at the exit side may be achieved. The incomplete hydrogen oxidation can lead to a positive hydrogen concentration at the subsurface which leads to a much higher concentration inside the bulk of the material. Vecchi *et al.* [93] indicated that overlooking this factor could mislead the interpretation and evaluation of the experimental results.

Next to the kinetics of the oxidation reaction and pH, both depending on the electrolyte, it was pointed out that the Tafel reaction, or chemical hydrogen recombination reaction, possibly had a big influence on the resulting data. The modelled permeation curves are shown in Figure I-13. Increasing the rate constant K_{rec} resulted in a lower steady state value and less time was needed to achieve it. This indicated the importance of the chemical recombination reaction on the experimental results in cases where it becomes significant. Unfortunately, the effective contribution of this recombination reaction is still unknown.

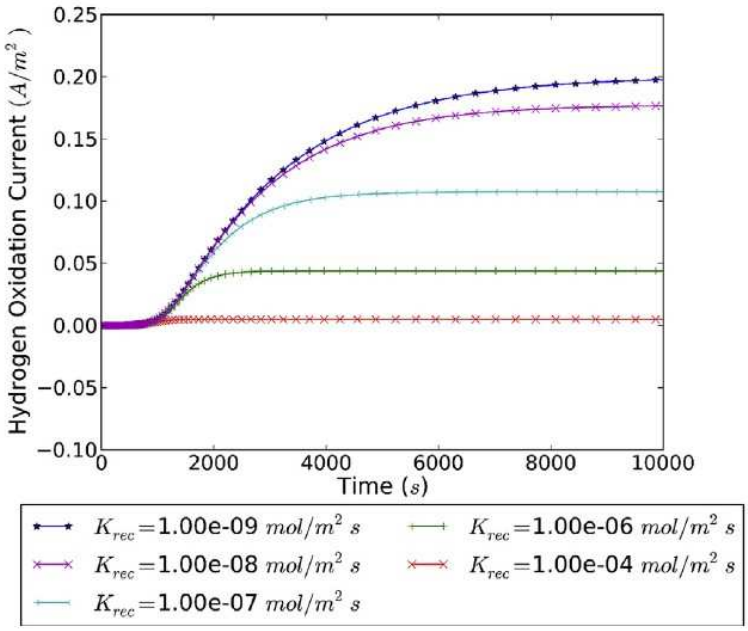

Figure I-13 Effect of the Tafel hydrogen recombination constant K_{rec} on the hydrogen oxidation current [93].

In conclusion, Vechhi *et al.* [92, 93] proposed a new model in order to study the hydrogen diffusion in the Devanathan-Stachurski cell. The model allowed a better interpretation of the experimental observations, highlighting the significant effect of the entrance and exit surfaces on the overall hydrogen transport process. Although the deduced kinetic parameters were not reliable, due to the lack of knowledge on the mechanism of hydrogen adsorption, absorption and desorption, the model allowed to investigate phenomena which have not been possible to study experimentally.

I.6 Scope

The presence of hydrogen is known to deteriorate the mechanical properties of steel. As such, there is an increased tendency for crack formation leading to a possible unforeseen failure of the construction. Nonetheless, a certain hydrogen concentration is required to initiate and propagate a crack in the microstructure. The susceptibility of the material to hydrogen induced damage depends thus on the amount of hydrogen able to diffuse to critical, for example stressed, regions in the microstructure. Since hydrogen is attracted to these regions, the required concentration for crack propagation can be reached more easily. However, next to the hydrogen concentration, the ability to reach the critical zones is a very important parameter which cannot be ignored. This ability is described by the hydrogen diffusion coefficient of the material.

The prominent role of the hydrogen diffusivity was demonstrated by Depover *et al.* [63]. By in-situ hydrogen charged tensile tests, the effect of hydrogen on the ductility of bainitic alloys was measured. Generally, the ductility loss was more significant with a lower crosshead deformation speed. In that case, the hydrogen had more time to diffuse and the critical concentration for crack initiation was reached earlier, increasing the hydrogen embrittlement index. Furthermore, the authors compared two bainitic alloys with a different carbon content of 0.2% and 0.4%. Even though the higher amount of carbon led to a higher hydrogen concentration in the material, a lower embrittlement index was determined at the lower crosshead deformation speed. This was attributed to the lower diffusion coefficient of the material which contained 0.4% C. The lower diffusivity decreased the ability to reach the critical zones and crack initiation and propagation were postponed. At a higher crosshead deformation speed, the 0.4% C steel showed a larger susceptibility to hydrogen embrittlement. In that case, only limited diffusion took place and therefore the amount of hydrogen played a more prominent role in the observed embrittlement index.

This work nicely demonstrated that the link between the amount of hydrogen and the susceptibility to hydrogen embrittlement is impossible without also incorporating the hydrogen diffusion coefficient of that specific microstructure into the discussion. Consequently, it is of high importance to consider the hydrogen diffusion coefficient when new materials are being developed with the purpose of decreasing the susceptibility to the hydrogen embrittlement phenomenon. Therefore, this work focuses on the experimental technique that allows to determine the hydrogen diffusion coefficient, namely the electrochemical permeation technique. Specific characteristics of the technique will be elaborated and the classic Devanathan and Stachurski set-up will be extended to incorporate the role of stress in the material.

I.7 References

[1] W. Johnson, "On some remarkable change produced in iron and steel by the action of hydrogen and acids," *Proceedings of the Royal Society of London,* vol. 23, pp. 168-179, 1875.

[2] A. Paxton, A. Sutton, and M. Finnis, "The challenges of hydrogen and metals," *Phil. Trans. R. Soc. A.,* vol. 375, 2017.

[3] T. Depover, D. P. Escobar, E. Wallaert, Z. Zermout, and K. Verbeken, "Effect of hydrogen charging on the mechanical properties of advanced high strength steels," *international journal of hydrogen energy,* vol. 39, pp. 4647-4656, 2014.

[4] J. Venezuela, Q. Zhou, Q. Liu, M. Zhang, and A. Atrens, "Influence of hydrogen on the mechanical and fracture properties of some martensitic advanced high strength steels in simulated service conditions," *Corrosion Science,* vol. 111, pp. 602-624, 2016.

[5] G. Lovicu, M. Bottazzi, F. D'Aiuto, M. De Sanctis, A. Dimatteo, C. Santus, *et al.*, "Hydrogen embrittlement of automotive advanced high-strength steels," *Metallurgical and Materials Transactions A,* vol. 43, pp. 4075-4087, 2012.

[6] J. Ćwiek, "Hydrogen degradation of high-strength steels," *Journal of Achievements in Materials and Manufacturing Engineering,* vol. 37, pp. 193-212, 2009.

[7] J. Toribio, M. Lorenzo, D. Vergara, and V. Kharin, "Numerical analysis of hydrogen-assisted rolling-contact fatigue of wind turbine bearings," *Frattura ed Integrità Strutturale,* vol. 8, pp. 40-47, 2014.

[8] T. Depover, E. Wallaert, and K. Verbeken, "On the synergy of diffusible hydrogen content and hydrogen diffusivity in the mechanical degradation of laboratory cast Fe-C alloys," *Materials Science and Engineering: A,* vol. 664, pp. 195-205, 2016.

[9] T. Carter and L. Comish, "Hydrogen in metals," *Engineering failure analyses,* vol. 8, pp. 113-121, 2001.

[10] M. Devanathan and Z. Stachurski, "The mechanism of hydrogen evolution on iron in acid solutions by determination of permeation rates," *Journal of the electrochemical society,* vol. 111, pp. 619-623, 1964.

[11] E. Dafft, K. Bohnenkamp, and H. Engell, "Investigations of the hydrogen evolution kinetics and hydrogen absorption by iron electrodes during cathodic polarization," *Corrosion Science,* vol. 19, pp. 591-612, 1979.

[12] J. M. Bockris, J. McBreen, and L. Nanis, "The Hydrogen Evolution Kinetics and Hydrogen Entry into a-Iron," *Journal of The Electrochemical Society,* vol. 112, pp. 1025-1031, 1965.

[13] M. G. de Chialvo and A. Chialvo, "Kinetics of hydrogen evolution reaction with Frumkin adsorption: re-examination of the Volmer–Heyrovsky and Volmer–Tafel routes," *Electrochimica acta,* vol. 44, pp. 841-851, 1998.

[14] P. Quaino, M. G. de Chialvo, and A. Chialvo, "Hydrogen electrode reaction: A complete kinetic description," *Electrochimica acta,* vol. 52, pp. 7396-7403, 2007.

[15] M. G. de Chialvo and A. Chialvo, "The Tafel–Heyrovsky route in the kinetic mechanism of the hydrogen evolution reaction," *Electrochemistry communications,* vol. 1, pp. 379-382, 1999.

[16] A. Turnbull, "Perspectives on hydrogen uptake, diffusion and trapping," *International Journal of Hydrogen Energy,* vol. 40, pp. 16961-16970, 2015.

[17] W. von Baeckmann, W. Schwenk, and W. Prinz, *Handbook of cathodic corrosion protection*: Elsevier, 1997.

[18] V. Ashworth, "4.18 Principles of Cathodic Protection," *Shreir's Corros,* pp. 2747-2762, 2010.

[19] W. D. C. a. D. G. Rethwisch, *Materials Science and Engineering An Introduction,* Seventh edition ed.: John Wiley & Sons, 2011.

[20] J. DeLuccia and D. Berman, "An electrochemical technique to measure diffusible hydrogen in metals (Barnacle electrode)," in *Electrochemical Corrosion Testing*, ed: ASTM International, 1981.

[21] J. Da Silva, S. Stafford, and R. B. McLellan, "The thermodynamics of the hydrogen-iron system," *Journal of the Less Common Metals,* vol. 49, pp. 407-420, 1976.

[22] V. Olden, C. Thaulow, and R. Johnsen, "Modelling of hydrogen diffusion and hydrogen induced cracking in supermartensitic and duplex stainless steels," *Materials & design,* vol. 29, pp. 1934-1948, 2008.

[23] N. Skorodumova, R. Ahuja, and B. Johansson, "Influence of hydrogen on the stability of iron phases under pressure," *Geophysical research letters,* vol. 31, 2004.

[24] Y. Fukai, *The metal-hydrogen system: basic bulk properties* vol. 21: Springer Science & Business Media, 2006.

[25] S. Lynch, "Hydrogen embrittlement (HE) phenomena and mechanisms," in *Stress Corrosion Cracking*, ed: Elsevier, 2011, pp. 90-130.

[26] G. Pressouyre, "Trap theory of hydrogen embrittlement," *Acta Metallurgica,* vol. 28, pp. 895-911, 1980.

[27] R. Oriani, "Hydrogen degradation of ferrous alloys," *Noyes Publications, Mill Rd. at Grand Ave, Park Ridge, New Jersey 7656, USA, 1985. 886*, 1985.
[28] G. Pressouyre and I. Bernstein, "An example of the effect of hydrogen trapping on hydrogen embrittlement," *Metallurgical Transactions A*, vol. 12, pp. 835-844, 1981.
[29] K. V. Lierop and M. Verhaege, "Experimentele bepaling van de H-huishouding in staal met behulp van thermische desorptie spectroscopie," Universiteit Gent, 2006.
[30] R. Gibala and D. DeMiglio, "Hydrogen in iron and steels: interactions, traps and crack paths," *Hydrogen Effects in Metals*, pp. 113-122, 1980.
[31] R. Gibala and A. Kumnick, "Hydrogen trapping in iron and steels," *Hydrogen embrittlement and stress corrosion cracking*, pp. 61-77, 1980.
[32] G. Pressouyre, "A classification of hydrogen traps in steel," *Metallurgical and Materials Transactions A*, vol. 10, pp. 1571-1573, 1979.
[33] W. Choo and J. Y. Lee, "Thermal analysis of trapped hydrogen in pure iron," *Metallurgical and Materials Transactions A*, vol. 13, pp. 135-140, 1982.
[34] R. L. Thomas, D. Li, R. P. Gangloff, and J. R. Scully, "Trap-governed hydrogen diffusivity and uptake capacity in ultrahigh-strength AERMET 100 steel," *Metallurgical and Materials Transactions A*, vol. 33, pp. 1991-2004, 2002.
[35] D. Li, R. P. Gangloff, and J. R. Scully, "Hydrogen trap states in ultrahigh-strength AERMET 100 steel," *Metallurgical and materials transactions A*, vol. 35, pp. 849-864, 2004.
[36] R. L. Thomas, J. R. Scully, and R. P. Gangloff, "Internal hydrogen embrittlement of ultrahigh-strength AERMET 100 steel," *Metallurgical and Materials Transactions A*, vol. 34, pp. 327-344, 2003.
[37] D. P. Escobar, K. Verbeken, L. Duprez, and M. Verhaege, "Evaluation of hydrogen trapping in high strength steels by thermal desorption spectroscopy," *Materials Science and Engineering: A*, vol. 551, pp. 50-58, 2012.
[38] H. Lee and J.-Y. Lee, "Hydrogen trapping by TiC particles in iron," *Acta Metallurgica*, vol. 32, pp. 131-136, 1984.
[39] J. Beeler Jr and R. Johnson, "Vacancy clusters in α-iron," *Physical Review*, vol. 156, p. 677, 1967.
[40] A. Kumnick and H. Johnson, "Deep trapping states for hydrogen in deformed iron," *Acta Metallurgica*, vol. 28, pp. 33-39, 1980.
[41] Y. Park, I. Maroef, A. Landau, and D. Olson, "Retained austenite as a hydrogen trap in steel welds," *Welding Journal-New York-*, vol. 81, pp. 27-S, 2002.
[42] W. Counts, C. Wolverton, and R. Gibala, "First-principles energetics of hydrogen traps in α-Fe: Point defects," *Acta Materialia*, vol. 58, pp. 4730-4741, 2010.
[43] D. Mirzaev, A. Mirzoev, K. Y. Okishev, and A. Verkhovykh, "Hydrogen–vacancy interaction in bcc iron: ab initio calculations and thermodynamics," *Molecular Physics*, vol. 112, pp. 1745-1754, 2014.
[44] M. Iwamoto and Y. Fukai, "Superabundant vacancy formation in iron under high hydrogen pressures: thermal desorption spectroscopy," *Materials Transactions, JIM*, vol. 40, pp. 606-611, 1999.
[45] C. Zapffe and C. Sims, "Hydrogen embrittlement, internal stress and defects in steel," *Trans. AIME*, vol. 145, pp. 225-271, 1941.
[46] A. TROIANO, "The Role of Hydrogen and Other Interstitials in the Mechanical Behavior of Metals," *Transactions of the ASM*, vol. 52, pp. 54-81, 1960.
[47] R. Oriani, "A mechanistic theory of hydrogen embrittlement of steels," *Berichte der Bunsengesellschaft für physikalische Chemie*, vol. 76, pp. 848-857, 1972.
[48] R. Oriani and P. Josephic, "Equilibrium aspects of hydrogen-induced cracking of steels," *Acta Metallurgica*, vol. 22, pp. 1065-1074, 1974.
[49] M. E. Stroe, "Hydrogen embrittlement of ferrous materials," *Romania: Universite Libre De Bruxelles*, 2006.
[50] C. Beachem, "A new model for hydrogen-assisted cracking (hydrogen "embrittlement")," *Metallurgical transactions*, vol. 3, pp. 441-455, 1972.
[51] H. K. Birnbaum and P. Sofronis, "Hydrogen-enhanced localized plasticity—a mechanism for hydrogen-related fracture," *Materials Science and Engineering: A*, vol. 176, pp. 191-202, 1994.
[52] N. Narita, C. Altstetter, and H. Birnbaum, "Hydrogen-related phase transformations in austenitic stainless steels," *Metallurgical and Materials Transactions A*, vol. 13, pp. 1355-1365, 1982.
[53] P. Ferreira, I. Robertson, and H. Birnbaum, "Hydrogen effects on the interaction between dislocations," *Acta materialia*, vol. 46, pp. 1749-1757, 1998.
[54] D. Shih, I. Robertson, and H. Birnbaum, "Hydrogen embrittlement of α titanium: in situ TEM studies," *Acta Metallurgica*, vol. 36, pp. 111-124, 1988.

[55] Q. Liu, B. Irwanto, and A. Atrens, "The influence of hydrogen on 3.5 NiCrMoV steel studied using the linearly increasing stress test," *Corrosion Science*, vol. 67, pp. 193-203, 2013.
[56] S. Lynch, "Comments on “A unified model of environment-assisted cracking”," *Scripta Materialia*, vol. 61, pp. 331-334, 2009.
[57] I. Moro, "Fragilisation par l'hydrogène gazeux d'un acier ferrito-perlitique de grade API X80," Institut National Polytechnique de Toulouse, 2009.
[58] A. Griesche, E. Dabah, T. Kannengiesser, N. Kardjilov, A. Hilger, and I. Manke, "Three-dimensional imaging of hydrogen blister in iron with neutron tomography," *Acta Materialia*, vol. 78, pp. 14-22, 2014.
[59] J.-L. Lee and J.-Y. Lee, "The effect of lattice defects induced by cathodic hydrogen charging on the apparent diffusivity of hydrogen in pure iron," *Journal of materials science*, vol. 22, pp. 3939-3948, 1987.
[60] A. Tetelman and W. Robertson, "The mechanism of hydrogen embrittlement observed in iron-silicon single crystals," DTIC Document 1961.
[61] D. P. Escobar, C. Minambres, L. Duprez, K. Verbeken, and M. Verhaege, "Internal and surface damage of multiphase steels and pure iron after electrochemical hydrogen charging," *Corrosion Science*, vol. 53, pp. 3166-3176, 2011.
[62] A. Laureys, E. Van den Eeckhout, R. Petrov, and K. Verbeken, "Effect of deformation and charging conditions on crack and blister formation during electrochemical hydrogen charging," *Acta Materialia*, 2017.
[63] T. Depover, E. Van den Eeckhout, and K. Verbeken, "The impact of hydrogen on the ductility loss of bainitic Fe–C alloys," *Materials Science and Technology*, vol. 32, pp. 1625-1631, 2016.
[64] A. Laureys, E. Van den Eeckhout, R. Petrov, and K. Verbeken, "Title," unpublished|.
[65] M. Devanathan and Z. Stachurski, "The adsorption and diffusion of electrolytic hydrogen in palladium," in *Proceedings of the Royal Society of London A: Mathematical, Physical and Engineering Sciences*, 1962, pp. 90-102.
[66] A. McNabb and P. Foster, "A new analysis of the diffusion of hydrogen in iron and ferritic steels," *Trans. Metall. Soc. AIME*, vol. 227, pp. 618-627, 1963.
[67] R. A. Oriani, "The diffusion and trapping of hydrogen in steel," *Acta metallurgica*, vol. 18, pp. 147-157, 1970.
[68] J. Leblond and D. Dubois, "A general mathematical description of hydrogen diffusion in steels—I. Derivation of diffusion equations from boltzmann-type transport equations," *Acta Metallurgica*, vol. 31, pp. 1459-1469, 1983.
[69] J. Leblond and D. Dubois, "A general mathematical description of hydrogen diffusion in steels—II. Numerical study of permeation and determination of trapping parameters," *Acta metallurgica*, vol. 31, pp. 1471-1478, 1983.
[70] Q. Liu, J. Venezuela, M. Zhang, Q. Zhou, and A. Atrens, "Hydrogen trapping in some advanced high strength steels," *Corrosion Science*, vol. 111, pp. 770-785, 2016.
[71] S. Frappart, X. Feaugas, J. Creus, F. Thebault, L. Delattre, and H. Marchebois, "Study of the hydrogen diffusion and segregation into Fe–C–Mo martensitic HSLA steel using electrochemical permeation test," *Journal of Physics and Chemistry of Solids*, vol. 71, pp. 1467-1479, 2010.
[72] N. Boes and H. Züchner, "Electrochemical methods for studying diffusion, permeation and solubility of hydrogen in metals," *Journal of the Less Common Metals*, vol. 49, pp. 223-240, 1976.
[73] M. D. Archer and N. Grant, "Achievable boundary conditions in potentiostatic and galvanostatic hydrogen permeation through palladium and nickel foils," in *Proceedings of the Royal Society of London A: Mathematical, Physical and Engineering Sciences*, 1984, pp. 165-183.
[74] S. J. Kim, D. W. Yun, H. G. Jung, and K. Y. Kim, "Determination of hydrogen diffusion parameters of ferritic steel from electrochemical permeation measurement under tensile loads," *Journal of The Electrochemical Society*, vol. 161, pp. E173-E181, 2014.
[75] J. McBreen, L. Nonis, and W. Beck, "A method for determination of the permeation rate of hydrogen through metal membranes," *Journal of the electrochemical society*, vol. 113, pp. 1218-1222, 1966.
[76] E. Fallahmohammadi, G. Fumagalli, G. Re, F. Bolzoni, and L. Lazzari, "Study on hydrogen diffusion in pipeline steels," in *Proc of Eurocorr*, 2011, p. 1e21.
[77] J. Crank, *The mathematics of diffusion*: Oxford university press, 1979.
[78] S. Frappart, "Des éléments de compréhension sur les mécanismes de transport et de ségrégation de l'hydrogène dans les aciers martensitiques trempés et revenus à haute limite d'élasticité," Université de La Rochelle, 2011.
[79] E. Hillier and M. Robinson, "Hydrogen embrittlement of high strength steel electroplated with zinc–cobalt alloys," *Corrosion science*, vol. 46, pp. 715-727, 2004.

[80] T. Zakroczymski and Z. Szklarska-Smialowska, "Activation of the iron surface to hydrogen absorption resulting from a long cathodic treatment in NaOH solution," *Journal of the Electrochemical Society,* vol. 132, pp. 2548-2552, 1985.
[81] P. Manolatos and M. Jerome, "A thin palladium coating on iron for hydrogen permeation studies," *Electrochimica Acta,* vol. 41, pp. 359-365, 1996.
[82] P. Manolatos, M. Jerome, and J. Galland, "Necessity of a palladium coating to ensure hydrogen oxidation during electrochemical permeation measurements on iron," *Electrochimica Acta,* vol. 40, pp. 867-871, 1995.
[83] H. Addach, P. Berçot, M. Rezrazi, and J. Takadoum, "Study of the electrochemical permeation of hydrogen in iron," *Corrosion Science,* vol. 51, pp. 263-267, 2009.
[84] T. Casanova and J. Crousier, "The influence of an oxide layer on hydrogen permeation through steel," *Corrosion Science,* vol. 38, pp. 1535-1544, 1996.
[85] J. Collet-Lacoste, "Intervention des phenomenes de surface sur la permeation electrochimique de l'hydrogene dans le fer. Role d'une couche d'oxyde ou de palladium," Paris 11, 1993.
[86] S.-I. Pyun and Y.-G. Yoon, "Hydrogen transport through metals determined by electrochemical methods," *International Materials Reviews,* 2000.
[87] F. Heubaum and B. Berkowitz, "The effect of surface oxides On the hydrogen permeation through steels," *Scripta Metallurgica,* vol. 16, pp. 659-662, 1982.
[88] A. Brass and J. Collet-Lacoste, "On the mechanism of hydrogen permeation in iron in alkaline medium," *Acta materialia,* vol. 46, pp. 869-879, 1998.
[89] E. Wu, "A mathematical treatment of the electrochemical method of hydrogen permeation and its application in hydrogen traps and embrittlement," *Journal of the Electrochemical Society,* vol. 134, pp. 2126-2133, 1987.
[90] S.-I. Pyun and R. Oriani, "The permeation of hydrogen through the passivating films on iron and nickel," *Corrosion science,* vol. 29, pp. 485-496, 1989.
[91] J. Yu, J. Luo, and P. Norton, "Effects of hydrogen on the electronic properties and stability of the passive films on iron," *Applied surface science,* vol. 177, pp. 129-138, 2001.
[92] L. Vecchi, H. Simillion, R. Montoya, D. Van Laethem, E. Van den Eeckhout, K. Verbeken, *et al.*, "Modelling of hydrogen permeation experiments in iron alloys: Characterization of the accessible parameters–Part I–The entry side," *Electrochimica Acta,* vol. 262, pp. 57-65, 2018.
[93] L. Vecchi, H. Simillion, R. Montoya, D. Van Laethem, E. Van den Eeckhout, K. Verbeken, *et al.*, "Modelling of hydrogen permeation experiments in iron alloys: Characterization of the accessible parameters–Part II–The exit side," *Electrochimica Acta,* vol. 262, pp. 153-161, 2018.
[94] W. Zhao, T. Zhang, Z. He, J. Sun, and Y. Wang, "Determination of the Critical Plastic Strain-Induced Stress of X80 Steel through an Electrochemical Hydrogen Permeation Method," *Electrochimica Acta,* vol. 214, pp. 336-344, 2016.
[95] S. J. Kim, "Effect of the elastic tensile load on the electrochemical corrosion behavior and diffusible hydrogen content of ferritic steel in acidic environment," *International Journal of Hydrogen Energy,* vol. 42, pp. 19367-19375, 2017.
[96] Y. Huang, A. Nakajima, A. Nishikata, and T. Tsuru, "Effect of mechanical deformation on permeation of hydrogen in iron," *ISIJ international,* vol. 43, pp. 548-554, 2003.
[97] M. Kurkela, G. Frankel, R. Latanision, S. Suresh, and R. Ritchie, "Influence of plastic deformation on hydrogen transport in 2 14 Cr-1Mo steel," *Scripta Metallurgica,* vol. 16, pp. 455-459, 1982.
[98] S. J. Kim and K. Y. Kim, "Electrochemical hydrogen permeation measurement through high-strength steel under uniaxial tensile stress in plastic range," *Scripta Materialia,* vol. 66, pp. 1069-1072, 2012.

CHAPTER II

Experimental procedure of the electrochemical permeation technique

II.1 Permeation test method 1

In this work, the electrochemical permeation technique was used to obtain the hydrogen diffusion coefficient of the material of interest. The permeation test method 1 was based on the earlier work of Simpelaere [1], who already performed experimental research at Ghent University in order to develop the permeation methodology. In this section, the permeation test method 1 is described. However, during the course of this research, a novel permeation set-up, that fits an external loading device has been developed. During the design stage, the focus was put on a better control of multiple parameters affecting the permeation transient. When samples were tested using this novel set-up, a reference to the permeation test method 2 (cf. section II.2) is made in the text. Procedures described in this chapter are the standard methods and modifications made to these methods are indicated throughout the next chapters.

The materials used in this research were pure Armco iron, dual phase (DP) steel and four carbide containing quenched and tempered Fe-C-X alloys, with X = W, Cr, Ti or V. More details about the microstructure and chemical composition are given in the following chapters. Permeation test samples were discs with a diameter of 20 mm and thickness of 1 mm. Using this thickness, the hydrogen permeation was assumed to be bulk controlled. Both sides, entrance and exit surface, were manually ground and polished with a final polishing step of 1 µm using a water-based diamond suspension. As was mentioned in the literature study, defects and/or oxides at a metal/Pd interface are easily introduced during the palladium plating process. These heterogeneities may affect the hydrogen diffusion in an uncontrolled manner, which is not desirable. Therefore, it was chosen not to put a Pd-layer at the exit side of the sample as it is believed that reliable results considering the diffusion properties can be obtained without the use of Pd as well [2-4]. After point welding a nickel-chromium wire to the sample, it was cleaned with acetone and placed in between two independent compartments where a surface of 1 cm^2 was available for exposure to the electrolyte. The set-up, schematically represented in Figure II-1, consisted of two double glass cells with the disc placed in between. A two-electrode system was present in the cathodic cell, i.e. the working electrode (WE) and the platinum counter electrode (CE). The anodic cell contained, beside the WE and CE, a Hg/Hg_2SO_4 reference electrode (RE, +650 mV vs the standard hydrogen electrode, SHE). The three electrodes in the anodic cell were connected to a Versastat3F potentiostat, while the two electrodes in the cathodic cell were coupled to an external battery supply. As such, the required floating conditions were accomplished. The temperature of the electrolyte, in both cells 0.1 M NaOH, was controlled at 25°C by circulating water in the outer layer of the cells. N_2–gas was blown into the cells to diminish the oxygen content and thus minimizing undesired oxidation reactions.

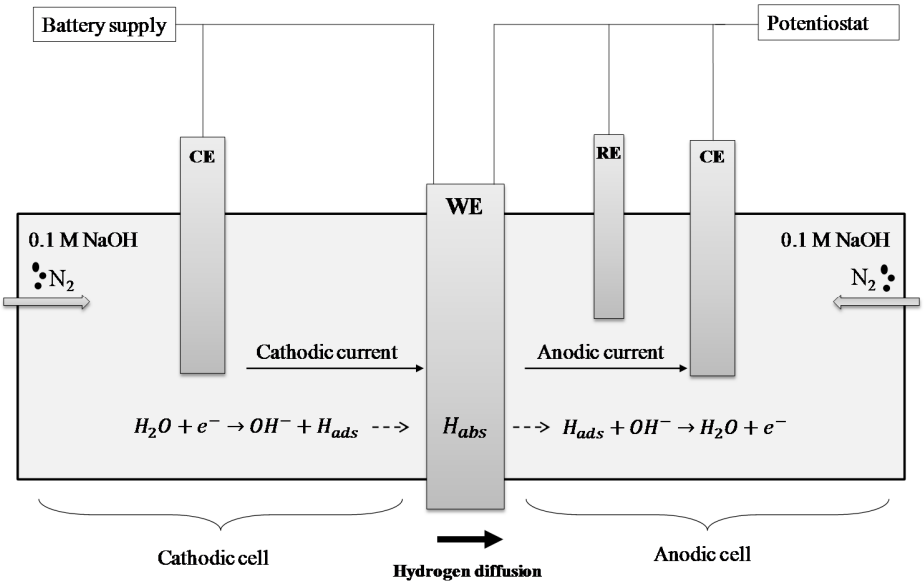

Figure II-1 Schematic representation of the permeation set-up. CE = counter electrode, RE = reference electrode, WE = working electrode.

Instead of plating a Pd-layer at the exit surface, a passive iron-oxide layer was imposed. This layer was created by applying a potential of -500 mV with respect to the RE before starting up the actual experiment. After 18 hours, the background current density was sufficiently low (maximum 100 nA/cm²) in order to detect the permeated hydrogen atoms. This current was then taken into account when processing the resulted data. Before the passivation step, the oxygen content of the electrolyte was lowered by blowing nitrogen gas through the solution for 2 hours.

After passivation, the hydrogen charging step was carried out. The cathodic cell was filled with deaerated NaOH solution under galvanostatic control (-3 mA/cm²). As such, the metal surface was immediately cathodically protected from undesired anodic reactions. Important to note is that, in Chapter III, the applied current density at the cathodic side of the sample, was indicated with a positive sign although the sign convention uses a negative one. The anodic compartment was kept polarized in the passivation range, hence, the hydrogen atoms at the exit side were oxidized. The sample was charged with hydrogen until a steady state current density value, i.e. hydrogen permeation flux, at the exit side was obtained. The hydrogen oxidation current density versus time, recorded by the potentiostat, was further processed to determine the hydrogen diffusion coefficient. In Figure II-2, a summary of the permeation method 1 is presented.

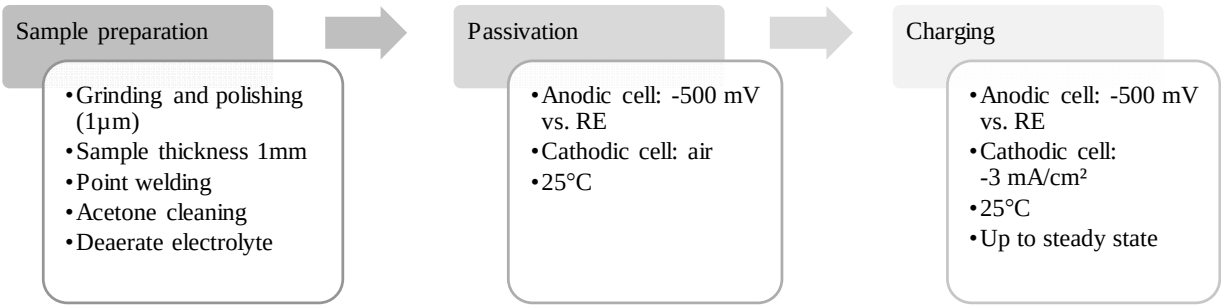

Figure II-2 Test procedure of the permeation test method 1.

II.2 Permeation test method 2

Test samples used in this method were again discs with a diameter of 20 mm and a thickness of about 1 mm. An average thickness of 5 different measurements in the zone of interest was used to calculate the diffusion coefficient. Both sides of the sample were ground and polished with a final polishing step of 1 µm. After point welding a nickel-chromium wire to the sample, it was cleaned with acetone and placed in between two independent air-tight compartments where a surface of 1.34 cm² was available for electrolyte exposure. The cathodic cell was then filled up with nitrogen gas to avoid oxide formation at the entrance side during the overnight passivation step at the exit side.

The set-up, represented in Figure II-3, consisted of two double glass cells with the sample in between. In both cells there is a three-electrode system: the WE, the platinum CE and the Hg/Hg_2SO_4 RE (+650mV vs the SHE). The three electrodes were connected to the Versastat3F and the CompactStat in the anodic and cathodic cell, respectively. The CompactStat was set in floating mode in such a way that the electrical circuits of the compartments were separated. The use of a second potentiostat allowed to record the entrance potential of the sample surface and hence also different current densities could be applied. The temperature of the electrolyte, in both cells 0.1 M NaOH, was controlled at 25°C by circulating water in the outer layer of the cells. N_2-gas, blown into the air-tight compartments diminished the oxygen content and consequently minimized undesired oxidation reactions.

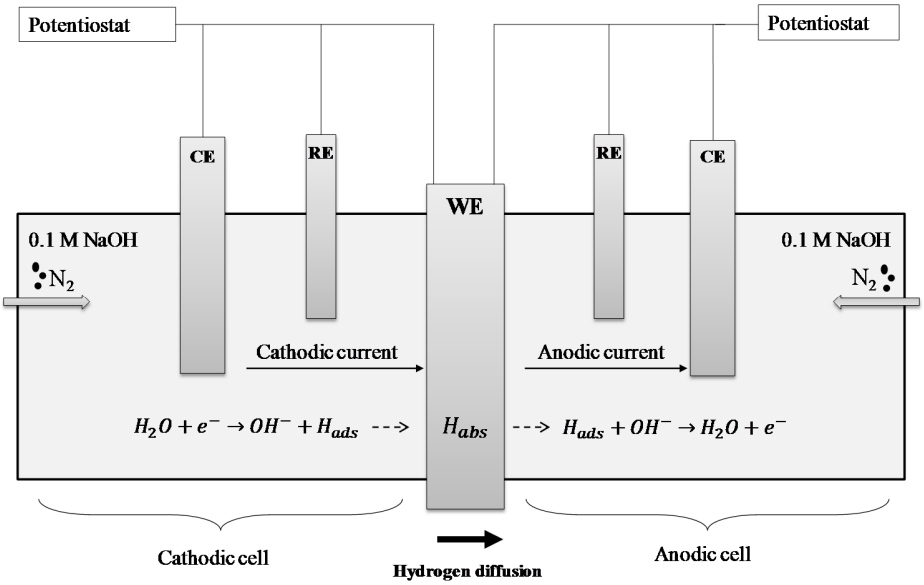

Figure II-3 Schematic representation of the newly designed permeation set-up. CE = counter electrode, RE = reference electrode, WE = working electrode.

At the exit side, a passive iron-oxide layer was imposed by applying a potential of -500 mV according to the RE. Before the start of the relaxation step, the electrolyte was heated to 25°C and the oxygen content was lowered by blowing nitrogen gas through the electrolyte for at least 1 hour. The anodic cell was filled with the solution by a peristaltic pump. Throughout the entire experiment, constant circulation in the anodic cell was maintained. When, after about 17 hours, a stable background current density (maximum 100 nA/cm²) was achieved, the hydrogen charging was started. After passivation, the hydrogen permeation was carried out. The cathodic cell was filled with deaerated NaOH solution under galvanostatic control (-3 mA/cm²). In the permeation test method 2, the electrolyte was preheated to 25°C. The time at which the hydrogen charging started, was noted and the hydrogen charging was performed until a steady state hydrogen permeation flux value was obtained. In some experiments, the decay and a second transient were registered. During the entire test, current densities and potentials on both sides were recorded. The hydrogen oxidation current density versus time, recorded by the potentiostat, was further processed to determine the hydrogen diffusion coefficient. In Figure II-4, the test procedure of the permeation method 2 is summarized. The differences with the permeation test method 1 were indicated in *italic*. When a second charging was performed, the entrance surface was polarized again by applying the desired current density.

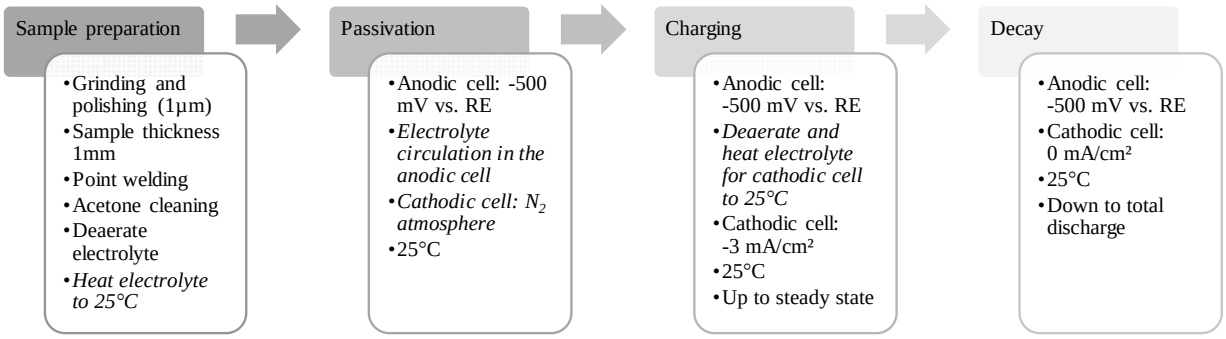

Figure II-4 Test procedure of the electrochemical permeation method 2.

II.3 Permeation with a constant load

In order to be able to measure the effect of stresses on the hydrogen diffusion process, a third type of set-up was developed. The novel set-up was designed in such a way it fitted around an external proof ring, which was manufactured by CORMET®. With the incorporation of the proof ring, a constant load between 10 and 20 kN could be applied while carrying out a permeation experiment. The required tensile load was achieved by compressing the ring and the actual load was determined from the load amplifier. For this purpose, rectangular samples were required, having a width of 25 or 47 mm and a length of 90 mm. The thickness was varied per material, but was approximately 1 mm. As such, the hydrogen diffusion was bulk controlled. An average thickness of 5 different measurements in the zone of interest was used to calculate the diffusion coefficient. The final grinding step, at both sides of the sample, consisted of at least 1.5 minutes of grinding with a 500 grit SiC disc at the Tegramine-30. The force at this grinding step was 35 N and the rotation speed of the grinding disc and sample holder were 300 rpm and 150 rpm, respectively. The choice of this grinding procedure, at both entrance and exit side, was based on experimental results and will be clarified in chapter III. Subsequently, the outer ends of the specimen were sand blasted in order to increase the friction coefficient between the specimen and sample holders. After point welding a nickel-chromium wire, the sample was cleaned with acetone. It was then mounted in the proof ring and the required load was applied. Finally, the permeation set-up was fitted around the specimen and the passivation step at the exit side was started. The test procedure to perform the permeation experiment followed the permeation test method 2 (Figure II-4).

II.4 Determining the diffusion coefficient

II.4.1. Single point method

As described in section I.3.2, Fick's theory can be used to determine the apparent hydrogen diffusion coefficient $D_{app.}$ One way to define D_{app} is by the mathematical relation derived from Fick's solutions given in Equation II-1 where L (m) is the specimen thickness and M a constant depending on the time value t_x (s), chosen in the normalized charging transient. In this work, this method is called the 'single point method'. The normalized hydrogen flux J_{norm} in mol·m^{-2}·s^{-1} is calculated using Equation II-2 where J_{back} is the background flux and J_∞ the steady state flux.

$$D_{app} = \frac{L^2}{M t_x} \tag{II-1}$$

$$J_{norm} = \frac{J - J_{back}}{J_\infty - J_{back}} \tag{II-2}$$

J_{norm} was obtained by associating the measured permeation current density I (A·m^{-2}) with the hydrogen oxidation reaction by Equation II-3, where F is the Faraday constant (A·s·mol^{-1}) and J the hydrogen diffusion flux (mol/m²·s).

$$I = F * J \tag{II-3}$$

As such, the hydrogen flux J could be replaced by the hydrogen permeation current density I. Therefore, when the steady state current density I_∞ was specified and the background current density I_{back} was taken into account, I_{norm} and D_{app} were calculated. A schematic representation of the normalized transient versus time is given in Figure II-5. M constants for different values of t_x are summarized in Table I-1.

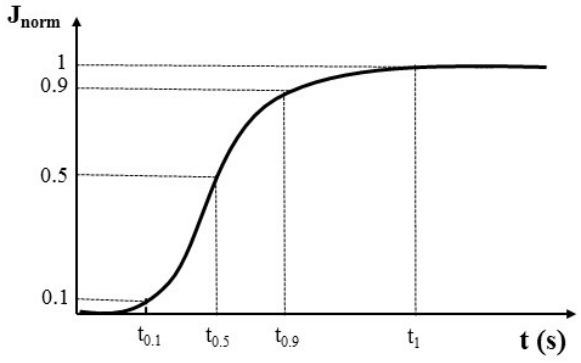

Figure II-5 Schematic representation of a normalized permeation rise transient for calculating D_{app} using the single point method.

Table I-1 M-values for different t-values using galvanostatic boundary conditions.

t_x	M-value
$t_{0.01}$	15.7
$t_{0.1}$	7.7
$t_{0.5}$	2.7
$t_{0.63}$	2.0
$t_{0.9}$	0.97

When calculating D_{app} at $t_{0.01}$, $t_{0.1}$, $t_{0.5}$, $t_{0.63}$, and $t_{0.9}$ of the normalized current, the highest reproducibility, i.e. lowest standard error (SE), was obtained at $t_{0.1}$. Hence, throughout this research, the diffusion coefficient was determined based on $t_{0.1}$. In addition, it must be mentioned that during the first build-up transient, it is difficult to avoid the effects of slower surface processes (involving hydrogen entry) and trapping (involving hydrogen transport). Hydrogen trapping and surface phenomena can be minimized by performing a second or partial permeation rise transient.

When a steady state condition during the first charging step was reached, the polarization at the entrance side was stopped and a decay transient at the exit side was recorded. When a sufficiently low background current was obtained, a second charging step could be started. As such, all diffusible and reversibly trapped hydrogen was removed from the specimen. Only the hydrogen in trapping sites having a very low leakage rate, i.e. irreversible trapping sites, is at that moment still present in the microstructure. Therefore, these trapping sites did not affect the second permeation transient and information could be obtained concerning the trapping ability of the material. Partial permeation transients were performed by increasing the applied cathodic current density at the entrance side after a steady state condition from the first charging step was reached. It is believed that partial transients were controlled by lattice diffusion only due to the preserved equilibrium between the diffusible and trapped hydrogen [5]. The experimental parameters of aforementioned tests are given throughout the text.

II.4.2. Curve fitting

In this method, D_{app} is determined by fitting the normalized experimental data with the theoretical permeation transient based on Fick's laws. Throughout the text, D calculated by using the fitting method will be labelled as $D_{app,\ fit}$. As elucidated in section I.3.1, using Fourier series and the right boundary conditions, Fick's first and second law could be solved. In this work, the experimental curves were fitted with the galvanostatic model (constant flux, CF) which is expressed Equation II-4 [6, 7]. According to the ASTM international standard, a value of at least n=6 is recommended [8]. In this work, a value of n=10 was used.

CF model $$\frac{J}{J_\infty} = 1 - \frac{4}{\pi}\sum_{n=0}^{10}\frac{(-1)^n}{2n+1}\exp\left(-\frac{(2n+1)^2\pi^2 Dt}{4L^2}\right) \quad \text{(II-4)}$$

The first step in the fitting procedure was to make a J_{norm} versus time diagram, which was then fitted to the CF theoretical model. The optimal fit was obtained by minimizing the total error (Equation II-5) between the experimental and theoretical curve. Therefore, D was varied using the solver Add-in in Excel. It was noticed that the experimental curve started to deviate from the theoretical one around a normalized current of 0.5. Therefore, in most cases, only the first half of the curve was fitted in order to determine D_{app}. When the full transient was used for the fitting procedure, it will be mentioned where needed throughout the text.

$$Total\ error = \sum\left(\frac{J_{exp} - J_{back}}{J_{exp,\infty} - J_{back}} - \frac{J_{th} - J_{back}}{J_{th,\infty} - J_{back}}\right)^2 \quad \text{(II-5)}$$

II.4.3. Decay transient

Diffusion coefficients were also obtained from decay transients. In that case, there was no influence on D_{app} by irreversible trapping sites and adsorption phenomena at the entrance site. The normalized decay transient was fitted to the CF model given in Equation II-6 [7, 9]. Fitting was done by minimizing the total error (Equation II-6) between the experimental and theoretical curve. Therefore, D was varied using the solver Add-in in Excel.

CF model $$\frac{J}{J_\infty} = \frac{4}{\pi}\sum_{n=0}^{\infty}\frac{(-1)^n}{2n+1}\exp\left(-\frac{(2n+1)^2\pi^2 Dt}{4L^2}\right) \quad \text{(II-6)}$$

II.5 Newly designed permeation cell

The aim of this PhD was to develop a new permeation set-up that combines electrochemical permeation with an external loading equipment. During the design stage, the focus was put on a better control of multiple parameters affecting the permeation transient. The oxygen level of the electrolyte should be maintained as low as possible, and thus air-tight cells and reservoirs were designed for the new set-up. More information concerning oxygen levels are given in the section below. Next, a continuous mixing of the electrolyte was preserved in the anodic cell during the experiment. This improved the transport of oxidised hydrogen atoms and gas molecules through the electrolyte, avoiding accumulation at the exit surface. Finally, the temperature control and nitrogen gas distribution were optimized.

The oxygen content is a very important parameter when considering corrosion of steel. To avoid undesired processes, the oxygen content in the electrolyte, must be minimized. Therefore, in the newly designed set-up, the double glass cells and the reservoir for heating and deaerating the electrolyte, were made air-tight

and sparge tubes for nitrogen gas were implemented. The dissolved oxygen was measured by using a KS MultiLine® 1 optical meter. Measurements, given in Figure II-6, were executed in the reservoir where the electrolyte was deaerated before it was poured into the cells. The beneficial effect of the sparge tubes and air tight reservoir were obvious. Hence, in the permeation test method 2, the electrolyte was deaerated for only 1 hour instead of 2 in the permeation test method 1.

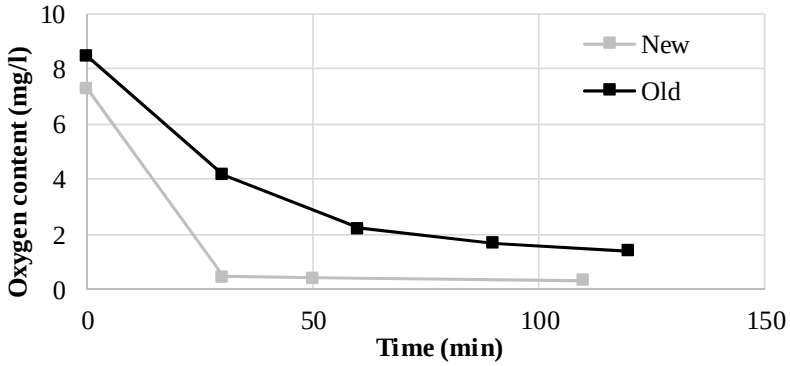

Figure II-6 Oxygen content vs deaeration time.

In the newly designed set-up, the electrolyte was inserted in the anodic cell by a peristaltic pumping system. As such, the oxygen level was maintained low and mixing of the electrolyte inside the cell was provided. For the cathodic cell, it was important that the electrolyte was inserted fast, in order to establish the connection and thus the cathodic protection. Hence, the electrolyte was poured in using a funnel. Furthermore, continuous mixing of the electrolyte caused noise in the hydrogen oxidation signal. By pouring in the solution, contact was made with the air and the oxygen level increased from about 0.3 mg/l to 2 mg/l. But due to the air-tight cells and fine sparge tube, the oxygen content decreased in about 10 minutes back to 0.3 mg/l. After a few hours the oxygen level in the cathodic and anodic cell dropped to about 0.03 mg/l. It is worth mentioning that these values were, with certainty, the maximum oxygen level in the solution, as it was required to open the cells to put in the oxygen meter. Due to the low oxygen concentration, undesired reactions, like oxide formation at the cathode surface, were suppressed. However, an even lower oxygen level should be obtained in order to fully eliminate reactions at the cathodic surface involving oxygen. For example, oxygen scavengers could be added to remove the residual oxygen. Or else, a solution based on borax and glycerol, which has a very low oxygen solubility and diffusivity, could be used. It was shown by Hajilou *et al.* [10] that the glycerol-borax electrolyte preserved the integrity of the sample surface. Surface analyses revealed minimal chemical and topography alteration of the surface after different electrochemical treatments. This was not investigated in this work, but is highly recommended for consecutive research.

II.6 References

[1] D. Simpelaere, "Methodologische optimalisatie van de elektrochemische technieken voor de studie van waterstofdiffusie in staal," Vakgroep Toegepaste Materiaalwetenschappen, Universiteit Gent, 2010.

[2] S. Frappart, "Des éléments de compréhension sur les mécanismes de transport et de ségrégation de l'hydrogène dans les aciers martensitiques trempés et revenus à haute limite d'élasticité," Université de La Rochelle, 2011.

[3] J. Collet-Lacoste, "Intervention des phenomenes de surface sur la permeation electrochimique de l'hydrogene dans le fer. Role d'une couche d'oxyde ou de palladium," Paris 11, 1993.

[4] S.-I. Pyun and R. Oriani, "The permeation of hydrogen through the passivating films on iron and nickel," *Corrosion science*, vol. 29, pp. 485-496, 1989.

[5] Q. Liu, J. Venezuela, M. Zhang, Q. Zhou, and A. Atrens, "Hydrogen trapping in some advanced high strength steels," *Corrosion Science*, vol. 111, pp. 770-785, 2016.

[6] W. Zhao, T. Zhang, Z. He, J. Sun, and Y. Wang, "Determination of the Critical Plastic Strain-Induced Stress of X80 Steel through an Electrochemical Hydrogen Permeation Method," *Electrochimica Acta*, vol. 214, pp. 336-344, 2016.

[7] E. Owczarek and T. Zakroczymski, "Hydrogen transport in a duplex stainless steel," *Acta materialia*, vol. 48, pp. 3059-3070, 2000.

[8] ASTM G148-97, "Standard Practice for Evaluation of Hydrogen Uptake, Permeation, and Transport in Metals by an Electrochemical Technique," 2011.

[9] B. Chaudhari and T. Radhakrishnan, "On hydrogen diffusivity in metals from electropermeation transients," *Surface Technology*, vol. 22, pp. 353-366, 1984.

[10] T. Hajilou, M. S. Hope, A. H. Zavieh, N. Kheradmand, R. Johnsen, and A. Barnoush, "In situ small-scale hydrogen embrittlement testing made easy: An electrolyte for preserving surface integrity at nano-scale during hydrogen charging," *International Journal of Hydrogen Energy*, 2018.

CHAPTER III

Methodology of the electrochemical hydrogen permeation test

III.1 Introduction

Experimental permeation curves, measured by the permeation test method 1 (section II.1), are shown in Figure III-1. However, the measured hydrogen oxidation current density did not reach the expected steady state condition as schematically depicted in Figure III-2. Instead of a steady state current density, the permeation curves in Figure III-1 showed different maxima. This unexpected shape was obtained for pure iron and dual phase (DP) steel. The chemical composition and processing of both materials are given in section III.2. In a first attempt to understand and clarify these unforeseen results, the tested materials were investigated on possible hydrogen damage (section III.3). Nevertheless, to provide consistent results, a good experimental methodology is of significant importance. Therefore, in this study, the permeation test method was investigated by systematically modifying experimental parameters which influence the permeation transient. Results are discussed in section III.4 and section III.5.

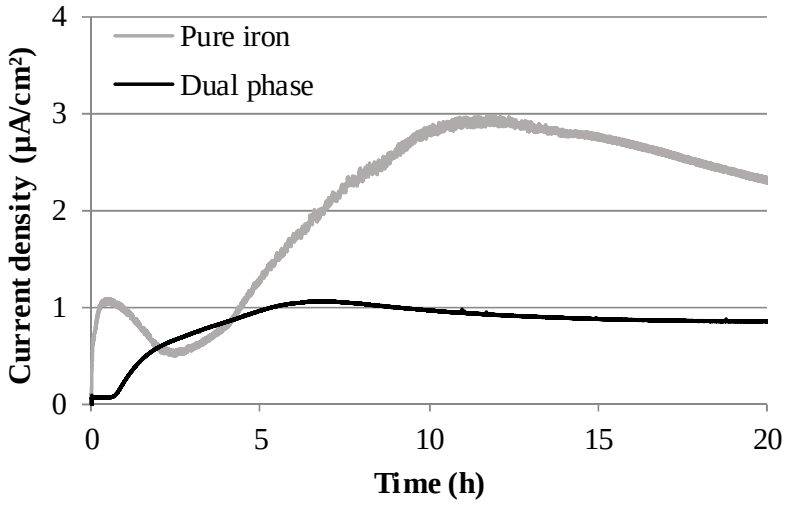

Figure III-1 Permeation curve of pure iron and dual phase steel tested by permeation method 1.

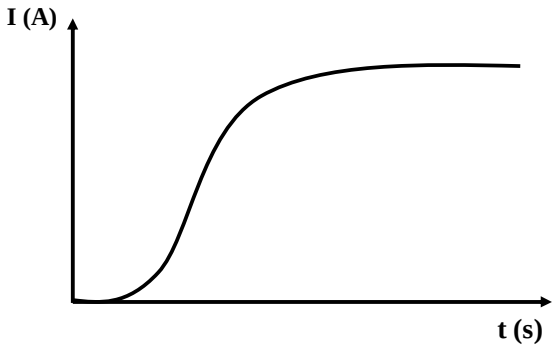

Figure III-2 A schematic representation of the expected permeation curve.

These peculiar permeation transients were already the subject of several studies [1-7]. Beck *et al.* [4] investigated the hydrogen diffusion through Armco iron and observed an anomalous behaviour in the permeation current when higher charging current densities were applied, i.e. when higher hydrogen concentrations were present in the metal. In their work, the permeation transients only showed a maximum when a certain critical concentration level was exceeded. They stated that, due to the high hydrogen concentration, hydrogen atoms recombined and caused the metal to expand leading to crack formation. As such, the specimen was irreversibly damaged, lowering the hydrogen oxidation current density measured at the exit side of the sample. Same conclusions were drawn by Tiegel *et al.* [5]; due to blister formation, a drop in hydrogen permeation was observed. Additionally, they observed that the permeation current decreased faster when higher cathodic charging currents were used. It was suggested that an increase in hydrogen activity, related to the growth rate of blisters, was responsible for this phenomenon.

Flis *et al.* [6] attained a near-steady state level after a few hours of hydrogen charging in a 0.1 M NaOH electrolyte. However, after about 8 hours the permeation current started to increase strongly, reaching a maximum after a few tens of hours. The increased hydrogen entry was associated with a higher hydrogen surface coverage due to an increased cathodic polarization. Moreover, a weakening of the bonds between the adsorbed hydrogen and the metal was supposed, facilitating the absorption process. These findings were explained by the presence of adsorbed oxygen-containing species. A more detailed clarification of the enhanced increase in permeation current due to the formation of surface layers in alkaline medium is given by Flis-Kabulska *et al.* [7]. The attained maximum in permeation current was then followed by a decrease, which was attributed to the growth of these oxides. With their low diffusivity they will act as a barrier for hydrogen, reducing its entry in the metal specimen. Due to thermodynamic reasons it is not possible for oxygen species to form in such conditions, but it was proposed that hydrogen bubbles could shield the surface, leading to an area that was less cathodically polarized than intended. As such, the iron oxide was given the opportunity to grow, acting as a barrier for hydrogen entrance. This latter phenomenon was proposed by Liu *et al.* [1] who experienced similar anomalous hydrogen permeation transients as Flis *et al.* [6].

It is thus very important to find out what is causing the anomalous behaviour of the permeation current. When the origin of the problem is determined, a better control of the experimental data may be established. First, it was verified that the hydrogen did not induce any damage in the specimens (section III.3). Subsequently, different experimental parameters influencing the permeation test were altered and the resulting permeation transient was examined. Next to the hydrogen oxidation flux at the exit side, the potential between the working and reference electrode at the entrance side was monitored. Amrani *et al.* [8] stated that the measured potential drop (V) was the sum of the ohmic drop (I·R) and the electrode overpotential (E), which is related to faradaic processes. The author expressed the fluctuations of the measured voltage by:

$$\Delta V(t) = I\Delta R(t) + \Delta E(t) \qquad \text{(III-1)}$$

The recorded potential drop at the entrance side is thus dependent on the specimen surface condition and is therefore an important parameter to analyse. When a change in ohmic resistance and/or electrode potential occurs, the measured voltage will regulate in order to preserve the applied constant current density. Such variations can be caused by electrochemical or chemical processes taking place at the sample surface. Hence, a stable entrance potential implies a stable surface state, and in turn, a constant hydrogen entry flux. Therefore, the recorded voltage was also studied in order to detect the cause of the anomalous permeation result.

In this chapter, permeation test results are discussed in order to gain more knowledge concerning the Devanathan-Stachurski technique. Different experimental test parameters such as the polarization potential at the exit side, the applied charging current density, the electrolyte, the oxygen content, the sample roughness, the electrolyte composition, and sample thickness, were altered to study their influence on the recorded exit current and/or entrance potential. In Figure III-3, a summary is given of all parameters that were investigated. Nevertheless, the investigated material was first checked on possible hydrogen induced damage. By analysing the effect of the different parameters, a better control and more knowledge was obtained concerning the experimental permeation set-up. In addition, the stability of the Pt-counter electrode was checked and the first rise transient, partial and consecutive charging transients were recorded and discussed.

Polarization potential at the exit side	•-500 mV vs RE •-200 mV vs RE
Charging electrolyte	•0.1 M NaOH (+ 1 g/l thiourea) •0.1 M H_2SO_4
Oxygen in the charging cell	•Deaerated •Aerated
Charging current density	•0.03 mA/cm² •0.3 mA/cm² •3 mA/cm² •10 mA/cm²
Roughness	•Polished •Roughened
Water	•Demi water •Ultrapure Milli Q®
Sample thickness	•600 µm •700 µm •1000 µm •1100 µm

Figure III-3 Experimental parameters which are modified in this chapter.

III.2 Materials of interest

Armco iron and Dual phase (DP) steel were both used in order to investigate the different parameters of the permeation experiment. The Armco iron was delivered by AK Steel in a highly pure and hot rolled condition. The microstructure was fully ferritic with a grain size of approximately 30 µm. The DP600 steel plate was hot and cold rolled, followed by subsequent annealing via industrial annealing parameters necessary to obtain the desired microstructure. The steel plate was delivered by Arcelor Mittal. Table III-1 shows the chemical composition of both materials.

Table III-1 Chemical composition Armco iron and DP steel in wt%.

Armco iron, hot rolled plate											
C	Si	Mn	P	S	Al	Cr	Cu	Mo	N	Ni	Sn
0.001	0.003	0.050	0.004	0.003	0.002	0.013	0.007	0.002	0.003	0.011	0.002
Dual phase steel											
C	Si	Mn	P	S	Al	Cr	Cu	Mo	V	Ni	Sn
0.08	0.129	0.948	0.037	0.003	0.028	0.568	0.019	0.005	0.005	0.025	0.001

III.3 Damage investigation

As mentioned in the introduction, the permeation current may be affected by hydrogen induced damage. It is thus necessary to investigate the surface and cross section of the samples after they were subjected to the permeation test. Optical microscopy, secondary electron microscopy (SEM) and energy dispersive X-ray (EDX) spectroscopy was done in order to assure no hydrogen damage was introduced during the permeation test at the imposed charging conditions. A detailed damage evaluation was done on deformed Armco iron which was tested by the permeation test method 1. By cold rolling, cold deformation was applied where the sample thickness was reduced by 70%. It is known that a higher degree of cold deformation increases the susceptibility to hydrogen damage [9, 10]. Therefore, the samples which were reduced in thickness with 70% were analysed. If no damage could be detected, samples having less deformation were also considered to be damage-free. Two different electrolytes, 0.1 M NaOH and 0.1 M H_2SO_4, were used for charging with a constant current density of 3 mA/cm². Both sides of the sample did not show any hydrogen blisters after the permeation test. Even when charging in the sulfuric acid based electrolyte, where the hydrogen production was higher compared to the alkaline condition, no hydrogen damage was visible on the surface. In Figure III-4, optical microscopy images of cross sections are shown. A standard grinding and polishing procedure was carried out until the OPU polishing step. For etching, the sample was immersed in 2% Nital solution for about five seconds. Figure III-4 A and B were taken after the OPU polishing step, while Figure III-4 C and D were taken after the etching step. In Figure III-4 A and B, small black voids were observed which may be linked to hydrogen induced damage. They could possibly form by hydrogen enhanced processes, like vacancy clustering, leading to void formation and growth as a result of the lower free energy when hydrogen combines with these vacancies and/or vacancy clusters [11]. When extra vacancies are created, they can capture hydrogen causing a decrease in the permeation current. The black voids, visible after the OPU polishing step, were not clearly visible after the etching step. Hence, the cross sections after the OPU polishing step were further evaluated by SEM and EDX in order to reveal the nature of these observed features in Figure III-4 A and B. A reference sample, which was not charged with hydrogen, was additionally studied.

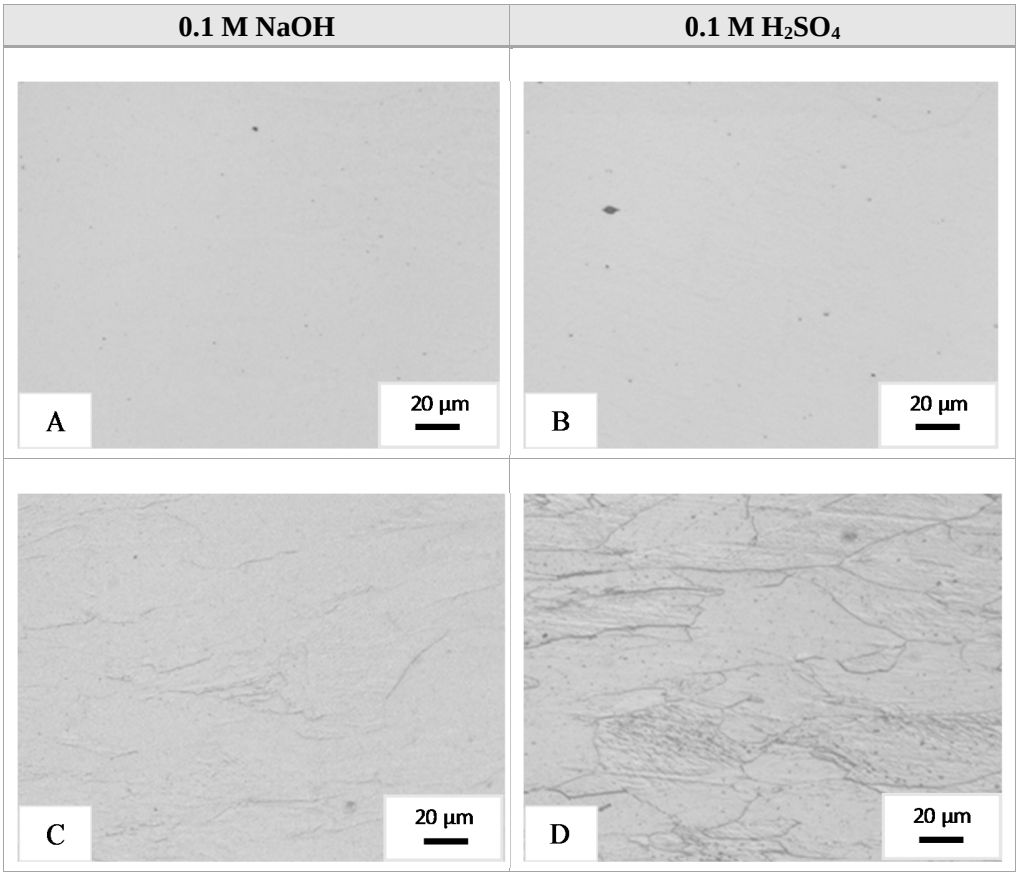

Figure III-4 Cross sections of 70% deformed Armco iron charged in 0.1 M NaOH and 0.1 M H_2SO_4. Images A and B are taken after the OPU polishing step, C and D after the etching step in 2% Nital.

SEM images are given in Figure III-5. As voids were also detected in the reference sample, their presence was not linked to hydrogen related processes. Nevertheless, EDX measurements were carried out to find out the nature of these features. The first EDX spectrum is one of the iron matrix and is given in Figure III-6. The EDX spectra of two voids present in the reference specimen are given in Figure III-7. The first spectrum was measured in an elongated void, while the second spectrum was taken in a globular void. Next to iron, both spectra show extra elements like Mn, Si, O and Au. Gold, also present in the spectrum of the matrix (Figure III-6), was measured since the embedded sample was coated with a gold layer to make the sample conductive. Mn and Si were present in the material's composition with an amount of 0.050 wt. % and 0.003 wt. %, respectively. Furthermore, Si is also present in the OPU polishing product which is a colloidal silica suspension. Although the sample was thoroughly rinsed with water and soap after the final polishing step, the silica particles could possibly still have been present in the voids of the microstructure. As such, the voids observed in the reference sample were presumably mainly originating from Mn containing inclusions. The globular and elongated void show an equal spectrum which indicates that the shape of the void is not of significant importance.

Representative spectra were obtained for voids observed in the hydrogen charged samples in both the NaOH and H_2SO_4 solution. As such, the anomalous behaviour of the permeation transient was not linked to hydrogen induced damage. Nevertheless, the inclusions may influence the diffusion behaviour of hydrogen through the sample. Similar results were obtained for DP steel, which will be discussed in more detail in Chapter VI.

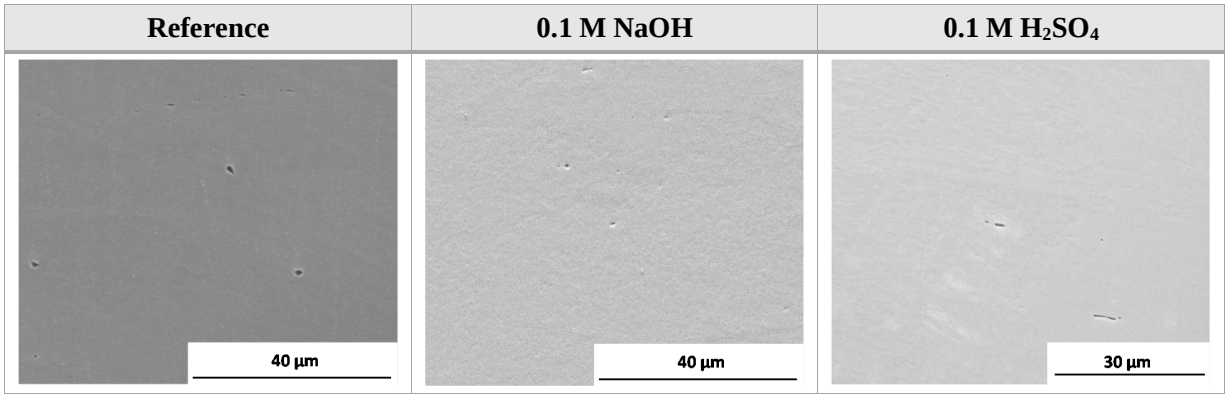

Figure III-5 SEM images of the cross sections of the 70% cold rolled specimen. A reference sample and samples charged in a 0.1 M H_2SO_4 and 0.1 M NaOH electrolyte are shown.

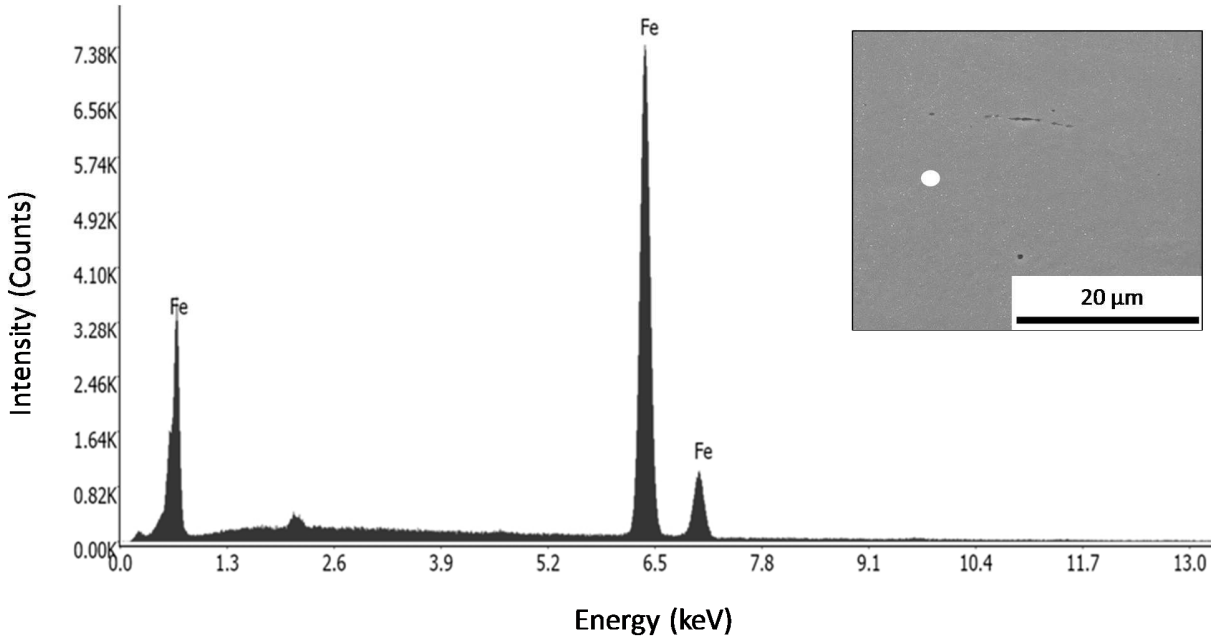

Figure III-6 EDX spectrum of the Armco iron matrix measured in the reference sample. The measurement was carried out on the white dot present on the SEM image.

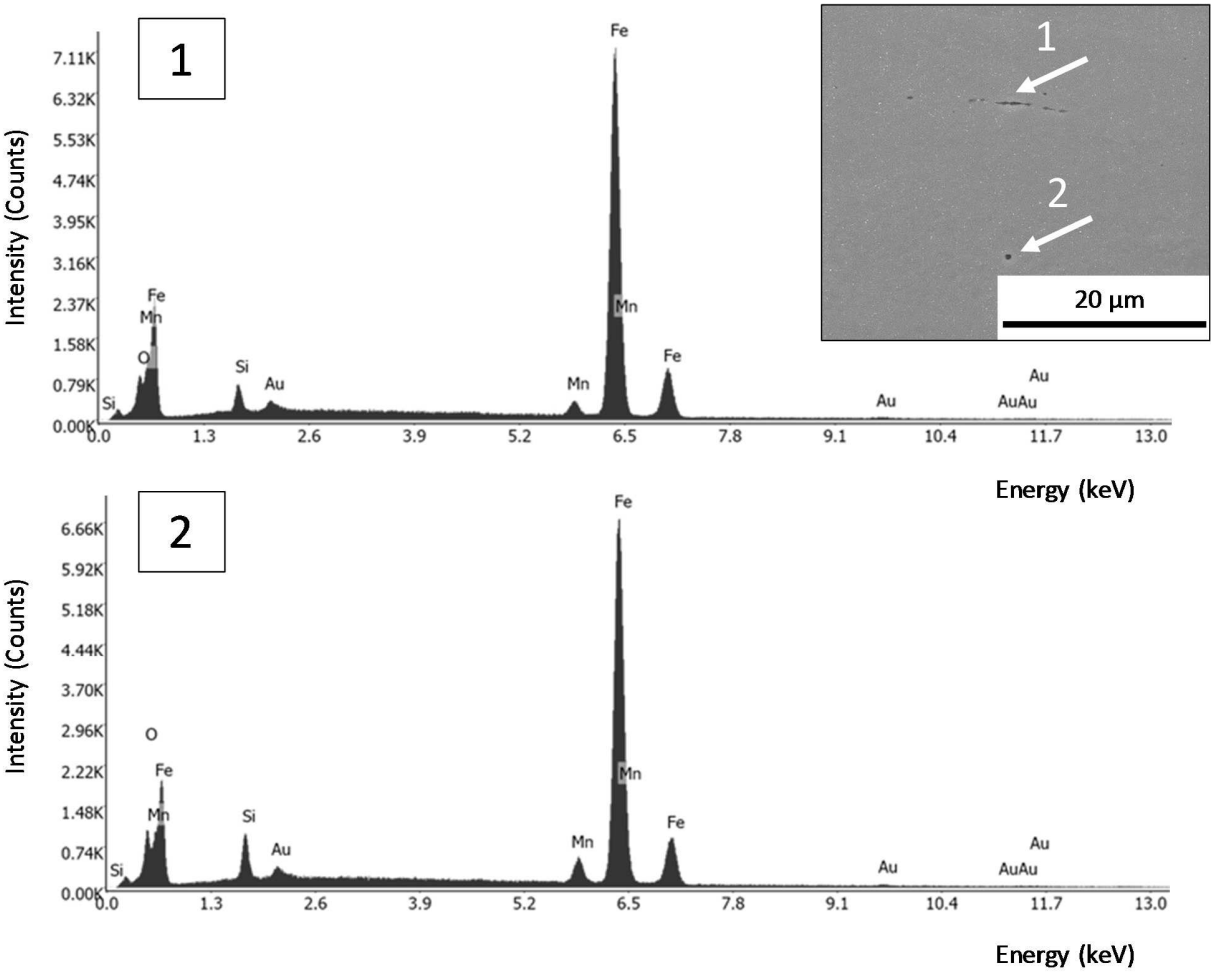

Figure III-7 EDX spectra of the observed voids in the reference sample.

III.4 Parameters influencing permeation measurements

In order to clarify the abnormal shape of the hydrogen permeation current, certain experimental test parameters such as the polarization potential at the exit side, the applied charging current density, the electrolyte, the oxygen content, the sample roughness and thickness, were varied, and the corresponding recorded hydrogen oxidation current density was examined subsequently. Besides the permeation flux at the exit side, the measured potential at the entrance side was also analysed. Furthermore, some additional parameters were investigated to gain further insights on the experimental test set-up.

III.4.1. Polarisation potential at the exit side

During a permeation test, the sample is anodically polarized at the exit side. As such, atomic hydrogen oxidizes and the released electrons originating from that oxidation reaction are recorded by the potentiostat. On the one hand, the potential must be sufficiently positive so the hydrogen immediately oxidizes. On the

other hand, the potential must be in the passivation range in order to establish a stable passivation layer before the start of the hydrogen charging. This layer will protect the metal surface against further corrosion processes. In Figure III-8, a cyclic voltammogram of a polished Armco iron sample is shown. Before the measurement, the 0.1 M NaOH electrolyte was deaerated for one hour with nitrogen gas and the scan rate was set at 0.01 V/s.

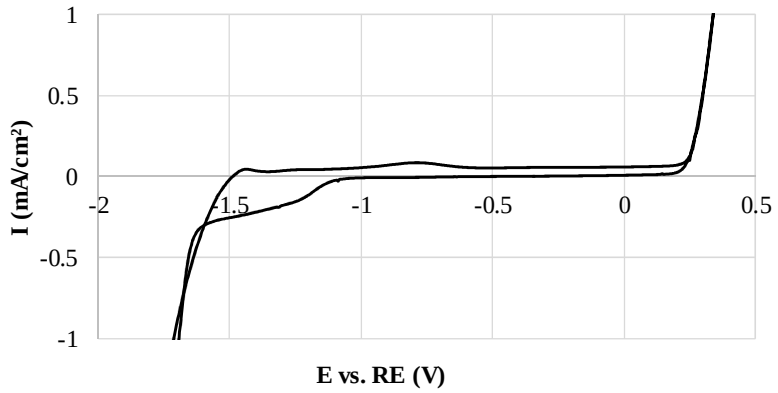

Figure III-8 Cyclic voltammogram of a polished Armco iron sample in 0.1 M NaOH. Scan rate was 0.01 V/s, initial potential -2 V vs RE (Hg/Hg_2SO_4 +650mV vs SHE)

At -500 mV vs the reference electrode, the sample passivated and the potential was sufficiently positive to oxidize the outcoming hydrogen. In order to see the effect of the driving force for hydrogen oxidation, permeation tests by method 2 were carried out with a potential of -500 mV and -200 mV vs the RE (Figure III-9). Both conditions delivered an unstable permeation current density. Furthermore, as the maximum value of the hydrogen oxidation current was not reproducible, no conclusions could be made from the obtained data.

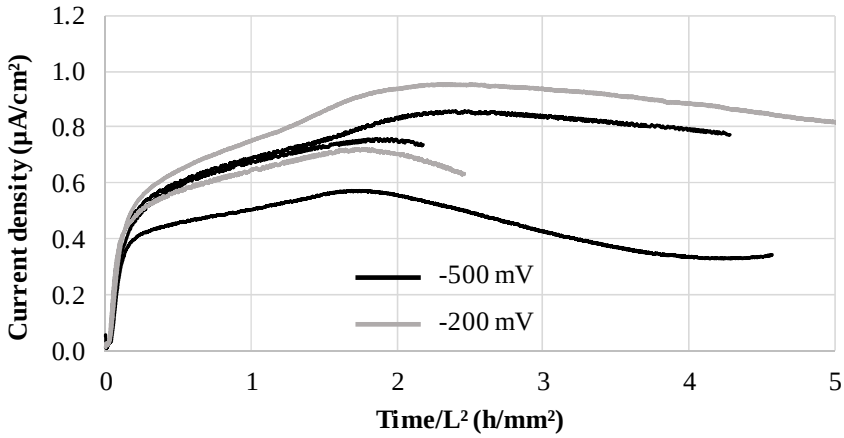

Figure III-9 Permeation results of Armco iron tested with different potentials at the exit side. Potentials are given with respect to the RE (Hg/Hg_2SO_4 +650mV vs SHE). L is the sample thickness and experiments were performed by the permeation test method 2.

Similar to the hydrogen oxidation reaction, the iron oxidation reaction will also experience a higher driving force when a more positive potential is applied. In order to know whether this affects the test results, background current densities, obtained after about 18 hours of passivation, were analysed. Comparable values between 15 and 35 nA/cm² were obtained. Consequently, it seems that both potentials were appropriate for the permeation conditions in this work. This was expected as both potentials were located in the stable passivation region of the cyclic voltammogram plotted in Figure III-8. Analysing the course of the passivation step, which takes 18 hours for both conditions, did not deliver pronounced differences. In further experiments throughout this work, a potential of -500 mV vs the reference electrode was imposed.

III.4.2. Pt counter electrode

In the cathodic cell, a three electrode system was used: a work, counter and reference electrode. As the working electrode is cathodically polarized, the counter electrode experiences anodic currents. Therefore, the counter electrode must be a noble metal in order to prevent its dissolution and subsequent deposition at the cathodic sample surface. When a compound is deposited at the working electrode, it could change the hydrogen evolution reactions (HER) mechanisms, varying the hydrogen entry flux. In this work, a Pt-Rh (90/10) counter electrode was used as it is known to behave inert in such conditions. However, Venezuela *et al.* [12] stated that a platinum counter electrode must be used with caution during hydrogen studies involving cathodic hydrogen charging. In their work, XPS measurements detected Pt at a metal surface after it was cathodically polarized for a certain time. During the experiment, the Pt counter electrode was oxidized to Pt ions, due to the high anodic polarization. These Pt ions then migrated to the negatively charged cathode where they were deposited on the surface. As expected, the hydrogen uptake was affected by the presence of the deposited Pt since Pt affected the HER mechanisms on the surface of the working electrode. Compared with a carbon counter electrode, the hydrogen ingress was reduced with 70%. Nevertheless, the deposited Pt had no influence on the hydrogen diffusion in the steel and egress from the steel.

The deposition of Pt could thus be responsible for a decreases in hydrogen absorption, leading to a decrease in the permeation current. XPS measurements on Armco iron and DP steel were carried out in order to evaluate the possible Pt deposition. XPS spectra of the Armco iron surfaces, with different times of Ar sputtering, are given in Figure III-10. Before the XPS measurement, a permeation test was performed on the iron in a 0.1 M NaOH electrolyte with a charging current density of 3 mA/cm². On the top surface layer, main elements like C, O and Fe were detected. Also a minimal amount of Zn (1.86 at%) and Sn (0.51 at%) were identified. Their origin is explained later in this chapter. When removing the top layer by Ar sputtering for 30 seconds, only Fe was detected next to small amounts of O and C. Pt, neither Rh, were never detected, nor on Armco or DP steel. This demonstrated the stability of the used counter electrode at the applied test conditions.

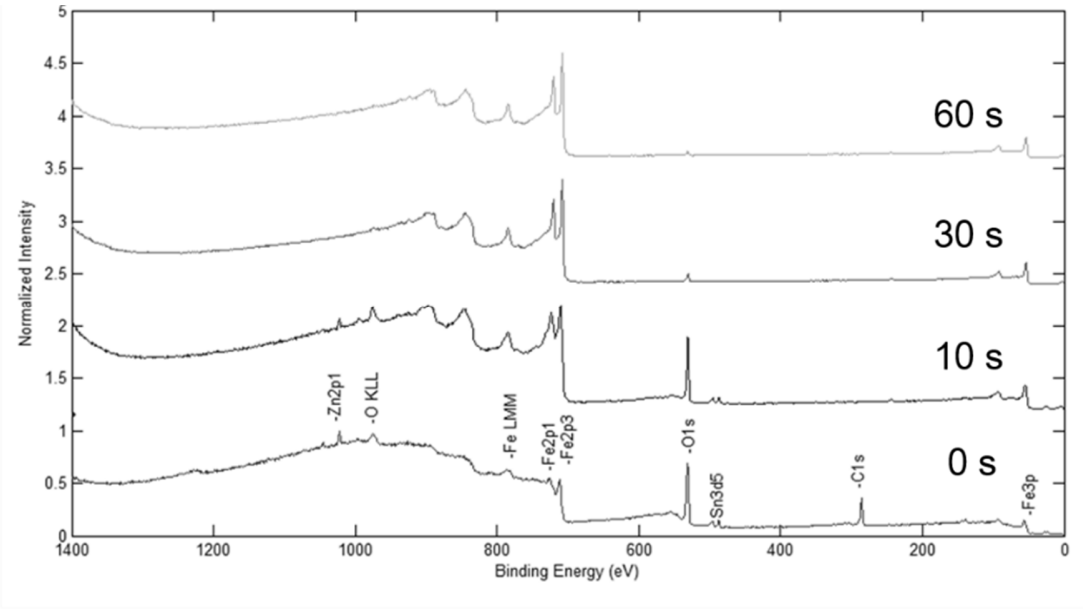

Figure III-10 XPS spectra of the Armco iron surface after 0, 10, 30 and 60 seconds of Ar sputtering.

III.4.3. Charging electrolyte

The anomalous behaviour of the permeation transient could possibly result from a non-constant hydrogen entering flux, due to an uncontrolled hydrogen absorption process. In other words, the distribution between hydrogen absorption (Volmer) and hydrogen gas formation (Heyrovski and Tafel) could have varied with time. As this relation depends on the surface state of the entrance side, it would suggest that the surface characteristics of the cathodic side of the specimen were not controlled. In order to vary these characteristics, permeation tests were carried out on pure Armco iron with three different electrolytes: 0.1 M NaOH, 0.1 M NaOH containing 1 g/l thiourea and 0.1 M H_2SO_4. In all permeation experiments, a 0.1 M NaOH solution was used for the hydrogen oxidation at the anodic side of the specimen. All tests were performed by the permeation test method 1 and a cathodic current density of 3 mA/cm² was applied by using a floatable potentiostat. In this way, the potential at the entrance side of the surface was recorded. The hydrogen permeation current densities vs time/L^2, with L the sample thickness, are depicted in Figure III-11. By dividing the time by L^2, the minor variations in sample thickness were eliminated. This analysing procedure was based on the formula of D given in Equation III-2 with D the diffusion coefficient (m²/s), L the thickness (m), t the time (s) and M a dimensionless constant. All tests were performed at least two times in order to exclude experimental errors.

$$D = \frac{L^2}{Mt} \qquad \text{(III-2)}$$

Methodology of the electrochemical hydrogen permeation test

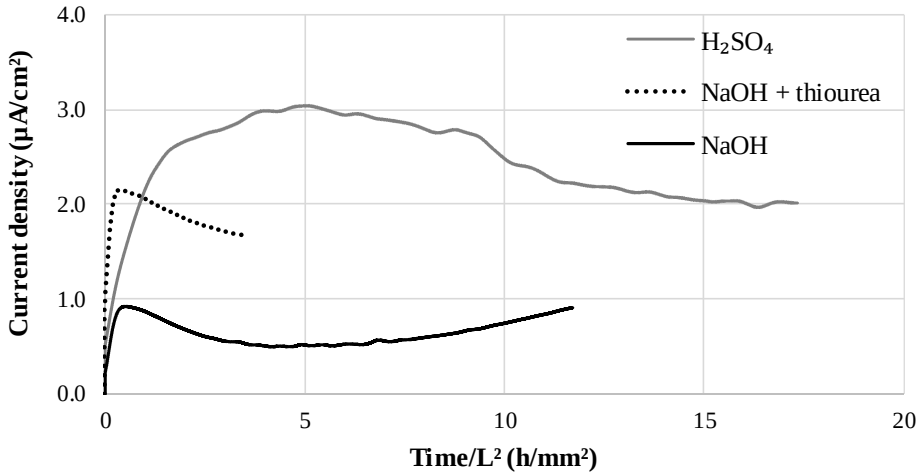

Figure III-11 Armco iron tested by the permeation test method 1 with different charging electrolytes. L is the sample thickness.

First, the surface characteristics were altered by the use of a poison, namely thiourea (CH_4N_2S). Thiourea can be added to the electrolyte in order to reduce the probability for hydrogen to recombine by occupying surface sites [13]. Results showed that the registered current density maximum was higher for the test with thiourea compared to the test without. The obtained current maxima of both experiments occurred approximately at the same time, indicating the beneficial effect of thiourea on the hydrogen entry processes. Nevertheless, the decrease in hydrogen oxidation current was still present, showing that thiourea did not ensure more stable surface characteristics which would have led to a more stable entering and out coming hydrogen flux.

As mentioned earlier, cathodic polarization of iron in 0.1 M NaOH could result in the formation of different oxygen containing deposits on the surface [6, 14]. These surface layers could be composed of Fe_3O_4 [15-17], γ-Fe_2O_3 [17, 18], γ-FeOOH, α-FeOOH, δ-FeOOH [17, 19] and other oxyhydroxides [20]. Oxides could alter the hydrogen entry mechanisms, varying the hydrogen entry flux. Although the oxygen content in the permeation cells was maintained low by continuously bubbling with nitrogen gas, it could not be confirmed that all oxygen was removed preventing the formation of surface films. More information concerning oxygen levels in the permeation cells is given in section II.5 and III.4.4. Furthermore, air-formed oxides were already present at the electrode surface before the start of the cathodic polarization. In alkaline solutions, the reduction of these oxides occurs only partially [21]. On the contrary, in acid electrolytes, the oxide film reduction is fast due to the high activity [22] and no formation of undesired surface layers is expected. Nevertheless, also in the acidic environment a maximum in current was detected, indicating uncontrollable hydrogen entry processes were not eliminated by using the acidic electrolyte. As such, oxides were not responsible for the varying permeation current, unless the unstable entry flux in alkaline and acidic media originated from different types of processes taking place at the cathodic surface.

When analysing the slope of the rising permeation current, the highest slope was observed for the thiourea containing electrolyte. Furthermore, the slope in the acidic medium was only slightly higher compared to

the NaOH solution without thiourea. Although the higher activity of the acidic electrolyte resulted in a larger hydrogen coverage of the input surface [23], an increased hydrogen gas production may have caused a reduction in the hydrogen entry efficiency. Therefore, the slope of the rising transient was lower than expected. Nevertheless, processes which were responsible for the decrease in the permeation transient were delayed and a higher maximum was obtained in the acidic environment.

As mentioned in the introduction, the potential drop between the reference electrode and the entrance side is affected by the surface characteristics of the specimen. This important parameter is therefore analysed and the related results for the different electrolytes are shown in Figure III-12. The most negative potential was observed when using the NaOH electrolyte containing thiourea. Compared to the experiment without thiourea, the poison occupied surface sites which increased the ohmic resistance, i.e. potential drop, between the reference electrode and the metal surface. This larger potential drop was required to preserve the imposed current density. In the acidic environment, the surface was free of oxides which led to a lower ohmic resistance and a reduction in overpotential. Furthermore, the electrode potential, also contributing to the measured voltage, depends on the used electrolyte (pH) and on the faradaic processes taking place at the electrode surface. As such, the low overpotential was also caused by the lower pH of the acidic solution.

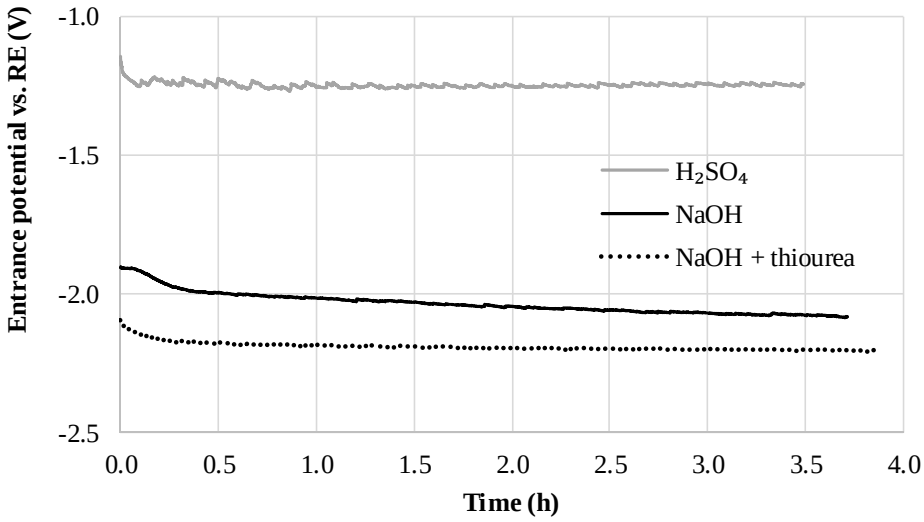

Figure III-12 Entrance potential with respect to the RE (Hg/Hg_2SO_4 +650 mV vs SHE) vs time for charging in different electrolytes.

Although the potential in the sulfuric acid was more stable over the full test duration, i.e. the difference between the measured end and start potential, more fluctuations with a shorter time period were visible. A detail of the measured potential in acidic and alkaline environment is given in Figure III-13. The saw tooth structure, noticeable in both experiments, was linked with hydrogen bubble formation at the sample surface. The growth of a gas bubble could shield the surface, leading to an increased potential drop between the work and reference electrode in order to preserve the imposed current density. Once the bubble detached from the surface, a sudden shift of the potential to less negative values was observed. This was evaluated

by Amrani *et al.* [8], who demonstrated that big bubbles gave rise to both ohmic drop and electrode potential fluctuations, while small bubbles mainly induced ohmic drop oscillations. The authors stated that the shielding effect of a gas bubble decreased the local flux of hydrogen into the metal membrane. In addition, the bigger the bubbles, i.e. the longer they were attached to the surface, the larger these concentration fluctuations were. It was clear from Figure III-13 that fluctuations, due to bubble formation, were more pronounced in the acidic electrolyte compared to the alkaline one. This was caused by the larger hydrogen activity of the electrolyte, associated with a low pH of 0.7. As such, the input surface was covered by a larger amount of hydrogen [23], which led to an intensive hydrogen gas production. Hence, bubble formation was less intensive in the alkaline solution and a more constant hydrogen entry flux was expected when considering a small time period. Based on these experiments, it was concluded that bubble formation should be minimized in order to achieve a more continuous entrance potential. Therefore, in this work, the NaOH based electrolyte was further used. Besides the choice of the electrolyte, other parameters such as current density and surface roughness, which both affect the hydrogen gas formation, should be considered.

The continuous reduction in potential, more pronounced in the alkaline medium, could possibly be related to the aforementioned oxygen related processes, i.e. the formation of iron oxides. Therefore, a permeation test without the deaeration of the electrolyte was carried out, as discussed in the next section.

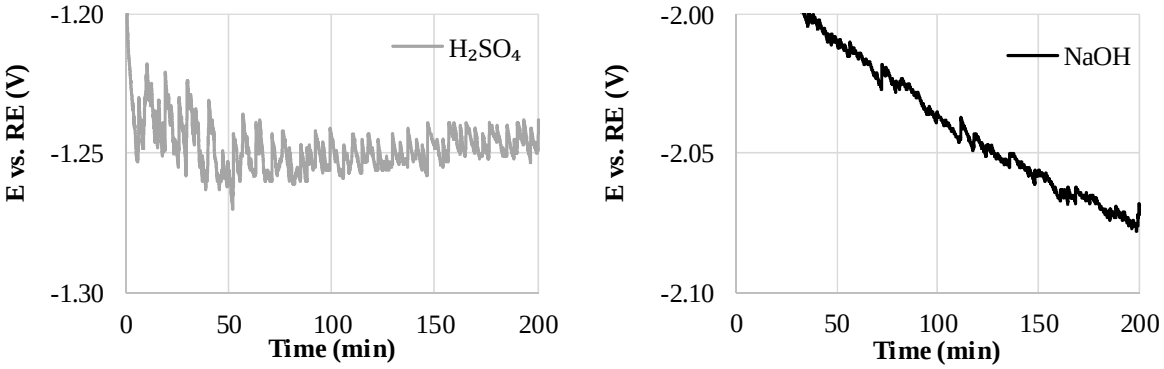

Figure III-13 Detail of the measured entrance potential (E) in NaOH and H_2SO_4 with respect to the RE (Hg/Hg_2SO_4 +650 mV vs SHE) vs time.

III.4.4. Effect of oxygen

The influence of oxygen on the permeation test was analysed by testing the Armco iron in a deaerated and aerated electrolyte. Just before pouring in the electrolyte in the cells, the oxygen content was about 8 mg/l and 1 mg/l for the solution with and without oxygen, respectively. Both experiments on Armco iron were tested by the permeation test method 1 in 0.1 M NaOH and with a current density of 3 mA/cm². The resulting hydrogen oxidation currents are presented in Figure III-14. It was obvious that the presence of oxygen accelerated the undesired processes taking place at the entrance surface, which led to an uncontrolled hydrogen uptake. In addition, the entrance potential, also depicted in Figure III-14, decreased more rapidly

with time in the presence of oxygen which indicated a faster modification of the cathodic surface characteristics. It is thus of significant importance to reduce the oxygen content in the electrolyte. Therefore, in the newly designed set-up, the reservoir for deaerating the electrolyte and permeation cells, were made air-tight.

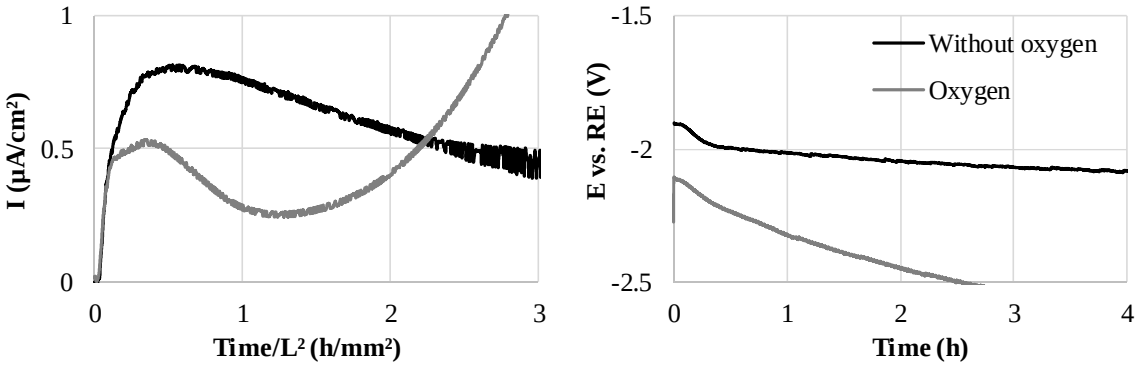

Figure III-14 Armco iron tested by the permeation test method 1 with or without the presence of oxygen at the charging cell. L is the sample thickness.

These results confirm that the instabilities could be associated to oxygen related processes at the cathodic surface. As mentioned earlier, the presence of oxides have the ability to alter the HER mechanisms, leading to an inconsistent hydrogen entering flux. Nevertheless, the formation of oxides require the oxidation of iron which is an electrochemical process. Hence, these undesired reactions must depend on the applied current density, a parameter which is studied in the next section.

III.4.5. Charging current density

The efficiency of the hydrogen ingress was assessed by comparing the charging current density and the hydrogen oxidation at the exit side and was found to be extremely low. For the permeation test done in NaOH and at 3 mA/cm², shown in Figure III-15, the efficiency at the maximum current density was only about 0.03%. The efficiency was calculated by dividing the current density of the first maximum by the applied current density at the entrance side. In order to increase the efficiency, and thus lowering the probability for hydrogen to recombine to hydrogen gas, the current density was decreased. As such, the hydrogen evolution mechanisms will change, perhaps leading to a more constant entering hydrogen flux. In addition, lowering the current density probably decreased the kinetics of the oxygen related processes, contributing to a more constant cathodic surface state.

Three different current densities, 3, 0.3 and 0.03 mA/cm² were applied and results are shown in Figure III-15. The experiments were performed on pure Armco iron by the permeation test method 1. The maximum in permeation current was the highest at 3 mA/cm². At this current density, more electrons were provided for the reduction reaction, resulting in a higher amount of absorbed hydrogen in the specimen. Nevertheless, for the sample charged with 0.3 mA/cm², the efficiency increased to about 0.18% at the time when the

permeation current density of the 3 mA/cm² charged sample reached its maximum. This was associated with the lower driving force for hydrogen recombination. Additionally, the maximum current density shifted to larger times for the 0.3 mA/cm² sample. This confirmed earlier proposed assumption: processes contributing to an unstable hydrogen entry flux, were retarded when lowering the applied cathodic current density. To confirm this, permeation tests were performed with a cathodic current density of 10 mA/cm². Results are given later in this section.

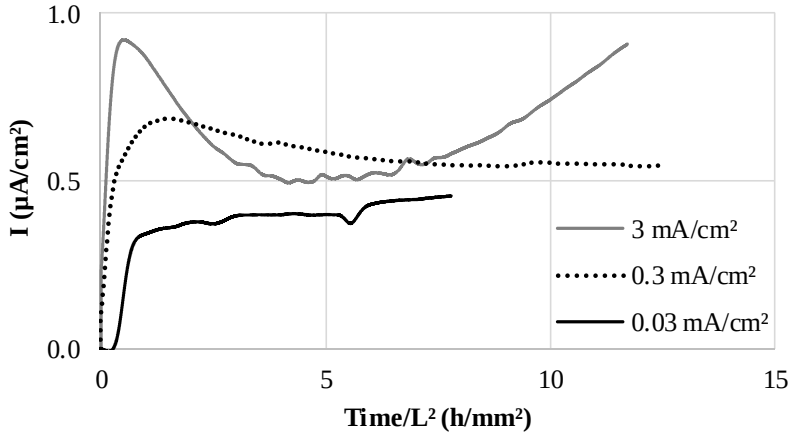

Figure III-15 Armco iron tested by the permeation test method 1 charged with three different current densities. L is the sample thickness.

At a current density of 0.03 mA/cm², no maximum in permeation current was observed. In addition, the permeation transient was shifted to the right, which was attributed to the fact that hydrogen was hindered on its diffusion path to the other side of the specimen. In order to explain this anomalous behaviour, the entrance potentials, measured during the permeation test, were plotted and evaluated (Figure III-16). It was expected that larger overpotentials are recorded when higher cathodic currents are applied. Consequently, a higher hydrogen uptake was detected, but the efficiency decreased due to a more intensive hydrogen gas production. This was also visible when investigating the measured potential in detail, plotted at the right side of Figure III-16. More fluctuations, associated with bubble formation, were observed for the highest current density. In addition, at the higher current density, a larger decrease in voltage was experienced over the full test duration. Hence, a lower current density implied more constant surface characteristics.

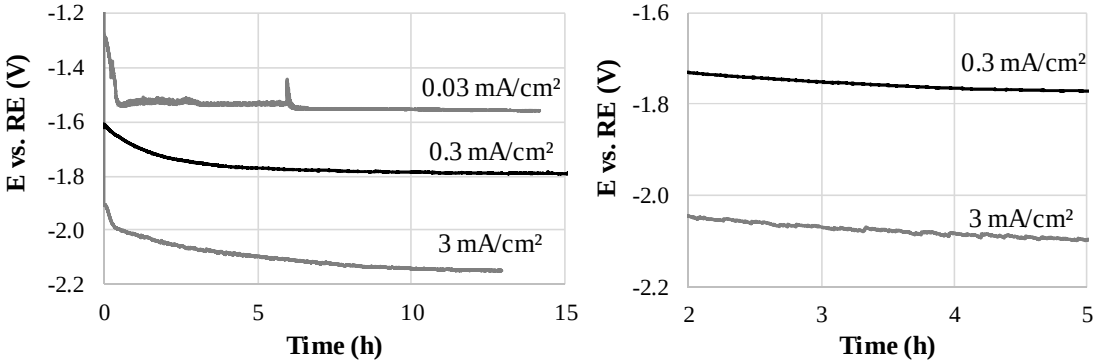

Figure III-16 Entrance potential (E) vs time when charging with different current densities. Right is a detail of the graph at the left.

The permeation transient for the sample charged with 0.03 mA/cm², showed a remarkable delay in the hydrogen breakthrough time (Figure III-15). As such, a barrier must have been present on the surface, slowing down the absorption and diffusion processes. Generally, when a cathodic current is applied to a metal, it is cathodically protected from corrosion. However, it was assumed that a current density of 0.03 mA/cm² was not sufficient to fully protect the metal and a poorly conductive oxide layer was formed. The growth of such a layer acted as an important additional resistance, and a shift to more negative potentials was necessary to preserve the applied current density. This decrease in potential was noticeable in the first part of the potential curve plotted in Figure III-166. This barrier formation explained the shift of the permeation curve to longer times. Furthermore, at lower current densities, the air-formed oxides will be reduced at a lower rate. This could also have contributed to the larger break-through time. The variation in potential observed at the entrance surface of the sample charged with 3 mA/cm² is discussed in more detail in section III.4.6.3.

Based on previous assumptions, the imposed current density should be large enough to avoid the formation of surface layers which possibly impede the hydrogen absorption and diffusion. Nevertheless, when charging with 0.3 mA/cm², the permeation curve exhibited reliable break-through times. Although the stability of the entrance potential and hydrogen efficiency was higher, a decrease in permeation current was still observed (Figure III-15). However, it will take longer times before detecting the instability of the permeation transient and therefore, a current density of 3 mA/cm² will be used when further elaborating the permeation method.

Kinetics of processes affecting the permeation current were retarded when lowering the cathodic charging current density. Consequently, they should be accelerated when increasing the current density. Therefore, the Armco iron was charged with a current density of 10 mA/cm². The resulting transient, plotted together with a test performed at 3 mA/cm², is given in Figure III-17. Both experiments were carried out by the permeation test method 2. Again, the efficiency decreased with a higher current density and the observed maximum occurred earlier. This observation confirmed previously drawn conclusion: processes responsible

for the decrease in hydrogen oxidation current, depend on the cathodic current density applied at the entrance side.

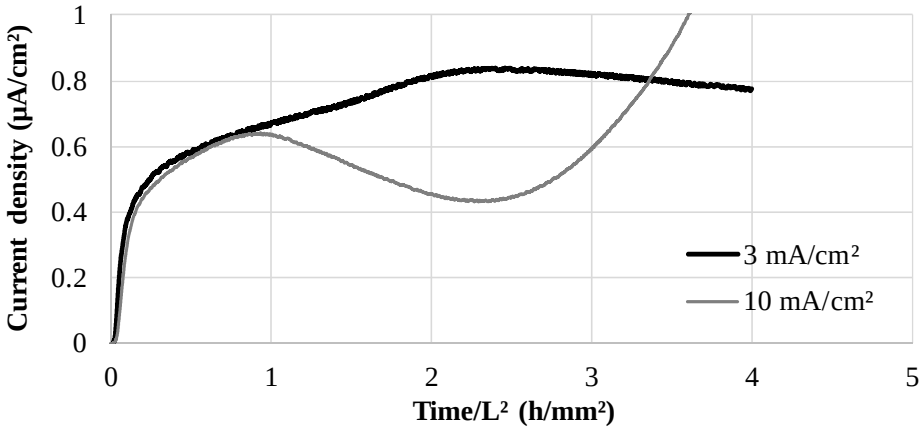

Figure III-17 Armco iron tested by the permeation test method 2 charged with 10 mA/cm² and 3 mA/cm². L is the sample thickness.

In Figure III-18, the entrance potential of the permeation experiments charged with 10 and 3 mA/cm² is depicted. As expected, a more negative potential was observed for the highest current density. Also more fluctuations, due to a more intensive hydrogen gas production, could be detected. However, next to small fluctuations comparable with these depicted in Figure III-13, oscillations with a longer period of about 15 minutes were observed as well. Catonne *et al.* [3] also observed this kind of oscillations and stated that the time period was too long to associate them with the formation of bubbles. In the work of DePetris-Wery *et al.* [24], they attributed these oscillations to the formation of stresses in the subsurface followed by a relaxation phenomenon. The accumulation of stresses in the material were ascribed to the saturation of reversible trapping sites and/or crystal rearrangements of the subsurface.

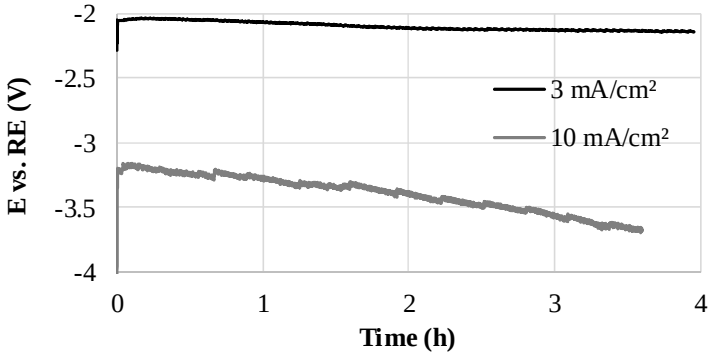

Figure III-18 Entrance potential (V) recorded during hydrogen charging by the permeation test method 2 and using a cathodic current density of 3 and 10 mA/cm².

III.4.6. Roughness

Another way to modify the hydrogen evolution mechanisms, is to change the surface roughness. Brown *et al.* [25] studied the influence of the surface roughness on the hydrogen evolution reaction kinetics and they observed a variation in Tafel slope and apparent exchange current density for samples having variable roughnesses. This indicated a change in the rate-determining step of the HER mechanism. In addition, a change in surface roughness will modify the real available surface area, and will affect the number and volume of the hydrogen gas bubbles formed at the hydrogen charging surface.

All permeation tests discussed in this section, were carried out by the permeation test method 2 and were repeated to confirm reproducibility. The surface roughness of both the entrance and exit surface was varied, i.e. polished or ground. The grinding was applied by an automated Struers® grinding and polishing equipment. For the last grinding step, a SiC disc of 500 grit was used. The experimental curves of two permeation tests on pure Armco iron, are shown in Figure III-19. The grey curve represents the result of a sample with a polished exit and ground entrance side, while the black curve represents the permeation transient where both sides of the sample were ground. The results showed a more or less stable steady state current density for both conditions. This confirmed that the unstable steady state condition, obtained in previous measurements (cf. Figure III-17), was caused by surface phenomena occurring at the entrance surface side.

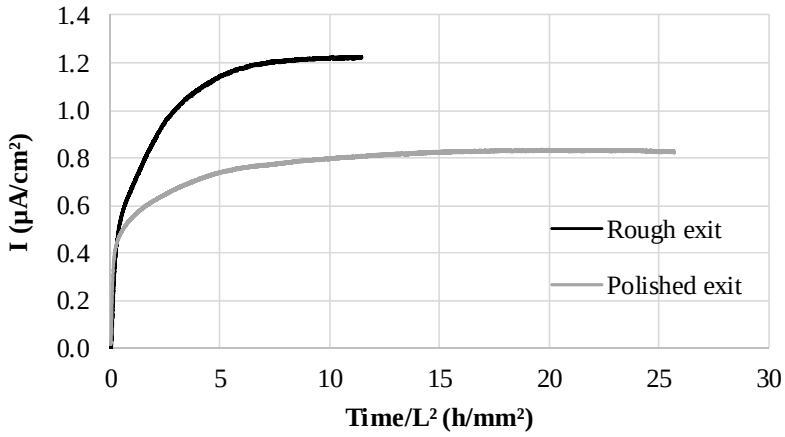

Figure III-19 Armco iron tested by the permeation test method 2. The black curve represents the transient of a sample where both entrance and exit surface were ground. The grey curve represents the result of a sample with a ground entrance and polished exit surface. L is the sample thickness.

Once a stable steady state hydrogen flux had been achieved, apparent diffusion coefficients could be determined. When calculating D_{app} at $t_{0.01}$, $t_{0.1}$, $t_{0.5}$, $t_{0.63}$, and $t_{0.9}$ of the normalized current, the highest reproducibility, i.e. lowest standard error (SE), was obtained at $t_{0.1}$. Hence, the average $D_{app,\,0.1}$, calculated by Equation III-3, was 6.27 ± 0.35 E-10 m²/s for the samples with a rough entrance and polished exit surface. When both entrance and exit side of the specimen were roughened, $D_{app,\,0.1}$ was 3.22 ± 0.15 E-10 m²/s.

$$D_{app,0.1} = \frac{L^2}{7.7\ t_{0.1}} \quad \text{(III-3)}$$

Another method to determine the diffusion coefficient is by fitting the experimental data to the theoretical one based on Fick's law ($D_{app,\,fit}$). The fitting procedure is described in detail in section II.4.2. It was observed that a much better fit was obtained when only the first part of the transient was used. This is illustrated in Figure III-20. When the normalized current reached a value of about 0.5, the experimental curve started to deviate from the theoretical one. Similar trends were observed for the other permeation experiments on the Armco and DP steel. This observation will be evaluated in more detail further in this section. When only fitting the first half of the curve, an average $D_{app,\,fit}$ of the samples with a rough entrance and polished exit surface was 6.16 ± 0.37 E-10 m²/s. When both entrance and exit side of the specimen were roughened, $D_{app,\,fit}$ was 2.41 ± 0.22 E-10 m²/s.

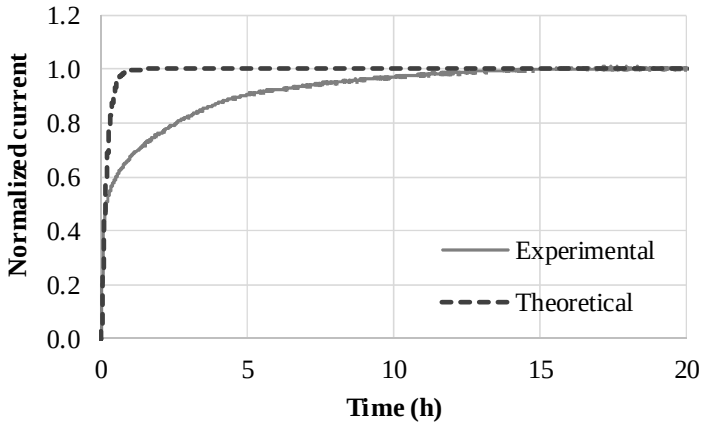

Figure III-20 Simulation of the experimental permeation transient with the theoretical model based on Fick's laws. The material tested is Armco iron with a roughened entrance and polished exit side.

The roughened exit side must be responsible for the lower $D_{app,\,0.1}$ and $D_{app,\,fit}$. Comparing both experiments (Figure III-19), the steady state condition was reached faster and its value was higher for the sample with the roughened exit side. Following equation III-4, if the thickness L and sub-surface concentration C_0 at the entrance side were constant, which was the case when comparing the experiments plotted in Figure III-19, J should decrease with a decreasing D_{app}.

$$J = \frac{C_0\ D_{app}}{L} \quad \text{(III-4)}$$

However, the roughened exit surface caused an increase in the hydrogen permeation flux (Figure III-19). Therefore, a change in the kinetics of the occurring reactions or a difference in the characteristics of the passivation layer was proposed. Addach *et al.* [26] and Manolatos *et al.* [27] already indicated that the thickness of the passivation layer influences the permeation test results. Furthermore, Vecchi *et al.* [28] stated that the kinetics of the hydrogen oxidation reaction depends on the exit surface chemistry and surface

state, which affects the experimental results. Huang *et al.* [29] showed that cold work increases the interior stored energy and the deformation slip steps on the surface, which changes the surface energy distribution. As such, differences in the passive film at a polished and ground surface at the exit side might then be reflected in the permeation results. However, this hypothesis requires further investigation for its validation.

On the other hand, the deformed exit surface contained a higher dislocation density, i.e. potential hydrogen traps, compared to the bulk of the material. Moreover, Legrand *et al.* [30] stated that these traps could have a larger effect on the hydrogen trapping capacity for annealed materials compared to materials which already contain a high trap density microstructure, such as martensite. Yet, it was believed that the passivation layer properties were mainly responsible for the difference in D_{app} as the grinding step mainly removes material instead of introducing additional surface deformation. For the surface preparation, a Struers® grinding disc of 500 grit was used which corresponds to a grain diameter of 30 µm. Hence, the deformed layer, introduced by the grinding step, was at maximum 30 µm in thickness and thus minimal compared to the sample thickness of about one millimetre. In addition, optical microscopy images did not show any noticeable deformation.

The roughened exit side was used for further experiments due to the experimental requirements needed to perform permeation tests in the combination with an applied constant load. Rectangular shaped samples were necessary for this type of tests which were challenging to polish. However, the roughened exit layer is present as a constant factor throughout all the experiments as it was prepared in a systematic way, which guarantees a reliable and reproducible assessment of the obtained permeation data.

Similar as for Armco iron, D_{app} was calculated for the DP-steel. The average $D_{app,\,0.1}$ for four experiments, calculated by Equation III-3, was 4.92 ± 0.34 E-11 m²/s. Yet again, a much better fit was obtained when only the first half of the transient was used. This is illustrated in Figure III-21. When the normalized current reached a value of 0.5, the experimental curve started to deviate from the theoretical one. Comparable trends were observed for the other permeation experiments on the DP steel. When only fitting the first half of the curve, an average of 5.59 ± 0.44 E-11 m²/s was obtained. It was believed that a more representative value of D_{app} can be obtained by the fitting procedure compared to the single point method. Therefore, the fitting procedure was used in the remaining part of this study. In order to achieve the perfect fit, extra experimental parameters were modified of which the results are discussed later on in this chapter.

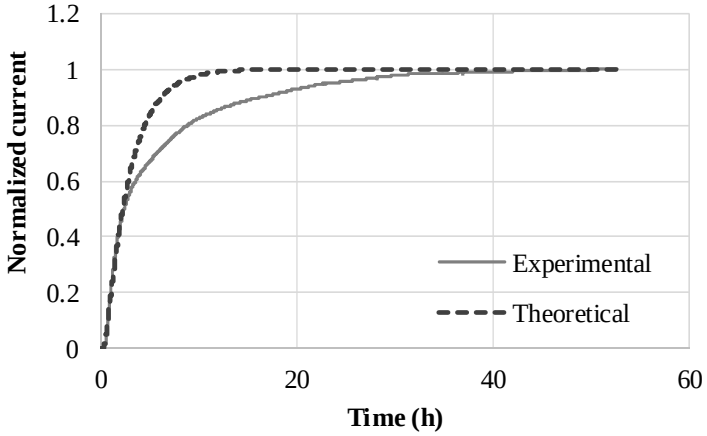

Figure III-21 Fitting the experimental permeation transient of DP steel with the theoretical model based on Fick's laws.

It is important to note that during the research in Chapter IV and V, the investigated samples were polished at both the entrance and exit side. Unfortunately, the beneficial effect of the roughened surface was not yet identified when performing the corresponding experiments. As such, no stable output was obtained and the maximum current density was taken as the steady state flux in order to normalize the experimental data. In Figure III-22, the first part of the normalized transient for a two-sided polished and roughened sample are plotted. As only one point of the curve was used to calculate $D_{app,\,0.1}$ (Equation III-4), based on Figure III-22, the obtained values and trends are trustworthy although no steady state condition was achieved for the polished condition. However, to obtain more optimal results, i.e. where a constant hydrogen flux was accomplished, the entrance surface should be roughened.

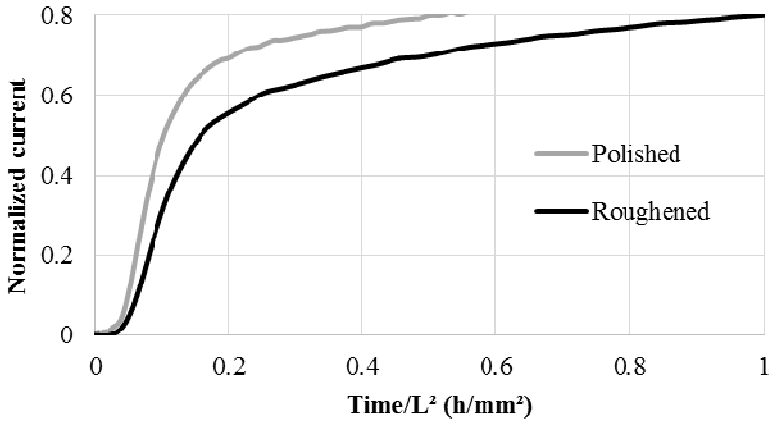

Figure III-22 Armco iron tested by the permeation test method 2. First part of the normalized curves for samples where both entrance and exit surface were ground or polished. L is the sample thickness.

Consequently, it is important to gain more insight how the difference in roughness was responsible for the more stable surface condition. Therefore, two kinds of experiments were performed to evaluate the variations in the hydrogen charging processes at a roughened or polished surface, respectively. First, the exact surface area was measured by performing roughness tests which allowed the calculation of the actual

current density. Secondly, the diffusible hydrogen amount present in the samples was measured by hot extraction measurements. As such, the hydrogen uptake was compared for the different surface pre-treatments.

III.4.6.1. Surface area measurements

3D roughness measurements were performed using a Taylor Hobson CCI HD non-contact optical profilometer using white light interferometry. Samples of Armco iron and DP steel with different roughness were tested and their roughness was determined with a 10x lens. The developed interfacial area ratio (S_{dr}), a parameter calculated by the software, is given in Table III-2. S_{dr} expresses the percentage of the additional surface area contributed by the surface texture as compared to a planar surface. For example, S_{dr} equals zero for a completely flat surface. A polished surface, for which a 1 µm diamond paste was used for the final polishing step, was used as a reference. The other samples were subjected to a grinding step by an automated Struers® grinding and polishing equipment. For the last grinding step, a SiC disc of 180, 500 or 1200 grit was used.

Table III-2 presents, next to the S_{dr}, the real surface area, and real current density. The presence of grinding lines indeed increased the actual surface area, but this was only to a small degree. Consequently, the real current density applied at the entrance side of the specimen was nearly similar for a ground sample than for a polished one. In addition, the material hardness played a role. For a softer material, the observed grinding lines were deeper, increasing the surface area. This was reflected in the higher S_{dr} for the soft Armco iron (±120 HV) compared to the harder DP steel (±190 HV). Nevertheless, only a minor variation in the calculated real current density was observed. These findings led to the conclusion that the different hydrogen reaction mechanisms were not considerably affected by an increased surface area, but rather due to the specific texture of the surface.

Table III-2 The S_{dr}, real surface area, and real current density for Armco iron (A) and dual phase (DP) steel. Final polishing step was 1 µm, final grinding step was 1200, 500 or 180 grit.

Parameter	Flat	A - polish	A - 1200	A - 500	DP - 500	DP - 180
S_{dr} (%)	0	0.000	0.673	1.300	1.119	1.159
Real surface area (cm²)	1	1	1.007	1.013	1.011	1.012
Real current density (mA/cm²)	3	3	2.980	2.876	2.947	2.913

III.4.6.2. Hot extraction

Hot extraction tests were done on both rough and polished DP samples in order to know if the hydrogen uptake efficiency was affected by roughening the surface. The rough samples were ground automatically

with an abrasive SiC disc of 500 grit until a thickness of about 1 mm was reached, while the polished samples were ground and subsequently polished with 3 μm and 1 μm diamond paste, also up to a thickness of 1 mm. All samples were disc-shaped with a diameter of 2 cm.

Before hot extraction, hydrogen was cathodically introduced in the sample by using a 0.1 M NaOH solution. The measured hydrogen amount was rather low and therefore, additional experiments were performed where 1 g/l thiourea was added to the electrolyte. As such, the hydrogen uptake efficiency increased, and the statistical accuracy of the experiment was improved. A cathodic current density of 3 mA/cm² was applied, and two Pt pieces, on both sides of the sample, were used as counter electrodes. After charging for 2 hours, the sample was cleaned, dried and transferred within one minute to an infrared furnace. In the furnace, the sample was heated up to 300 °C, which is the definition of diffusible hydrogen as proposed by Akiyama *et al.* [31]. The hydrogen within the sample was released as gaseous H_2, which was taken up by a nitrogen flow and sent to a thermal conductivity measuring cell. The conductivity of the N_2/H_2 mixture depends on the amount of H_2 because of the significant difference in conductivity between H_2 and N_2. Subsequently, the software calculated the amount of hydrogen that was released from the sample based on the thermal conductivity variation. The experiment was repeated four times for both the ground and polished samples. The average diffusible hydrogen amount is given in Figure III-23.

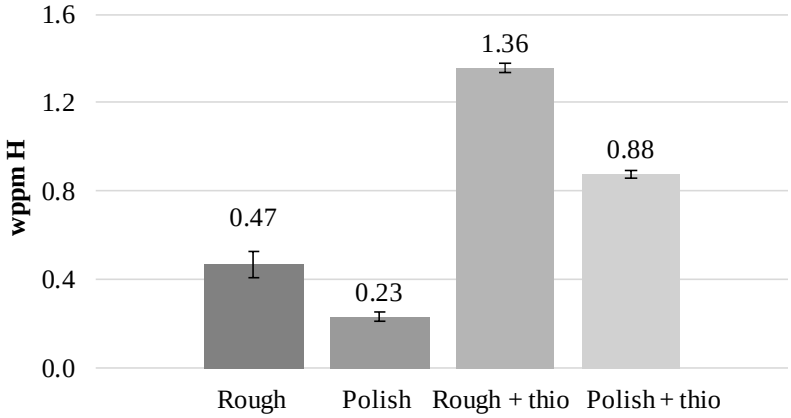

Figure III-23 Hot extraction results of DP steel for variable surface finishes. Hydrogen was cathodically charged using a 0.1 M NaOH electrolyte with or without thiourea. A cathodic current density of 3 mA/cm² was applied.

When the sample was ground, a higher hydrogen uptake was observed for both electrolytes. This implied that less hydrogen recombined to hydrogen gas, i.e. an increased hydrogen uptake efficiency, or that the sub-surface hydrogen concentration was increased due to the deformed surface state. The increase in real area, due to a higher roughness, leads to a lower current density and thus a higher hydrogen uptake efficiency. However, there was only a minimal decrease in actual current density (Table III-2) which could not be responsible for the observed increased hydrogen absorption. Therefore, the electrochemical reaction rate of the HER was studied by recording Tafel plots of the polished and roughened surface. Results are shown in Figure III-24. First, for the roughened surface, the open circuit potential (OCP) showed a more

negative value. This result gives an indication that a roughened surface is probably less noble and therefore more prone to corrosion processes. Although this result was shown to be reproducible by repeating the experiment, more tests are required to further verify this statement.

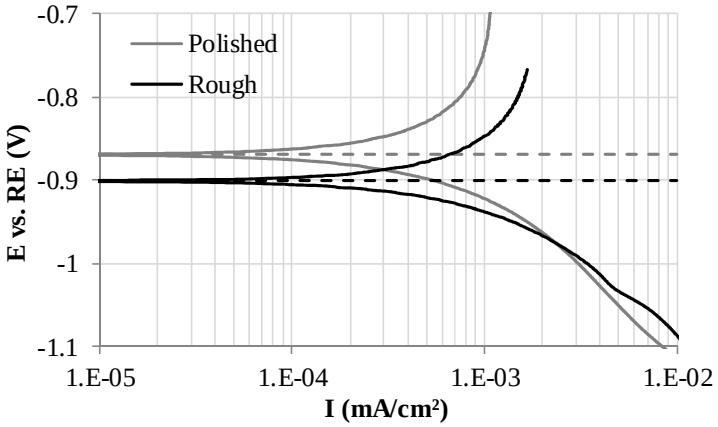

Figure III-24 Tafel plot for the polished and roughened surface.

Second, the exchange current density (i_0), obtained from the Tafel plot by extrapolating the linear portions of the curve and indicated in Figure III-25, was higher for the roughened sample. As i_0 is related to the kinetics of the electrochemical reaction at an electrode [32], the reduction reactions proceeded faster at the ground surface. Furthermore, i_0 is linked with the overpotential η following the Tafel equation (Equation III-5). In the Tafel region, η is related to the activation overpotential, i.e. the energy barrier for electron transfer [33, 34]. Consequently, at a constant current density i, a smaller required η led to the enhancement of the discharge reaction and a higher hydrogen amount at the roughened surface (Figure III-23). In Figure III-25 the overpotential vs the current density is plotted which corresponds with Equation III-5.

$$\eta = -\frac{RT}{\alpha n F} ln \frac{i}{i_0} \tag{III-5}$$

with η the overpotential (V), R the molar gas constant (J K^{-1} mol^{-1}), T the temperature (K), α the charge transfer coefficient (dimensionless), n number of electrons involved in the electrode reaction, F the faraday constant (J V^{-1} mol^{-1}), i the electrode current density (A/m^2) and i_0 the exchange current density (A/m^2).

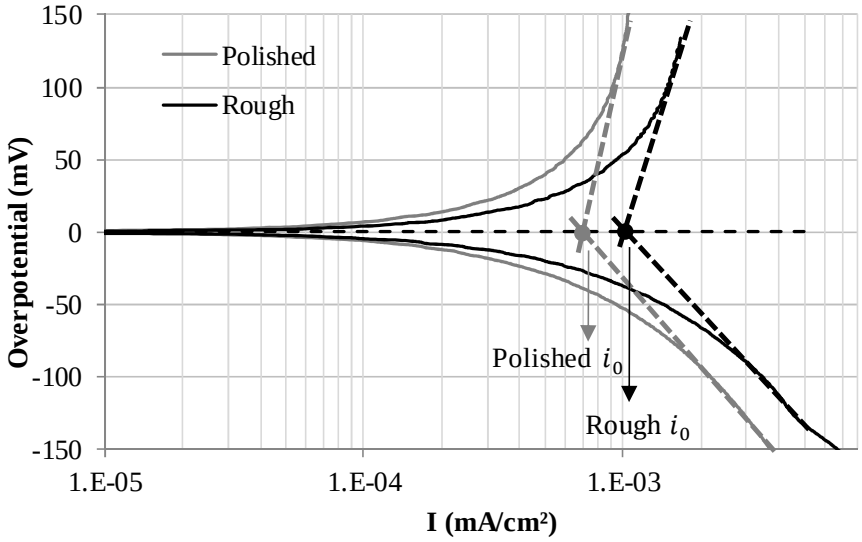

Figure III-25 Overpotential vs I for the polished and roughened Armco iron sample. The exchange current density i_0 is indicated for both conditions.

In addition, during the hydrogen charging procedure on the polished surface, it was observed that large bubbles were formed. The H_2 molecule, before it left the surface, had thus the possibility to grow due to the coalescence with other H_2 molecules. In contrast to the rough specimen, the bubbles were a lot smaller when they left the surface, however, an increased number of bubbles was observed in this case. When recombination took place on the rough sample, the H_2 molecules were somewhat confined in the grinding lines which, to some extent, impeded them from coalesce.

From an electrical point of view, a gas bubble forces the current lines to deflect around it, since the inner volume of a gas bubble is not conductive. Consequently, just next to the bubble a higher current density may be locally observed, while behind the bubble a much lower current density existed. As such, a heterogeneous current distribution was present over the sample surface. Furthermore, surface areas, which experienced a low current density, i.e. polarisation, may not be sufficiently protected against the formation of oxides. These corrosion products could then be responsible for the variable hydrogen uptake at the entrance of the specimen leading to an unstable permeation flux measured at the exit. When comparing both conditions, it was believed that a large amount of homogeneously spread small bubbles, resulted in a more evenly distributed current. As such, a textured surface was favourable to create more stable surface conditions, which was reflected in the corresponding permeation experiments. Next to the more stable surface conditions, the hydrogen uptake efficiency was increased as well. It is thus believed that bubble formation plays a major role in the stability of the surface condition and cannot be ignored when charging hydrogen in an electrochemical way.

III.4.6.3. The entrance potential

In Figure III-26, the entrance potential measured during the permeation experiments on Armco iron is plotted. The black curves are the recorded potentials of the roughened samples, while the grey curves represent the Armco specimens having a polished entrance surface. In both cases, the potential varied during the course of the permeation experiment which demonstrated that the surface characteristics of the entrance side during the test were unstable. Hydrogen gas bubbles shielding the surface could, for example, cause this instability. Nevertheless, the potential difference, between the end and start of the experiment, was clearly smaller for the roughened surface. As such, a more stable entrance potential was obtained when the surface was ground, leading to a more stable hydrogen flux at the exit side (Figure III-19). This implied that the inconsistent permeation result was caused by surface phenomena which were more pronounced for a polished entrance surface side. As the potential is affected by the surface state of the material, it was required to analyse this parameter in depth for both the polished and ground condition.

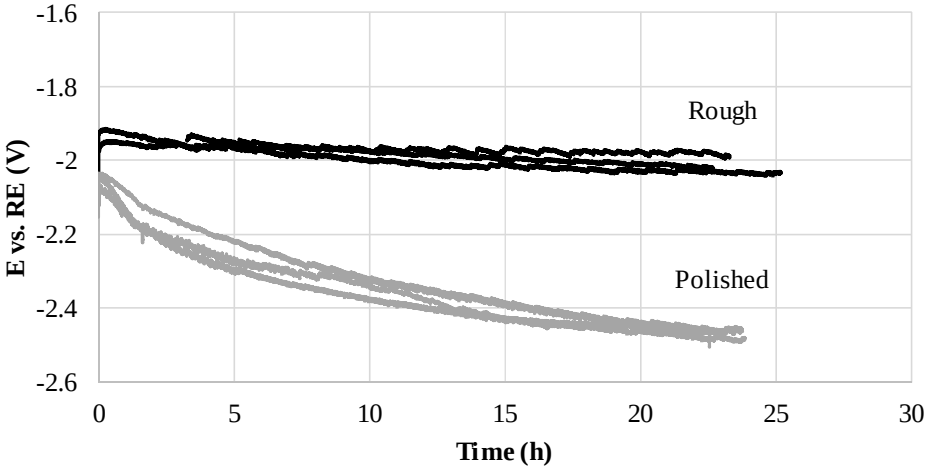

Figure III-26 Entrance potential (E) vs RE (Hg/Hg_2SO_4 +650 mV vs SHE) during the permeation experiment. Black and grey curves represent measurements with a ground and polished surface, respectively.

Small potential fluctuations, as mentioned previously in section III.4.5, were attributed to hydrogen bubble formation. These variations were present for both the polished and ground condition, however, due to the large time scale of Figure III-26, they are not clearly visible. Oscillations with a larger time period (± 1 hour) were observable for both the roughened and polished condition. These time periods were too long to attribute to the hydrogen gas bubble formation and to confirm this, the gas production at the cathode surface should be recorded. Based on the observations of DePetris-Wery *et al.* [24], the cyclic signal could be attributed to the formation/relaxation of stresses in the subsurface.

The overall course of the potential was clearly more stable for the roughened sample than for the polished condition. Therefore, a closer look was taken at the shape of both the variable entrance potential and hydrogen oxidation current density. The experiment, plotted in Figure III-27, was carried out on Armco iron by permeation test method 2 where 3 mA/cm² was applied at the entrance side and -200 mV vs RE at the

exit side. The maximum of the permeation current density coincided with a change in slope of the measured potential. This confirmed once more that the changing entrance surface characteristics being responsible for the instabilities in the outgoing hydrogen flux. Similar results were obtained in experiments where a potential of -500 mV vs the RE was applied and where a polished entrance surface was used.

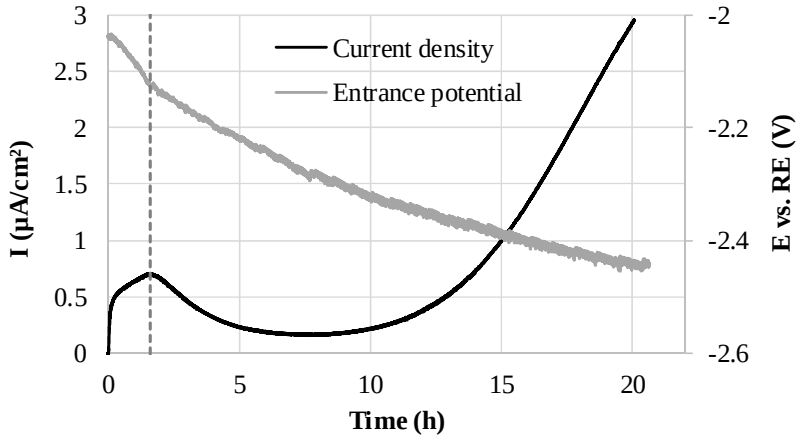

Figure III-27 Link between entrance potential (grey) and exit hydrogen oxidation current density (black). Permeation test was performed on a polished pure Armco iron specimen by permeation test method 2. The applied cathodic current density at the entrance and exit potential were 3 mA/cm² and -200 mV, respectively.

When a ground surface was tested, no distinct change in slope of the entrance potential was detected which indicated that the grinding lines must prevent the undesired change of the surface state. This change was probably responsible for a modification in the hydrogen adsorption, absorption and desorption mechanisms. If the change in slope was caused by the formation of some specific surface film, it could be investigated by in-situ surface analyse techniques such as XPS or RAMAN. However, the use of RAMAN to visualize the variations of the surface during hydrogen charging was found to be difficult due to hydrogen gas production which complicated the measurement.

Catonne *et al.* [3] also analysed both the cathodic potential at the entrance surface (E_{in}) and the permeation current density at the exit side. They stated that the measured potential E_{in} was related to the absorbed hydrogen in the subsurface $(H_{abs})_s$ based on following equations:

$$H_{ads} \leftrightarrow (H_{abs})_s \tag{III-6}$$

$$E_{in} = \frac{RT}{F} \ln \frac{K_w}{(OH^-)(H_{ads})} \tag{III-7}$$

As such, E_{in} had to vary as $-\ln(H_{ads})$ and based on Equation III-6, $\ln(H_{ads}) = \ln(H_{abs})_s$ and consequently $E_{in} \sim -\ln(H_{abs})_s$. Moreover, they divided the absorption flux (Φ_{abs}) in a desorption (Φ_{dsp}) and an insertion flux (Φ_{ins}) (Figure III-28). The desorption flux (Φ_{dsp}) being the hydrogen flux from the absorbed to the adsorbed state, and the insertion flux (Φ_{ins}) being the flux of absorbed hydrogen in the

subsurface to the bulk of the material. In the beginning of charging, it was possible to envisage a competition between the insertion and desorption flux. If the desorption flux was larger than the insertion flux, (H_{ads}) and $(H_{abs})_s$ (Equation III-6) increased leading to a decrease, i.e. a more negative value of E_{in}. Consequently, when the insertion flux was higher, $(H_{abs})_s$ decreased again, leading to a less negative E_{in} until the stress in the subsurface facilitated the hydrogen desorption process. When these fluxes balance themselves, the measured entrance potential should be constant.

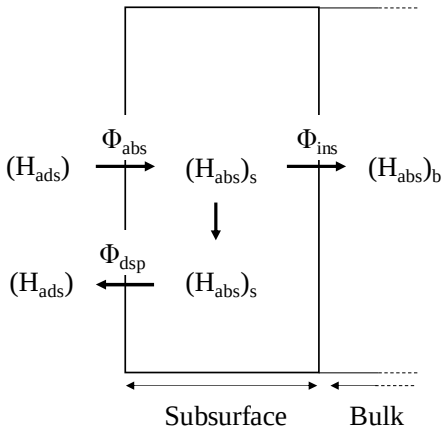

Figure III-28 Schematic distribution of hydrogen fluxes in the subsurface of the membrane during a permeation test.

Based on the conclusions made by Catonne *et al.* [3], the continuously decreasing measured potential drop could be related to a hydrogen desorption flux which was larger than the hydrogen insertion flux. This could be an explanation for the decrease in permeation current, but not for its increase, which was observed for the polished sample after about 8 hours (Figure III-27). As mentioned previously, the increase in permeation current could be related to the presence of certain oxides at the entrance side [7] which were formed due to the occurrence of large hydrogen bubbles. These bubbles could shield the surface in such a way that the potential behind it was not sufficiently low to protect the metal from oxidation [8]. Hence, after a certain time, these oxides could have led to an increased hydrogen uptake. Generally, oxides increase the ohmic resistance which results in a larger overpotential needed to preserve the imposed current. This oxide formation, together with a higher desorption flux, could have contributed to the continuously decreasing potential. However, the formation of these oxides should be verified with in-situ surface analysing techniques and also the interpretations based on the observations of Catonne *et al.* [3] should be further verified.

In the case of the roughened sample, the continuous decrease in potential was less pronounced. During the hydrogen charging in the hot extraction experiments, it was noted that the hydrogen gas bubbles, formed at the surface cathodic surface, were much smaller. Consequently, the large amount of homogeneously spread small bubbles, resulted in a more evenly distributed current. This implied that oxides were more likely formed at a polished surface. This could clarify the more stable surface conditions in the case of a roughened

surface which was then reflected in the measured entrance potential and the hydrogen oxidation current density.

However, there was still some decrease in potential observed for the sample having a rough entrance side. On the one hand, this could be due to the uncontrollable absorption flux of hydrogen, based on the statements made by Catonne *et al.* [3]. On the other hand, similar as for the polished surface, this could be due to the formation of oxides, increasing the ohmic resistance. To know which process was responsible for the overall decrease in potential, a permeation test was carried out without deaeration of the electrolyte in the cathodic cell (cf. section III.4.6.4.). If the decrease in potential was related to the formation of oxides, a larger decrease was expected in the case of a higher oxygen concentration. Moreover, silver, as a noble metal, was charged with hydrogen as well, in order to diminish the possible oxidation of the working electrode. In that case, the recorded potential should show a constant value.

A final difference between the potential of the two conditions was, that at the start of the experiment the potential of the ground surface was less negative compared to the polished one. Similar results were obtained by Mouanga *et al.* [35] who also observed a less negative potential for the mechanically abraded iron membrane compared to the polished one. As mentioned previously in section III.4.6.2, for the roughened surface, a smaller overpotential was required in order to preserve a certain imposed current density. The higher activity of the deformed layer was confirmed by the higher exchange current density and the less noble OCP value (Figure III-24).

III.4.6.4. Oxidation of the entrance surface

The effect of oxygen content on the continuous decrease in potential was evaluated by using an electrolyte which was not deaerated. Reflecting on the results in section III.4.4, a much faster decrease in potential was observed when oxygen was present during the charging process of a polished surface. This indicated that oxygen was an important parameter concerning the stability of the signal. In addition, silver was also cathodically charged in the permeation set-up. As silver is much nobler compared to iron, oxidation of the electrode may be considered negligible. Consequently, a more stable entrance potential was expected if oxidation of the electrode is responsible for the varying potential. For all experiments, a cathodic current density of 3 mA/cm² was applied and results of the measured potential are summarized in Figure III-29.

Comparing the potential of Armco iron in the electrolyte with and without nitrogen bubbling, no significant difference was observed. In contrast with the polished surface (Figure III-14), oxygen did not influence the recorded potential indicating the continuous decrease could not be associated with oxygen related processes. This could be clarified by the aforementioned different types of hydrogen gas bubble formation for a roughened and polished surface. Also the noble silver showed a decrease in potential during the hydrogen charging step which confirmed that oxides were not responsible for the decrease in potential. However, a deposited brownish layer was visible at the cathodic surface. As silver was not expected to oxidise, other

elements must have reduced and deposited at the surface. Therefore, an XPS analysis was carried out for which the results are depicted in Figure III-30. The layer present at the silver surface consisted mainly of C, O, Cu and Zn. No brass contacts were present in the cell and thus, it was thought that the used demi water still contained Cu and Zn ions which could be deposited on the surface during the hydrogen charging. In order to confirm this theory, permeation tests were carried out in 0.1 M NaOH electrolyte based on ultrapure Milli Q® water. In addition, ICP-MS (inductively coupled plasma mass spectrometry) was performed on the electrolyte before and after the charging step to examine the difference in concentration of specific ions.

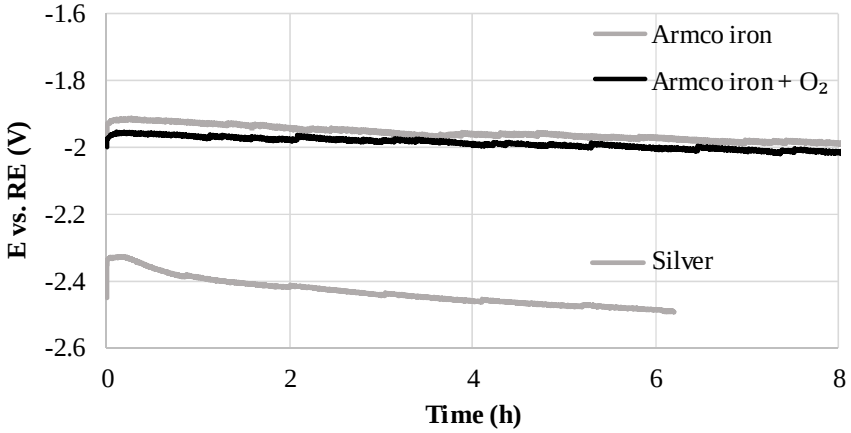

Figure III-29 Entrance potential of iron and silver vs RE (Hg/Hg_2SO_4 +650 mV vs SHE) during the permeation experiment.

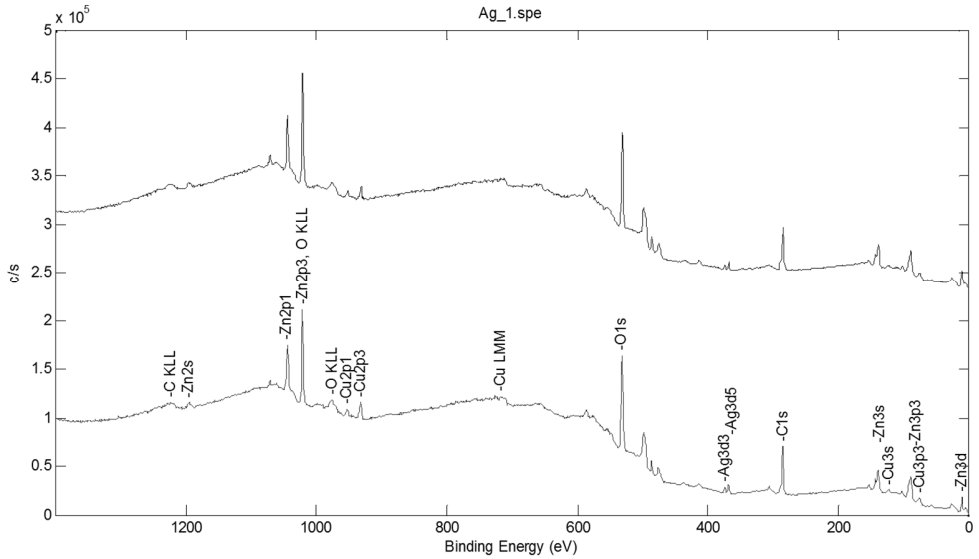

Figure III-30 XPS spectra of two different spots on the Ag surface.

III.5 Permeation results with ultrapure electrolyte

III.5.1.The entrance potential and ICP-MS

In order to track down the origin of the surface contamination and the resulting decrease in potential, experiments were performed by the permeation test method 2 with the use of ultrapure Milli Q water for the electrolyte. The high resistivity (18.2 MΩ·cm) of the Milli Q water was obtained by successive steps of filtration and deionization. The measured potential of the entrance surface is shown in Figure III-31. As expected, the potential was more stable with the Milli Q water. This indicated that less cations were present which could deposit on the sample surface, and thus a more stable condition was obtained. The effect of the ultrapure electrolyte on the outgoing hydrogen permeation current at the exit side, is discussed in next section III.5.2.

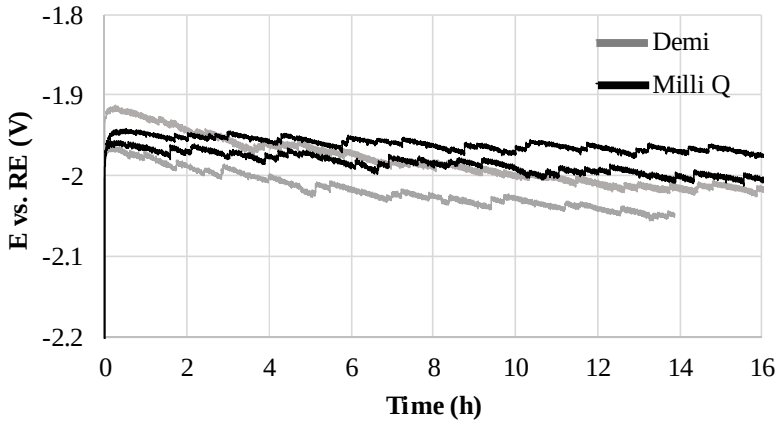

Figure III-31 Entrance potential vs RE (Hg/Hg_2SO_4 +650 mV vs SHE) during the permeation experiment. Grey and black curves were recorded in the electrolyte based on demi and Milli Q water, respectively.

The electrolyte of the cathodic cell was analysed with ICP-MS (Nexion 300D, Perkin Elmer) in order to determine the concentration of a specific element. Next to Cu and Zn ions, detected on the Ag surface, the Sn concentration was also measured as it was identified on the iron surface when analysing the possible dissolution of the Pt electrode (Figure III-10). Average from 3 ICP-MS measurements are given in Table III-3, the relative standard deviation for all measurements was lower than 10%. The Cu and Zn ions showed a decrease in concentration after the hydrogen charging step. This confirms that the deposited ions, detected at the surface, were indeed originating from the electrolyte. The unexpected increase of the Sn ion concentration was rather small and was therefore thought to be negligible.

The increased concentration of the Cu and Zn ions in the Milli Q-based electrolyte after the experiment was clarified by some contaminations of the set-up resulting from previous measurements. Hence, a concentration lower than two ppb could possibly remain although all parts of the set-up are flushed several times with the Milli Q water prior to the experiment. The Sn concentration was similar before and after the test which endorsed the idea of the aforementioned insignificant increase detected for the electrolyte with demi water.

Table III-3 ICP-MS results before and after the permeation test. The use of demi or Milli Q water are compared. Ion concentration is given in µg/l.

Water	Ion concentration (µg/l)		
	Cu	Zn	Sn
Demi – before	97.4	195.0	16.4
Demi – after	64.8	190.0	17.2
Milli Q – before	< 2	< 2	< 2
Milli Q – after	7.3	19.2	< 2

The surface contamination on the cathodic iron surface tested in the ultrapure electrolyte was studied by XPS measurements. In Figure III-10, the XPS spectra of the Armco iron indicated the presence of Zn (1.86 at%) and Sn (0.51 at%) on the cathodic surface when standard demi water was used. The results of the specimen tested in the ultrapure electrolyte is given in Figure III-32. Except for Pb (1 at%), no other contaminating elements could be detected. Most likely, the Pb also originated from the electrolyte. In addition, spectra were taken after certain Ar sputtering times which confirmed that Pb was indeed deposited during the charging process.

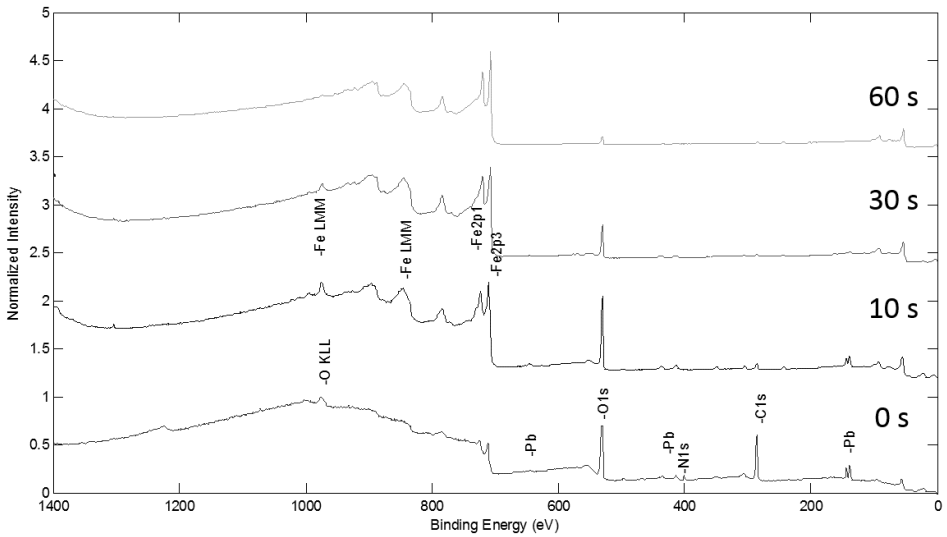

Figure III-32 XPS spectra of the Armco iron surface after 0, 10, 30 and 60 seconds of Ar sputtering. The charging was done in 0.1 M NaOH based on ultrapure Milli Q water.

To conclude, the concentration of cations in the electrolyte is reduced at the cathode during the hydrogen charging step. These processes affect the surface state of the considered material and thus its entrance potential. Subsequently, the HER mechanisms could be modified leading to variations in the hydrogen entry and hence the resulting exit flux. The effect of the ultrapure electrolyte on the hydrogen permeation flux is elaborated in more detail in the next section.

III.5.2. The permeation flux

By using the ultrapure Milli Q water instead of demi water, a more stable surface condition was obtained. The permeation experiments on Armco iron were performed by the permeation test method 2 and the $D_{app, fit}$ of the first half of the curve was 3.71 ± 0.16E-10 m²/s. Compared to the tests performed with the use of demi water (2.41 ± 0.22E-10 m²/s), $D_{app, fit}$ slightly increased. The normalized experimental and theoretical curves of both conditions are depicted in Figure III-33. The dotted line represents the theoretical curve, while the solid line is the normalized experimental curve. When using the ultrapure Milli Q water, a much better fit was obtained. The deflection of the experimental curve from the theoretical one was delayed and the steady state condition was reached earlier. Hence, the abovementioned deviation of Fick's model can be explained by the cations which were present in the demi water. During charging, they were attracted to the cathode where they deposited and consequently affected the hydrogen entry flux. The composition of the electrolyte is thus of significant importance when trying to approach the ideal conditions based on Fick's diffusion laws.

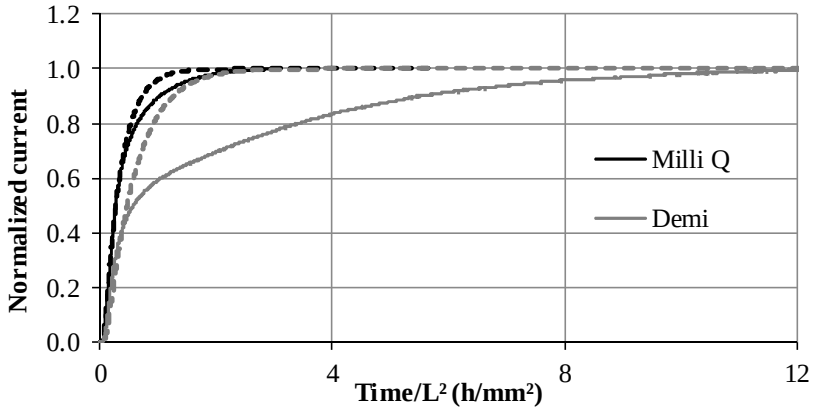

Figure III-33 The experimental (solid line) and theoretical (dotted line) permeation transient of Armco iron charged in 0.1 M NaOH electrolyte based on Milli Q (black) or demi water (grey).

To clarify the increased $D_{app, fit}$ obtained when using the Milli Q water, the experimental curves were plotted and compared. The left side of Figure III-34 shows the full transients and a detail is given at the right side. From the left figure, an increased steady state value was observed for the experiments with demi water. Nevertheless, the slope of both experiments in the first part of the transient, clearly visible on the right figure, was comparable. Thus, when normalizing the data, a decreased slope was expected for the experiments in the electrolyte with demi water which led to a decrease in the determined $D_{app, fit}$. Furthermore, the figure at the right demonstrates that the deposited ions only affect the permeation flux at a later stage of the experiment.

Since a higher steady state flux was obtained in the electrolyte based on demi water, the deposition of cations caused a higher hydrogen concentration in the subsurface of the material. More specific, copper is a very good electro-catalyst for producing hydrogen [36]. Kumar et al. [37], for example, investigated copper

nanoparticles as a catalyst for the hydrogen evolution reaction. Based on the statement of Catonne *et al.* [3], that E_{in} had to vary as $-\ln(H_{abs})_s$, the continuous decrease in potential (Figure III-31) was clarified. The author linked the increasing absorbed hydrogen concentration to a desorption flux which was larger compared to the insertion flux. However, in this work, it was demonstrated that the increasing H_{abs} was caused by the deposition of cations at the cathodic surface.

The difference in $D_{app,\,fit}$ of the two conditions was thus attributed to the different steady state value caused by the varying hydrogen entry flux. As the same material was tested, it was not possible that the hydrogen diffusivity of the material changed when comparing both conditions. As such, the most representative value of $D_{app,\,fit}$ was obtained by the use of the electrolyte based on the ultrapure Milli Q water. Moreover, a more consistent steady state value will be obtained as it was strongly dependent on the water composition.

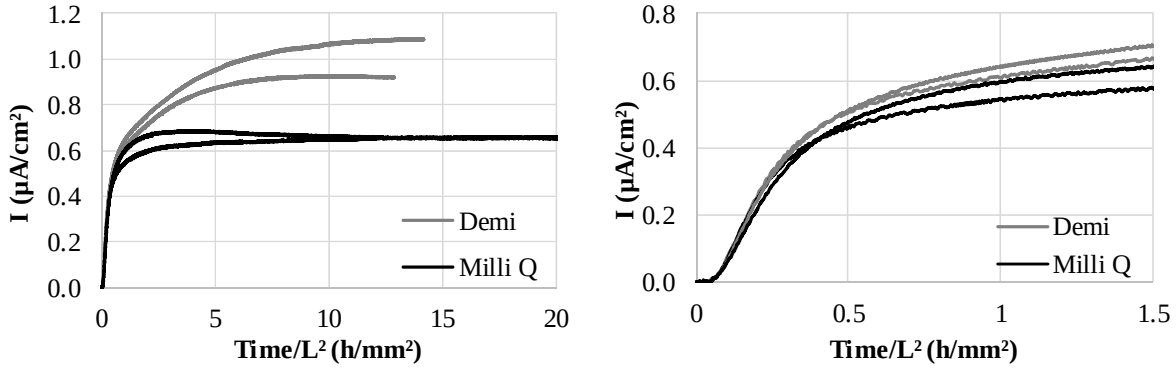

Figure III-34 Experimental permeation curves on Armco iron charged in 0.1 M NaOH electrolyte based on Milli Q or demi water (left). A detail of the first part of the transients is given at the right.

III.6 Partial transients

During the first hydrogen charging step, slow surface processes upon hydrogen entry and/or hydrogen trapping upon hydrogen transport take place, which partially determine the shape of the resulting transient. In turn, when stopping the hydrogen charging, the complete decay reflects the release of hydrogen from the lattice and trapping sites. In iron, and some of its alloys, these effects are non-negligible as the mobility and trapping ability of hydrogen is high. Due to these disturbing effects, a large scale of diffusivity and solubility data are obtained in literature by the permeation method. Therefore, to exclude these effects, Zakroczymski *et al.* [38] proposed a different approach for the effective use of the classical permeation technique. In their earlier work [39], they demonstrated that surface and trapping effects were not observed for a pre-charged specimen during a partial build-up or decay transient caused by a relatively small decrease or increase of the applied cathodic current density. They also stated that, in this way, the lattice diffusivity and solubility of hydrogen could be determined. Researchers like Lan *et al.* [40], Fallamohammadi *et al.* [41], and Liu and Atrens [42] adopted the method. In this work, the partial hydrogen permeation technique was applied on the pure Armco iron.

The Armco sample, which had a thickness of 1015 µm, consisted of a ground entry and exit side. The electrolyte in both cells was 0.1 M NaOH. The hydrogen charging was carried out in electrolytes based on demi water and ultrapure Milli Q water. At first, the results with the use of demi water are discussed. For the first transient, a current density of 3 mA/cm² was applied. When the oxidation current reached its steady state value, the charging current density was reduced to 1.5 mA/cm² in order to record the partial decay curve. Subsequently, the partial rise transient was obtained by increasing the current density again to 3 mA/cm². The normalized first and partial transient are shown in Figure III-35. The partial transient reached the steady state condition much quicker compared to the first transient. This could be related to the surface and trapping effects which were minimized during the partial rising transient [38, 39]. Instead of fitting the first half of the transient, the full experimental transient was used. As such, the results were more appropriate to compare with the work of Zakroczymski *et al.* [38]. When fitting the full experimental curves with the theoretical model based on Fick's laws, the partial transient showed a much better fit. The theoretical transients are presented by the dotted line in Figure III-35. In section III.5.2, it was shown that the deflection of the experimental curve from the theoretical one was mainly neutralized by the use of ultrapure Milli Q water. Since less cations were deposited on the surface, a more constant hydrogen entry flux was achieved in section III.5.2. Consequently, here, the better fit for the partial transient was, next to the minor effects of the trapping sites, due to less variations of the surface state during the shorter charging stage.

The determined diffusion coefficient was 1.10 ± 0.12 E-10 m²/s and 1.12 E-09 m²/s for the first and partial transient, respectively. Zakroczymski *et al.* [38] found a value of 7.3 E-09 m²/s for the partial transient and considered this value as the real diffusivity for Armco iron at room temperature. For the first transient, the author determined a D_{app} of 1.3 E-09 m²/s. Besides the rising transients, also the partial decay curves could be used to define D_{app}. Fitting the partial experimental decay with the model based on Fick's laws, resulted in a value of 1.04 E-09 m²/s, which was comparable with D_{app} of the partial rising transient. D_{app} obtained from the decay transient by Zakroczymski *et al.* [38] was 7.7 E-09 m²/s. An overview of the diffusion coefficients, comparing different methods to determine them, is given in Table III-4.

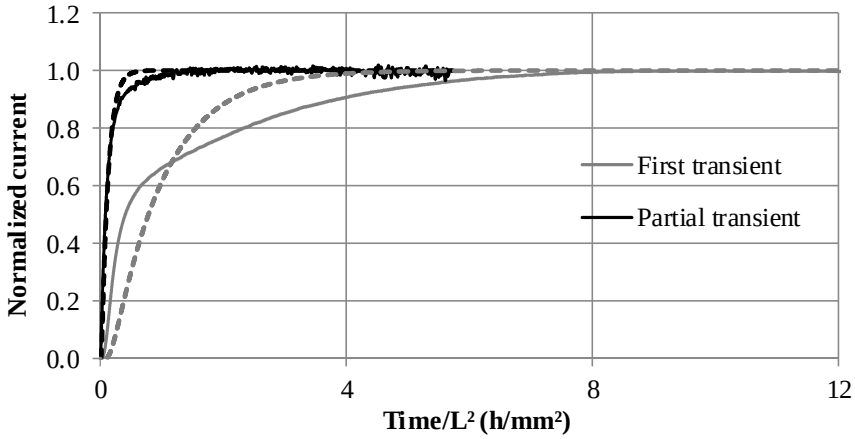

Figure III-35 The experimental (solid line) and theoretical (dotted line) permeation transient of Armco iron tested by the partial permeation technique based on the permeation test method 2.

Table III-4 Diffusion coefficients (m^2/s) of Armco iron compared with the work of Zakroczymski *et al.* [38].

Research	First (m^2/s)	Partial (m^2/s)	Partial decay (m^2/s)
This study	1.14 ± 0.10 E-10	1.12 E-09	1.04 E-09
Zakroczymski *et al.* **[38]**	1.3 E-09	7.3 E-09	7.7 E-09

The lower D_{app} of the first transient, compared to the work of Zakroczymski *et al.* [38], may be attributed to an increased amount of trapping sites caused by differences in the manufacturing process of the Armco iron. In this research, the as-received Armco iron was a hot rolled plate, while in the work of Zakroczymski *et al.* [38], the membranes were machined out of a hot-drawn rod, perpendicular to its axis. On the other hand, their exit side of the samples were coated with palladium, while in this work, they were roughened before a passivation layer was imposed.

The lower value of the partial transient could however not be clarified by an increased trap density as it was supposed that trapping sites did not influence the partial transient in a great manner. As such, the passivation layer at the exit side could be responsible for a lower D_{app}. Yet, another difference between this study and the work of Zakroczymski *et al.* [38] was the charging current density. The author recorded the partial transient by increasing the current density from 5 to 10 mA/cm^2, while in this study it was increased from 1.5 to 3 mA/cm^2. If D_{app} increases with increasing cathodic current density, as stated in several works [43-46], the lower diffusivity obtained in this research could be explained by the hydrogen concentration dependence of D_{app}.

The partial permeation technique was also performed on Armco iron when using the electrolyte based on the ultrapure Milli Q water. The experimental data, together with the theoretical curves, fitted with the full transient, are shown in Figure III-36. Again, an increased diffusivity was obtained for the partial rise transient, indicating the reduced effect of the trapping sites. In Table III-5, the apparent diffusion coefficients

of the experiments in the electrolyte based on demi and Milli Q water, are given. The higher diffusivity for the first transient in the Milli Q based electrolyte was explained in section III.5. For the partial transients, a similar value was expected as trapping sites were believed not to influence the transient during this partial charging step. However, a somewhat lower $D_{app,\ fit}$ was obtained when using the ultrapure electrolyte.

As mentioned previously, the deposited copper on the entrance surface, originating from the electrolyte, induced a higher hydrogen uptake [37]. Consequently, more hydrogen was present in the subsurface when recording the partial transient in the demi water based electrolyte. Based on these findings, an increased hydrogen concentration in the subsurface of the material resulted in an increased $D_{app,\ fit}$. This led to the conclusion that the trapping process was perhaps not completely eliminated since the concentration dependence of D_{app} is related to a competition between the hydrogen diffusion and trapping process, which was clearly demonstrated in the work of Frappart *et al.* [44]. By increasing the hydrogen concentration of the entrance subsurface, the trapping effect can be suppressed and a value closer to the intrinsic diffusivity can be obtained [43]. This theory also confirms aforementioned conclusion concerning the higher diffusivity obtained by Zakroczymski *et al.* [38].

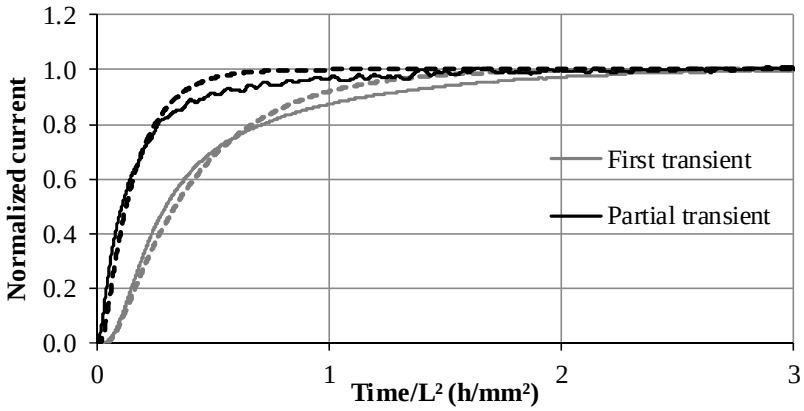

Figure III-36 The experimental (solid line) and theoretical (dotted line) permeation transients of Armco iron tested by the partial permeation technique based on the permeation method 2 and using the ultrapure electrolyte.

Table III-5 Apparent diffusion coefficients (m²/s) of Armco iron tested by the partial transient method with different charging electrolytes.

	Demi (m²/s)	Milli Q (m²/s)
First	1.14 ± 0.10 E-10	3.04 ± 0.04 E-10
Partial	1.12 E-09	8.26 E-10

III.7 Consecutive charging

In steel, two kinds of hydrogen trapping sites are present; reversible and irreversible. The influence of these irreversible trapping sites on the hydrogen diffusivity can be detected through the permeation technique by a procedure performed by several researchers such as Turnbull *et al.* [47] and Manolatos *et al.* [27]. It consisted of a first rise transient, followed by a complete outgassing of hydrogen. Once the background current was sufficiently low, a second rise transient was recorded by applying the same current density as in the first transient. The difference between the two rise transients can then be attributed to the effect of the irreversible trapping sites, if the boundary conditions were exactly similar. As the irreversible trapping sites demonstrate a very low leakage rate, they did not affect the second charging step. If the second transient had a lower breakthrough time, the material indeed contained a relevant amount of irreversible trapping sites, which would lead to a higher D_{app}. In contrast, if there were no irreversible trapping sites present, the second transient should overlap the first one.

This procedure was tested on cold rolled Armco iron (0.002 wt% C), containing a slightly different chemical composition compared to the hot rolled plate (Table III-1). No irreversible trapping sites were present as the matrix only consisted of grain boundaries and dislocations showing an activation energy lower than 60 kJ/mol [48-50]. Hence, consecutive curves should overlap with the first transient. In Figure III-37, a first, second and third transient of the Armco iron is shown. A reduced slope and steady state value was obtained with increasing number of charging steps. $D_{app,\,fit,}$ obtained by fitting the first half of the normalized transient was 2.11 E-10 m²/s, 1.18 E-10 m²/s and 1.10 E-10 m²/s for the first, second and third transient, respectively. This result indicated, that during the outgassing treatment, processes took place which retarded the hydrogen diffusivity through the specimen.

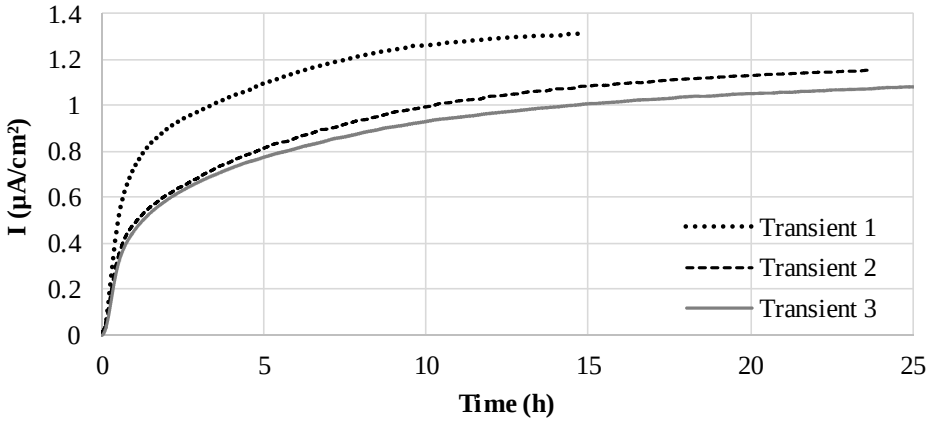

Figure III-37 Consecutive charging steps performed by the permeation test method 2 on cold rolled Armco iron.

Indeed, it is difficult to fulfil the prerequisite on the boundary conditions. During the outgassing step, the entrance surface was not cathodically protected and the chance for oxidation of the iron surface was much

higher. Consequently, as most likely there was still some oxygen present in the electrolyte, an oxide layer could have formed on the sample surface, causing a change in the hydrogen entry processes which was then reflected during the second charging. Besides the entrance side, the exit side was subjected to the same polarization potential over the full test duration. As such, the passivation layer kept on growing, becoming more resistant to hydrogen transport. The obtained results, shown in Figure III-37, agreed well with the findings of Manolatos *et al.* [27] and Addach *et al.* [26]. They both demonstrated that the exit side surface state was responsible for the observed behaviour of the second transient, or at least masked the influence of the entrance side. During the outgassing step, the passivation layer at the exit side became a larger barrier for the hydrogen transport, which was reflected in a reduced slope and steady state value. These results illustrated nicely the importance of the passive layer and, consequently, the passivation time before the start of the experiment. Therefore, it was necessary to keep passivation time constant, as then, this experimental factor could be excluded as a variable. A modelling approach that provides deeper insights in the hydrogen diffusion through the oxide layer and its consecutive oxidation can be found in the work of Vecchi *et al.* [51]. The authors highlighted the complexity of the mechanism and discussed the possible reactions taking place in and at the steel-oxide interface.

The third transient only showed limited differences compared to the second one. This can be explained by the minor differences in the passivation layer in between the start of the second and third charging. The background current density, just before the first, second and third transient, was 60, 20, and 13 nA/cm², respectively. The differences between the current densities, reflected nicely the variations in the permeation curves.

III.8 Sample thickness

When analysing the hydrogen diffusion by electrochemical permeation experiments, it is supposed that the bulk material defines the outcome of the experiment. Hence, the diffusion coefficient should inherently not be affected by the sample thickness [52, 53]. However, if the sample is too thin, surface reactions could become the rate determining step which would affect the measured hydrogen oxidation current density. In that case, the diffusion coefficient cannot be determined correctly. It is therefore of significant importance to study the effect of the sample thickness on the hydrogen permeation to assure the diffusion is bulk controlled. As such, permeation experiments were carried out on DP steel samples with different thicknesses, varying from 1100 μm to 590 μm. The resulting transient curves are plotted in Figure III-38.

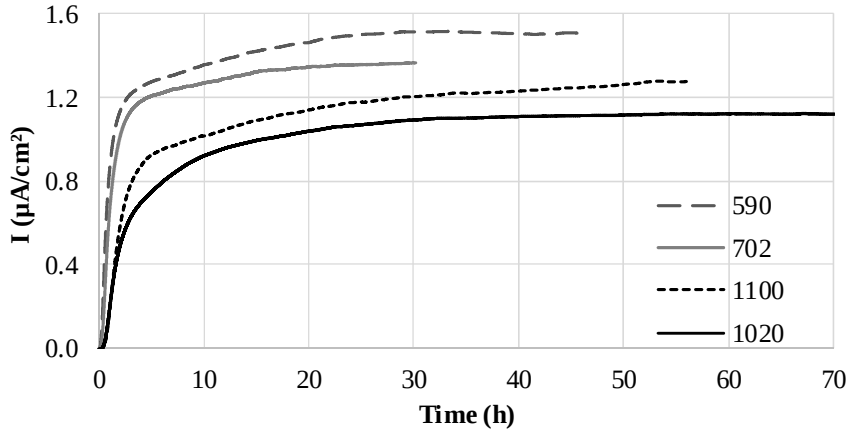

Figure III-38 DP steel with different thicknesses (µm) tested by the permeation test method 2.

Generally, an increased thickness resulted in a lower steady state value, as demonstrated in [26, 53-55]. Addach *et al.* [26] related this reduction in hydrogen flux to the hydrogen trapping which was more dominant in the sample having the highest thickness. Furthermore, hydrogen had also the possibility to diffuse to the sides of the specimen where it could desorb and leave the material. This hydrogen did not get detected at the exit side and could have led to an additional reduction in steady state value. The thicker the sample, the bigger the surface area of the sides, and thus the more hydrogen is lost. The inverse relation between the steady-state value and sample thickness was not fully obtained in this study, since the steady state value of the specimen with a thickness of 1100 µm was higher than the 1020 µm one. This anomalous result could be due to a variation in thickness of the passive layer at the exit side (cf. section III.7) or by the difference in the demi water composition (cf. section III.5).

As mentioned in section III.7, the passivation layer influences the slope and steady state value of the permeation transient [26, 27, 51]. In this case, the background current density of the 1020 µm and 1100 µm sample, was 46 and 57 nA/cm², respectively. Although the difference was minimal, the passive layer at the 1020 µm specimen was denser and could have led to a lower steady state value and a reduced transient slope. This effect of the oxide layer on the permeation transient was also demonstrated in the work of Legrand *et al.* [56]. The background current density of the thinnest specimen, was similar to the 1020 µm thick sample, and thus, did reveal the influence of the sample thickness.

On the other hand, in section III.5, it was shown that the kation concentration in the demi water also affects the hydrogen entry flux, and in turn, the steady state value. A higher concentration of ions decreased the entrance potential and increased the steady state value of the experiment. To confirm this, the entrance potential of the 1020 and 1100 sample was plotted in Figure III-39. A faster decrease in time was observed for the 1100 sample indicating more kations were deposited on the entrance surface during hydrogen charging. Hence, the composition of the electrolyte and the thickness of the passivation layer at the exit side, contributed both to the increased steady state value of the 1100 sample, overcompensating the influence of the thickness.

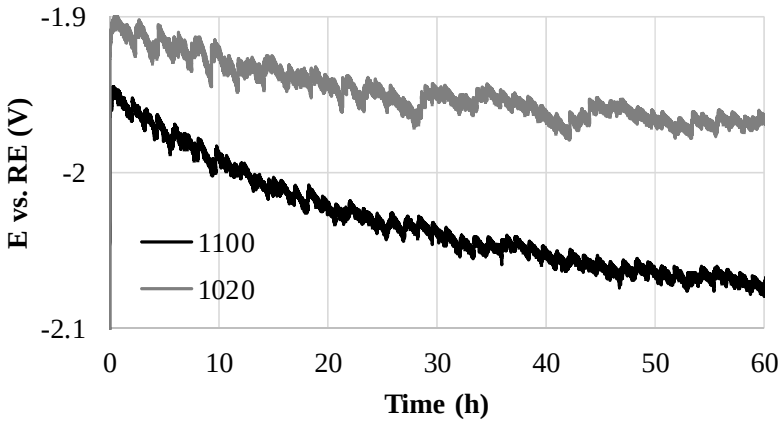

Figure III-39 Entrance potential vs RE (Hg/Hg_2SO_4 +650 mV vs SHE) during the permeation test on samples with a thickness of 1100 µm (black) and 1020 µm (grey).

The apparent diffusion coefficients corresponding with the transients shown in Figure III-38 are summarized in Table III-6. For both methods, the average D_{app} and the SE was calculated. It was concluded that the sample thickness in the tested range did not influence the hydrogen diffusion significantly. Also the sample having a thickness of 1100 µm, which exhibited a higher J_∞ than expected, showed a similar D_{app} and clearly demonstrated the relevance of the experiment. For the single point method, $D_{app,\ 0.1}$ was calculated by Equation III-3 which indicated that $t_{0.1}$ vs L^2 is linear only if $D_{app,\ 0.1}$ is unaffected by the thickness of the membrane. This independency was confirmed by the obtained linearity of $t_{0.1}$ vs L^2 which is plotted in Figure III-40. The curve did not pass by the origin which could be related to surface phenomena [26].

Table III-6 Diffusion coefficients calculated at 10% of the normalized current density ($D_{app,\ 0.1}$) and by fitting 50% of the experimental curve ($D_{app,\ fit}$).

L (µm)	$D_{app,\ 0.1}$ (10^{-11} m²/s)	$D_{app,\ fit}$ (10^{-11} m²/s)
590	4.08	4.46
702	3.96	4.60
1020	4.45	4.76
1100	4.89	4.85
Average	**4.35 ± 0.18**	**4.67 ± 0.07**

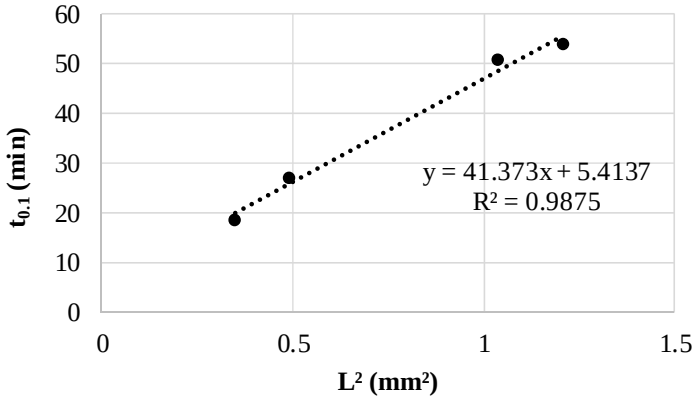

Figure III-40 The time necessary to reach 10% of the normalized steady state value vs L^2 (sample thickness).

III.9 Conclusions

In this chapter, several parameters of the permeation experiment were evaluated in detail to obtain a better understanding of the electrochemical hydrogen permeation technique. It was found that the surface roughness and possible contaminations from of the electrolyte are of high importance for realizing a stable entrance surface state, i.e. hydrogen entry flux. Due to the specific texture of the surface, the hydrogen gas bubble formation was modified and iron oxidation was hindered, leading to a more consistent hydrogen uptake. An even more stable entrance potential, i.e. surface state, was obtained by using the ultrapure Milli Q water instead of demi water for making the electrolyte. Cations, which were present in the demi water, were deposited at the cathodic surface causing an increase in the hydrogen uptake during the experiment. This resulted in large deflection of the experimental transient from the theoretical one based on Fick's law. The high resistivity of the Milli Q water mainly excluded this undesired effect and as such, almost a perfect fit with the experiment was obtained.

Furthermore, the partial transient procedure can be used for determining a diffusion coefficient which approaches the lattice diffusion coefficient. Consecutive charging cannot be performed when oxidation of the entrance surface is possible or when the exit surface is not constant in between the two transients. Both affect the permeation results of the second and third transient leading to inconsistent values of D_{app}. Finally, it was verified that the apparent diffusion coefficient is independent of the sample thickness.

Important to note is that this methodology has been developed over the entire period of the PhD. Therefore, in chapter IV & V, D_{app} was calculated by the single point method. Moreover, the beneficial effect of the ultrapure Milli Q water was discovered at the end of this research and was therefore also not used in the following chapters.

III.10 References

[1] Q. Liu, A. D. Atrens, Z. Shi, K. Verbeken, and A. Atrens, "Determination of the hydrogen fugacity during electrolytic charging of steel," *Corrosion Science*, vol. 87, pp. 239-258, 2014.

[2] T. Zakroczymski and J. Flis, "Impedance characterization of the activation of iron surface for hydrogen entry from alkaline solution," *Electrochimica acta*, vol. 41, pp. 1245-1250, 1996.

[3] J. Catonne and M. DePetris-Wery, "Comparative study of hydrogen permeation into iron: Effects of cathodic polarization and of cyanide," *Materials Chemistry and Physics*, vol. 126, pp. 325-329, 2011.

[4] W. Beck, J. M. Bockris, J. McBreen, and L. Nanis, "Hydrogen permeation in metals as a function of stress, temperature and dissolved hydrogen concentration," *Proc. R. Soc. Lond. A*, vol. 290, pp. 220-235, 1966.

[5] M. C. Tiegel, M. L. Martin, A. K. Lehmberg, M. Deutges, C. Borchers, and R. Kirchheim, "Crack and blister initiation and growth in purified iron due to hydrogen loading," *Acta Materialia*, vol. 115, pp. 24-34, 2016.

[6] J. Flis, T. Zakroczymski, V. Kleshnya, T. Kobiela, and R. Duś, "Changes in hydrogen entry rate and in surface of iron during cathodic polarisation in alkaline solutions," *Electrochimica acta*, vol. 44, pp. 3989-3997, 1999.

[7] I. Flis-Kabulska, J. Flis, and T. Zakroczymski, "Enhanced hydrogen entry into iron from 0.1 M NaOH at definite potentials," *Electrochimica Acta*, vol. 53, pp. 3094-3101, 2008.

[8] Z. Amrani, F. Huet, M. Jerome, P. Manolatos, and F. Wenger, "Fluctuations of permeation rate through an iron membrane induced by hydrogen bubbles," *Journal of the Electrochemical Society*, vol. 141, pp. 2059-2061, 1994.

[9] E. Van den Eeckhout, A. Laureys, Y. Van Ingelgem, and K. Verbeken, "Hydrogen permeation through deformed and heat-treated Armco pure iron," *Materials Science and Technology*, vol. 33, pp. 1515-1523, 2017.

[10] A. Laureys, R. Petrov, and K. Verbeken, "Internal and surface damage after electrochemical hydrogen charging for ultra low carbon steel with various degrees of recrystallization," *Procedia Structural Integrity*, vol. 2, pp. 541-548, 2016.

[11] J. Condon and T. Schober, "Hydrogen bubbles in metals," *Journal of nuclear Materials*, vol. 207, pp. 1-24, 1993.

[12] J. Venezuela, Q. Zhou, Q. Liu, M. Zhang, and A. Atrens, "Influence of hydrogen on the mechanical and fracture properties of some martensitic advanced high strength steels in simulated service conditions," *Corrosion Science*, vol. 111, pp. 602-624, 2016.

[13] C. Gabrielli, G. Maurin, L. Mirkova, and H. Perrot, "Transfer function analysis of hydrogen permeation through a metallic membrane in a Devanathan cell: Part II: Experimental investigation on iron membrane," *Journal of Electroanalytical chemistry*, vol. 590, pp. 15-25, 2006.

[14] Z. Szklarska-Smialowska, T. Zakroczymski, and C. J. Fan, "Effect of EDTA on the cathodic reduction of oxide films on iron in sodium hydroxide solution," *Journal of The Electrochemical Society*, vol. 132, pp. 2543-2548, 1985.

[15] Z. Huang and J. Ord, "An optical study of the iron electrode in alkaline electrolyte," *Journal of the Electrochemical Society*, vol. 132, pp. 24-28, 1985.

[16] H. Gräfen, "Derzeitiger Stand der Kenntnisse über die Spannungsrißkorrosion unlegierter und schwach legierter Stähle," *Materials and Corrosion*, vol. 20, pp. 305-313, 1969.

[17] A. Hugot-Le Goff, J. Flis, N. Boucherit, S. Joiret, and J. Wilinski, "Use of Raman spectroscopy and rotating split ring disk electrode for identification of surface layers on iron in 1M NaOH," *Journal of the Electrochemical Society*, vol. 137, pp. 2684-2690, 1990.

[18] C. Foley, J. Kruger, and C. Bechtoldt, "Electron diffraction studies of active, passive, and transpassive oxide films formed on iron," *Journal of the Electrochemical Society*, vol. 114, pp. 994-1001, 1967.

[19] J. C. Rubim and J. Dünnwald, "Enhanced Raman scattering from passive films on silver-coated iron electrodes," *Journal of electroanalytical chemistry and interfacial electrochemistry*, vol. 258, pp. 327-344, 1989.

[20] R. Grauer, "Feste Korrosionsprodukte–II. Aluminium und Eisen," *Materials and Corrosion*, vol. 32, pp. 113-118, 1981.

[21] A. Brass and J. Collet-Lacoste, "On the mechanism of hydrogen permeation in iron in alkaline medium," *Acta materialia*, vol. 46, pp. 869-879, 1998.

[22] A.-M. Brass and J. Chêne, "Influence of tensile straining on the permeation of hydrogen in low alloy Cr–Mo steels," *Corrosion science*, vol. 48, pp. 481-497, 2006.

[23] L. Nanis and T. G. Namboodhiri, "Mathematics of the electrochemical extraction of hydrogen from iron," *Journal of The Electrochemical Society,* vol. 119, pp. 691-694, 1972.
[24] M. DePetris-Wery, S. Wery, and J. Catonne, "Study of the input-side subsurface reorganization vs. the outside current density in hydrogen permeation under constant cell voltage through iron membrane according to RHC concept," *Materials Chemistry and Physics,* vol. 119, pp. 279-286, 2010.
[25] A. P. Brown, M. Krumpelt, R. Loutfy, and N. Yao, "The effect of surface roughness on the hydrogen evolution reaction kinetics with mild steel and nickel cathodes," *Electrochimica Acta,* vol. 27, pp. 557-560, 1982.
[26] H. Addach, P. Berçot, M. Rezrazi, and J. Takadoum, "Study of the electrochemical permeation of hydrogen in iron," *Corrosion Science,* vol. 51, pp. 263-267, 2009.
[27] P. Manolatos, M. Jerome, C. Duret-Thual, and J. Le Coze, "The electrochemical permeation of hydrogen in steels without palladium coating. Part I: Interpretation difficulties," *Corrosion Science,* vol. 37, pp. 1773-1783, 1995.
[28] L. Vecchi, H. Simillion, R. Montoya, D. Van Laethem, E. Van den Eeckhout, K. Verbeken, *et al.*, "Modelling of hydrogen permeation experiments in iron alloys: Characterization of the accessible parameters–Part II–The exit side," *Electrochimica Acta,* vol. 262, pp. 153-161, 2018.
[29] H. Huang and W. Shaw, "Cold work effects on sulfide stress cracking of pipeline steel exposed to sour environments," *Corrosion science,* vol. 34, pp. 61-78, 1993.
[30] E. Legrand, A. Oudriss, S. Frappart, J. Creus, X. Feaugas, and J. Bouhattate, "Computational analysis of geometrical factors affecting experimental data extracted from hydrogen permeation tests: III–Comparison with experimental results from the literature," *International Journal of Hydrogen Energy,* vol. 39, pp. 1145-1155, 2014.
[31] E. Akiyama and S. Li, "Electrochemical hydrogen permeation tests under galvanostatic hydrogen charging conditions conventionally used for hydrogen embrittlement study," *Corrosion Reviews,* vol. 34, pp. 103-112, 2016.
[32] J. K. Nørskov, T. Bligaard, A. Logadottir, J. Kitchin, J. G. Chen, S. Pandelov, *et al.*, "Trends in the exchange current for hydrogen evolution," *Journal of the Electrochemical Society,* vol. 152, pp. J23-J26, 2005.
[33] H. J. Flitt and D. P. Schweinsberg, "Evaluation of corrosion rate from polarisation curves not exhibiting a Tafel region," *Corrosion Science,* vol. 47, pp. 3034-3052, 2005.
[34] S. Chan, K. Khor, and Z. Xia, "A complete polarization model of a solid oxide fuel cell and its sensitivity to the change of cell component thickness," *Journal of power sources,* vol. 93, pp. 130-140, 2001.
[35] M. Mouanga, P. Berçot, and J. Takadoum, "Effect of residual stresses on hydrogen permeation in iron," *Corrosion Science,* vol. 52, 2010.
[36] B. Behzadian, D. Piron, C. Fan, and J. Lessard, "Electrocatalytic effect on hydrogen evolution from copper materials plated from a chloride-containing bath," *International journal of hydrogen energy,* vol. 16, pp. 791-796, 1991.
[37] B. Kumar, S. Saha, M. Basu, and A. K. Ganguli, "Enhanced hydrogen/oxygen evolution and stability of nanocrystalline (4–6 nm) copper particles," *Journal of Materials Chemistry A,* vol. 1, pp. 4728-4735, 2013.
[38] T. Zakroczymski, "Adaptation of the electrochemical permeation technique for studying entry, transport and trapping of hydrogen in metals," *Electrochimica Acta,* vol. 51, pp. 2261-2266, 2006.
[39] T. Zakroczymski and Z. Szklarska-Smialowska, "Activation of the iron surface to hydrogen absorption resulting from a long cathodic treatment in NaOH solution," *Journal of the Electrochemical Society,* vol. 132, pp. 2548-2552, 1985.
[40] L. Lan, X. Kong, Z. Hu, C. Qiu, D. Zhao, and L. Du, "Hydrogen permeation behavior in relation to microstructural evolution of low carbon bainitic steel weldments," *Corrosion Science,* vol. 112, pp. 180-193, 2016.
[41] E. Fallahmohammadi, F. Bolzoni, and L. Lazzari, "Measurement of lattice and apparent diffusion coefficient of hydrogen in X65 and F22 pipeline steels," *International journal of hydrogen energy,* vol. 38, pp. 2531-2543, 2013.
[42] Q. Liu and A. Atrens, "Reversible hydrogen trapping in a 3.5 NiCrMoV medium strength steel," *Corrosion Science,* vol. 96, pp. 112-120, 2015.
[43] A. Turnbull, "Perspectives on hydrogen uptake, diffusion and trapping," *International Journal of Hydrogen Energy,* vol. 40, pp. 16961-16970, 2015.
[44] S. Frappart, X. Feaugas, J. Creus, F. Thebault, L. Delattre, and H. Marchebois, "Study of the hydrogen diffusion and segregation into Fe–C–Mo martensitic HSLA steel using electrochemical permeation test," *Journal of Physics and Chemistry of Solids,* vol. 71, pp. 1467-1479, 2010.

[45] W. Choo, "Effect of cathodic charging current density on the apparent hydrogen diffusivity through pure iron," *Journal of materials science*, vol. 19, pp. 2633-2638, 1984.
[46] T. G. Namboodhiri and L. Nanis, "Concentration dependence of hydrogen diffusion in Armco iron," *Acta Metallurgica*, vol. 21, pp. 663-672, 1973.
[47] A. Turnbull, M. Carroll, and D. Ferriss, "Analysis of hydrogen diffusion and trapping in a 13% chromium martensitic stainless steel," *Acta Metallurgica*, vol. 37, pp. 2039-2046, 1989.
[48] G. Pressouyre, "A classification of hydrogen traps in steel," *Metallurgical and Materials Transactions A*, vol. 10, pp. 1571-1573, 1979.
[49] W. Choo and J. Y. Lee, "Thermal analysis of trapped hydrogen in pure iron," *Metallurgical and Materials Transactions A*, vol. 13, pp. 135-140, 1982.
[50] R. L. Thomas, D. Li, R. P. Gangloff, and J. R. Scully, "Trap-governed hydrogen diffusivity and uptake capacity in ultrahigh-strength AERMET 100 steel," *Metallurgical and Materials Transactions A*, vol. 33, pp. 1991-2004, 2002.
[51] L. Vecchi, D. Pecko, N. Van den Steen, M. H. Mamme, B. Özdirik, D. Van Laethem, *et al.*, "A modelling approach on the impact of an oxide layer on the hydrogen permeation through iron membranes in the Devanathan-Stachurski cell," *Electrochimica Acta*, 2018.
[52] J. Bouhattate, E. Legrand, and X. Feaugas, "Computational analysis of geometrical factors affecting experimental data extracted from hydrogen permeation tests: I–Consequences of trapping," *international journal of hydrogen energy*, vol. 36, pp. 12644-12652, 2011.
[53] T. Radhakrishnan and L. Shreir, "Hydrogen permeation through iron and steel by electrochemical transfer—II. Influence of metallurgical factors on hydrogen permeation," *Electrochimica Acta*, vol. 12, pp. 889-903, 1967.
[54] M. Devanathan and Z. Stachurski, "The mechanism of hydrogen evolution on iron in acid solutions by determination of permeation rates," *Journal of the electrochemical society*, vol. 111, pp. 619-623, 1964.
[55] S. Frappart, "Des éléments de compréhension sur les mécanismes de transport et de ségrégation de l'hydrogène dans les aciers martensitiques trempés et revenus à haute limite d'élasticité," Université de La Rochelle, 2011.
[56] E. Legrand, J. Bouhattate, X. Feaugas, and H. Garmestani, "Computational analysis of geometrical factors affecting experimental data extracted from hydrogen permeation tests: II–consequences of trapping and an oxide layer," *international journal of hydrogen energy*, vol. 37, pp. 13574-13582, 2012.

CHAPTER IV

Hydrogen permeation through deformed and heat-treated Armco iron*

IV.1 Introduction

Deformation phenomena in polycrystalline materials are relatively complex due to various interactions between dislocations and grain boundaries [1-3]. Additionally, changes take place in the density and distribution of mainly vacancies and dislocations. Vacancies in thermodynamic equilibrium are homogeneously distributed whereas dislocations show a strong tendency to cluster with progressive deformation [4, 5].

Darken and Smith [6] were the first to investigate the effect of cold work on hydrogen diffusion in low alloy steel. They observed a delay in the hydrogen diffusivity with increasing applied strain. The higher the applied strain, the more hydrogen traps, identified as microstructural defects, were introduced. As it is well known that with increasing strain the dislocation density increases in the material, the authors considered dislocations to be the hydrogen traps reducing the hydrogen diffusion coefficient. This observation has been confirmed by several other studies [7-10].

Dislocations were also considered as hydrogen traps by Kumnick *et al.* [7]. They observed a lower effective diffusion coefficient after deforming annealed Armco iron. The deformation induced traps were divided in two groups by the author: type 1 and type 2 traps. Type 1 traps were defined thermally stable as they could not be removed by a 1 hour annealing treatment at 850°C and were assigned to microvoids. On the other hand, almost all type 2 traps were removed by annealing the Armco iron at 400°C. In the temperature range where most of the type 2 traps disappeared, no change in hardness was measured and therefore, the dislocation density was expected to be constant. Hence, type 2 traps were not correlated to stress fields of isolated dislocations, but they were attributed to the dislocation configurations in the cell walls which changed during the recovery annealing treatment. Castaño-Rivera *et al.* [8] observed that these dislocation arrays are of low energy and are developed at high levels of plastic strain. These are traps where hydrogen is not easily evacuated and might be proportional to the density of arrays, i.e. to subgrain boundaries.

Some researchers also believe that the retarding effect of trapping sites on the hydrogen diffusivity is partially compensated by a phenomenon called pipe-diffusion. This is correlated with a higher hydrogen diffusivity along dislocations [11]. Kirchheim *et al.* [12] observed a higher diffusivity in deformed

* This chapter is based on the following publication: E. Van den Eeckhout, A. Laureys, Y. Van Ingelgem, and K. Verbeken, *Materials Science and Technology,* vol. 33, pp. 1515-1523, 2017.

palladium when the overall hydrogen concentration was very low. They assumed that the dislocation core provides lower energy sites for hydrogen, implying an enhanced diffusion along the dislocation pipe. When the hydrogen concentration increases, the dislocation core will have less hydrogen free sites, which are necessary for hydrogen transport, impeding hydrogen transport along the dislocation line. Castaño-Rivera *et al.* [13] also observed weak traps along a dislocation line which could serve as an easy path for hydrogen diffusion. However, these authors excluded the existence of pipe diffusion as hydrogen diffusion in bcc iron is fast enough.

Next to dislocations, it is generally recognized that microvoids, grain boundaries and vacancy clusters are also potential trapping sites for hydrogen [14]. Choo and Lee [15] indicated these trapping sites by thermal desorption spectroscopy and they claimed that microvoids are the main trapping site in pure iron. The hydrogen activation energy observed for grain boundaries, dislocations and microvoids in pure iron were 17.2 kJ/mol, 26.8 kJ/mol, and 35.2 kJ/mol, respectively. This was confirmed by Lee and Lee [16] who obtained energies of 26.04 kJ/mol for dislocations and 19.68 kJ/mol for grain boundaries. The effect of microvoids on the hydrogen diffusivity was studied by Wang *et al.* [17]. Microvoids decreased the hydrogen diffusivity through electroslag refined steel (0.2% C) with increasing volume of the microvoid, however, they did not retain hydrogen permanently.

Grain boundaries are quoted to be both trapping sites as well as diffusion sites, depending on the hydrogen binding energy. Lee *et al.* [18] and Mine *et al.* [10, 19] concluded that grain boundaries act as a fast diffusion path in face-centred cubic (fcc) metal and as trapping sites in a body-centred cubic (bcc) metal. The trapping behaviour in bcc iron has also been confirmed by many other authors [20-22]. Oudriss *et al.* [23] investigated the effect of grain size and grain boundaries on diffusion and trapping in pure nickel and observed that random high-angle grain boundaries are responsible for the acceleration of hydrogen diffusion. This is due to their disordered structure and their large excess in free volume in which hydrogen can diffuse more easily than in a crystalline structure. On the contrary, grain boundaries having low misorientations and some “special” boundaries are designated as hydrogen traps. These kinds of boundaries are accommodated by dislocations and vacancies which trap hydrogen, and thus, affect the diffusion mechanisms.

Besides impeding hydrogen diffusion in iron, the aforementioned microstructural heterogeneities are also suitable nucleation sites for hydrogen induced cracks. Such cracks develop when the material is excessively charged with hydrogen. At these heterogeneities, hydrogen can recombine, resulting in the formation of high pressure hydrogen gas bubbles [24, 25]. This phenomenon was clarified by the internal pressure theory by Zapffe and Sims [26] and Tetelman and Robertson [27]. When the internal hydrogen gas pressure reaches a certain threshold, plastic deformation takes place. Consequently, crack initiation and propagation can occur, even without an externally applied stress. When this phenomenon takes place just below the sample surface, the metal layer is lifted up by the gas pressure and a blister is formed [28]. As deformation introduces microstructural defects, it is expected that hydrogen induced cracks will develop more easily in highly deformed material.

With this study a deeper insight is obtained on the influence of dislocations and grain boundaries on the hydrogen diffusivity in pure Armco iron. Cold deformation and a recovery heat treatment were applied to vary the dislocation density and modify grain boundary characteristics. Observations reported in literature were validated and extra information was obtained by performing EBSD measurements and analysing blister behaviour of the materials. EBSD was used to elucidate microstructural features and their evolution, while blister tests were carried out to relate microstructural features to hydrogen damage initiation. Permeation tests were additionally performed to connect the observed results to the hydrogen diffusivity.

IV.2 Materials and methods

IV.2.1. Material characterization

The studied material was highly pure Armco iron delivered by AK Steel. Table IV-1 shows the chemical composition. To obtain different degrees of plastic deformation the as-received 4 mm hot rolled plate (AR) was cold rolled. Consequently, the plate was reduced in thickness by 10%, 50%, and 70%, labelled as A10, A50 and A70, respectively. The latter was heat treated in order to attain a recovered microstructure (H70). The plate was heated, in a nitrogen atmosphere, to 360°C and was kept there for approximately 1h. Subsequently, it was oven cooled to room temperature. The different materials were all characterized by light optical microscopy. For this purpose, samples were ground, polished (OPU) and etched with 2% Nital solution. The average grain size of the as-received iron was measured by the grain intercept method and the Vickers hardness of the materials was equally measured.

Table IV-1 Chemical composition Armco iron from AK steel.

Chemical composition, wt%											
C	Si	Mn	P	S	Al	Cr	Cu	Mo	N	Ni	Sn
0.001	0.003	0.050	0.004	0.003	0.002	0.013	0.007	0.002	0.003	0.011	0.002

IV.2.2. Determination of the hydrogen diffusion coefficient

To determine the diffusion coefficient, all microstructures were subjected to the permeation test method 1. Throughout the experiment, the ambient temperature was kept constant at 25°C. In both cell compartments, the electrolyte (0.1 M NaOH) was stirred using a nitrogen flow and in this way dissolved oxygen was removed. In this study, the sample was galvanostatically polarized using a cathodic current density of 3 mA/cm². In order to accomplish this oxidation reaction, the sample was anodically polarized applying a constant potential of -500 mV with respect to the reference electrode (Hg/Hg_2SO_4). The apparent hydrogen diffusion coefficient was calculated using the hydrogen oxidation current in combination with following formula:

$$D_{app,0.1} = \frac{L^2}{7.7t}\ (m^2 s^{-1}) \qquad \text{IV-1}$$

where t is the time (s) when the normalized steady-state value has reached 0.1 and L is the specimen thickness (m), which was kept constant at 1 mm. A more detailed description of the permeation test method 1 can be found in section II.1.

IV.2.3. Blister formation

Blisters were introduced on the surface with the same set-up described by Laureys *et al.* [29]. The 0.5 M H_2SO_4 water based electrolyte contained 1 g/l thiourea. All samples were charged at room temperature for 48 hours applying a current density of 10 mA/cm². After charging, all discs were cleaned with isopropanol and distilled water to remove possible surface deposits. Finally, the damaged surface was examined with optical microscopy.

IV.2.4. EBSD

EBSD (electron backscatter diffraction) was performed to obtain more information about dislocation densities and about low and high angle grain boundary lengths. The examinations were executed on the TD-plane. The samples were ground and polished up to 1 µm, followed by an additional step using colloidal silica (Struers OPU suspension). This final step was performed long enough to remove the layers affected by polishing with coarser particles. The SEM utilized for EBSD measurements was an FEI Quanta 450 with field emission gun (FEG). Following settings were applied: 20 kV acceleration voltage, emission current of 200 µA, specimen tilt of 70 degrees and a scan step size of 80 nm on a hexagonal scan grid. In this study, the Geometrically Necessary Dislocation (GND) density was calculated by the TSL-OIM Data Analysis V7 software. The GND density was calculated using local misorientations below 5 degrees and a second neighbour misorientation averaging. Before determination of the GND density a clean-up procedure of neighbour confidence index (CI) correlation was applied. CI quantifies the reliability of the indexed pattern and the minimum was set at 0.1. Also, the fractions of low and high angle grain boundaries were determined. Low angle grain boundaries (LAGB) were defined with a misorientation angle between 5 and 15 degrees, high angle grain boundaries (HAGB) above 15 degrees.

IV.3 Results and discussion

IV.3.1. Material characterization

The ferritic microstructures are shown in Figure IV-1. Rolling and normal directions are also indicated. AR and A10 have a grain size of approximately 30 µm. Due to the rolling process, grains became elongated (A50 and A70). It can be verified that no recrystallization occurred during the heat treatment as the grain structure remained intact. However, during the heat treatment, recovery processes can take place. Then, dislocations annihilate and reconfigure to structures with lower strain energies [30, 31]. In the case of small strains, the annealing causes the dislocations to rearrange into local bands, which may develop into a subgrain structure. In heavily deformed metals, on the other hand, an additional softening prior to the onset of recrystallization will take place which appears to be controlled by subgrain growth [32]. Figure IV-2 clearly shows that a higher amount of cold work increases the Vickers hardness, which can be mainly related to an increased dislocation density. The decrease in hardness after recovery is rather small, which implies that only limited dislocation annihilation occurred. The hardness values in Figure IV-2 represent averages of eight measurements taken along the cross section of the sample.

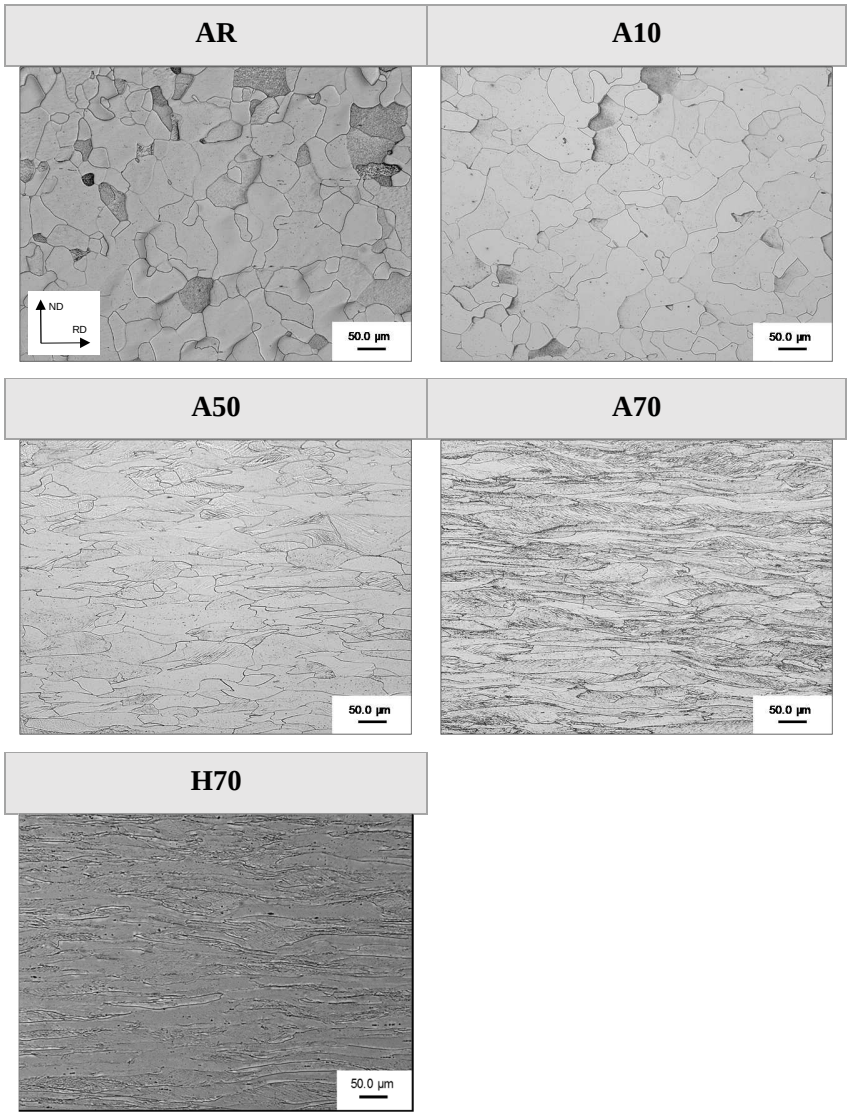

Figure IV-1 Microstructures of as-received, deformed and heat treated Armco iron.

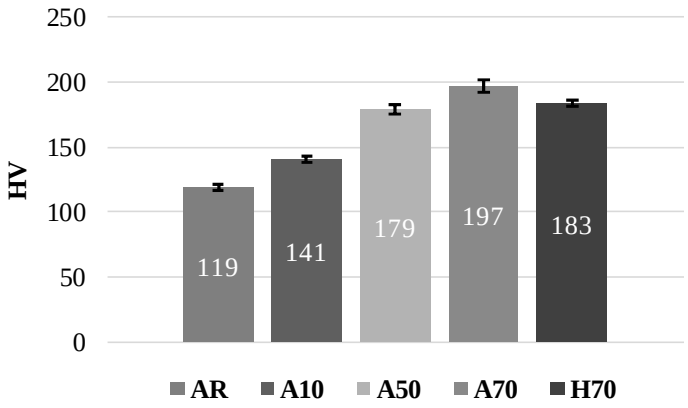

Figure IV-2 Hardness results (HV) of the Armco iron microstructures. The average of 8 measurements is given ± the standard error (SE).

IV.3.2. Determination of the hydrogen diffusion coefficient

Hydrogen permeation tests were performed and the apparent hydrogen diffusion coefficients were calculated. Coefficients and normalized permeation transients are depicted in Figure IV-3 and Figure IV-4, respectively. Due to the cold rolling process, the hydrogen diffusivity decreases with increasing deformation. As was already mentioned above, this deformation introduces extra lattice defects which can hinder the hydrogen diffusion through the material. The trapping ability of dislocations and grain boundaries has been observed by many other authors [7, 10, 18, 20, 25]. Next to dislocations, generated vacancies and microvoids also have the ability to hinder hydrogen diffusion [18, 33].

Castaño-Rivera *et al.* [8] studied hydrogen trapping in plastically deformed API 5LX60 steel. They correlated a lower hydrogen diffusivity not only to a higher trap density, but also to a higher trap binding energy. Deformation induced traps with a binding energy (E_b) higher than 35 kJ/mol were labelled as strong traps. These traps were correlated to carbides, microvoids, microcracks, vacancy aggregates and to special defects around dislocations with higher energy than to normal dislocation cores. Weak traps ($E_b < 35$kJ/mol) were more likely to be associated to stress fields around dislocations or second phase particles.

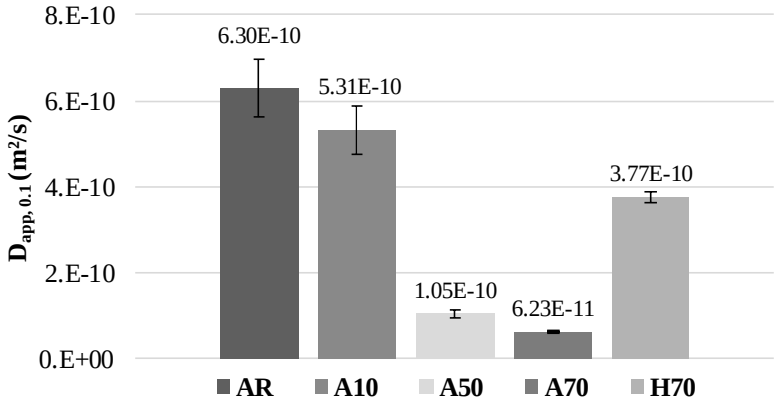

Figure IV-3 Apparent diffusion coefficients of Armco iron in specific cold deformed and cold deformed and annealed conditions.

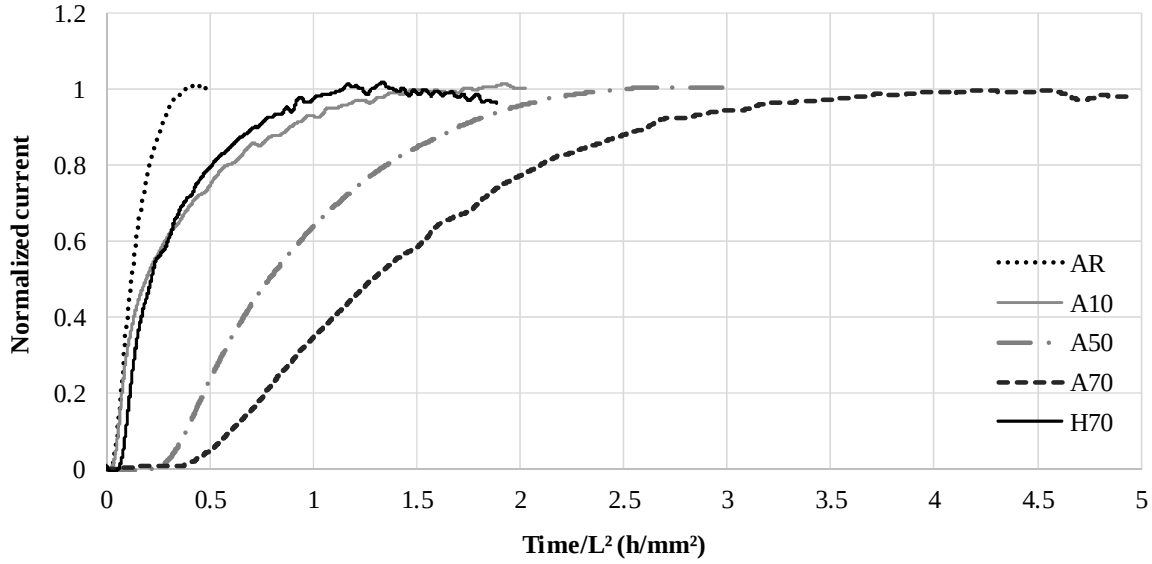

Figure IV-4 Permeation transients of Armco iron in specific cold deformed and cold deformed and annealed conditions. L is the sample thickness.

Comparing the apparent diffusion coefficient of AR and A10, no significant difference is observed. Hardness results, however, show a higher value for the A10 sample. Consequently, a higher amount of dislocations is expected, and the increased hardness can thus be related to this expectation. This higher amount of dislocations, however, apparently did not significantly influence the hydrogen diffusivity as determined by the permeation test. However, it should be mentioned that when such a small rolling reduction is applied, deformation is typically more concentrated in the A10 top surface layer. This layer was removed prior to the permeation test in order to obtain the required constant 1 mm thickness. Therefore, as the bulk of the material was largely unaffected by the cold rolling, this limited rolling reduction had almost no effect on the hydrogen diffusion coefficient.

The decrease in hydrogen diffusivity from AR to A50 can be attributed to an increased dislocation density. This was confirmed by Choo *et al.* [15] who also stated that when the deformation degree in iron is less than 50%, dislocations act as the major trapping sites. At higher degrees of cold work, microvoids were claimed to become more important [15]. Besides, the authors also confirmed, based on TDS results, that the dislocation density remains constant above 40% of cold work. In that context, the lower hydrogen diffusivity and higher hardness in A70 compared with A50 should be attributed to the creation of microvoids.

Next to dislocations, also an increased amount of vacancies may have contributed to the decreased diffusivity. By applying plastic deformation, a vacancy concentration larger than the thermal equilibrium concentration can be introduced in the material. The increased vacancy concentration caused by plastic deformation, taking into account the vacancy diffusion and annihilation, was theoretically estimated by Mecking and Estrin [34]. The excess vacancy concentration from the thermal equilibrium values was given as a function of temperature and strain rate. Even at low temperatures, they found a strong excess of vacancies. Although the additional vacancies can annihilate at sub-zero temperatures due to their high mobility, they are able to form vacancy agglomerates which have an elevated annihilation temperature in a range between 227-327°C [35]. In addition, vacancy clusters are reported to form during the cold rolling process [36]. As mentioned previously, the present vacancy clusters are capable of trapping hydrogen, and thus, lowering the hydrogen diffusivity [14, 37] .

It is clear from Figure IV-4 that after the heat treatment, comparing A70 with H70, the hydrogen diffusivity increases again, implying less hydrogen traps in the microstructure. In the case of H70, based on the hardness results, only a small decrease in the amount of lattice defects is observed. A completely recovered iron microstructure is obtained after annealing at higher temperatures (500°C) [38]. Based on the abovementioned work of Kumnick *et al.* [7], only a small decrease in dislocation density is expected, while microvoids are thermally stable. The higher hydrogen diffusion through H70 must therefore rather be related to the rearrangement of dislocations and internal stress relief than to a significant decrease in dislocation density. As stated by Kumnick *et al.* [7], during the recovery treatment, changes in the dislocation configurations in the cell walls take place. In the temperature range between 300 and 500°C, subgrain sizes increase and grains become less elongated. The mechanisms proposed by Lan *et al.* [31] indicate that subgrain growth takes place by subgrain boundary movement and coalescence of dislocations. Kumnick *et al.* [7] noted that the weak traps they observed in iron, related to a specific dislocation configuration, can be eliminated by a thermal treatment at temperatures where the dislocation density remains stable. Stronger traps were ascribed to heterogeneous sites along dislocation cores. Presumably, these traps cannot be removed by an annealing treatment at low temperatures.

Nagumo *et al.* [39] stated that for 60% plastically deformed pure iron, vacancy clusters are removed from the microstructure when annealing at 327°C. As such, the annihilation of vacancy clusters contributed to the observed increase in hydrogen diffusivity. However, this assumption was not verified. Other hydrogen traps such as microvoids can remain present. The specificities of the dislocation configuration explains on

the one hand the changes in hydrogen diffusion coefficient between A70 and H70, but, on the other hand, also confirms the lower hydrogen diffusivity in H70 as compared to the as-received Armco iron. As the dislocation density is an important parameter, an effort was done to quantify this microstructural feature by EBSD.

IV.3.3. EBSD

EBSD measurements were performed on the cross sections of the different samples. The GND density results, as determined with the TSL analysis software, are shown in Figure IV-5. AR and A10 show equal density, although the Vickers hardness increases from AR to A10 with 20 HV approximately. As mentioned above, the deformation is more concentrated in the top surface layer when such a small rolling reduction was applied. The EBSD measurements were taken in the bulk of the material, hence, no effect on the dislocation density could be expected. The higher hardness is thus related to a local increased GND density at the surface, to small misorientations in the microstructure or maybe to some statistically stored dislocations (SSDs). SSDs are randomly distributed in the material, have no geometrical consequence [40] and are therefore not detectable by EBSD [41]. This is in contrast with GNDs which are needed to preserve the lattice continuity through accommodating lattice misorientations [42]. With higher degrees of deformation, dislocation density increases significantly. Kumnick *et al.* [7] referred to the work of Keh *et al.* [43] who measured a dislocation density of approximately $2 \cdot 10^{10}$ m^{-2} after applying a deformation of about 40% and they suggested that dislocations have the ability to trap hydrogen, as the change in effective hydrogen diffusivity with deformation is similar in shape to the dislocation density vs % strain. It is clear that A70 shows a higher dislocation density compared to A50 which is in contradiction with the TDS results of Choo *et al.* [15], who claimed that the dislocation density remains constant above 40% of cold work. Thus, the lower hydrogen diffusivity and higher hardness in A70 compared with A50 can not only be attributed to the creation of microvoids, but also to a higher amount of dislocations.

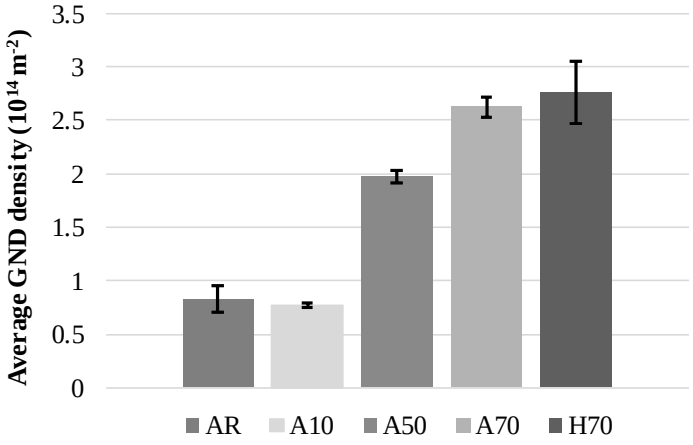

Figure IV-5 Average GND density (10^{14} m^{-2}) ± SE of Armco iron in specific cold deformed and cold deformed and annealed conditions.

After the annealing treatment, a higher hydrogen diffusion was expected due to the annihilation of vacancy clusters and to a decrease in dislocation density. However, although the difference between both values (A70 vs H70) is within the experimental error, EBSD does not indicate a change in GND density after annealing. The release of strain energy, which is quoted as the driving force for recovery [44], took place, but the material was definitely not fully recovered. This confirms that the higher hydrogen diffusivity in H70 must be due to other recovery processes than the annihilation of GNDs. The performed heat treatment thus mainly annihilates vacancy clusters, and no dislocation annihilation occurs. This was confirmed by Nagumo et al. [39] who stated that dislocations annihilate at about 527°C. The obtained results also explains the small hardness drop for H70. Kumnick *et al.* [7] correlated traps, which are removed by annealing in the recovery range between 100°C and 400°C, to the cellular dislocation structure caused by deformation. The fact that the local arrangement of dislocations can be altered during recovery to obtain a lower total elastic energy, even when dislocation density remains nearly the same, has also been stated by Vandermeer and Rath and by Stuwe *et al.* [45, 46]. These considerations imply that both the GND and SSD density remain unchanged.

Next to annihilation processes, subgrain formation can take place during the heat treatment. The latter is confirmed by the higher LAGB length fraction in H70 (Figure IV-6). The fraction was calculated using following formula:

$$LAGB\ length\ fraction = \frac{LAGB\ (\mu m)}{LAGB + HAGB\ (\mu m)}\, x\ 100\% \qquad \text{(IV-2)}$$

LAGBs were defined as boundaries with a misorientation angle between 5 and 15 degrees. These boundaries are often considered as consisting of an array of dislocations. This clear microstructural change due to annealing can affect the diffusivity of hydrogen through the material. The increased diffusivity after annealing can be related to the fact that LAGBs are sometimes considered as a diffusion path for hydrogen,

as a grain boundary corresponds to a higher free volume i.e. more space for hydrogen to diffuse [47]. Nevertheless, this is in contradiction with the research of Lee *et al.* [18] and Mine *et al.* [10, 19] discussed in the introduction who claimed grain boundaries slow down hydrogen diffusion. However, due to the dislocation reconfiguration which creates the LAGBs in the material, the microstructural area consisting of tangled dislocation structures, as commonly observed in highly deformed metals, decreases. This means that there is an increased amount of defect-free volume in the material after annealing although the number of GNDs after annealing remains equal and although there is just a small decrease in hardness. Consequently, there are less obstacles for hydrogen diffusion in the material and this explains the effect of annealing on the hydrogen diffusion coefficient.

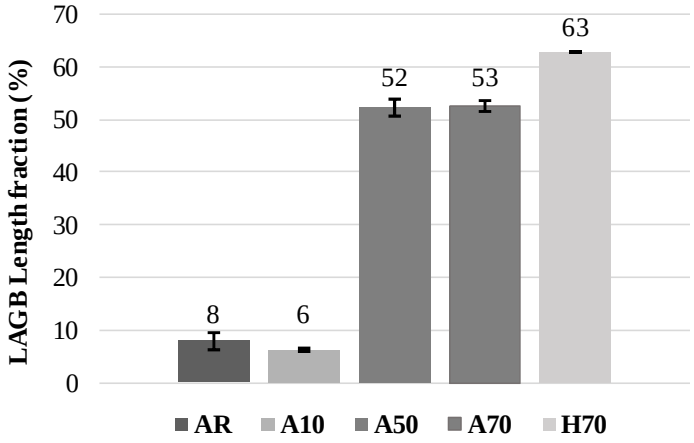

Figure IV-6 Length fraction (%) of the low angle grain boundaries with respect to the total grain boundary length. EBSD measurements were performed on the annealed, deformed and heat treated Armco iron.

IV.3.4. Blister formation

Blisters are formed due to hydrogen accumulation at microstructural defects such as dislocations and voids. Although the exact nucleation mechanism of a hydrogen blister is still under debate, it is related to the fact that when the accumulated absorbed hydrogen recombines to hydrogen gas and the critical pressure for plastic deformation and crack initiation is reached, a blister appears at the surface. On top of the visible surface blisters, internal cracks can be formed as well, as such also damaging the integrity of the material. As a result of the blister formation, the sample surface is severely damaged. In the present work, a previously developed routine for blister formation was applied on the materials under investigation [29, 48].

Figure IV-7 presents optical images of the sample surfaces after cathodic hydrogen charging. It is clear that more blisters are formed with increasing amount of cold deformation. Increased deformation introduces a larger amount of microstructural defects and internal stresses in the material. Clearly, the higher amount of microstructural defects provides a higher amount of potential blister nucleation sites, as can be correlated

with the increase in the number of blisters for the cold deformed samples. Once the critical hydrogen concentration in a specific hydrogen accumulation spot is reached, a blister is formed. The presence of internal stresses after cold deformation also implies that the critical pressure for plastic deformation and crack initiation is reached more easily, which gives rise to smaller blister sizes with increasing amount of cold deformation.

Comparing the A70 and H70 samples, significant differences in the amount and size of the blisters are observed. The surface of H70 contains only a few very large blisters while the A70 is covered with many small blisters. This confirms that the heat treatment has an effect on the microstructure and is responsible for recovery processes, such as a relief of the internal stresses. Indeed, as mentioned above, hydrogen diffusivity increases due to the heat treatment which indicates less microstructural defects, and thus, less potential blister initiation spots. The sample surface of H70 shows some very large blisters which corresponds with the limited amount of nucleation sites. It is also clear from the H70 sample surface in Figure IV-7 that small blisters are formed on top of the larger ones. Hoshihira *et al.* [49] observed in Al a higher hydrogen concentration in the material on the surface of blisters as compared to the non-blistered areas, while Griesche *et al.* [24] confirmed this observation for Armco iron. Once a large blister is formed, hydrogen is attracted to that highly stressed and plastically deformed area. Similarly to the cold deformed samples, multiple places for hydrogen to accumulate are formed due to the blister formation itself. Moreover, incoming hydrogen cannot easily diffuse away from the sample surface when it enters the material via a blistered surface as there is a crack underneath this area blocking its diffusion. Consequently, the critical hydrogen concentration to form additional blisters will be reached more rapidly [29, 50].

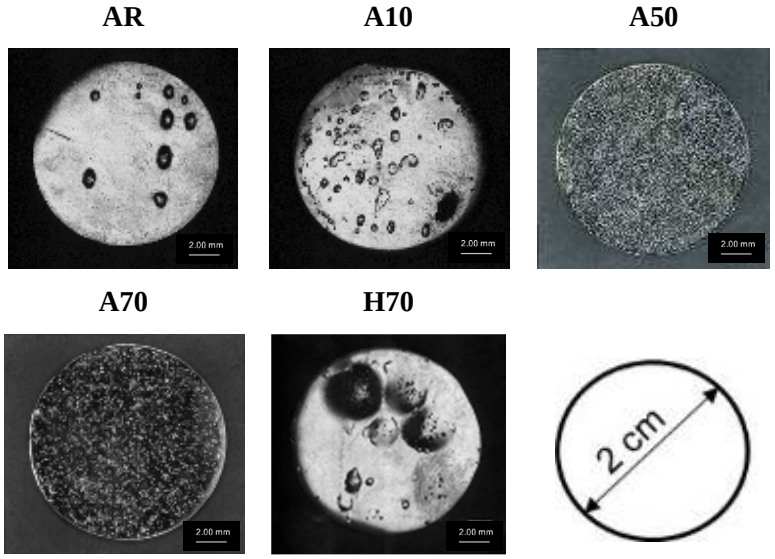

Figure IV-7 Blistered surfaces of the annealed and deformed Armco iron.

IV.4 Conclusion

In this work, the effect of cold deformation and subsequent annealing on hydrogen diffusion and blister formation was investigated and correlated with the accompanying changes in the material structure. A higher amount of deformation reduces the hydrogen diffusivity and results in a more heavily blistered sample surface. Microstructural changes induced by the cold deformation process are responsible for these observations as they create additional barriers for hydrogen diffusion and provide suitable nucleation places for blisters.

The recovery heat treatment results in rearrangements of the dislocation configurations as no decrease in geometrically necessary dislocation density is observed. The SSD density is considered to be constant as the hardness drop, due to the heat treatment, is rather small. This heat treatment causes an increased hydrogen diffusion coefficient and a decreased number of potential blister nucleation sites. Therefore, it is argued that the hydrogen diffusivity cannot be directly correlated with dislocation density, but rather with dislocation configuration and internal stresses.

IV.5 References

[1] T. Wider, S. Hansen, U. Holzwarth, and K. Maier, "Sensitivity of positron annihilation to plastic deformation," *Physical Review B*, vol. 57, p. 5126, 1998.

[2] K. Mostafa, F. G. Cámara, R. Petrov, P. R. Calvillo, E. De Grave, D. Segers, *et al.*, "Defect evolution during annealing of deformed FeSi alloys studied by positron annihilation spectroscopy," *Journal of Applied Physics*, vol. 109, p. 07E303, 2011.

[3] B. McKee, S. Saimoto, A. Stewart, and M. Stott, "Positron trapping at dislocations in copper," *Canadian Journal of Physics*, vol. 52, pp. 759-765, 1974.

[4] U. Essmann, "Elektronenmikroskopische Untersuchung der Versetzungsanordnung verformter Kupferein kristalle III. Bestimmung der Versetzungsdichte," *physica status solidi (b)*, vol. 17, pp. 725-737, 1966.

[5] H. Mughrabi, "Description of the dislocation structure after unidirectional deformation at low temperatures," *Constitutive Equations in Plasticity. Massachusetts Institute of Technology Press, Cambridge. 1975, 199-250*, 1975.

[6] L. S. Darken and R. P. Smith, "Behavior of Hydrogen in Steel During and After Immersion in Acid," *Corrosion*, vol. 5, pp. 1-16, 1949.

[7] A. Kumnick and H. Johnson, "Hydrogen transport through annealed and deformed Armco iron," *Metallurgical Transactions*, vol. 5, pp. 1199-1206, 1974.

[8] P. C. Rivera, V. Ramunni, and P. Bruzzoni, "Hydrogen trapping in an API 5L X60 steel," *Corrosion Science*, vol. 54, pp. 106-118, 2012.

[9] U. Bhat and H. Lloyd, "Effect of cold work on hydrogen in steel," *Journal of the iron and steel institute*, vol. 165, pp. 382-389, 1950.

[10] Y. Mine, Z. Horita, and Y. Murakami, "Effect of high-pressure torsion on hydrogen trapping in Fe–0.01 mass% C and type 310S austenitic stainless steel," *Acta Materialia*, vol. 58, pp. 649-657, 2010.

[11] K. Kiuchi and R. McLellan, "The solubility and diffusivity of hydrogen in well-annealed and deformed iron," *Acta Metallurgica*, vol. 31, pp. 961-984, 1983.

[12] R. Kirchheim, "Interaction of hydrogen with dislocations in palladium—I. Activity and diffusivity and their phenomenological interpretation," *Acta Metallurgica*, vol. 29, pp. 835-843, 1981.

[13] P. Castaño-Rivera, N. De Vincentis, R. Bolmaro, and P. Bruzzoni, "Relationship between Dislocation Densityand Hydrogen Trappingin a Cold Worked API 5L X60 Steel," *Procedia Materials Science*, vol. 8, pp. 1031-1038, 2015.

[14] S.-L. Chou and W.-T. Tsai, "Effect of grain size on the hydrogen-assisted cracking in duplex stainless steels," *Materials Science and Engineering: A,* vol. 270, pp. 219-224, 1999.
[15] W. Choo and J. Y. Lee, "Thermal analysis of trapped hydrogen in pure iron," *Metallurgical Transactions A,* vol. 13, pp. 135-140, 1982.
[16] J.-Y. Lee and J.-L. Lee, "A trapping theory of hydrogen in pure iron," *Philosophical Magazine A,* vol. 56, pp. 293-309, 1987.
[17] M. Wang and P. Shewmon, "A Study of the Effect of Voids on Hydrogen Diffusion Through Electroslag Refined Steel," in *Hydrogen Embrittlement: Prevention and Control*, ed: ASTM International, 1988.
[18] J.-Y. Lee and S. Lee, "Hydrogen trapping phenomena in metals with BCC and FCC crystals structures by the desorption thermal analysis technique," *Surface and Coatings Technology,* vol. 28, pp. 301-314, 1986.
[19] Y. Mine, K. Tachibana, and Z. Horita, "Grain-boundary diffusion and precipitate trapping of hydrogen in ultrafine-grained austenitic stainless steels processed by high-pressure torsion," *Materials Science and Engineering: A,* vol. 528, pp. 8100-8105, 2011.
[20] D. Yao and W. Chen, "Hydrogen trapping phenomenon at grain boundaries in a 18Ni maraging steel," *Chin J Met Sci Technol,* vol. 6, pp. 200-205, 1990.
[21] D. P. Escobar, T. Depover, L. Duprez, K. Verbeken, and M. Verhaege, "Combined thermal desorption spectroscopy, differential scanning calorimetry, scanning electron microscopy and X-ray diffraction study of hydrogen trapping in cold deformed TRIP steel," *Acta Materialia,* vol. 60, pp. 2593-2605, 2012.
[22] H. Addach, P. Berçot, M. Rezrazi, and J. Takadoum, "Study of the electrochemical permeation of hydrogen in iron," *Corrosion Science,* vol. 51, pp. 263-267, 2009.
[23] A. Oudriss, J. Creus, J. Bouhattate, E. Conforto, C. Berziou, C. Savall, *et al.*, "Grain size and grain-boundary effects on diffusion and trapping of hydrogen in pure nickel," *Acta Materialia,* vol. 60, pp. 6814-6828, 2012.
[24] A. Griesche, E. Dabah, T. Kannengiesser, N. Kardjilov, A. Hilger, and I. Manke, "Three-dimensional imaging of hydrogen blister in iron with neutron tomography," *Acta Materialia,* vol. 78, pp. 14-22, 2014.
[25] J.-L. Lee and J.-Y. Lee, "The effect of lattice defects induced by cathodic hydrogen charging on the apparent diffusivity of hydrogen in pure iron," *Journal of materials science,* vol. 22, pp. 3939-3948, 1987.
[26] C. Zapffe and C. Sims, "Hydrogen embrittlement, internal stress and defects in steel," *Trans. AIME,* vol. 145, pp. 225-271, 1941.
[27] A. Tetelman and W. Robertson, "The mechanism of hydrogen embrittlement observed in iron-silicon single crystals," DTIC Document 1961.
[28] D. P. Escobar, C. Minambres, L. Duprez, K. Verbeken, and M. Verhaege, "Internal and surface damage of multiphase steels and pure iron after electrochemical hydrogen charging," *Corrosion Science,* vol. 53, pp. 3166-3176, 2011.
[29] A. Laureys, R. Petrov, and K. Verbeken, "Internal and surface damage after electrochemical hydrogen charging for ultra low carbon steel with various degrees of recrystallization," *Procedia Structural Integrity,* vol. 2, pp. 541-548, 2016.
[30] W. D. Callister and D. G. Rethwisch, *Materials science and engineering: an introduction* vol. 7: Wiley New York, 2007.
[31] Y. Lan, H. Klaar, and W. Dahl, "Subgrain growth in armco-iron during recovery," *Scripta metallurgica et materialia,* vol. 24, pp. 2459-2463, 1990.
[32] K. Mostafa, P. Calvillo, J. De Baerdemaeker, K. Verbeken, C. Palacio, D. Segers, *et al.*, "Physical, microstructural and mechanical study of isochronal annealing of deformed commercial iron," *Journal of Alloys and Compounds,* vol. 656, pp. 378-382, 2016.
[33] M. Nagumo, "Hydrogen related failure of steels–a new aspect," *Materials Science and Technology,* vol. 20, pp. 940-950, 2004.
[34] H. Mecking and Y. Estrin, "The effect of vacancy generation on plastic deformation," *Scripta Metallurgica,* vol. 14, pp. 815-819, 1980.
[35] A. Vehanen, P. Hautojärvi, J. Johansson, J. Yli-Kauppila, and P. Moser, "Vacancies and carbon impurities in α-iron: electron irradiation," *Physical review B,* vol. 25, p. 762, 1982.
[36] H. F. Mohamed, J. Kwon, Y.-M. Kim, and W. Kim, "Vacancy-type defects in cold-worked iron studied using positron annihilation techniques," *Nuclear Instruments and Methods in Physics Research Section B: Beam Interactions with Materials and Atoms,* vol. 258, pp. 429-434, 2007.
[37] M. Nagumo, M. Nakamura, and K. Takai, "Hydrogen thermal desorption relevant to delayed-fracture susceptibility of high-strength steels," *Metallurgical and Materials Transactions A,* vol. 32, pp. 339-347, 2001.

[38] A. Rollett, F. Humphreys, G. S. Rohrer, and M. Hatherly, *Recrystallization and related annealing phenomena*: Elsevier, 2004.
[39] M. Nagumo, *Fundamentals of hydrogen embrittlement*: Springer, 2016.
[40] U. Kocks, "A statistical theory of flow stress and work-hardening," *Philosophical Magazine,* vol. 13, pp. 541-566, 1966.
[41] J. Jiang, T. Britton, and A. Wilkinson, "Measurement of geometrically necessary dislocation density with high resolution electron backscatter diffraction: effects of detector binning and step size," *Ultramicroscopy,* vol. 125, pp. 1-9, 2013.
[42] M. Ashby, "The deformation of plastically non-homogeneous materials," *Philosophical Magazine,* vol. 21, pp. 399-424, 1970.
[43] A. S. KEH, *Direct observation of imperfections in crystals*. New York: Interscience Publishers, 1962.
[44] J.-L. Lee, J. T. Waber, Y.-K. Park, and J. De Hosson, "Stages in the recovery of deformed single crystals of iron studied by position annihilation techniques," *Materials Science and Engineering,* vol. 81, pp. 379-390, 1986.
[45] H. Stüwe, A. Padilha, and F. Siciliano, "Competition between recovery and recrystallization," *Materials Science and Engineering: A,* vol. 333, pp. 361-367, 2002.
[46] R. Vandermeer and B. Rath, "Interface migration during recrystallization: the role of recovery and stored energy gradients," *Metallurgical Transactions A,* vol. 21, pp. 1143-1149, 1990.
[47] W. D. C. a. D. G. Rethwisch, *Materials Science and Engineering An Introduction,* Seventh edition ed.: John Wiley & Sons, 2011.
[48] D. P. Escobar, T. Depover, E. Wallaert, L. Duprez, M. Verhaege, and K. Verbeken, "Thermal desorption spectroscopy study of the interaction between hydrogen and different microstructural constituents in lab cast Fe–C alloys," *Corrosion Science,* vol. 65, pp. 199-208, 2012.
[49] T. Hoshihira, T. Otsuka, and T. Tanabe, "Visualization of hydrogen distribution around blisters by tritium radio-luminography," *Journal of Nuclear Materials,* vol. 386, pp. 776-779, 2009.
[50] A. Laureys, E. Van den Eeckhout, R. Petrov, and K. Verbeken, "Effect of deformation and charging conditions on crack and blister formation during electrochemical hydrogen charging," *Acta Materialia,* 2017.

CHAPTER V

The effect of microstructural characteristics on the hydrogen permeation transient in quenched and tempered martensitic alloys*

V.1 Introduction

Steels subjected to high stresses and with a large number of potential fracture initiation sites, show high susceptibility to the hydrogen embrittlement phenomenon [1-4]. This arises questions concerning the promising advanced high strength steels for many types of applications. Therefore, during the last decade, much research has been done on the hydrogen interaction with these high strength steels [3, 5-9]. Depover *et al.* [3] examined the hydrogen induced ductility loss of four different high strength steels, i.e. a Transformation Induced Plasticity (TRIP), Dual Phase (DP), Ferritic Bainitic (FB), and a High Strength Low Alloy (HSLA) steel. All materials showed a considerable degree of HE except for the HSLA steel, which was almost unaffected by hydrogen. This satisfying result was attributed to the beneficial effect of Ti- and Nb- carbonitrides and led to the conclusion that the investigation of the hydrogen interaction with different carbides in a metal matrix is of crucial importance to comprehend the hydrogen related issues. However, due to the complex microstructure of the abovementioned commercial steel grades, simplified microstructures are required as they allow a more straightforward interpretation of the hydrogen related phenomena.

Next to precipitation hardening increasing the strength of the material, precipitates are indeed also considered to be beneficial hydrogen trapping sites. Since they lower the amount of harmful highly diffusible hydrogen, the susceptibility of the material to HE is decreased [10, 11]. However, when trapping sites have irreversible hydrogen trapping characteristics, they lose their effectiveness once they are filled [12]. Consequently, deep trapping sites are only beneficial when the hydrogen charging is not continuous but only a one-off event such as in welding, material processing or electroplating. TiC and NbC precipitates in low alloy steels are examples of particles that act as deep trapping sites capturing hydrogen with a very low release rate. Hence, the probability for hydrogen to reach possible cracking initiation places is drastically reduced. The ideal trap site for decreasing the susceptibility to HE has a very large hydrogen desorption activation energy together with a small activation energy for hydrogen to enter the trap site [13].

Hydrogen diffusion through a metal is one of the main factors that determines the HE behaviour. Therefore, permeation experiments have been used to study hydrogen diffusion properties and the corresponding HE phenomenon [14, 15]. Although electrochemical charging changes the surface conditions of the metallic

* This chapter is based on the following publication: E. Van den Eeckhout, T. Depover, and K. Verbeken, *Metals* ***2018***, 8, 779.

specimen and the measured hydrogen diffusivity does perhaps not fully reflect the actual diffusion taking place in the substrate, permeation tests can provide valuable information concerning trapping sites, for instance when materials with different microstructural features are compared. It should be noted that a comparative study is only valid when the materials are tested in one set of experimental conditions as the apparent diffusion coefficient (D_{app}) may depend on the applied experimental parameters of the permeation test set-up, as clearly demonstrated in chapter III.

Grain boundaries, dislocations, precipitates and vacancies are among the microstructural features which affect the hydrogen diffusivity. Based on their hydrogen desorption activation energy, these traps are commonly classified as reversible or irreversible ones. Carbides like TiC and NbC are examples of potential irreversible traps in contrast with dislocations and grain boundaries, which are considered to be reversible ones [16-18]. It is generally known that all of these trapping sites decrease the diffusion of hydrogen, as evaluated by the permeation technique [19, 20]. Sakamoto and Hanada [21] observed a decrease of the D_{app} by tempering a martensitic stainless steel in the tempering range of 300 – 550°C. This decrease was correlated to the precipitation of Cr-containing carbides which were coherent with the ferritic matrix. As such, micro strains, i.e. dislocations, were introduced acting predominantly as trapping sites for hydrogen and decreasing the hydrogen diffusivity. When tempering at higher temperatures, coherency was lost and the diffusion rate through the microstructure increased again.

Whether a certain trap is beneficial for the HE susceptibility depends on the trap release rate, residual stresses in the metal matrix and hydrogen concentration [22]. V_4C_3 carbides, for example, contain an empty carbon site which may act as a hydrogen trap next to traps at the interface between the matrix and precipitates. However, in the work of Depover *et al.* [23], their presence increased the HE susceptibility. This observation was attributed to the higher hydrogen concentration, upon saturation level, in the carbide containing material compared to the as-quenched condition where no V-based carbides were present. Nevertheless, Nagao *et al.* [12] showed that a high density of nanosized (Ti,Mo)C precipitates had the ability to trap hydrogen and as such improved the hydrogen resistance of a high-strength tempered lath martensitic steel. Moreover, Spencer and Duquette [24] stated that Mo_2C is a beneficial hydrogen trap with respect to decrease the HE susceptibility. Their findings were confirmed by Depover and Verbeken [25].

This chapter discusses the influence of W_2C, $Cr_{23}C_6$, TiC and V_4C_3, respectively, together with other potential trapping features in the microstructure, on the permeation transient and hydrogen diffusivity. Therefore, input was beneficially used from earlier extensive work on the trapping ability of the different carbide containing materials via thermal desorption spectroscopy (TDS) and hot extraction results [23, 25-29]. The permeation transients were compared with these results to thoroughly evaluate the hydrogen diffusivity in the different materials. Very relevant to indicate is the fact that the alloy processing as well as all experimental analysis was executed in an identical and systematic way to allow a fair comparison of the different materials.

V.2 Experimental procedure

V.2.1. Materials

Four laboratory Fe-C-X alloys with a stoichiometric amount of a ternary alloying element (=X) were cast and processed. The chemical composition is given in Table V-1. To avoid nitride formation, Al was added. The different steel grades were produced in a Pfeiffer VSG100 vacuum melting and casting unit, operating under an argon gas atmosphere. After hot rolling until 1.5 mm, an appropriate heat treatment was applied to obtain a quenched and tempered (Q&T) microstructure in which carbides were introduced. At first, an austenitizing treatment at 1250°C for 10 minutes was performed and was followed by brine water quenching. This procedure was carried out to obtain a complete martensitic structure and to dissolve as much as possible of the existing carbides from the materials processing. The Q&T state of all materials, except for the Cr-alloy, was obtained by a tempering treatment of 1 hour at 600°C, followed by brine quenching. For the Fe-C-Cr alloy the tempering was carried out at 550°C. These temperatures were chosen based on the most outspoken secondary hardening effect due to carbide formation. The hardness profiles versus different tempering temperatures illustrating this behaviour can be found elsewhere [23, 26, 27, 29]. Transmission electron microscopy (TEM) was carried out to characterize the carbides in terms of their size, distribution and morphology. Diffraction patterns were further taken to identify the tempered induced precipitates, for which we refer to the corresponding works [23, 26, 27, 29]. The carbides were identified as W_2C, $Cr_{23}C_6$, TiC and V_4C_3, respectively.

Table V-1 Chemical composition of the different alloys in wt%.

Alloy Fe-C-X	C	X	Other
Fe-C-W	0.277	8.700	200-300 ppm Al
Fe-C-Cr	0.184	2.200	
Fe-C-Ti	0.313	1.340	
Fe-C-V	0.286	1.670	

V.2.2. Determination of the hydrogen diffusion coefficient

To determine the diffusion coefficient, all alloys were subjected to the permeation test method 1 (section II.1). In both cell compartments, the electrolyte (0.1 M NaOH) was stirred using a nitrogen flow and as such, the amount of dissolved oxygen was minimized. Throughout the experiment, the ambient temperature was kept constant at 25°C. The polished sample was polarized in a cathodic manner at the left side of the set-up by applying a constant cathodic current density of 3 mA/cm². In this way, a hydrogen flux was produced by following reaction:

$$H_2O + e^- \rightarrow OH^- + H_{ads} \qquad \text{V-1}$$

The subsequently absorbed hydrogen diffused through the sample to the anodic cell. There, the hydrogen was oxidized, producing an external current recorded by a Versastat 3F potentiostat. In order to accomplish this oxidation reaction, i.e. the reversed reaction of V-1, the sample was anodically polarized by applying a constant potential of -500 mV with respect to the reference electrode (Hg/Hg_2SO_4, +650mV vs SHE). $D_{app,\ 0.1}$ was calculated using the hydrogen oxidation current in combination with following formula:

$$D_{app,\ 0.1} = \frac{L^2}{7.7t} \qquad \text{V-2}$$

Where $D_{app,\ 0.1}$ is the apparent diffusion coefficient (m^2/s), t the time (s) when the normalized steady-state value has reached a value of 0.1 and L the specimen thickness (m), which was about 1 mm.

V.2.3. Hot extraction

Hot extraction experiments were performed to determine the diffusible hydrogen (H_{diff}) content. Hydrogen was introduced in the specimen by electrochemical pre-charging for one hour using a 0.5 M H_2SO_4 electrolyte containing 1 g/l thiourea at a current density of 0.8 mA/cm^2. During the charging step no internal damage was detected and no blisters appeared at the surface [30, 31]. Subsequently, the sample was rinsed and dried with water and ethanol, respectively, and was placed in a pre-heated oven at 300°C for 15 minutes. As such, the effusing hydrogen was measured by a thermal conductivity detector [29].

V.2.4. Thermal desorption spectroscopy

Thermal desorption spectroscopy (TDS) analysis was executed on all materials to characterize the hydrogen trapping sites and their corresponding activation energies. Samples were charged with hydrogen by electrochemical pre-charging for one hour using a 1 g/l thiourea in a 0.5 M H_2SO_4 electrolyte at a current density of 0.8 mA/cm^2. Three different heating rates (200°C/h, 600°C/h and 1200°C/h) were used. The desorption activation energy E_a of the hydrogen traps was calculated by equation V-3 which is a simplification of the original Kissinger formula [32]:

$$\frac{d\left(ln\frac{\phi}{T_{max}^2}\right)}{d\left(\frac{1}{T_{max}}\right)} = -\frac{E_a}{R} \qquad \text{V-3}$$

where ϕ is the heating rate (K/min), T_{max} (K) the TDS peak temperature, R ($J{\cdot}K^{-1}{\cdot}mol^{-1}$) the universal gas constant and E_a (J/mol) the detrapping activation energy for the hydrogen trap associated with T_{max}. The

peak temperatures were determined by deconvolution of the TDS results and $ln(\frac{\phi}{T_{max}^2})$ vs (T_{max}^{-1}) was plotted in order to calculate the corresponding E_a.

Although the hydrogen charging conditions for hot extraction and TDS experiments differ from permeation tests, the resulting trends can be compared as the relative behaviour of the different alloys with respect to each other is of main importance. In permeation tests, where long charging times are required, a sulfuric acid based electrolyte is too severe affecting the entrance side of the specimen in a way that can lead to inaccurate measurements. In contrast with the hydrogen charging conditions for hot extraction and TDS experiments, a higher amount of hydrogen could be obtained upon saturation level when using an electrolyte having a higher activity. This higher H concentration allows a straightforward analysis and subsequent evaluation of the available hydrogen trapping sites present in the material.

V.3 Results and discussion

Structures, sizes and size distributions of the carbides present in the different alloys were determined. The hydrogen diffusivity of the different materials was measured by the permeation technique and the permeation transient was analysed. Hot extraction results were given to evaluate to the slope of the permeation curve. TDS spectra are shown and, in order to attain more information concerning the overall trapping ability of the different carbides, permeation and TDS results were compared.

V.3.1. Material characterization

Tempered martensitic materials were studied in which precipitates were induced during tempering. A martensitic matrix was observed for all different alloys. The four types of carbides were W_2C, $Cr_{23}C_6$, TiC and V_4C_3 which are presented in Figure V-1. Their corresponding size distribution maps are shown in Figure V-2. Particles with sizes less than 10 nm were observed in all alloys, except for Fe-C-W, where the particles were between 20 and 50 nm. In Fe-C-Cr, a broad variety of carbides with sizes ranging from 0 to 200 nm were identified. Next to large (>100 nm) incoherent carbides, remaining from the material processing and undissolved during austenitizing, Fe-C-Ti also showed tempered induced carbides having a maximum size of 30 nm. Finally, Fe-C-V only contained nano-sized carbides smaller than 20 nm.

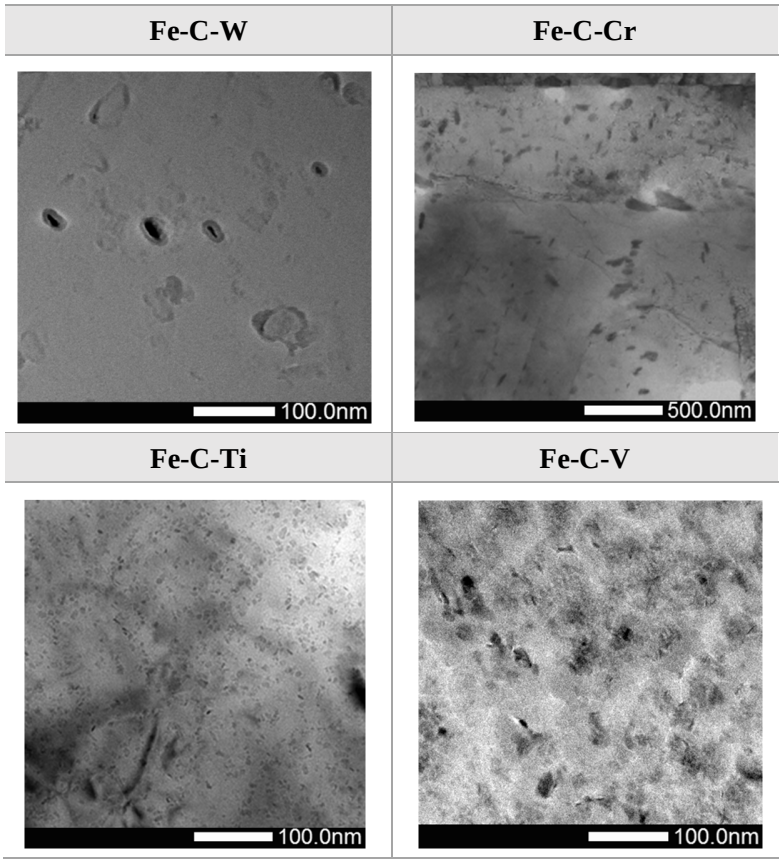

Figure V-1 TEM images of the different alloys.

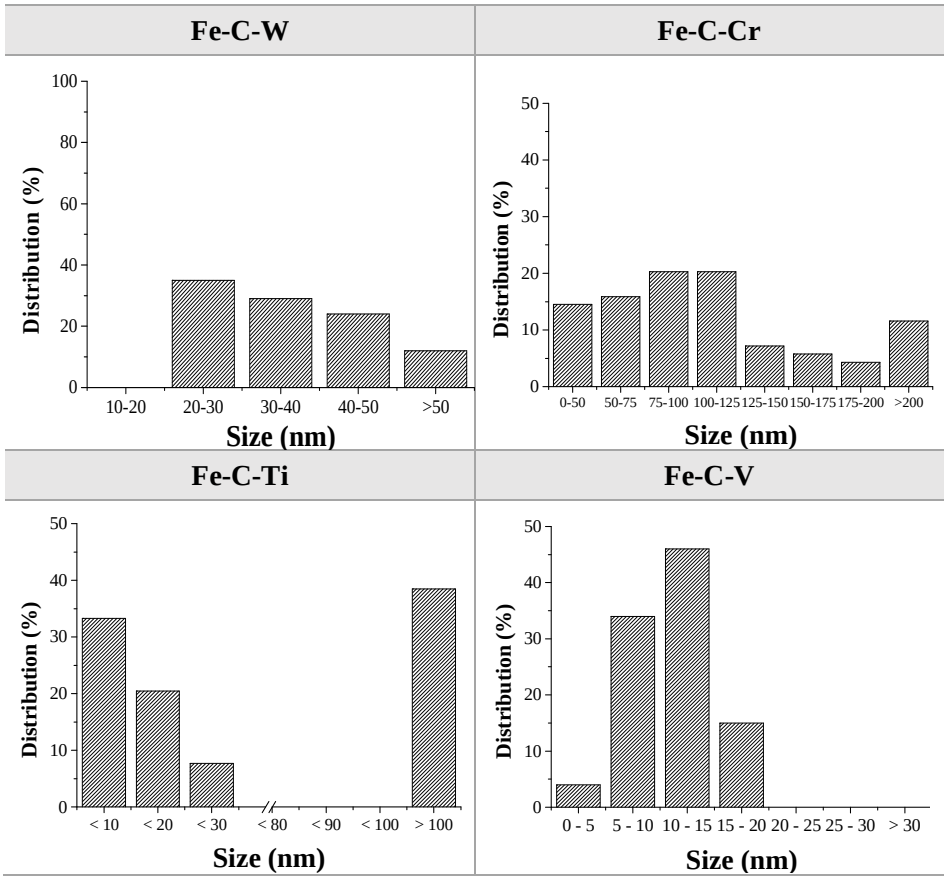

Figure V-2 Carbide size distributions for the different alloys.

V.3.2. Determination of the hydrogen diffusion coefficient

The permeation test results are represented in Figure V-3. The normalized current is plotted vs time/L^2 in order to eliminate the dependence of experimental data on the maximum current and minor variations in sample thickness. Apparent diffusion coefficients are given in Table V-2. The hydrogen diffusion slowed down in following order: Fe-C-W, Fe-C-Cr, Fe-C-Ti, Fe-C-V. A delay in the permeation curve was caused by a higher trap density, which could be associated with a higher hydrogen breakthrough time [33]. As such, Figure V-3 indicates that the W-containing alloy contained the lowest trap density, whereas the V-containing alloy showed the highest. As mentioned in the introduction, two different kinds of trapping sites may be present in the material: reversible and/or irreversible ones. Microstructural defects such as dislocations, grain boundaries in the Fe-matrix are examples of reversible trapping sites. At these sites, the residence time of hydrogen at room temperature is relatively low. Reversible traps, also called weak traps, are characterized by their low activation energies (E_a) with hydrogen. In this research, the E_a boundary between reversible and irreversible sites was selected to be 60 kJ/mol, based on the work of Dadfarnia *et al.* [34] and Depover and Verbeken [29]. Strong trapping sites, with higher activation

desorption energies, are quickly saturated when hydrogen enters the material as hydrogen is attracted to regions having a large chemical potential well. This was confirmed by Dadfarnia *et al.* [34], who showed that diffusible hydrogen is consumed from the matrix to saturate the strongest traps first before it is available to fill up the weak traps and before it continues to diffuse to other locations. Hence, it is believed that the overall trap density shifts the permeation curve by increasing the delay of the curve, i.e. the hydrogen breakthrough time. In addition, the presence of strong traps will have a higher impact on the decrease in hydrogen diffusivity compared to the reversible ones [35].

Next to the delay of the permeation curve, the slope is influenced by the material's trapping sites. It is clear from Figure V-3 that the slope of Fe-C-W and Fe-C-Cr is much steeper compared to the other two alloys. In other words, from hydrogen breakthrough, it takes less time to reach the steady state value. Several authors claim this is due to a lower hydrogen trap density [33, 34, 36-39]. As mentioned in the previous paragraph, strong traps will be saturated quickly once hydrogen enters the material and in combination with a very low hydrogen release rate at room temperature, they will not necessarily affect the shape of the permeation transient [40]. Reversible trapping sites are thus considered to be the main features affecting the slope of the curve. The time, from hydrogen breakthrough, needed to reach the normalized or experimental steady state value increases in the following order: Fe-C-W, Fe-C-Cr, Fe-C-Ti, Fe-C-V. Therefore, the Fe-C-V alloy is assumed to contain the highest reversible trap density. This statement will be evaluated in the next section on the interaction between hydrogen and the materials, as evaluated by hot extraction and TDS, to assess the influence of the tempered induced carbides on the obtained D_{app}.

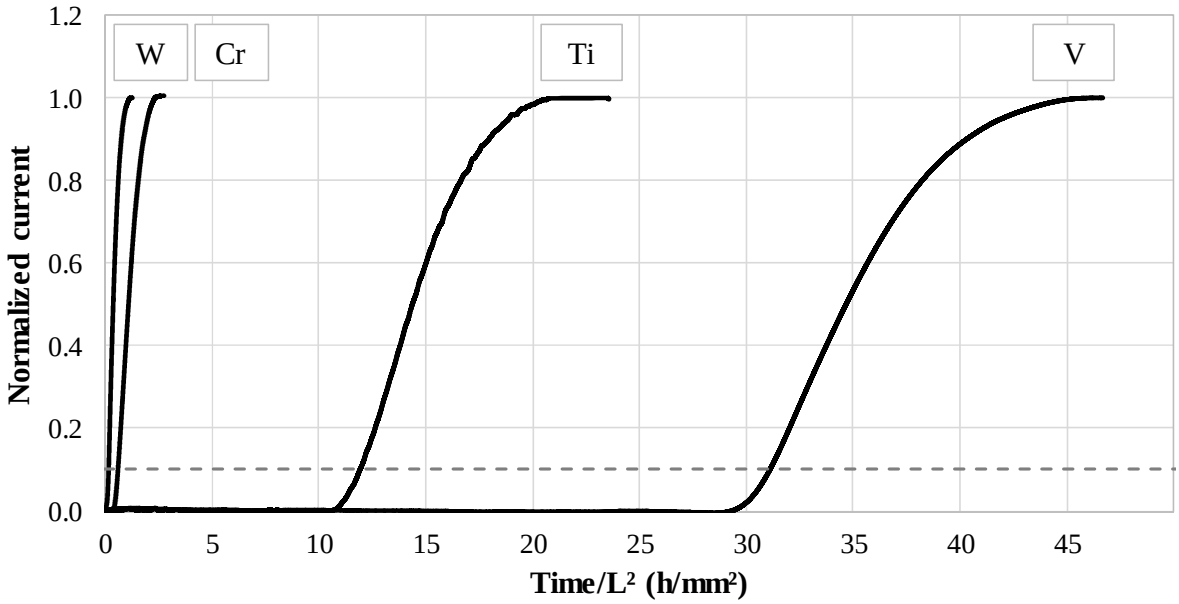

Figure V-3 Normalized permeation transients for the different materials.

Table V-2 Hydrogen apparent diffusion coefficients of the different materials.

Alloy	$D_{app,\ 0.1}$ (m^2/s)
Fe-C-W	7.21E-11
Fe-C-Cr	5.78E-11
Fe-C-Ti	3.02E-12
Fe-C-V	1.16E-12

V.3.3. Evaluation of the hydrogen trapping ability

The diffusible hydrogen (H_{diff}) amount measured by the hot extraction technique represents mainly reversibly trapped hydrogen. Figure V-4 presents this amount of diffusible hydrogen plotted together with the time between the breakthrough time and the moment the steady state condition is reached. This time allows to evaluate the slope of the permeation transient. The H_{diff} amount increases in the alloys as follows: Fe-C-W, Fe-C-Cr, Fe-C-Ti, Fe-C-V and a good correlation was observed with the transient slope. This confirms the high influence of weak traps on the slope of the permeation transient.

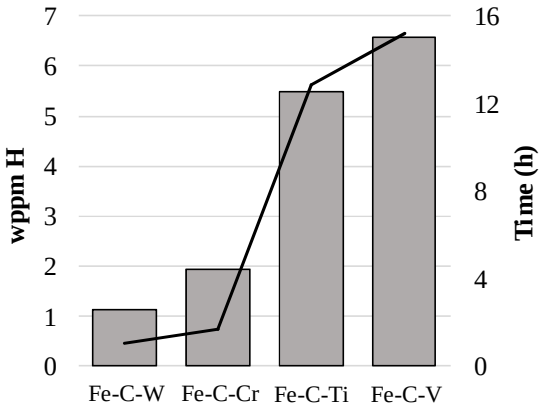

Figure V-4 H_{diff} obtained by hot extraction in wppm (grey bars) and the time (h) from hydrogen breakthrough till the steady state condition is reached (black line).

To determine the trapping characteristics of the tempered induced carbides, TDS analysis was performed for the different alloys. The TDS spectra together with their deconvoluted peaks are shown in Figure V-5. Every peak corresponds with a specific activation energy and can be attributed to different trapping sites in the material matrix. These energies are also incorporated in Figure V-5. The first peak of all spectra can be correlated to dislocations or martensitic lath boundaries, as both show similar value of E_a. Nevertheless, based on the work of Pérez Escobar *et al.* [41], the first peak may be attributed to hydrogen trapped solely at the martensitic lath boundaries. The authors demonstrated that hydrogen trapped by dislocations in pure iron was released from the sample during the 1 hour needed to obtain the required vacuum before the start of the TDS measurement. However, the diffusion of hydrogen in pure iron is much faster compared to the quenched and tempered structure investigated in this work. It may thus be possible that there is still some

hydrogen remaining at the dislocation trapping sites. Therefore, Depover and Verbeken [42] further evaluated this hypothesis by increasing the dislocation density in alloys having a martensitic structure. The higher dislocation density could not be detected by the TDS equipment which needed 1 hour to attain the required vacuum, while an increase of hydrogen was observed by hot/melt extraction, which was carried out only one minute after charging. Hence, the first peak of the TDS spectra was attributed to the martensitic lath boundaries, whereas the hydrogen trapped at dislocations was already released before the start of the TDS measurement.

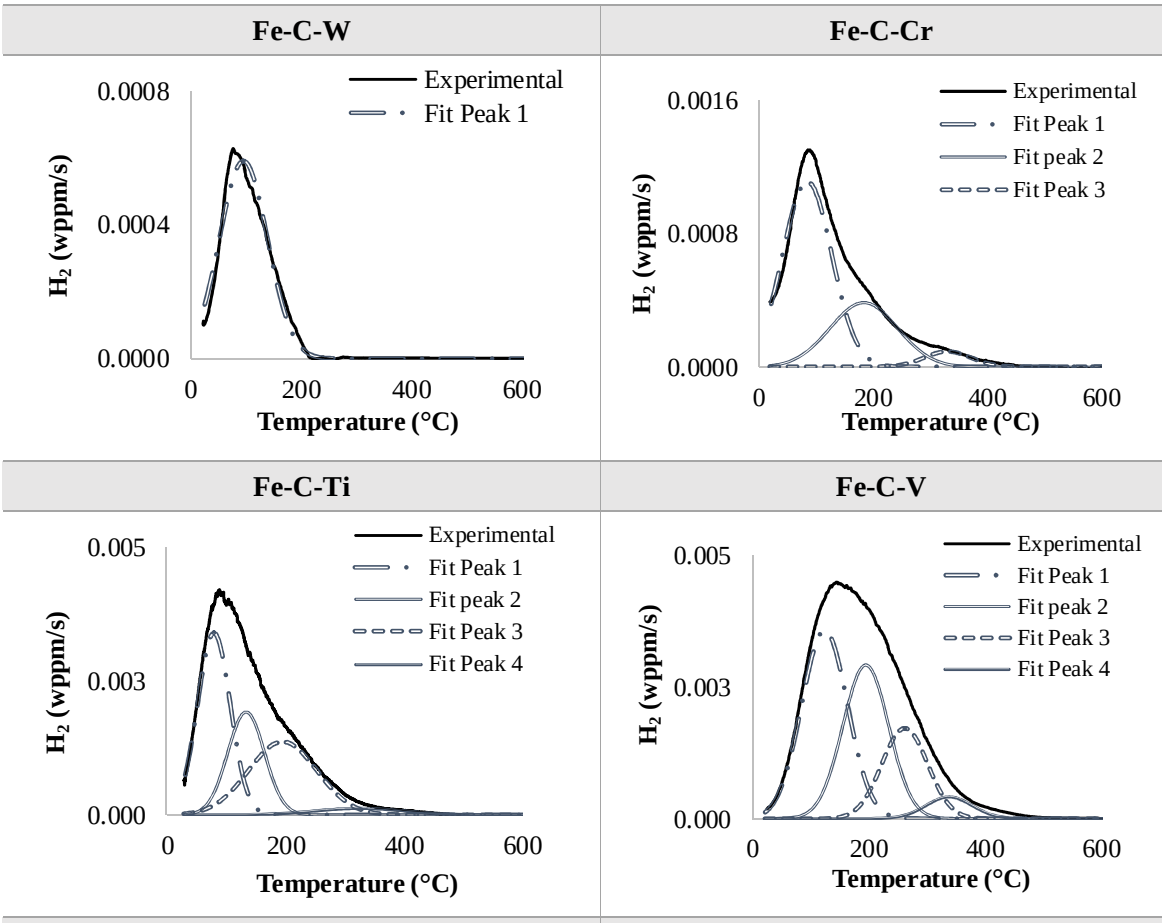

Activation energy (kJ/mol)					H amount TDS	
	Peak 1	**Peak 2**	**Peak 3**	**Peak 4**		**H (wppm)**
Fe-C-W	30	-	-	-	**Fe-C-W**	0.37
Fe-C-Cr	23	51	55	-	**Fe-C-Cr**	1.1
Fe-C-Ti	48	53	47	60	**Fe-C-Ti**	3.9
Fe-C-V	33	53	57	62	**Fe-C-V**	5.28

Figure V-5 TDS spectra, activation energies (kJ/mol) corresponding to the deconvoluted peaks and the amount of hydrogen (wppm) determined from the TDS spectra.

The Fe-C-W alloy only showed one peak, attributed to the martensitic lath boundaries, as described in previous paragraph. The W_2C precipitates, formed during the tempering process, were not able to trap hydrogen and permeation test results confirm the relatively higher diffusivity of this alloy compared to the other alloys. In addition to the first peak, two extra peaks were observed in the deconvoluted TDS spectrum of Fe-C-Cr. Both peaks were due to the present Cr-carbides [27]. The second peak of about 50 kJ/mol was attributed to hydrogen trapped at precipitates having a size between 50 and 100 nm, which were also present before the temper treatment. The third peak was associated to the tempered induced particles smaller than 50 nm. This was confirmed by modifying the carbide size distribution by extra tempering treatments and evaluation of the corresponding TDS spectra [27]. All trapping sites related to the Cr-carbides were assumed to be reversible as the desorption activation energy was lower than 60 kJ/mol. Particles larger than 100 nm were no longer able to trap hydrogen and were therefore believed not to influence the hydrogen permeation results significantly. Compared to the Fe-C-W alloy, the tempered induced $Cr_{23}C_6$ particles were able to trap hydrogen, but only causing a small decrease in diffusivity (Figure V-3). In addition, the hydrogen amount released during the TDS measurement is calculated from the experimental TDS curve and is given in Figure V-5. This, together with hot extraction results (Figure V-4), clearly showed that the Fe-C-Cr alloy had a higher trapping ability, but only hindering the hydrogen diffusion through the material to a minimal degree when compared with Fe-C-W.

Besides the effect of hydrogen trapping by the carbides, the matrix in which they were embedded may also affect hydrogen diffusion. As such, the rather small difference in diffusivity between the two alloys may be ascribed to differences related to the martensitic matrix. When comparing both alloys, the Cr-based one has a lower carbon and Cr content (Table V-1) leading to a less distorted martensitic matrix. In addition, since Cr carbides dissolve fast, they could not pin the grain boundaries during austenitization [42]. Therefore, a larger prior austenite grain size and thus increased block and packet size in the martensitic matrix was obtained for Fe-C-Cr compared to Fe-C-W. This implied a lower density of high angle grain boundaries in Fe-C-Cr [43, 44] which compensated for the retarding effect of the Cr carbides on the hydrogen diffusivity. As such, quite similar permeation transients for these two alloys were observed. Permeation experiments were also performed on both alloys in their as-quenched state [26, 27]. The corresponding diffusion coefficients of 5.11E-11 m^2/s and 1.71E-10 m^2/s for Fe-C-W and Fe-C-Cr, respectively, demonstrated a lower diffusion for Fe-C-W due to its more distorted martensitic structure. In conclusion, the different characteristics of the martensitic structure accounts for the small observed difference in diffusivity when comparing both materials in their Q&T state.

Next to the small carbides, precipitates larger than 100 nm were also observed in the Fe-C-Cr alloy. However, these were demonstrated not to be able to trap hydrogen [27]. Nevertheless, they can be seen as diffusion obstacles surrounded by a very high potential barrier. When these obstacles would occupy a volume inaccessible to hydrogen, they are able to lower the hydrogen solubility and diffusivity of the material. Leblond and Dubois [45] proposed an equation where the lowering of diffusion due to the presence of obstacles is incorporated. They stated that the influence of these obstacles should be negligible, except in

some special cases where there is a localized high obstacle concentration. However, in the present material, the concentration of these large particles is rather limited. Hence, it is believed that the low amount of large Cr-carbides will not affect the diffusion significantly.

The TDS spectrum of the Fe-C-Ti alloy showed three additional peaks next to the one attributed to the martensitic lath boundaries. Due to the tempering treatment, a high amount of carbides with a maximum size of 30 nm was introduced, which was set responsible for these three additional peaks [29]. The second and third peak of the TDS spectrum represent reversible trapping sites having an E_a of about 45-55 kJ/mol. Based on the work of Depover and Verbeken [29] these trapping sites were related with hydrogen trapped at the interface between a coherent TiC and the matrix. This was also demonstrated earlier by Wei *et al.* [46].

The fourth peak with a corresponding E_a of 60 kJ/mol was first associated with semi-coherent carbides [46-48]. The irreversible nature of this trapping site was considered in the already published work of Depover and Verbeken [29]. A sample charged with hydrogen was put in vacuum for 72 hours. In this time period, reversibly trapped hydrogen had the ability to effuse from the sample before TDS measurements were performed. The obtained spectra designated that the first three peaks attributed to reversible trapping sites disappeared, while the fourth peak was still present, yet a small decrease was observed. This indicated that the trapping sites, corresponding to an E_a of 60 kJ/mol, were indeed more irreversible in nature compared to the trapping sites with lower energies. Recently, Drexler *et al.* [49] accomplished a model-based interpretation of the very same Fe-C-Ti TDS spectrum using finite element modelling. In their study, the fourth peak could be attributed to the carbon vacancies in the TiC precipitates. In addition, the authors confirmed aforementioned conclusions: i.e. the first peak was associated to the martensitic lath boundaries, while the second and third peak were attributed to the matrix/carbide interface.

Compared to the Fe-C-Cr alloy, an important decrease in diffusivity was observed for the Fe-C-Ti alloy. This lower diffusivity is notable in Figure V-3 by the pronounced delay in the permeation transient of the Ti-containing alloy. On the one hand, the increased delay could be related to a higher amount of hydrogen traps. More small carbides were observed in the Fe-C-Ti alloy leading to an increased surface to volume ratio. This resulted in a higher amount of available traps for hydrogen at the matrix/carbide interface which is also reflected in a larger peak area for peak 2 and 3 in the Fe-C-Ti TDS spectrum as compared to the Fe-C-Cr spectrum. On the other hand, in the Fe-C-Ti alloy, traps with higher desorption activation energies were detected (Figure V-5). As already stated, traps with higher activation energies have a larger impact on the decrease in hydrogen diffusivity compared to these with lower energies [35].

The TiC carbides larger than 100 nm, also present in the microstructure, were unable to trap hydrogen. These were not fully dissolved during the austenitizing treatment due to the slow dissolution process of Ti-based carbides. Hence, a large volume of carbides, which were not able to trap hydrogen, were present in the Fe-C-Ti alloy. As mentioned previously, when obstacles occupy a volume inaccessible to hydrogen, they will lower the hydrogen diffusivity of the material [45]. Whether, in the Fe-C-Ti alloy, these large

carbides significantly affect the diffusion cannot be established conclusively. Their amount is larger than for the Fe-C-Cr case but not necessarily sufficient to hinder diffusion.

Also the Fe-C-V alloy showed three extra peaks, which could be attributed to the tempered induced carbides. The small V_4C_3 particles were able to trap a significant amount of hydrogen. Both the matrix/carbide interface and vacancies available in the V_4C_3 can act as trapping site [50]. These trapping sites were associated with the second and third peak of the TDS spectrum. The fourth peak (62 kJ/mol) can be linked with carbides smaller than 5 nm. Performing the TDS measurement after 72 h of hydrogen desorption time, hydrogen could still be detected in the second, third and fourth peak indicating the more irreversible nature of the trapping sites. Carbides larger than 20 nm did not play a significant role in hydrogen trapping [23]. The lower diffusivity of the V-containing alloy compared to the Ti-based material is explained by the higher amount of V-based carbides due to the higher amount of C in solid solution after the quenching process. This higher C content results from the faster and complete dissolution of the V carbides compared to the Ti-based precipitates during the austenitization annealing treatment.

The difference in hydrogen diffusivity or trapping ability between all alloys can also be explained by the released hydrogen amount during the TDS measurement. The calculated hydrogen amounts are given in Figure V-5. The Fe-C-V alloy contained the highest amount of trapped hydrogen, followed by the Fe-C-Ti, the Fe-C-Cr and the Fe-C-W material. The measured hydrogen could be located at martensitic lath boundaries, at the interface between carbide and matrix, at stress fields surrounding the carbides or in vacancies present in a carbide. All trapping sites, both reversible and irreversible, lowered the hydrogen diffusivity. Consequently, an increased hydrogen amount measured with the TDS equipment resulted in a higher hydrogen trapping ability of the material, as was reflected in the obtained permeation transients (Figure V-3).

V.4 Conclusion

This work correlates the microstructural characteristics with the permeation curves and hydrogen diffusivity for four carbide containing quenched and tempered Fe-C-X alloys, with X = W, Cr, Ti or V. The delay of the permeation transient was associated with the overall trap density while the slope of the transient was related to the amount of reversible trapping sites. The highest trapping ability was observed for the V-based alloy followed in decreasing order by the Fe-C-Ti, Fe-C-Cr and the Fe-C-W material. All carbides, except for the W-based ones, had the ability to lower the hydrogen diffusion in the material. Next to the carbide amount and size, the martensitic matrix characteristics and E_a of the trapping sites also played a crucial role in the hydrogen diffusivity of the material.

V.5 References

[1] T. Hilditch, S. Lee, J. Speer, and D. Matlock, "Response to hydrogen charging in high strength automotive sheet steel products," SAE Technical Paper 0148-7191, 2003.

[2] M. Koyama, E. Akiyama, Y.-K. Lee, D. Raabe, and K. Tsuzaki, "Overview of hydrogen embrittlement in high-Mn steels," *International Journal of Hydrogen Energy*, vol. 42, pp. 12706-12723, 2017.

[3] T. Depover, D. P. Escobar, E. Wallaert, Z. Zermout, and K. Verbeken, "Effect of hydrogen charging on the mechanical properties of advanced high strength steels," *international journal of hydrogen energy*, vol. 39, pp. 4647-4656, 2014.

[4] J. C. Villalobos, S. A. Serna, B. Campillo, and E. López-Martínez, "Evaluation of mechanical properties of an experimental microalloyed steel subjected to tempering heat treatment and its effect on hydrogen embrittlement," *International Journal of Hydrogen Energy*, vol. 42, pp. 689-698, 2017.

[5] M. Nagumo, M. Nakamura, and K. Takai, "Hydrogen thermal desorption relevant to delayed-fracture susceptibility of high-strength steels," *Metallurgical and Materials Transactions A*, vol. 32, pp. 339-347, 2001.

[6] J. Venezuela, Q. Liu, M. Zhang, Q. Zhou, and A. Atrens, "The influence of hydrogen on the mechanical and fracture properties of some martensitic advanced high strength steels studied using the linearly increasing stress test," *Corrosion Science*, vol. 99, pp. 98-117, 2015.

[7] H. Yu, J. S. Olsen, A. Alvaro, V. Olden, J. He, and Z. Zhang, "A uniform hydrogen degradation law for high strength steels," *Engineering Fracture Mechanics*, vol. 157, pp. 56-71, 2016.

[8] S. Ramamurthy, W. Lau, and A. Atrens, "Influence of the applied stress rate on the stress corrosion cracking of 4340 and 3.5 NiCrMoV steels under conditions of cathodic hydrogen charging," *Corrosion Science*, vol. 53, pp. 2419-2429, 2011.

[9] G. Lovicu, M. Bottazzi, F. D'Aiuto, M. De Sanctis, A. Dimatteo, C. Santus, *et al.*, "Hydrogen Embrittlement of Automotive Advanced High-Strength Steels," *Metallurgical and Materials Transactions A*, vol. 43, pp. 4075-4087, November 01 2012.

[10] M. A. Stopher, P. Lang, E. Kozeschnik, and P. E. Rivera-Diaz-del-Castillo, "Modelling hydrogen migration and trapping in steels," *Materials & Design*, vol. 106, pp. 205-215, 2016.

[11] T. Michler and J. Naumann, "Microstructural aspects upon hydrogen environment embrittlement of various bcc steels," *International journal of hydrogen energy*, vol. 35, pp. 821-832, 2010.

[12] A. Nagao, M. L. Martin, M. Dadfarnia, P. Sofronis, and I. M. Robertson, "The effect of nanosized (Ti, Mo) C precipitates on hydrogen embrittlement of tempered lath martensitic steel," *Acta Materialia*, vol. 74, pp. 244-254, 2014.

[13] A. Turnbull, "Perspectives on hydrogen uptake, diffusion and trapping," *International Journal of Hydrogen Energy*, vol. 40, pp. 16961-16970, 2015.

[14] C. Zhou, X. Chen, Z. Wang, S. Zheng, X. Li, and L. Zhang, "Effects of environmental conditions on hydrogen permeation of X52 pipeline steel exposed to high H2S-containing solutions," *Corrosion Science*, vol. 89, pp. 30-37, 2014.

[15] G. Wang, Y. Yan, J. Li, J. Huang, Y. Su, and L. Qiao, "Hydrogen embrittlement assessment of ultra-high strength steel 30CrMnSiNi2," *Corrosion Science*, vol. 77, pp. 273-280, 2013.

[16] S. Zhang, Y. Huang, B. Sun, Q. Liao, H. Lu, B. Jian, *et al.*, "Effect of Nb on hydrogen-induced delayed fracture in high strength hot stamping steels," *Materials Science and Engineering: A*, vol. 626, pp. 136-143, 2015.

[17] C. Wuyang, "Hydrogen Embrittlement and Stress Corrosion Cracking," L. J. L. Qiao, Y. Su, Y. Yu, B. Yang, R. Xuechong, H. Haiyou, Ed., ed. Beijing: Science Press, 2013.

[18] W. Zhao, T. Zhang, Y. Zhao, J. Sun, and Y. Wang, "Hydrogen permeation and embrittlement susceptibility of X80 welded joint under high-pressure coal gas environment," *Corrosion Science*, vol. 111, pp. 84-97, 2016.

[19] R. Valentini, A. Solina, S. Matera, and P. De Gregorio, "Influence of titanium and carbon contents on the hydrogen trapping of microalloyed steels," *Metallurgical and Materials Transactions A*, vol. 27, pp. 3773-3780, 1996.

[20] X. Yuan, "Precipitates and hydrogen permeation behavior in ultra-low carbon steel," *Materials Science and Engineering: A*, vol. 452, pp. 116-120, 2007.

[21] Y. Sakamoto and U.-i. Hanada, "Effect of Heat Treated Structure on Diffusion of Hydrogen in Martensitic Type 403 Stainless Steel," *Transactions of the Japan Institute of Metals*, vol. 18, pp. 466-470, 1977.

[22] A. Begić Hadžipašić, J. Malina, and M. Malina, "The influence of microstructure on hydrogen diffusion and embrittlement of multiphase fine-grained steels with increased plasticity and strength," *Chemical and biochemical engineering quarterly,* vol. 25, pp. 159-169, 2011.
[23] T. Depover and K. Verbeken, "Evaluation of the effect of V4C3 precipitates on the hydrogen induced mechanical degradation in Fe-CV alloys," *Materials Science and Engineering: A,* vol. 675, pp. 299-313, 2016.
[24] G. Spencer and D. Duquette, "The Role of Vanadium Carbide Traps in Reducing the Hydrogen Embrittlement Susceptibility of High Strength Alloy Steels," ARMY ARMAMENT RESEARCH DEVELOPMENT AND ENGINEERING CENTER WATERVLIET NY BENET LABS1998.
[25] T. Depover and K. Verbeken, "Evaluation of the role of Mo2C in hydrogen induced ductility loss in Q&T FeCMo alloys," *International Journal of Hydrogen Energy,* vol. 41, pp. 14310-14329, 2016.
[26] T. Depover, E. Van den Eeckhout, and K. Verbeken, "Hydrogen induced mechanical degradation in tungsten alloyed steels," *Materials Characterization,* vol. 136, pp. 84-93, 2018.
[27] T. Depover and K. Verbeken, "Hydrogen trapping and hydrogen induced mechanical degradation in lab cast Fe-C-Cr alloys," *Materials Science and Engineering: A,* vol. 669, pp. 134-149, 2016.
[28] T. Depover and K. Verbeken, "Thermal desorption spectroscopy study of the hydrogen trapping ability of W based precipitates in a Q&T matrix," *international journal of hydrogen energy,* vol. 43, pp. 5760-5769, 2018.
[29] T. Depover and K. Verbeken, "The effect of TiC on the hydrogen induced ductility loss and trapping behavior of Fe-C-Ti alloys," *Corrosion Science,* vol. 112, pp. 308-326, 2016.
[30] D. P. Escobar, T. Depover, E. Wallaert, L. Duprez, M. Verhaege, and K. Verbeken, "Thermal desorption spectroscopy study of the interaction between hydrogen and different microstructural constituents in lab cast Fe–C alloys," *Corrosion Science,* vol. 65, pp. 199-208, 2012.
[31] D. P. Escobar, C. Minambres, L. Duprez, K. Verbeken, and M. Verhaege, "Internal and surface damage of multiphase steels and pure iron after electrochemical hydrogen charging," *Corrosion Science,* vol. 53, pp. 3166-3176, 2011.
[32] H. E. Kissinger, "Reaction kinetics in differential thermal analysis," *Analytical chemistry,* vol. 29, pp. 1702-1706, 1957.
[33] L. Lan, X. Kong, Z. Hu, C. Qiu, D. Zhao, and L. Du, "Hydrogen permeation behavior in relation to microstructural evolution of low carbon bainitic steel weldments," *Corrosion Science,* vol. 112, pp. 180-193, 2016.
[34] M. Dadfarnia, P. Sofronis, and T. Neeraj, "Hydrogen interaction with multiple traps: can it be used to mitigate embrittlement?," *international journal of hydrogen energy,* vol. 36, pp. 10141-10148, 2011.
[35] R. A. Oriani, *Acta Metallurgica,* vol. 18, pp. 147-57, 1970.
[36] A. Turnbull, M. Carroll, and D. Ferriss, "Analysis of hydrogen diffusion and trapping in a 13% chromium martensitic stainless steel," *Acta Metallurgica,* vol. 37, pp. 2039-2046, 1989.
[37] J. Yang, F. Huang, Z. Guo, Y. Rong, and N. Chen, "Effect of retained austenite on the hydrogen embrittlement of a medium carbon quenching and partitioning steel with refined microstructure," *Materials Science and Engineering: A,* vol. 665, pp. 76-85, 2016.
[38] E. Van den Eeckhout, A. Laureys, Y. Van Ingelgem, and K. Verbeken, "Hydrogen permeation through deformed and heat-treated Armco pure iron," *Materials Science and Technology,* vol. 33, pp. 1515-1523, 2017.
[39] W. Dietzel, M. Pfuff, and G. Juilfs, "Hydrogen permeation in plastically deformed steel membranes," *Materials Science,* vol. 42, pp. 78-84, 2006.
[40] M. Iino, "Trapping of hydrogen by sulfur-associated defects in steel," *Metallurgical Transactions A,* vol. 16, pp. 401-409, 1985.
[41] D. P. Escobar, T. Depover, L. Duprez, K. Verbeken, and M. Verhaege, "Combined thermal desorption spectroscopy, differential scanning calorimetry, scanning electron microscopy and X-ray diffraction study of hydrogen trapping in cold deformed TRIP steel," *Acta Materialia,* vol. 60, pp. 2593-2605, 2012.
[42] T. Depover and K. Verbeken, "The detrimental effect of hydrogen at dislocations on the hydrogen embrittlement susceptibility of Fe-CX alloys: An experimental proof of the HELP mechanism," *International Journal of Hydrogen Energy,* 2018.
[43] Y. Prawoto, N. Jasmawati, and K. Sumeru, "Effect of prior austenite grain size on the morphology and mechanical properties of martensite in medium carbon steel," *Journal of Materials Science & Technology,* vol. 28, pp. 461-466, 2012.
[44] J. Hidalgo and M. J. Santofimia, "Effect of prior austenite grain size refinement by thermal cycling on the microstructural features of as-quenched lath martensite," *Metallurgical and Materials Transactions A,* vol. 47, pp. 5288-5301, 2016.

[45] J. Leblond and D. Dubois, "A general mathematical description of hydrogen diffusion in steels—II. Numerical study of permeation and determination of trapping parameters," *Acta metallurgica,* vol. 31, pp. 1471-1478, 1983.
[46] F. Wei, T. Hara, and K. Tsuzaki, "Precise determination of the activation energy for desorption of hydrogen in two Ti-added steels by a single thermal-desorption spectrum," *Metallurgical and Materials Transactions B,* vol. 35, pp. 587-597, 2004.
[47] G. Pressouyre and I. Bernstein, "A quantitative analysis of hydrogen trapping," *Metallurgical transactions A,* vol. 9, pp. 1571-1580, 1978.
[48] H. Lee and J.-Y. Lee, "Hydrogen trapping by TiC particles in iron," *Acta Metallurgica,* vol. 32, pp. 131-136, 1984.
[49] A. Drexler, T. Depover, K. Verbeken, and W. Ecker, "Model-based interpretation of thermal desorption spectra of Fe-C-Ti alloys," *Submitted to Journal of Alloys and Compounds,* 2018.
[50] G. Pressouyre, "A classification of hydrogen traps in steel," *Metallurgical and Materials Transactions A,* vol. 10, pp. 1571-1573, 1979.

CHAPTER VI

The effect of a constant tensile load on the hydrogen permeation

VI.1. Introduction

When steel is used in structural applications, it will experience different levels of stress during its lifespan. Plastic deformations typically occur during production, whereas elastic stresses are ubiquitous in most mechanical applications. If the hydrogen diffusivity increases with these stresses, the critical concentrations necessary for hydrogen induced damage will be reached sooner. Therefore, it is important to study the influence of stress on the hydrogen diffusion through the material.

Generally, literature data indicate that stresses will affect the hydrogen uptake and hydrogen diffusion rate through the material. Huang *et al.* [1] observed that the hydrogen diffusivity decreased with increasing plastic deformation. This was also reported by other authors [2, 3] and was attributed to dislocation generation. Tensile stresses in the elastic range were found to have no significant effect on the hydrogen diffusion in pure iron and AISI 4340 steel [1, 4, 5]. Nevertheless, the elastic stress induced a higher permeation current which Huang *et al.* [1] attributed to the lattice expansion, i.e. the increased lattice energy. Since the dissolution of hydrogen into the lattice is endothermic, the increase in lattice energy could account for the increased hydrogen uptake. This enlarged permeation current with tensile stresses in the elastic range was in agreement with other research [3, 4]. In these studies, they also ascribed the increased permeation flux to an increased hydrogen uptake, as there was no change in diffusivity reported. Kim [6] associated the higher hydrogen uptake to an increased corrosion current and a decreased polarization resistance. As such, under load, it was proposed that the cathodic reduction reaction rate at the input surface was considerably higher compared to the unloaded condition. Moreover, Brass *et al.* [7] reported a shift of the measured surface potential to more anodic values when the specimen was tensile strained. This indicated that the internal stresses affect significantly the intrinsic potential of the metal surface.

In contrast with aforementioned observations, Zhao *et al.* [8] reported an increased diffusivity in X80 steel with elastic stresses up to 60% of the yield stress (YS) determined at 0.5% strain. The higher diffusivity was attributed to the enlargement of the unit cell, which was beneficial to hydrogen diffusion. At 70% of the YS, an increased diffusion, with respect to the condition before loading, was observed. However, after unloading the specimen, the value of D_{app} slightly decreased. This indicated that the critical stress for initiating plastic deformation was reached, and dislocations were generated. A phenomenon called micro-plasticity took place and it represented the transition from a pure elastic deformation state to an elastic-plastic coexisting regime. Yet, another study by Kim *et al.* [3] reported a decrease in D_{app} with an increased applied elastic load at a pressure vessel steel (ASTM A516). This was again attributed to the lattice expansion, claiming

the lattice could accommodate more hydrogen in interstitial sites under tensile stress as such hindering hydrogen diffusion. These results are contradictory with aforementioned statements made by Zhao *et al.* [8]. Therefore, the influence of the elastic stress on the hydrogen diffusivity is an important topic to study.

In this chapter, permeation experiments combined with a constant load were performed on DP600 for which different stress levels in the elastic and plastic region were applied. The concentration dependence on the hydrogen diffusivity was investigated and the strain state of the material was obtained by digital image correlation (DIC) measurements. Next to the DP steel, the effect of an elastic tensile load on the hydrogen diffusivity, was also investigated for Armco iron.

VI.2. DP600 steel

The DP600 steel plate was delivered by Arcelor Mittal and Table VI-1 shows the chemical composition. The steel plate was hot and cold rolled, followed by subsequent annealing via industrial annealing parameters necessary to obtain the desired microstructure. In order to characterize the material by SEM, it was ground, polished and etched using a 2% Nital solution. Subsequently, the samples were cleaned with ethanol and acetone. The microstructure of the as-received material, shown in Figure VI-1, consists of a soft ferrite matrix with a hard dispersed martensitic phase (approximately 23%). The two phases are indicated in the figure. The grain size of the ferritic and martensitic grains are about 7 µm and 2 µm, respectively [9].

Table VI-1 Chemical composition DP steel in wt%.

DP steel											
C	Si	Mn	P	S	Al	Cr	Cu	Mo	V	Ni	Sn
0.08	0.129	0.948	0.037	0.003	0.028	0.568	0.019	0.005	0.005	0.025	0.001

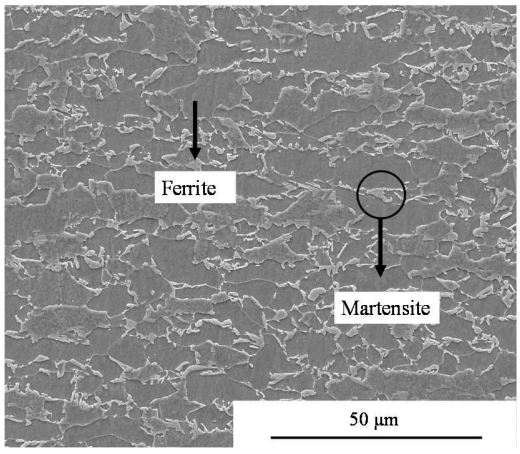

Figure VI-1 SEM image of the as-received DP steel.

Besides the two phases, inclusions were observed in the microstructure which are depicted in Figure VI-2. In order to investigate the chemical nature, EDX analysis was performed and the resulted spectrum of the inclusion indicated in Figure VI-2, is given in Figure VI-3. As a reference, an EDX measurement was taken from the matrix as well and the corresponding spectrum is shown in Figure VI-4. Based on the results, the inclusions appeared to be aluminium oxides. Unfortunately, these oxides were not homogeneously dispersed in the matrix of the as-received steel plate. As such, an increased scatter on the permeation results could be related to the presence of these inclusions. Tensile stresses are concentrated at incoherent regions such as a sharp edge or tip of the inclusion, leading to the creation of a triaxial stress field where hydrogen atoms are preferentially trapped [10]. This could affect the permeation results. However, to which extent they influence the hydrogen diffusion was not investigated, but it could be interesting to do so.

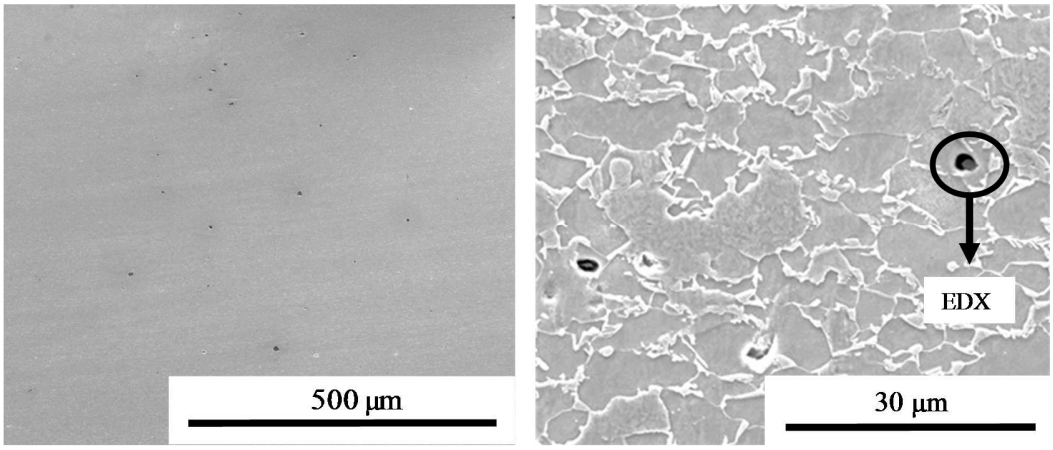

Figure VI-2 SEM image of the as-received DP steel. An overview (left) and in detail (right).

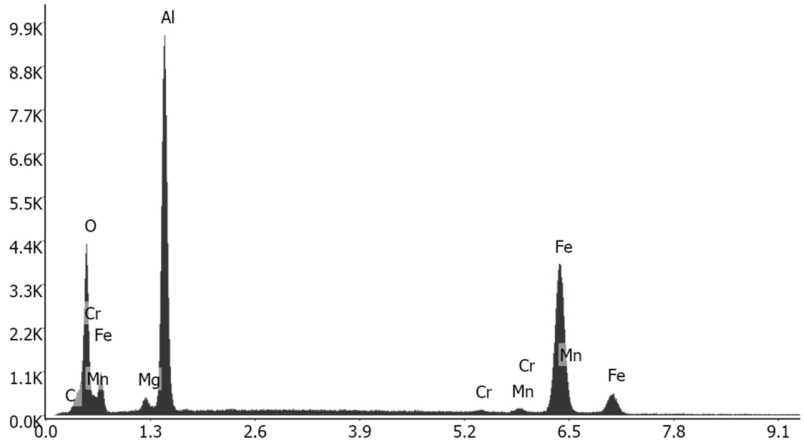

Figure VI-3 EDX spectrum of the inclusion in the as-received DP steel. Zone of interest is indicated in Figure VI-2.

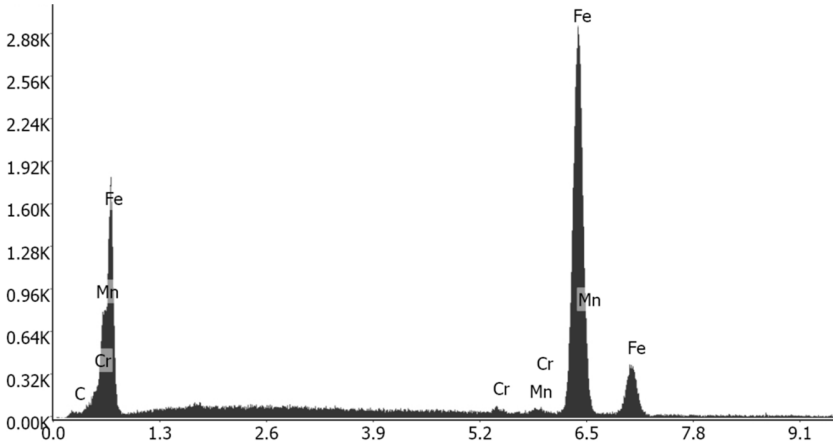

Figure VI-4 EDX spectrum of the DP matrix.

Next to the aluminium oxides, the SEM images of the as-received DP steel showed globular voids of about 1 µm in size. These empty cavities in the microstructure could have contained an aluminium oxide which was removed due to the grinding and polishing procedure. Furthermore, a Mn-rich segregation line was present in the centre of the material. It has been reported in literature that non-metallic inclusions like MnS may accumulate hydrogen, resulting in a local increase of hydrogen pressure and easier crack initiation [11]. Fortunately, in this work, SEM analysis did not reveal any hydrogen related damage when examining samples after the hydrogen permeation experiment with or without loading.

VI.3. Armco iron

The as-received Armco iron was delivered by AK Steel in a highly pure, cold rolled condition. The microstructure was fully ferritic with a grain size of approximately 30 µm (Figure VI-5). The chemical composition is given in Table VI-2.

Table VI-2 Chemical composition Armco iron in wt%.

Armco iron, cold rolled plate											
C	Si	Mn	P	S	Al	Cr	Cu	Mo	N	Ni	Sn
0.002	0.003	0.050	0.005	0.003	0.002	0.016	0.009	0.001	0.003	0.004	0.002

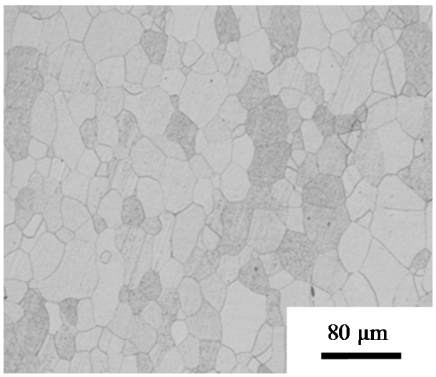

Figure VI-5 Optical microscopy image of the cold rolled Armco iron (TD plane).

VI.4. Determination of the yield stress

To investigate the effect of stress on the hydrogen diffusivity, the permeation set-up was extended with a load cell that allowed to impose a constant tensile load on the sample during the permeation experiment. Different tensile stresses were imposed varying from 0% to 140% of the YS which was determined by a tensile test performed following the standard ASTM international procedure [12]. The test was strain controlled by a rate of 0.015 min^{-1}. The strain was measured by a strain gauge which was attached to the sample surface. A tensile specimen ready for testing is shown in Figure VI-6. The stress-strain curve was measured with an Instron® 8801 servo-hydraulic testing system and the transition from the elastic to the plastic region for the DP steel is depicted in Figure VI-7. The YS, determined by the 0.2% strain offset method, results in a value of approximately 325 MPa. This value will be used throughout this work as the YS of the considered DP steel.

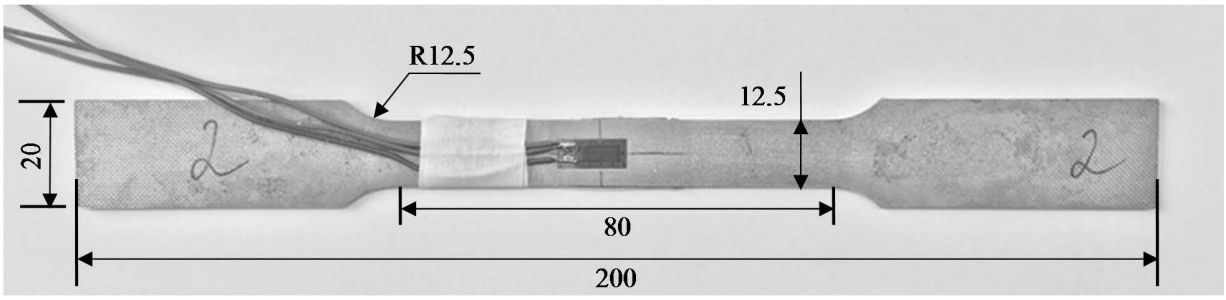

Figure VI-6 Tensile test specimen and strain gauge. Dimensions are given in mm.

Permeation combined with a constant tensile load

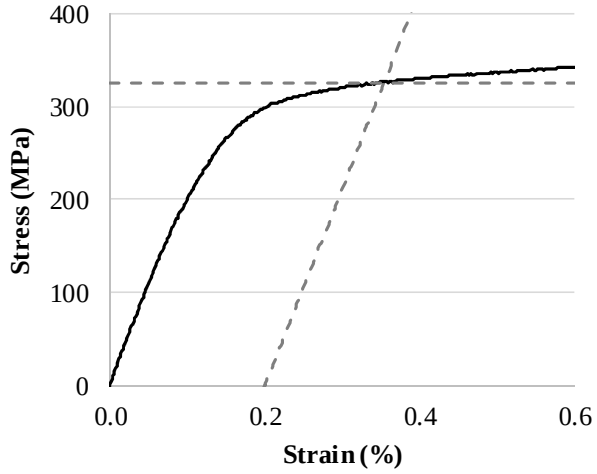

Figure VI-7 Stress-strain curve for DP steel. Strain rate of 0.015 min^{-1}. Yield stress determined using the 0.2% strain offset method.

The elastic part of the stress-strain curve for the Armco iron is presented in Figure VI-8. The transition from the elastic to the plastic region occurs abruptly at a stress which is defined as the upper yield point. In this case, the upper yield point occurs at about 280 MPa and is indicated with a dotted line in Figure VI-8. At that specific stress, plastic deformation initiated, and a clear decrease in stress was observed. Due to the complexity of the phenomena occurring at the yield point, it was not possible to investigate the hydrogen diffusivity at a specific load within the plastic region for these materials. Nevertheless, the effect of an elastic stress on the hydrogen diffusion rate was investigated and will be compared to the DP-values.

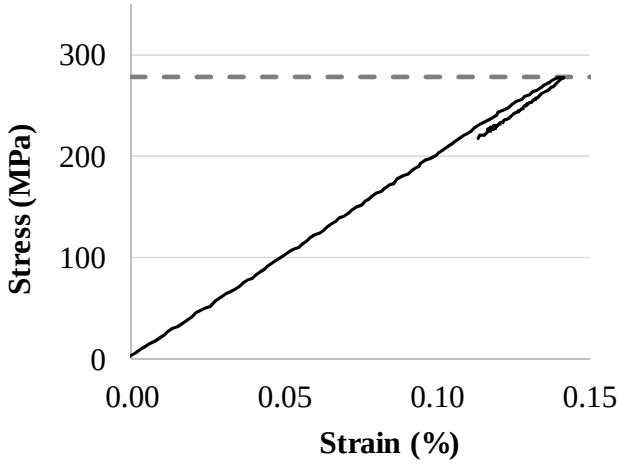

Figure VI-8 Stress-strain curve for Armco iron. Strain rate of 0.015 min^{-1}. The dotted line indicates the upper yield point.

VI.5. Permeation experiments combined with a constant load

To determine the diffusion coefficient, rectangular samples were subjected to a constant load prior to the start of the permeation test. The permeation test was performed following the permeation test method 2 described in section II.3. The roughened sample was cathodically polarized by applying a constant current density of 3 mA/cm². At the exit side a potential of -500 mV vs the RE (+650 mV vs SHE) was imposed. In both cells, a solution of 0.1 M NaOH was used and the thickness of the samples was between 1000 and 1060 µm. For the experiments in the elastic range, the samples required a width of 47 mm, while samples tested in the plastic range were only 25 mm in width. These sizes were selected in order to have the requested stress condition keeping in mind the experimental requirements of the loading device. More details concerning the sample preparation are given in section II.3.

The apparent diffusion coefficient ($D_{app,\ fit}$) was calculated by fitting the theoretical permeation transient based on Fick's law with the first half of the normalized experimental data (section II.4.2.). This method was chosen since the experimental curve started to deviate from the theoretical one at about a normalized current of 0.5. This deviation was clarified by the deposition of cations which were present in the electrolyte. A more detailed explanation can be found in section III.5.

Hydrogen permeation experiments were performed on the DP steel with a variety of loadings. The stress level is expressed as a fraction of the YS and is mentioned in the sample code. Stresses of approximately 60%, 80%, 120% and 140% of the YS (325 MPa) were applied. For each stress level, at least two repetitions were carried out and results are discussed in the following sections.

VI.5.1. Elastic stresses

Prior to the start of the permeation experiment, a constant load of 60%, 80% or 100% of the YS was applied. The imposed stresses are indicated at the stress-strain curve in Figure VI-9. Due to the elastic stress, the lattice will expand and a higher hydrogen uptake can be expected. As mentioned in the introduction, the cathodic reduction reaction rate at the input surface is higher at a stressed surface leading to a higher hydrogen concentration in the subsurface of the specimen.

Permeation combined with a constant tensile load

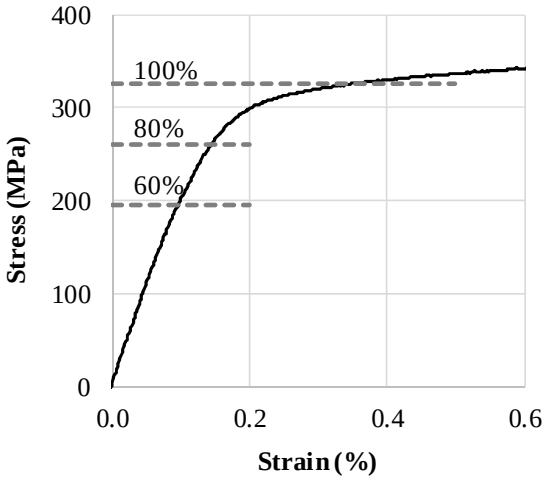

Figure VI-9 Stress-strain curve of the DP steel with indicated stress levels applied prior to the permeation experiment.

$D_{app,\ fit}$ obtained by fitting the first half of the normalized current, is plotted in Figure VI-10. The first half of the normalized transients are shown in Figure VI-11. When comparing the 60%YS and the 80%YS sample, a higher applied load resulted in a higher hydrogen diffusivity. This could be clarified by two reasons. On the one hand, the elastic tensile stress increases the volume of the unit cell and of its interstitial positions, which is beneficial to hydrogen diffusion [8]. On the other hand, an imposed stress will increase the hydrogen concentration of the subsurface (C_0) which could be responsible for a higher value of $D_{app,\ fit}$, since several authors detected an increased $D_{app,\ fit}$ with increasing C_0 [13-15]. Hence, the concentration dependency of $D_{app,\ fit}$ was investigated and results are discussed in section VI.6.

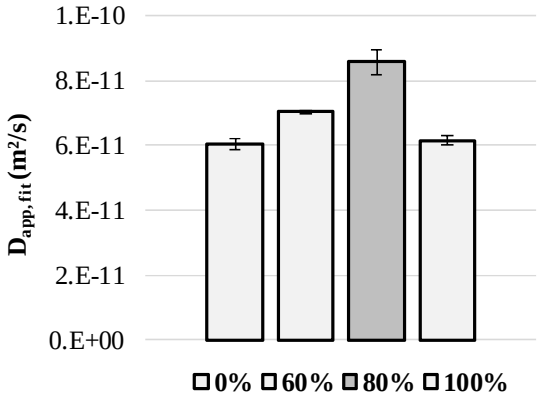

Figure VI-10 Apparent diffusion coefficients for the DP steel under constant elastic stress.

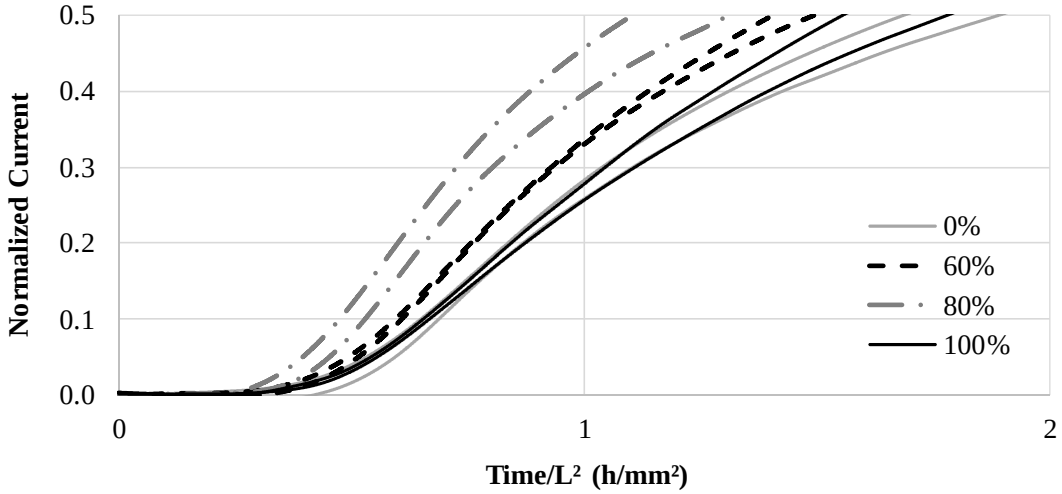

Figure VI-11 First half of the normalized permeation curves for different loading conditions. L is the sample thickness.

Zhao *et al.* [8] also detected an increase in D_{app} with elastic stresses. In their work, a two-phase steel containing ferrite and bainite was investigated, which is somehow comparable to the microstructure of the DP steel studied in this work. Next to the DP steel, in this work, Armco iron, which consisted of a fully ferritic structure, was also tested and yet again an increased diffusivity was observed when a constant load within the elastic region was applied. Tests were performed by the permeation test method 2 and were also repeated twice. $D_{app, fit}$ values are given in Table VI-3. The applied load was 50% and 70% of the upper yield point (280 MPa).

Table VI-3 Apparent diffusion coefficients (10^{-10} m²/s) for Armco iron. The applied load is indicated as a percentage of the upper yield point.

Armco iron	0%	50%	70%
$D_{app, fit}$	1.86 ± 0.19	3.02 ± 0.13	3.49 ± 0.28

At 100% of the YS, the diffusivity decreased again reaching values similar to the 0%YS-value (Figure VI-10). Since the YS was determined by the 0.2% strain offset method, the stress strain curve already exhibited some deviation from the linear part before the YS was reached (Figure VI-9). As such, some plasticity was present in the specimen and correspondingly dislocations were formed and dislocation density increased which had a retardant effect on the hydrogen diffusion and which compensated for the influence of the lattice expansion. These findings were in agreement with the results of Zhao *et al.* [8] and Jin Kim *et al.* [10], who also observed a decrease in diffusion when applying a stress close or equal to the yield point. On the other hand, next to dislocations, the formation of vacancies and vacancy clusters is enhanced in the presence of hydrogen [16]. As demonstrated in literature, vacancies and vacancy clusters have the ability to hinder diffusion by trapping hydrogen [17, 18]. As such, they probably also contributed to the decreased diffusivity of the 100%YS specimen.

Permeation combined with a constant tensile load

In contrast with literature findings, no clear trend was found in the value of the steady state permeation flux. This was attributed to the deposition of anions present in the electrolyte (section III.5), or to the passivation layer at the exit side of the sample. When stresses are applied, a passivation layer with different properties may be formed at the exit surface [19]. The influence of the passivation layer on the exit side permeation current density was nicely demonstrated in the work of Addach *et al.* [20] and Manolatos *et al.* [21] and is also discussed in section III.7. Nevertheless, the structure and chemical composition of the passive layer for different applied stresses should be investigated by, for example, in-situ RAMAN spectroscopy. However, the combination of a constant loading device, an electrochemical cell, and a surface analysing technique is not at all straightforward and would be challenging to realize.

VI.5.2. Plastic stresses

The average diffusion coefficients, determined by fitting the first half of the normalized curve, are plotted in Figure VI-12. Also $D_{app,\ fit}$ of the reference sample is shown. The decreased diffusivity, observed for the imposed load of 120% and 140% of the YS, was caused by the additional lattice defects introduced by increased plastic straining of the material. As such, the impact of the plastic stress on the diffusivity significantly exceeded the one of the expanded lattice, since both are present under constant loading conditions. The decrease in diffusion due to plastic stresses was also discussed by other authors [1, 3, 22].

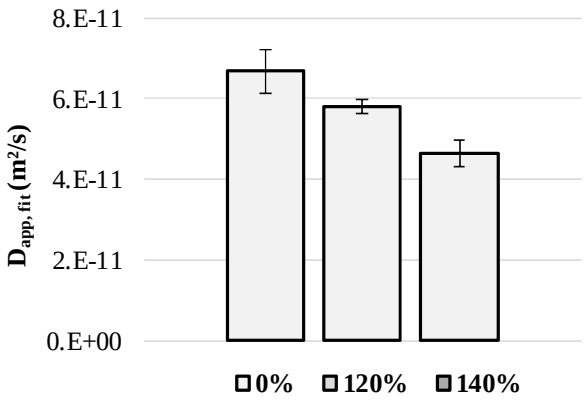

Figure VI-12 Apparent diffusion coefficients for the DP steel under constant plastic stress.

When a constant load was applied in the plastic region of the stress strain curve, self-evidently, the maximal contribution of the elastic strain also remained present during the entire permeation test. As mentioned previously, the elastic stress causes a higher diffusivity (Figure VI-10). Therefore, a new test was designed with the aim of separating the contribution of elastic and plastic stresses. For this purpose, samples were tested where first a load of 120% of the YS was applied and which was released before the start of the experiment. As such, the elastic stress contribution was removed from the permeation transient result and only the plastic contribution remained and its effect could be evaluated. The average $D_{app,\ fit}$ obtained by this procedure is indicated in Figure VI-13 as 120% *. A further decrease in $D_{app,\ fit}$ was observed when the

elastic stresses were absent. This confirmed once more that elastic stresses caused a higher diffusion of hydrogen through the microstructure while the microstructural consequences of plastic deformation accounted for a decrease in the hydrogen diffusion coefficient.

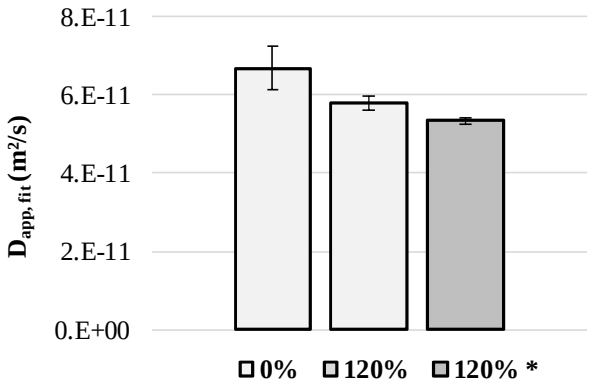

Figure VI-13 Apparent diffusion coefficients for the DP steel under plastic stress. 120%* was unloaded prior the permeation experiment.

VI.6. Concentration dependence

The concentration dependence of D_{app} was evaluated by charging with a cathodic current density of 3 and 1 mA/cm² in a 0.1 M NaOH electrolyte based on Milli Q® water. At the higher current density, the entrance subsurface hydrogen concentration was higher, as well as the concentration difference over the sample thickness. Based on Fick's law, the diffusion coefficient is independent of the concentration, while the steady state flux increases with an increased concentration difference over the sample thickness. The apparent diffusion coefficient was determined by fitting the first half of the normalized permeation transient and a value of 7.79 ± 0.23 E-11 m²/s and 7.37 ± 0.10 E-11 m²/s was obtained for the high and low applied current density respectively.

Supposing the charging surface is at steady state, the subsurface concentration C_0 in wt ppm of the two charging conditions can be determined by [13]:

$$C_0 = \frac{j_\infty L}{F D_{app}} \frac{M_H}{\rho_{Fe}} 10^6 \qquad \text{(VI-1)}$$

where j_∞ is the steady state permeation current density (A/m^2), L the thickness of the membrane (m), D_{app} the apparent diffusion coefficient (m²/s), F the Faraday constant (96.485 C/mol), M_H the molar mass of hydrogen (1g/mol) and ρ_{Fe} the iron density ($7.87 \cdot 10^6$ g/m^3). As such, a subsurface concentration of 1.38 ± 0.06 wt ppm and 1.00 ± 0.01 wt ppm was obtained for the high and low current density.

Permeation combined with a constant tensile load

Unfortunately, for the experiments under load, the steady state value was affected due to the deposited anions on the cathodic surface originating from the electrolyte when no Milli Q® water was used. As such, the subsurface concentration could not be determined unambiguously. Nevertheless, Doshida *et al.* [16] calculated the hydrogen content of the subsurface for different loading conditions from 0% to 80% of the tensile strength. Although in their research, the material of interest had a fully martensitic microstructure and a much more corrosive environment was used (pH = 2; 50°C), the hydrogen concentration increased only with 0.5 wt ppm for the different loading conditions in the elastic range. As such, it was supposed that the difference in hydrogen concentration in our work, imposed by the different applied charging current densities of 1 and 3 mA/cm², was large enough to compare with the difference in hydrogen concentration of the stressed and unstressed condition. Hence, theoretical transients based on the specific average $D_{app,\,fit}$ are plotted in Figure VI-14. It is clear from the figures that there is a larger difference between the transients obtained from our experiments with variable stress. Therefore, the increased $D_{app,\,fit}$ due to an elastic load of 80% of the YS can indeed be related to the lattice expansion and not to a higher hydrogen subsurface concentration. However, to verify that the comparison of the subsurface hydrogen concentration with the different applied current densities was representative, the experiments should be repeated with the electrolyte prepared with the ultrapure Milli Q® water. This will allow to calculate the more consistent values of C_0 for the permeation tests combined with a constant load.

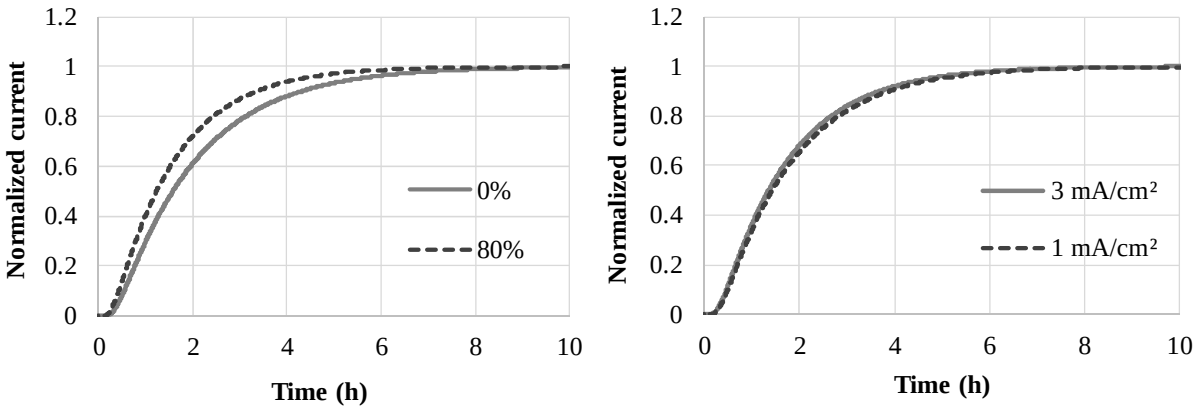

Figure VI-14 Theoretical transient for different loading conditions (left) and charging current densities (right).

VI.7. DIC measurements

The actual strain state of the DP material can be obtained by 3D DIC measurements. Therefore, Point Grey® cameras were used. By DIC, the displacement can be measured and a strain field can be computed of a specimen under a specific load in three dimensions. In this work, the specimens were prepared similar to a permeation experiment (section II.3). Subsequently, they were cleaned and a black speckle pattern with a white background layer was applied by painting. The specimens where then mounted in between the claws which were then installed in the constant loading device. Finally, the constant load ring was tightened manually and at specific loads, DIC images were taken.

VI.7.1. Elastic stresses

The engineering strain at loads of 60% and 80% of the YS in vertical (ε_{yy}) and transverse (ε_{xx}) direction are presented in Figure VI-15 and Figure VI-16, respectively. The zone which is in contact with the electrolyte during the permeation experiment, is indicated with a white circle. In addition, for the 80% condition, an image was taken after a dwell time of 5 minutes in order to detect strain evolutions with time. Figure VI-15 indicates a tensile strain in the vertical direction which increased with the amount of applied load. Figure VI-16, on the other hand, shows that at 60% of the YS limited strain in the transverse direction was present. At the 80%YS condition, a compressive strain was observed in the zone of interest. With respect to the possible effect of time, it became clear that when stresses where applied within the elastic region, no significant changes with time could be observed.

In conclusion, when an elastic strain was imposed, a macroscopic strain was observed with DIC which microscopically results in a distortion in the crystal lattice. In the case of a body centred cubic (bcc) structure, the initial lattice constant a will extend to $a \cdot (1 + \varepsilon)$ along the stretched y-direction. In the other directions, a will contract to $a \cdot (1 - \nu\varepsilon)$, with ν the Poisson's ratio which is 0.3 for steel [23]. For example, at the 80% loading condition after the dwell time, the average ε_{yy} in the zone of interest is 0.16% (Figure VI-15 (c)) and ε_{xx} is -0.05% (Figure VI-16 (c)) which gives a Poisson's ratio of 0.31. As such, there is a volume change in each unit cell after applying a tensile load which can be described as [8]:

$$\Delta V = a^3 \cdot (0.09\varepsilon^3 - 0.51\varepsilon^2 + 0.4\varepsilon) \qquad \text{(I-2)}$$

The atomic number and atomic volume in each unit cell is constant, and therefore, the volume change originates from a density change. The elastic load enlarges thus the interstitial sites, which was demonstrated to be beneficial to hydrogen diffusion (Figure VI-10).

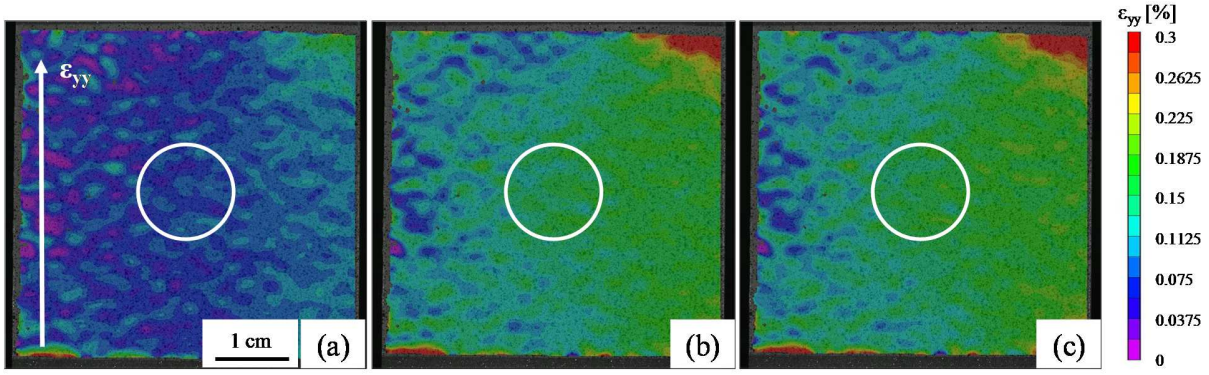

Figure VI-15 DIC images of the vertical engineering strain with an applied load of 60% (a) and 80% (b) of the YS. Image (c) was taken after a dwell time of 5 minutes following the 80% condition.

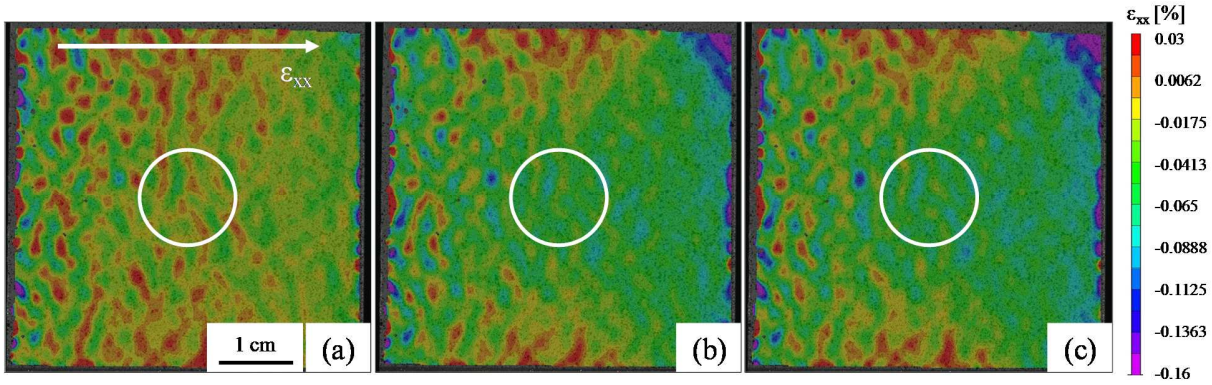

Figure VI-16 DIC images of the transverse engineering strain with an applied load of 60% (a) and 80% (b) of the YS. Image (c) was taken after a dwell time of 5 minutes following the 80% condition.

Important to mention is that the strain is not homogeneously distributed over the full sample. This is attributed to the manual procedure of tightening the claws which resulted in claws that were not perfectly aligned. Subsequently, when applying the required force to the constant load equipment, the stress was not homogeneously distributed over the cross-section of the sample. This phenomenon is even more distinct in Figure VI-17, where a load equally to the YS was applied. It must, however, be stressed that the strain field of the zone in contact with the electrolyte shows a more or less evenly distributed strain, and at a reasonable distance from the extremes.

In Figure VI-17, DIC images of two similar experiments (A&B) are shown in order to check the reproducibility of the measurements. The images at the left were taken at the time when a load of 100% of the YS, determined from the static tensile test according to the standard ASTM international procedure [12], was reached. The ones at the right were taken after a dwell time of five minutes. The results show that the reproducibility was not perfect. Therefore, attention must be taken when mounting the sample in the constant loading device. It is important to do this in a systematic way to diminish the experimental spread of the permeation experiments. Furthermore, the permeation test may not be started directly after applying the required load as deformation processes continued during the dwell time of 5 minutes. In addition, it was observed that the applied force decreased about 200 N during the dwell time. The clarification of this phenomenon was based on specific features of the set-up, namely the constant load ring. After applying the required force, the specimen slightly extended a little further. As such, the ring, which functions as a spring, was displaced in the direction of its original condition. This displacement resulted then in a lower force which the ring exerted on the specimen.

At a force required to attain the YS, which was determined from the stress-strain curve (Figure VI-9), the DIC images after a dwell time of five minutes showed an average strain of 0.55% and 0.50% in the zone of interest for permeation for measurement A and B, respectively (Figure VI-17). However, from the stress-strain curve, at the YS, only a strain of about 0.35% was observed. This indicated that, due to the nature of the set-up, the strain obtained in the constant loading device is not identical as the strain obtained from the uniaxial tensile test. This observation becomes relevant when forces are needed to reach the YS

determined from the standard tensile test. Consequently, it was assumed that already a higher degree of plastic deformation, than expected, was present. This result supported the observed lower hydrogen diffusivity of the 100%YS specimen (Figure VI-10).

The engineering strain of measurement A in the transverse direction at the YS and after five minutes interval time, is shown in Figure VI-18. Within the white circle, the strain displays a negative value which is associated with the constriction of the specimen. Similar as in the vertical direction, deformation processes continued during the dwell time. At the upper and lower edge of the specimen, the effect of the claws is clearly visible. Due to the clamping, the material was restrained from constriction near the claws.

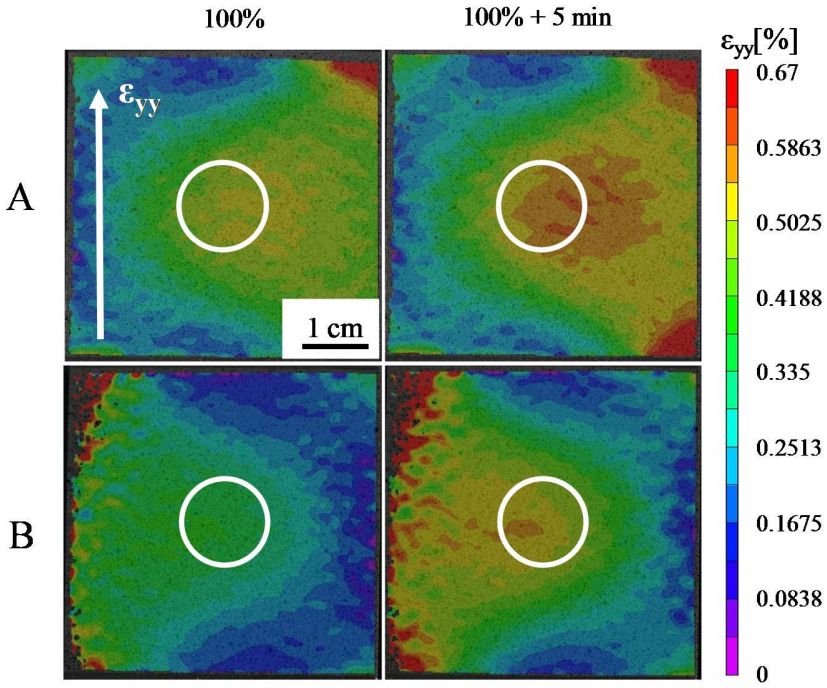

Figure VI-17 DIC images of the vertical engineering strain with an applied load of 100% (left) of the YS. Images at the right were taken after a dwell time of 5 minutes. Measurements A and B were carried out in similar experimental conditions.

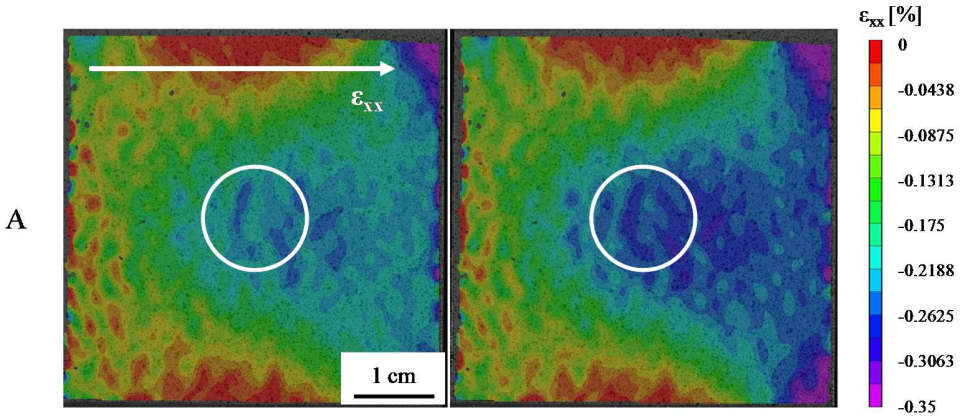

Figure VI-18 DIC images of the transverse engineering strain with an applied load of 100% (left) of the YS. The image at the right was taken after a dwell time of 5 minutes.

VI.7.2. Plastic stresses

Figure VI-19 (a) shows the strain field at a load of 120% of the YS. In addition, images are given after a dwell time of five (b) and ten minutes (c), and when the load was released to 0% (d). After a dwell time of five minutes, a higher degree of deformation was detected. The strain field observed after ten minutes did not show significant differences, and thus, it was stated that the strain distribution remained stable with time after a dwell time of five minutes. The residual plastic strain for the unloaded specimen is presented at Figure VI-19 (d). The difference in strain, which disappeared by releasing the load, is the elastic contribution that was responsible for the higher diffusivity of the 120% sample compared to the 120% * one (Figure VI-13).

The higher degree of vertical strain at a stress of 140% of the YS, is shown in Figure VI-20. As mentioned in section VI.1, the increased plastic deformation, lowered the diffusion of hydrogen through the material due to the increased density of lattice defects. The engineering strain in the transverse direction shows negative and homogeneously distributed values in the permeation zone of interest for both conditions (120% and 140%). These figures were not shown here.

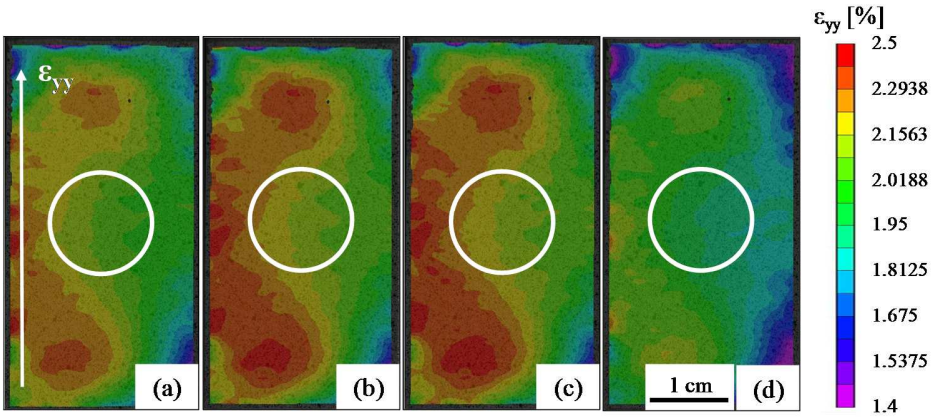

Figure VI-19 DIC images of the vertical engineering strain with an applied load of 120% of the YS (a). Image (b) and (c) were taken after a dwell time of 5 and 10 minutes, respectively. Image (c) was taken after releasing the load back to 0%.

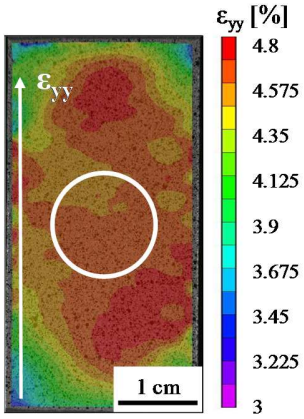

Figure VI-20 DIC image of the vertical engineering strain with an applied load of 140% of the YS.

VI.8. Conclusion

Elastic tensile stresses increased the hydrogen diffusivity of DP steel and Armco iron. Due to the volume increase of the unit cell, interstitial positions were enlarged and hydrogen diffusion was facilitated. When the imposed stress was equal to the yield stress, the increasing amount of hydrogen traps compensated the increase of the diffusion coefficient resulting from the lattice expansion. Significant plastic deformation, on the other hand, slowed down the diffusion due to the formation of lattice defects.

DIC images demonstrated the strain state of the specimen in the constant loading device at different loading conditions. Results showed nicely the enlarged strain in the vertical direction and the contraction in the transverse direction. However, when reaching stresses in the plastic region, the amount of strain implied by the constant loading device cannot be compared with the uniaxial tensile test. Based on the DIC

measurements, it became clear that one should mount the sample with care and in a systematic way. Nevertheless, in the zone of interest for the permeation experiments, a homogeneously strain distribution was observed which remained stable with time after an initial dwell time of about five minutes.

VI.9. References

[1] Y. Huang, A. Nakajima, A. Nishikata, and T. Tsuru, "Effect of mechanical deformation on permeation of hydrogen in iron," *ISIJ international*, vol. 43, pp. 548-554, 2003.

[2] M. Kurkela, G. Frankel, R. Latanision, S. Suresh, and R. Ritchie, "Influence of plastic deformation on hydrogen transport in 2 14 Cr-1Mo steel," *Scripta Metallurgica*, vol. 16, pp. 455-459, 1982.

[3] S. J. Kim and K. Y. Kim, "Electrochemical hydrogen permeation measurement through high-strength steel under uniaxial tensile stress in plastic range," *Scripta Materialia*, vol. 66, pp. 1069-1072, 2012.

[4] W. Beck, J. M. Bockris, J. McBreen, and L. Nanis, "Hydrogen permeation in metals as a function of stress, temperature and dissolved hydrogen concentration," *Proc. R. Soc. Lond. A*, vol. 290, pp. 220-235, 1966.

[5] B. J O'M, W. Beck, M. Genshaw, P. Subramanyan, and F. Williams, "The effect of stress on the chemical potential of hydrogen in iron and steel," *Acta Metallurgica*, vol. 19, pp. 1209-1218, 1971.

[6] S. J. Kim, "Effect of the elastic tensile load on the electrochemical corrosion behavior and diffusible hydrogen content of ferritic steel in acidic environment," *International Journal of Hydrogen Energy*, vol. 42, pp. 19367-19375, 2017.

[7] A.-M. Brass and J. Chêne, "Influence of tensile straining on the permeation of hydrogen in low alloy Cr–Mo steels," *Corrosion science*, vol. 48, pp. 481-497, 2006.

[8] W. Zhao, T. Zhang, Z. He, J. Sun, and Y. Wang, "Determination of the Critical Plastic Strain-Induced Stress of X80 Steel through an Electrochemical Hydrogen Permeation Method," *Electrochimica Acta*, vol. 214, pp. 336-344, 2016.

[9] T. Depover, E. Wallaert, and K. Verbeken, "Fractographic analysis of the role of hydrogen diffusion on the hydrogen embrittlement susceptibility of DP steel," *Materials Science and Engineering: A*, vol. 649, pp. 201-208, 2016.

[10] S. J. Kim, D. W. Yun, H. G. Jung, and K. Y. Kim, "Determination of hydrogen diffusion parameters of ferritic steel from electrochemical permeation measurement under tensile loads," *Journal of The Electrochemical Society*, vol. 161, pp. E173-E181, 2014.

[11] T. Goldenberg, T. Lee, and J. Hirth, "Ductile fracture of U-notched bend specimens of spheroidized AISI 1095 steel," *Metallurgical Transactions A*, vol. 9, pp. 1663-1671, 1978.

[12] ASTM International, "Standard Test Methods for Tension Testing of Metallic Materials," ed. West Conshohocken, PA, 2016.

[13] S. Frappart, X. Feaugas, J. Creus, F. Thebault, L. Delattre, and H. Marchebois, "Study of the hydrogen diffusion and segregation into Fe–C–Mo martensitic HSLA steel using electrochemical permeation test," *Journal of Physics and Chemistry of Solids*, vol. 71, pp. 1467-1479, 2010.

[14] A. Turnbull, "Perspectives on hydrogen uptake, diffusion and trapping," *International Journal of Hydrogen Energy*, vol. 40, pp. 16961-16970, 2015.

[15] T. G. Namboodhiri and L. Nanis, "Concentration dependence of hydrogen diffusion in Armco iron," *Acta Metallurgica*, vol. 21, pp. 663-672, 1973.

[16] T. Doshida, H. Suzuki, K. Takai, N. Oshima, and T. Hirade, "Enhanced lattice defect formation associated with hydrogen and hydrogen embrittlement under elastic stress of a tempered martensitic steel," *ISIJ international*, vol. 52, pp. 198-207, 2012.

[17] W. Counts, C. Wolverton, and R. Gibala, "First-principles energetics of hydrogen traps in α-Fe: Point defects," *Acta Materialia*, vol. 58, pp. 4730-4741, 2010.

[18] M. Nagumo, K. Takai, and N. Okuda, "Nature of hydrogen trapping sites in steels induced by plastic deformation," *Journal of alloys and compounds*, vol. 293, pp. 310-316, 1999.

[19] F. Navai, "Effects of tensile and compressive stresses on the passive layers formed on a type 302 stainless steel in a normal sulphuric acid bath," *Journal of Materials Science*, vol. 30, pp. 1166-1172, 1995.

[20] H. Addach, P. Berçot, M. Rezrazi, and J. Takadoum, "Study of the electrochemical permeation of hydrogen in iron," *Corrosion Science*, vol. 51, pp. 263-267, 2009.

[21] P. Manolatos, M. Jerome, C. Duret-Thual, and J. Le Coze, "The electrochemical permeation of hydrogen in steels without palladium coating. Part I: Interpretation difficulties," *Corrosion Science,* vol. 37, pp. 1773-1783, 1995.

[22] E. Fallahmohammadi, F. Bolzoni, G. Fumagalli, G. Re, R. Ballinger, Y. Maruno, *et al.*, "Effect of plastic deformation on hydrogen diffusion of X65 pipeline steel," *Proceedings of NACE Corrosion,* 2014.

[23] J. A. Ávila, C. O. Ruchert, P. R. Mei, R. R. Marinho, M. T. Paes, and A. J. Ramirez, "Fracture toughness assessment at different temperatures and regions within a friction stirred API 5L X80 steel welded plates," *Engineering Fracture Mechanics,* vol. 147, pp. 176-186, 2015.

Chapter VII

Conclusions

VII.1 Introduction

In this work, an improved hydrogen permeation test methodology was developed. An innovative design of the set-up was constructed in order to combine the hydrogen permeation test with an external loading equipment. As such, permeation experiments could be carried out when the specimen was subjected to a constant tensile load. During the design stage, the focus was put on a better control of the wide variety of parameters affecting the features of the permeation transient. Successively, the different experimental parameters influencing the permeation transient were systematically modified as was discussed in detail in Chapter III. In this way, a better understanding of the electrochemical hydrogen permeation technique was obtained combined with a clear understanding of the effect of the different parameters on the permeation transient.

Different microstructural features, such as dislocations, grain boundaries and carbides, all play a role in the hydrogen/material interaction and consequently also affect the hydrogen diffusivity to a large extent. Therefore, the role of these features were studied and discussed in this work. In Chapter IV, a link was demonstrated between the degree of applied cold deformation, and the resulting dislocation density, the hydrogen diffusivity and blister formation. In Chapter V, the focus was put on four different types of carbides and their influence on the hydrogen permeation results.

Besides microstructural features, macroscopic stresses imposed by an applied constant tensile stress, and consequently affecting the characteristics of the crystal lattice also impact the hydrogen diffusion rate. This was demonstrated by permeation experiments with a constant load in the elastic regime. Complementary tests with loads in the plastic range also affected hydrogen diffusion due to the increased amount of lattice defects. The corresponding results were discussed in Chapter VI. Finally, in this chapter, apart from a brief summary of the main results, some suggestions for further research are given.

VII.2 Methodology of the electrochemical permeation technique

During this methodological study, it was found that the surface roughness and the limited amount of impurities present in the electrolyte, have a large impact on realizing a stable entrance surface state, and thus, a constant hydrogen entry flux. Due to the specific texture of the surface, the hydrogen gas bubble formation was modified in a way which led to a more consistent hydrogen uptake. An even more stable entrance potential, i.e. surface state, is obtained by using the ultrapure Milli Q water instead of standard

demi water for making the electrolyte. During the permeation experiment, cations, which were present in the demi water, were indeed deposited on the cathodic surface causing an increase in the hydrogen uptake. This resulted in a clear deflection of the experimental transient from the theoretical one based on Fick's law. The characteristics of the Milli Q water mainly excluded this undesired effect, and, as such, almost a perfect fit was obtained.

Furthermore, it was demonstrated that the partial transient procedure can be used for determining a hydrogen diffusion coefficient which approaches the lattice diffusion coefficient. Consecutive charging cannot be performed when oxidation of the entrance surface is possible or when the exit surface characteristics may vary in between the two transients. Both affect the permeation results of the second and third transient leading to inconsistent values of D_{app}. Finally, it was verified that the apparent diffusion coefficient is independent of the sample thickness.

VII.3 The effect of microstructural features on the hydrogen diffusivity

It is well known that all lattice defects affect the diffusion rate of hydrogen through the microstructure. In this work, it was confirmed that an increased amount of deformation reduced the hydrogen diffusivity. Also, a higher degree of cold rolling resulted in a more heavily blistered sample surface. Microstructural changes induced by the cold deformation process were responsible for these observations as they created additional barriers for hydrogen diffusion and provided suitable nucleation places for blisters.

A recovery heat treatment of the deformed iron specimen did not result in the annihilation of GNDs, but in the rearrangements of the dislocation configurations. This was confirmed by EBSD, which only measured an increased amount of LAGBs. This enlarged LAGB concentration was responsible for an increased amount of defect-free volume in the microstructure and, as such, for a faster hydrogen diffusion. Therefore, it is argued that the hydrogen diffusivity cannot be directly correlated with dislocation density, but rather with the dislocation configurations. Moreover, the heat treatment also resulted in a decreased number of potential blister nucleation sites.

Next to hydrogen trapping sites introduced by cold deformation, the effect on the hydrogen diffusivity of four different types of carbides was also studied during this PhD. The four carbide containing materials were quenched and tempered Fe-C-X alloys, with X = W, Cr, Ti or V. It was found that the delay of the permeation transient was associated with the overall trap density, while the slope of the transient was related to the amount of reversible trapping sites. The highest trapping ability was observed for the V-based alloy followed in decreasing order by the Fe-C-Ti, Fe-C-Cr and the Fe-C-W material. All carbides, except for the W-based ones, had the ability to lower the hydrogen diffusion in the material. Next to the carbide amount and size, the martensitic matrix characteristics and E_a of the trapping sites played a crucial role in the hydrogen diffusivity of the material.

VII.4 Permeation combined with a constant tensile load combined

An applied constant load in the elastic range of the Armco pure iron and DP steel increased the hydrogen diffusivity. Due to the volume increase of the unit cell, interstitial lattice sites were enlarged and hydrogen diffusion was facilitated. At an imposed stress of about the yield stress, which was determined in the uniaxial tensile test, the increasing hydrogen trap density neutralized the increase of the diffusion coefficient caused by the lattice expansion. Additional plastic deformation, on the other hand, continued to slow down the hydrogen diffusion due to the cumulative formation of lattice defects.

The strain field of the specimen at different loading conditions in the constant loading device was mapped by using 3D DIC. Results showed nicely the enlarged strain in the vertical direction and the contraction in the transverse direction in the zone of interest for permeation. However, when reaching stresses in the plastic region, the amount of strain applied by the constant loading device could not be directly related with the one obtained from the uniaxial tensile test. Higher strains were demonstrated in the case of the constant load set-up. Over the full sample, the obtained strain distribution was not homogeneous due to the manual procedure of clamping the sample. Nevertheless, in the zone of interest for the permeation experiments, a homogeneous strain distribution was demonstrated.

VII.5 Suggestions for further research

During this research several important insights and conclusions were drawn. However, when interpreting new results, one comes always up with new issues and ideas which may be investigated in future studies. In this section, some suggestions for further research are formulated.

- In-situ RAMAN measurements may be interesting in order to visualize the variations of the surface during hydrogen charging. As such, the oxidation of the iron surface may be followed in time and earlier conclusions concerning the unstable entering flux may be confirmed. The stability of the passive layer, present at the exit side of the permeation specimen, could also be an important parameter to study. Next to the stability of the layer during the hydrogen charging, it should be interesting to compare the structure of the layer of different materials and of materials with different amount plastic deformation.
- The importance of the surface roughness, which led to a more constant hydrogen entry flux, was shown during this study. However, due to time constraints, it was not possible to investigate the potential effect of different degrees of roughness. It is believed that the groove depth affects the bubble formation, and thus, the hydrogen evolution mechanisms. In addition, instead of mechanical grinding, electrolytic etching or pickling may be another way to introduce a specific roughness pattern playing a role in the hydrogen absorption process.
- When a lower cathodic current density is applied, the efficiency of the hydrogen entry process increases. Therefore, it could be interesting to search for the optimal current density. On the one

hand, it should be as low as possible to avoid hydrogen gas bubbles, but, on the other hand, it should be high enough to ensure the cathodic protection of the sample. Together with a certain roughness pattern, it is believed that an optimal condition exists to ensure the stability of the surface state.

- In order to eliminate the oxygen related reactions at the cathodic surface, a solution based on borax and glycerol, which has a very low oxygen solubility and diffusivity, could be used. It was shown by Hajilou *et al.* [1] that the glycerol-borax electrolyte preserved the integrity of the sample surface. Surface analyses revealed minimal chemical and topography alteration of the surface after different electrochemical treatments. Moreover, if the investigated material shows an inert behaviour in this solution, it could perhaps be used in the exit cell of the permeation set-up.
- During the recovery treatment of deformed Armco pure iron, it was assumed that vacancy clusters annealed out, a process which perhaps contributed to the observed increased hydrogen diffusivity. However, this assumption was not verified. A challenge can be to investigate the hydrogen trapping ability of vacancies and vacancy clusters by combined thermal desorption spectroscopy and isothermal internal friction measurements.
- In this work, a first indication was given concerning the concentration dependence of the hydrogen diffusivity. The concentration was changed by modifying the current density in the cathodic cell of the permeation set-up. However, it was not assured that the concentration difference imposed by the different current density could be associated to the higher uptake caused by the applied constant load. Therefore, it should be interesting to find a link between the hydrogen uptake and the applied load.

[1] T. Hajilou, M. S. Hope, A. H. Zavieh, N. Kheradmand, R. Johnsen, and A. Barnoush, "In situ small-scale hydrogen embrittlement testing made easy: An electrolyte for preserving surface integrity at nano-scale during hydrogen charging," *International Journal of Hydrogen Energy*, 2018.